

LARGE SCALE SEA-AIR ENERGY FLUXES
AND
GLOBAL SEA SURFACE TEMPERATURE FLUCTUATIONS

by

Jane Hsiung Wojcik

A.B., Barnard College, Columbia University
(1974)

M.S., Massachusetts Institute of Technology
(1978)

Submitted to the Department of
Earth, Atmospheric and Planetary Sciences
in Partial Fulfilment of the Requirement of the

Degree of

DOCTOR OF PHILOSOPHY

at the

MASSACHUSETTS INSTITUTE OF TECHNOLOGY

©1983, Massachusetts Institute of Technology

Signature of Author _____

Department of Earth, Atmospheric, and
Planetary Sciences, December, 1983

Certified by: _____

Professor Reginald E. Newell
Thesis Supervisor

Accepted by: _____

Professor Theodore R. Madden
Chairman, Departmental Committee
on Graduate Students

WITHDRAWN
LIBRARIES
MASSACHUSETTS INSTITUTE
OF TECHNOLOGY
APR 19 1984
MIT LIBRARIES

LARGE SCALE SEA-AIR ENERGY FLUXES
AND
GLOBAL SEA SURFACE TEMPERATURE FLUCTUATIONS

by

Jane Hsiung Wojcik

Submitted to the Department of Earth, Atmospheric,
and Planetary Sciences in December, 1983 in partial
requirements for the Degree of Doctor of Philosophy

ABSTRACT

A newly available Consolidated Data Set (CDS) from the U.S. Navy's Fleet Numerical Weather Central in Monterey, California is utilized to investigate large scale energy fluxes at the sea-air interface and global sea surface temperature fluctuations. Sea surface temperature data from January, 1949 to December, 1979 were extracted from the data set along with air temperature, sea level pressure, dew point temperature, wind speed, wind direction, and cloud cover. Five degree latitude by five degree longitude spatial averaging and monthly temporal averaging were applied to the parameters in the data set for the purpose of studying long term large scale fluctuations. The statistical properties of global sea surface temperature are documented through its long term annual and monthly means and variances and frequency distributions. The heat balance of the global ocean surface layer is calculated using bulk flux formulations.

Estimates of oceanic meridional energy transport for the Pacific, the Atlantic and the Indian oceans are made using calculated annual mean surface energy fluxes. The results show a northward transport at all latitudes in the Atlantic Ocean; a poleward transport in both hemispheres centered around 10°S in the Pacific Ocean with a northward transport south of 25°S, and a southward transport at all latitudes in the Indian Ocean. A hypothesis is made on the possible relationship between the cooling of the sea surface temperature in the Northern Hemisphere oceans during 1965-1979 and the large latent heat loss in the Indian Ocean during the same period.

Characterization of nonseasonal global SST variations is made through empirical orthogonal function (EOF) analysis. The first mode is the so-called El Nino mode with a warm eastern tropical Pacific together with a cold north central Pacific. The second mode shows a cooling trend in the northern hemispheric oceans. Nonseasonal fluctuations of SST at two key regions of the Pacific Ocean (the eastern tropical and north central regions in the first global EOF) are investigated further

through autoregressive modeling. It is found that a first order model is adequate to explain variations in the north central Pacific while a second order model is needed for regions in the eastern tropical Pacific. Results from EOF analysis on the nonseasonal component of the net heat flux, the incoming solar radiation and the latent heat flux show that the variation in the net energy flux is completely dominated by the variation in the latent heat flux. The first EOF time series of the net energy flux shows a cooling trend and the first EOF time series of the incoming radiation resembles the time series of the El Nino mode.

Relationships between nonseasonal SST and other nonseasonal sea surface parameters are explored briefly. The variation in air temperature follows closely with that of contemporaneous sea surface temperature. The nonseasonal variation in net energy flux (mostly from the latent heat flux) correlates negatively with SST anomalies while a positive correlation is obtained between the finite difference form of $\partial(\Delta SST)/\partial t$ and the anomalies of the net energy flux.

Thesis Supervisor: Reginald E. Newell
Title : Professor of Meteorology

This thesis is dedicated to
my parents Teh-shu Hsiung and Shiu-fong Hsieh
and to
my husband Michael Wojcik

TABLE OF CONTENTS

ABSTRACT - - - - -	-2
DEDICATION - - - - -	-4
TABLE OF CONTENTS - - - - -	5
LIST OF FIGURES - - - - -	7
LIST OF APPENDIX FIGURES - - - - -	12
LIST OF TABLES - - - - -	13
I. INTRODUCTION - - - - -	-14
II. THE DATA SET - - - - -	20
II.1 History	
II.2 Contents	
II.3 Processing	
II.4 Data Density	
II.5 Notation and Definition of Quantities	
III. STATISTICAL PROPERTIES OF SEA SURFACE TEMPERATURE - - - - -	31
III.1 Annual Mean and Variance	
III.2 Monthly Mean and Variance	
III.3 Frequency Distribution	
IV. ENERGY BUDGET - - - - -	-45
IV.1 Theory	
IV.2 Sensitivity of Flux Formulations	
IV.3 Results	
IV.4 Error Analysis	
V. ESTIMATES OF OCEANIC MERIDIONAL ENERGY TRANSPORT - - - - -	104
V.1 Theory	
V.2 Computation and Results	
V.3 Discussion	
V.4 Differences in Transport between two Periods	

VI. NONSEASONAL VARIATIONS OF SST AND ENERGY FLUXES - - - - -	135
VI.1 EOF Analysis of SST	
VI.2 Statistical Properties of Δ SST:Autoregressive Models	
VI.3 EOF Analysis of Nonseasonal Heat Fluxes	
VI.4 Relationship Between Nonseasonal SST and Other Nonseasonal Parameters	
VII.CONCLUSION - - - - -	-190
APPENDICES	
A. List of Parameters Available on the Data Set - - - - -	-197
B. Problems Associated with 5° by 5° Grid Averaging - - - - -	-199
C. Monthly Mean Maps of Input Meteorological Parameters - - - - -	-204
D. Empirical Orthogonal Functions and Single Value Decomposition	217
E. Wind Stress Calculation - - - - -	223
REFERENCES - - - - -	-235
ACKNOWLEDGEMENT - - - - -	241
BIOGRAPHICAL NOTE- - - - -	-242

LIST OF FIGURES

- Figure 2.1 Indian Ocean SST: average number of observations at each grid square and number of years with observation (January)
- Figure 2.2 Same as 2.1 except for Pacific Ocean SST
- Figure 2.3 Same as 2.1 except for Atlantic Ocean SST
- Figure 2.4 Total number of months with observations at each grid square for Indian, Pacific and Atlantic oceans
- Figure 2.5 Monthly time series of the number of observations averaged over all grid squares
- Figure 3.1 Atlantic Ocean SST: Long term annual mean and standard deviation
- Figure 3.2 Same as 3.1 except for Pacific Ocean SST
- Figure 3.3 Same as 3.1 except for Indian Ocean SST
- Figure 3.4 Contour plot of global long term annual mean SST
- Figure 3.5 Long term monthly mean of SST for January
- Figure 3.6 Long term monthly mean of SST for April
- Figure 3.7 Long term monthly mean of SST for July
- Figure 3.8 Long term monthly mean of SST for October
- Figure 3.9 Indian Ocean SST: long term monthly standard deviation for January and July
- Figure 3.10 Same as 3.9 except for Pacific Ocean SST
- Figure 3.11 Same as 3.9 except for Atlantic Ocean
- Figure 3.12 Typical frequency distribution of SST at selected grid squares
- Figure 3.13 Histograms of frequency distribution of SST and air temperature for three oceans
- Figure 4.1 Frequency distribution histogram of the three oceans for wind speed, zonal and meridional wind components, dew point temperature, cloud cover, and drag coefficients
- Figure 4.2 Transfer coefficients (C_e) and drag coefficients (C_d) versus wind speed for seven different stability classes

- Figure 4.3 Latent heat flux as a function of $q_a - q_s$ and wind speed
- Figure 4.4 Outgoing radiation as a function of cloud cover and air temperature
- Figures 4.5-4.8 Long term monthly mean of net heat flux for January, April, July and October
- Figures 4.9-4.12 Long term monthly mean of incoming solar radiation for January, April, July and October
- Figures 4.13-4.16 Long term monthly mean of latent heat flux for January, April, July and October
- Figures 4.17-4.20 Long term monthly mean of outgoing radiation for January, April, July and October
- Figures 4.21-4.24 Long term monthly mean of sensible heat flux for January, April, July and October
- Figures 4.25-4.28 Seasonal cycle of heat flux components at selected grid squares of the three oceans
- Figure 4.29 February and August zonal mean SST for the Atlantic and Pacific Oceans (from Newell et al, 1981)
- Figure 4.30 Long term annual mean of net heat flux
- Figure 4.31 Long term annual mean of incoming solar radiation
- Figure 4.32 Long term annual mean of latent heat flux
- Figure 4.33 Long term annual mean of outgoing radiation
- Figure 4.34 Long term annual mean of sensible heat flux
- Figure 4.35 Long term annual mean of cloud cover
- Figure 4.36 Long term annual mean of wind speed
- Figure 4.37 Long term annual mean of air-sea temperature difference
- Figure 4.38 Long term annual mean of specific humidity difference
- Figure 4.39 Long term annual mean of drag coefficient (C_e)
- Figure 4.40 Zonal average of heat flux components for the three oceans
- Figure 4.41 Zonal average of SST, air, dew point, $q_s - q_a$, $T_a - T_s$, wind speed, C_e , cloud cover, and wind stress

- Figure 4.42 Meridional profile of annual energy budget for all oceans
- Figure 5.1 Schematic representation of the heat balance of earth-atmosphere-ocean system
- Figure 5.2 The net flux divergence for each 5° latitude belt and the direction of the purposed meridional transport of heat
- Figure 5.3 Meridional heat transport for three oceans separately and combined (positive indicates northward transport)
- Figure 6.1 Global nonseasonal SST: The eigenvalues and the associated sampling errors for the first twenty modes. The eigenvalues are normalized by the total variance and therefore can be considered as percentage of variance explained
- Figure 6.2 First nonseasonal SST eigenvector pattern for 1949-1979 (7.6% of total variance explained)
- Figure 6.3a Time series of the first eigenvector patterns for 1949-1979
- Figure 6.3b Same as 6.3a except for two separate periods: 1949-1964 and 1965-1979
- Figure 6.3c Same as 6.3a except for four seasonally stratified data
- Figure 6.4 Standard deviation of SST for the period 1949-1979
- Figure 6.5 Correlation coefficients of EOF #1 time series and each 5° by 5° grid squares
- Figure 6.6 Cross correlation between time series of EOF #1 and selected squares
- Figure 6.7 Global SST anomaly patterns for November, 1957 and November, 1982
- Figure 6.8 Global SST anomaly pattern for November, 1982
- Figure 6.9 Nonseasonal time series of SST and incoming solar radiation at two selected grid squares
- Figure 6.10 Second nonseasonal SST eigenvector pattern for 1949-1979 (4.29% of total variance explained)
- Figure 6.11 Time series of second eigenvector for the period 1949-1979 and for two separate half periods
- Figure 6.12 Second nonseasonal SST eigenvector pattern for:
a) 1949-1964 (4.62% of total variance explained),
b) 1965-1979 (5.70% of total variance explained)

- Figure 6.13a Third nonseasonal SST eigenvector pattern for 1949-1979 (3.44% of total variance explained)
- Figure 6.13b Time series of third eigenvector for 1949-1979
- Figure 6.14 Autocorrelation functions for the first three eigenvector time series computed for the entire period and for the two half periods separately
- Figure 6.15 Nonseasonal time series of SST for grid squares at 5°S, 80°W (eastern tropical Pacific) and at 30°N, 165°W (north central Pacific)
- Figure 6.16 Autocorrelation function of nonseasonal SST at eastern tropical Pacific and north central Pacific
- Figure 6.17 Autocorrelation coefficient at lag=1 for all grid squares in the global oceans
- Figure 6.18 Residual plots of the first order and second order autoregressive fit at north central Pacific and eastern equatorial Pacific
- Figure 6.19 Autocorrelation of residual from first and second order fit for eastern tropical Pacific and north central Pacific
- Figure 6.20 Time series plots of the net heat flux anomaly and zonal wind anomaly at eastern tropical Pacific and north central Pacific
- Figure 6.21 Autocorrelation function of zonal wind anomalies and net heat flux anomalies at eastern tropical Pacific and north central Pacific
- Figure 6.22a EOF #1 of net heat flux anomalies and its associated time series
- Figure 6.22b EOF #1 time series of latent heat flux anomalies
- Figure 6.23 EOF #1 of incoming solar radiation anomalies and its associated time series
- Figure 6.24 Scattergrams of surface air temperature vs. surface sea temperature at four selected grid squares
- Figure 6.25 Global map of correlation coefficients between air temperature and sea temperature
- Figure 6.26 Correlation coefficients between anomalies of SST and net heat flux

- Figure 6.27 Correlation coefficients between anomalies of SST and incoming solar radiation
- Figure 6.28 Correlation coefficients between anomalies of SST and latent heat flux
- Figure 6.29 Correlation coefficients between anomalies of SST and sensible heat flux
- Figure 6.30 Correlation coefficients between anomalies of SST and outgoing radiation flux
- Figure 6.31 Correlation coefficients between anomalies of net heat flux and dT/dt
- Figure 6.32 Correlation coefficients between anomalies of SST and zonal wind stress
- Figure 6.33 Correlation coefficients between anomalies of SST and meridional wind stress

LIST OF APPENDIX FIGURES

- Figure A.1 List of possible parameters present in each of the marine reports in the consolidated data set
- Figure B.1 Time series plots for grid square at 40°N, 60°W of:
 a) monthly mean number of observations,
 b) monthly mean latitudinal position, and
 c) monthly mean longitudinal position
- Figure B.2 Time series plots of SST anomalies at grid 40°N, 60°W using three different averaging methods:
 a) average of anomalies at 25 1° by 1° subsquares,
 b) average with respect to 1° by 1° long term monthly means, and
 c) average with respect to 5° by 5° long term monthly means
- Figures C.1-C.4 Long term monthly means of wind speed for January, April, July and October
- Figures C.5-C.8 Long term monthly means of cloud cover for January, April, July and October
- Figures C.9-C.12 Long term monthly means of specific humidity difference for January, April, July and October
- Figures C.13 C.16 Long term monthly means of surface wind for January April, July and October
- Figures C.17-C.20 Long term monthly means of air temperature for January, April, July and October
- Figures C.21-C.24 Long term monthly means of sea level pressure for January, April, July and October
- Figures E.1-E.4 Long term monthly means of zonal wind stress for January, April, July and October
- Figures E.5-E.8 Long term monthly means of meridional wind stress for January, April, July and October
- Figures E.9-E.12 Long term monthly means of wind stress vector for January, April, July and October

LIST OF TABLES

Table II.1	Summary of CDS source data sets
Table III.1	Range of input parameters
Table IV.1	Total short wave radiation received at the top of the atmosphere (from Ledley, 1983)
Table IV.2	Oceanic albedo as a function of month and latitude (from Payne, 1972)
Table V.1	Heat flux divergence, meridional heat transport and area of 5° latitude belts for Indian, Pacific and Atlantic oceans
Table V.2	Total meridional heat transport by all three oceans
Table V.3a	Comparison of estimates of meridional heat transport for Indian Ocean
Table V.3b	Comparison of estimates of meridional heat transport for Pacific Ocean
Table V.3c	Comparison of estimates of meridional heat transport for Atlantic Ocean
Table V.4	Comparison of estimates of meridional heat transport for all three oceans combined
Table V.5a	Net heat flux estimates for two separate periods(1949-1964 and 1965-1979) and their differences
Table V.5b	Same as Table V.5a except for latent heat flux
Table V.5c	Same as Table V.5a except for incoming solar radiation
Table V.5d	Same as Table V.5a except for sensible heat flux
Table V.5e	Same as Table V.5a except for outgoing radiation flux
Table V.6	Hypothesis test of the differences between latent heat flux means from two separate periods in the Indian Ocean
Table VI.1	Percentage of total variance explained for separate EOF analysis of nonseasonal SST
Table VI.2	Autoregressive model identification using Bayesian Information Criterion
Table VI.3	Percentage of total variance explained of EOF analysis for nonseasonal net heat flux, nonseasonal incoming solar radiation and nonseasonal latent heat flux

CHAPTER I. INTRODUCTION

The world's population has been increasing at an alarming rate. Accompanying this is an increasing demand on our natural resources. It is well known that food production is extremely sensitive to weather fluctuations from year to year. Consumption of our natural resources (as heating fuel and for electricity production, for example) is also, to a large extent, weather dependent. The scarcity of our limited supply of natural resources has made it increasingly important to understand the problem of interannual variability of the weather and, eventually, to explore the possibility of making long range forecasts.

The absorption of solar radiation - the ultimate driving force of the atmosphere - occurs primarily at the earth's surface. The atmospheric circulation and climate are inextricably tied to the energy balance of the earth's land and ocean surfaces. The influence of the ocean on climate is especially important in the area of long range climate forecasting for a number of reasons. First of all, the oceans cover approximately 72% of the earth's surface. Secondly, the heat capacity of the ocean is much greater than that of the atmosphere. The ability of the oceans to 'store' information from past fluctuations on a smaller time scale makes the oceans a potentially promising candidate for the investigation of climatic forecasting. The understanding of the ocean-atmosphere interactions will be a crucial step towards realizing the future goal of a long range climate forecast.

Historically, studies concerning the ocean's role in influencing the climate had been hampered by a lack of adequate data coverage. With recent improvements in collection and archiving historical ship reports of surface observations, there has been a tremendous growth in research related to air-sea interactions. One of the most often reported parameters is sea surface temperature (hereby denoted as SST). The conductive heat loss (sensible heat loss) of the ocean to the air is a function of the temperature difference between the sea and the air. Latent heat loss to the air is a function of the specific humidity difference between the air and the sea, where the specific humidity at the surface is also a function of the surface temperature. Ocean surface temperature is thus one of the main variables in determining the heat content of the air and its temperature. It is the most frequently used parameter in characterizing the fluctuations of the oceanic surface. In order to have an understanding of the air temperature change and hence the climate, we need to have a good understanding of the variability of the sea surface temperature and the physical factors that control the observed changes.

Recent diagnostic studies on the interrelationship between the SST's and the atmosphere have given us new insights into the behavior of this complex system. With advancements made in computer technology and increasingly available data, there have been many articles that concentrate on empirical studies of the air-sea interaction. However, because of the lack of unique or universally agreed on criteria and procedure for processing data and defining relationships, it is very difficult to compare and synthesize these studies into a comprehensive

picture. In addition, most of the works have traditionally concentrated on specific geographic regions. The North Pacific and the North Atlantic have received most of the attention because data coverage in these areas is most complete. Due to the complexity of this coupled system of the oceans and the atmosphere, each having its own time scale of behavior, there exist many different interpretations of how the ocean exerts its influence on climate. Newell and Weare (1976) have found that changes in the Pacific Ocean SST precede atmospheric changes. Frankignoul and Hasselmann (1977) think the ocean is a low pass filter of the shorter range atmospheric fluctuations. Presumably the difference in these conclusions came about because different regions and/or different time periods were studied.

Theoretical studies, in trying to simulate the observed behavior and explain the differences observed in diagnostic studies, have had limited success. One can either use a very simple model which does not always treat the two way feedback mechanisms realistically, or, use general circulation models (GCM) to simulate observed atmospheric circulations given a set of anomalous SST's. The conclusions from these studies do not always clarify the picture. Rowntree (1972,1976a,b) conducted a series of experiments on a GCM using tropical SST anomalies and found local and remote responses in the atmosphere similar to those described by Bjerknes (1966). Others (Chervin and Schneider (1976), Kutzbach et al (1977)), using mid-latitude SST anomalies, have found little resemblance in the model atmosphere compared to what was observed. Most recent studies (Webster (1981) and Pedlosky (1975)) have given us a clue as to why the contradictory conclusions arose. It

seems that two important factors that determine how the atmosphere reacts to a change in SST are : a) the atmospheric mean state when SST anomalies are imposed, and b) the location of the SST anomalies.

There are three main causes of variations in observed SST: radiative transfer which is a function of the cloudiness; heat exchange at the ocean surface; and advective heat transfers from ocean currents, both horizontally and vertically. A clarification of these relationships would be useful in obtaining a more comprehensive theory of sea-air interaction. So far most of the work done on the heat and radiative budget of the oceans is limited to specific regions and periods. Hastenrath and Lamb (1978) have published an atlas of oceanic heat budget for the Indian Ocean, the tropical Atlantic and Pacific Oceans. Bunker (1976) has results for the North Atlantic. Clark (1965) and Wyrтки (1965) have estimates for the North Pacific. Weare et al (1981) have done calculations for the tropical Pacific.

In addition to modulating climate changes through anomalous SST's, the oceans play a major role in maintaining the observed climate on earth. Because of the sphericity of the earth, high latitudes receive less radiation than low latitudes. Without the modifying influence of the oceans the climate would be more severe than it is today. The large heat capacity enables the oceans to store the large amount of radiation received in the summer and to release it in winter. The oceans also assist the atmosphere in transporting the surplus of energy received in the low latitudes to high latitudes where there is an energy deficit. A better knowledge of the exact nature of this oceanic transport is important in understanding how the earth's climate works.

Previous estimates on the magnitudes of the ocean's heat transport have shown that it is comparable to atmospheric heat transport. Vonder Haar and Oort (1973), Newell et al (1974), and Oort and Vonder Haar (1976) have estimated this parameter as a residual in atmospheric energy balance. Oceanographers, (Bryan (1962), Bennett (1978), Wunsch (1980), to name a few,) have also made estimates using direct measurements at hydrographic stations for specific seasons and years. Sverdrup (1957), Budyko (1953), Emig (1967), and Hastenrath (1980,1982) made the calculation using surface energy balance. The uncertainty associated with these estimates, different data base used, and different computation methods used make it difficult to compare these results to obtain a global picture of the oceanic transports.

A comprehensive data set covering the global ocean surface for a period of 1946-1979 became available recently from Fleet Numerical Weather Central in Monterey, California. This data set from the Navy contains ship observations of marine parameters that are needed to calculate the radiative and heat fluxes at the ocean's surface. The completeness of this data set in both space and time provides us the opportunity to take a new look at the energy balance of the global ocean surface. In this study, a survey of global oceanic variability is performed through the analysis of seasonal and nonseasonal variations of the sea surface temperature and the components of the energy balances (incoming and outgoing radiation, sensible and latent heat fluxes) at the surface of the oceans. Oceanic meridional energy transport is estimated for all three oceans using calculated surface energy balance

data and the relationship between the nonseasonal SST and energy fluxes is explored.

Chapter II of this thesis describes the data set. The history, contents, processing and density of observations are discussed. Chapter III presents the annual and monthly mean and variance of the global sea surface temperature. Chapter IV deals with the energy budget calculations. The theory of the energy balance is reviewed and the results of this calculation presented. Chapter V presents the estimates of oceanic meridional transport of energy using data calculated in Chapter IV. The theory and method of computation are discussed and previous estimates reviewed. The results of oceanic energy transport for this 31-year data period are presented. Differences in transports between two shorter periods are calculated. The results and their implication on short period climatic changes are discussed. In Chapter VI, nonseasonal variation of global SST are characterized through empirical orthogonal function analysis. Statistical properties of nonseasonal SST at key regions of the global ocean are found through autoregressive modeling. The nonseasonal variation of global energy flux is also examined using empirical orthogonal function analysis. The relationships between SST and other nonseasonal parameters such as the surface air temperature and the components of energy fluxes are investigated to see how well local energy balance accounts for the observed SST variations. Finally, significant results from this study are summarized in the conclusion.

CHAPTER II THE DATA SET

The data set used for this study is derived from the Consolidated Data Set (CDS) prepared by the Navy's Fleet Numerical Weather Central (FNWC) in Monterey, California. In this chapter, we briefly describe the history, the contents, the processing and the density of this consolidated data set.

II.1 History

The original purpose of the Navy producing a marine data set was to obtain synoptic analysis of hourly sea-level pressure data to diagnose wind fields which are in turn used to drive the FNWC Spectral Wave Model. The model was to be used to produce a 20-year (1956-1975), 6-hourly set of wave fields. The data base of marine surface observations in which this input data existed is the so-called Tape Data Family-11 (TDF-11) data base. However, the format of TDF-11 is such that it was unsuitable for use in synoptic analysis. The relevant data needed to be extracted and reorganized. Since they were undertaking a major effort in processing the data, it was decided that they would include all parameters of the TDF-11 data for the period 1946-1975. This would not only satisfy the needs of the wave spectral modelling study, but would also be useful to future research purposes. After the project was started, new TDF-11 supplemental data and the marine observations archived by FNWC since 1966 (the so-called 'SPOT' reports) became available. In order to form an exceptionally comprehensive data

base, it was decided to consolidate all the above mentioned data sets into a common format. The end product of this effort was the Consolidated Data Set covering a period from January 1946 to January 1980.

II.2 Contents

The basic data categories which were used as input into the CDS were the TDF-11 and FNWC Spot reports of marine surface observations. Table II.1 below list the various data sources and periods covered:

Table II.1

Summary of CDS Source Data

Source Data	Period
TDF -11	1946-1968
TDF -11 Supp. A	1968-1972
TDF -11 Supp. B	1973-1975
TDF -OSV	1946-1970
KUNIA-SPOT	1966-1970
NEDN-SPOT	1970
NEDN-SPOT	1971-1979

The basic TDF-11 data was the product of the first monumental effort made to collect, digitize and organize ships logs of marine observations into machine readable magnetic tapes. This initial effort covered the period from 1946 to 1968. Additional data beyond 1968 were issued in supplemental forms which not only included the post-1968 data but also some historical data back to 1854. The TDF-11 Ocean station

Vessel (OSV) data was maintained as a separate file by FNWC and was not contained in the basic TDF-11 data base supplements. The OSV data also has been included in this consolidation. The FNWC's SPOT data are archived meteorological data reports collected by FNWC. The name 'KUNIA' and 'NEDN' are used to distinguish different formats used. Because of the archiving procedure, tape handling techniques and reporting inconsistencies, the 'SPOT' data set has become a notoriously 'dirty' data set. Altogether, approximately 55 million observations were included in building the CDS data set.

II.3 Processing

The CDS from FNWC consisted of 36 magnetic tapes of 6250 bpi density containing ship log observations in packed binary format. The data set obtained was organized by mardsen squares (10° by 10° square). Within each mardsen square, data were sorted in ascending order by 1° by 1° subsquares. For each 1° subsquare, data have been ordered chronologically over the period 1946-1979. In the original report, up to 43 parameters were recorded including: source, longitude, latitude, data, time and the marine observations such as wind and sea surface temperature. A detailed list of the parameters available within each report is included in Appendix A.

Of the 43 marine parameters available, 9 were extracted from each report. They are: sea-level pressure, air temperature, sea surface temperature(SST), dew point temperature, wind direction, wind speed, total cloud amount, low level cloud amount and wet bulb temperature.

In addition, we extracted the associated time and space parameters: year, month, day, hour, longitude ,and latitude.

In order to have a better handle on this copious amount of data, a decision was made to perform some averages over space and time so that the amount of data would be manageable for research purposes. In addition, averaging minimizes small-scale noise and data inhomogeneity. Since we are primarily interested in large-scale, global phenomena of climatic variations, we decided to take a 5° latitude and 5° longitude average in space, and a monthly average in time. Before each averaging, each parameter was checked for gross errors and duplications. Duplicate checking was done by comparing consecutive records for an exact match of date, location and time, plus one physical parameter. Due to the limitation of computer time, a more elaborate duplication procedure was out of the scope of this project. Since the Navy has already done some preliminary processing in checking for duplications and validity ranges of data parameters, we believe the final result of averaged data is in fairly good shape.

II.4 Data Density

The final processed data set consists of data from 65°N to 50°S (a total of 1100 5° by 5° squares) for the period January 1949 to December 1979 (a total of 372 months). 504 grid squares are in the Pacific, 312 squares are in the Atlantic and 284 squares are in the Indian Ocean. The average number of observations per month for each grid square is calculated and the results for January are presented in Figures 2.1

a) Indian Long Term(1949-1979) Averaged No. of observations for Month=1 Sea_Surface_Temperature

	20	25	30	35	40	45	50	55	60	65	70	75	80	85	90	95	100	105	110	115	120	125	130	135	140	145	150
35---	143	60	9																								
30---	13	152	69																								
25---				5+																							
20---																											
15---																											
10---																											
5---																											
0---																											
-5---																											
-10---																											
-15---																											
-20---																											
-25---																											
-30---																											
-35---	40	48	65	28	17	14	13	10	9	9	9	10	10	11	11	12	13	19	51	13	2	3	2	2	1	1	
-40---	24	33	10	9	9	10	10	9	9	9	7	8	8	8	9	8	8	7	9	36	42	45	45	39	26	30	
-45---																											
-50---																											

20 25 30 35 40 45 50 55 60 65 70 75 80 85 90 95 100 105 110 115 120 125 130 135 140 145 150

b) Indian Long Term(1949-1979) No. of Year with Observation(maximum 31 yrs) for Month=1 Sea_Surface_Temperature

	20	25	30	35	40	45	50	55	60	65	70	75	80	85	90	95	100	105	110	115	120	125	130	135	140	145	150
35---	23	22	21																								
30---	21	22	23																								
25---				26																							
20---																											
15---																											
10---																											
5---																											
0---																											
-5---																											
-10---																											
-15---																											
-20---																											
-25---																											
-30---																											
-35---	30	30	29	25	72	23	24	22	23	23	23	24	23	23	22	23	24	26	29	25	16	10	9	14	5	4	
-40---	29	24	22	21	22	21	23	22	21	21	22	23	20	21	21	22	23	24	27	26	25	26	25	25	25	26	
-45---																											
-50---																											

20 25 30 35 40 45 50 55 60 65 70 75 80 85 90 95 100 105 110 115 120 125 130 135 140 145 150

Figure 2.1 Indian Ocean SST: a) Average number of observations, and b) number of years with observation at each grid square (January).

through 2.3 . A maximum number of observations up to four hundred a month are found at several places. These are locations where there were ocean station vessels. Included in these figures are the number of years each grid square had observations in January. This is an indication of how complete the time series is in each grid square (31 indicates a complete time series of 31-years.) Figure 2.4 presents the total number of months with observations in each square for the 31-year

Indian Total number of Month with Observation for Sea_Surface_Temperature.

Table with columns for months (20-150) and latitude ranges (-50 to 35). Data represents the number of months with observations for sea surface temperature in the Indian Ocean.

Pacific Ocean Long Term Mean (1949-1979) for NO-ob-Obs-for-SST

Table with columns for months (135-90) and latitude ranges (-50 to 65). Data represents the number of months with observations for sea surface temperature in the Pacific Ocean.

Atlantic Total number of Month with Observation for Sea_Surface_Temperature_in_10*Deg.C

Table with columns for months (-100 to 20) and latitude ranges (-50 to 65). Data represents the number of months with observations for sea surface temperature in the Atlantic Ocean.

Figure 2.4 Total Number of months with observations at each grid square for Indian, Pacific and Atlantic oceans

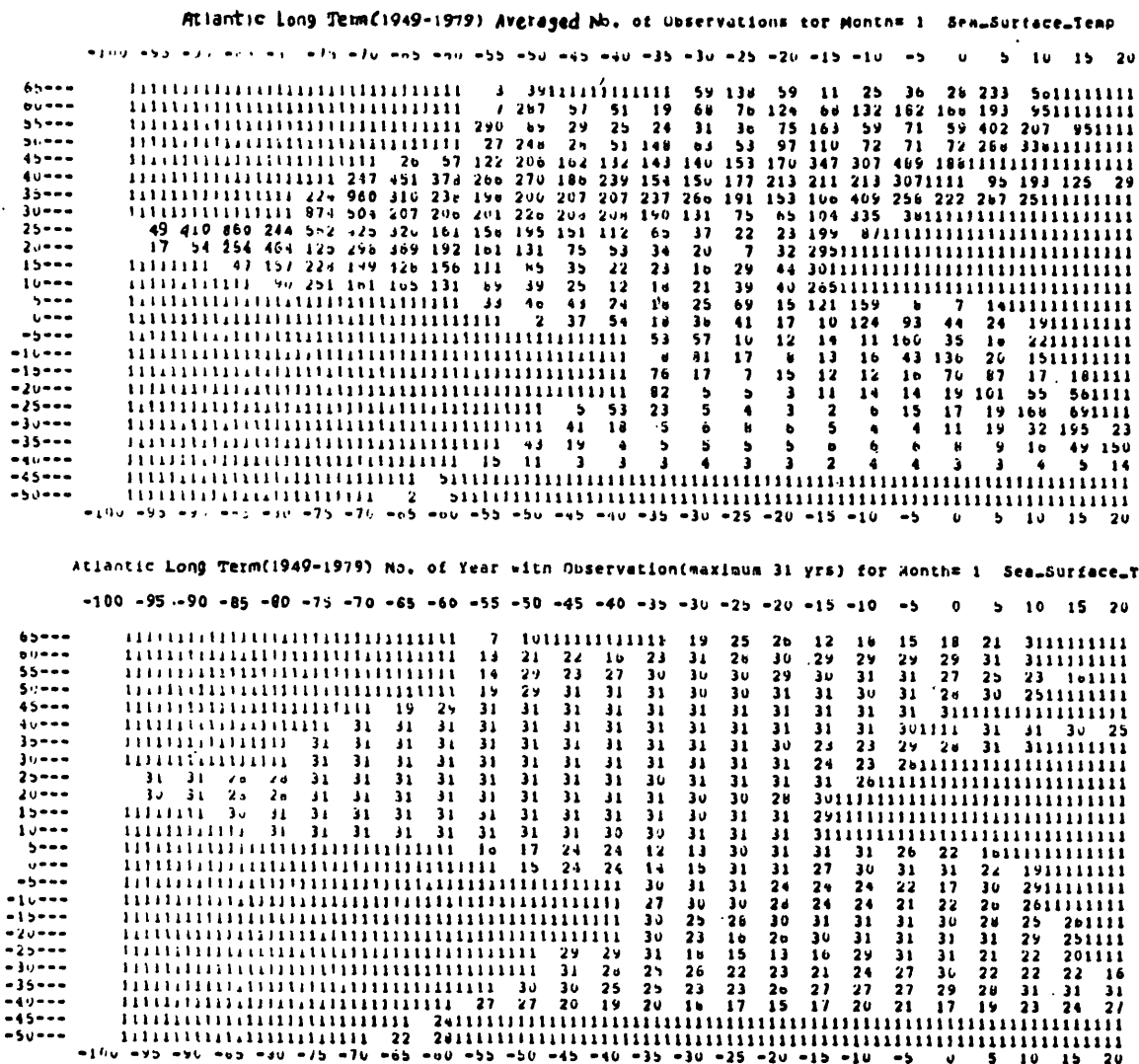


Figure 2.3 Same as 2.1 except for Atlantic Ocean SST

period. Here 372 indicates a complete time series. These figures also outline the geographical boundaries defined in this study for each ocean.

It can be seen from Figures 2.1 through 2.4 that there are serious data gaps for certain regions of the oceans. In the tropics, except for

Pacific Ocean Monthly Mean (1949-1979) for Months 1 for No.-of-Dbs-for-65T

135	140	145	150	155	160	165	170	175	180	-175	-170	-165	-160	-155	-150	-145	-140	-135	-130	-125	-120	-115	-110	-105	-100	-95	-90	-85	-80	-75	-70												
0	0	0	0	0	0	0	0	0	0	0	0	0	0	0	0	0	0	0	0	0	0	0	0	0	0	0	0	0	0	0	0	0	0	0	0	0	0						
0	0	0	0	0	0	0	0	0	0	0	0	0	0	0	0	0	0	0	0	0	0	0	0	0	0	0	0	0	0	0	0	0	0	0	0	0	0	0					
0	0	0	0	0	0	0	0	0	0	0	0	0	0	0	0	0	0	0	0	0	0	0	0	0	0	0	0	0	0	0	0	0	0	0	0	0	0	0	0				
0	0	0	1	13	32	140	40	37	49	62	54	100	98	46	22	51	38	0	0	0	0	0	0	0	0	0	0	0	0	0	0	0	0	0	0	0	0	0	0	0			
0	0	60	52	83	82	96	109	95	84	68	82	74	67	70	72	80	114	170	106	91	0	0	0	0	0	0	0	0	0	0	0	0	0	0	0	0	0	0	0	0	0		
45	88	115	179	131	182	122	91	66	58	66	58	74	59	53	54	56	57	60	70	136	91	49	0	0	0	0	0	0	0	0	0	0	0	0	0	0	0	0	0	0	0		
112	68	457	198	139	111	112	102	98	80	65	75	133	126	133	133	126	133	133	126	133	126	133	126	133	126	133	126	133	126	133	126	133	126	133	126	133	126	133	126	133	126	133	
155	188	216	287	217	171	171	184	173	163	160	123	133	126	133	126	133	126	133	126	133	126	133	126	133	126	133	126	133	126	133	126	133	126	133	126	133	126	133	126	133	126	133	
276	135	76	59	81	108	129	139	131	124	102	87	88	76	60	78	201	187	100	59	43	26	113	99	0	0	0	0	0	0	0	0	0	0	0	0	0	0	0	0	0	0	0	0
176	93	105	57	43	46	49	48	50	72	96	107	125	132	100	132	117	52	47	52	59	63	60	54	105	223	142	28	0	0	0	0	0	0	0	0	0	0	0	0	0	0	0	0
64	37	73	91	25	14	10	10	14	12	8	4	9	10	11	8	7	10	12	9	8	8	6	7	9	12	22	48	121	176	0	0	0	0	0	0	0	0	0	0	0	0	0	
16	18	16	52	25	9	8	11	4	2	2	4	3	2	4	2	3	4	4	5	4	5	5	4	5	5	4	7	18	30	36	38	0	0	0	0	0	0	0	0	0	0		
8	14	9	27	26	4	2	2	2	1	1	2	1	1	2	1	2	1	1	2	1	1	2	1	1	2	1	1	2	1	1	2	1	1	2	1	1	2	1	1	2	1	1	
-59	0	0	0	0	0	0	0	0	0	0	0	0	0	0	0	0	0	0	0	0	0	0	0	0	0	0	0	0	0	0	0	0	0	0	0	0	0	0	0	0	0	0	
-108	0	0	0	0	0	0	0	0	0	0	0	0	0	0	0	0	0	0	0	0	0	0	0	0	0	0	0	0	0	0	0	0	0	0	0	0	0	0	0	0	0	0	
-158	0	0	0	0	0	0	0	0	0	0	0	0	0	0	0	0	0	0	0	0	0	0	0	0	0	0	0	0	0	0	0	0	0	0	0	0	0	0	0	0	0	0	
-208	0	0	0	0	0	0	0	0	0	0	0	0	0	0	0	0	0	0	0	0	0	0	0	0	0	0	0	0	0	0	0	0	0	0	0	0	0	0	0	0	0	0	0
-258	0	0	0	0	0	0	0	0	0	0	0	0	0	0	0	0	0	0	0	0	0	0	0	0	0	0	0	0	0	0	0	0	0	0	0	0	0	0	0	0	0	0	0
-308	0	0	0	0	0	0	0	0	0	0	0	0	0	0	0	0	0	0	0	0	0	0	0	0	0	0	0	0	0	0	0	0	0	0	0	0	0	0	0	0	0	0	0
-358	0	0	0	0	0	0	0	0	0	0	0	0	0	0	0	0	0	0	0	0	0	0	0	0	0	0	0	0	0	0	0	0	0	0	0	0	0	0	0	0	0	0	0
-408	0	0	0	0	0	0	0	0	0	0	0	0	0	0	0	0	0	0	0	0	0	0	0	0	0	0	0	0	0	0	0	0	0	0	0	0	0	0	0	0	0	0	0
-458	0	0	0	0	0	0	0	0	0	0	0	0	0	0	0	0	0	0	0	0	0	0	0	0	0	0	0	0	0	0	0	0	0	0	0	0	0	0	0	0	0	0	0
-508	0	0	0	0	0	0	0	0	0	0	0	0	0	0	0	0	0	0	0	0	0	0	0	0	0	0	0	0	0	0	0	0	0	0	0	0	0	0	0	0	0	0	0

Figure 2.2 Same as Fig. 2.1 except for Pacific Ocean SST

areas right off coastal regions, data is generally sparse. This is especially true in the central tropical Pacific. There are also voids in major parts of the southern Atlantic Ocean, southern Indian Ocean, and southeast Pacific Ocean. The grid squares with high numbers of observations seem to lie along the ship routes. Overall the north Atlantic and north Pacific have the best coverage.

In addition to variations in number of observations per month in space, there are large fluctuations in the average number of observations in the 31-year period as well. Figure 2.5 presents the number of observations averaged over all the available squares for each of the three oceans as a function of time. Note there is a large jump in data density in 1964 and onward. Presumably this is from the infusion of data from various countries under a WMO agreement to collect and archive marine reports. The drop of number of observations in 1970 is puzzling. (Sources from British Meteorological Office in Bracknell,

NO. OF OBSERVATIONS FOR THREE OCEANS

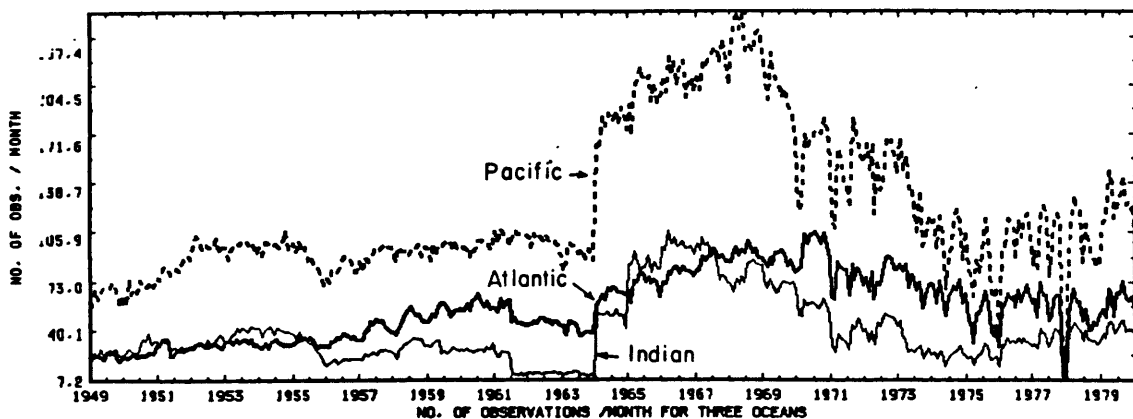


Figure 2.5 Average number of observations per month

England claim that the data source from the Soviet Union has stopped since 1970.) We suspect there are also more recent reports that were not available when the consolidated data set was prepared.

The 5° by 5° averaging in space presented another problem in regions where there are strong temperature gradients within the square (for example the Gulf Stream region). There would not be any problem if the observations within each square were evenly distributed. However, this was not always the case. We found instances where there were significant drifts in the movement of ships during our data period. In some squares, the drift was severe enough to introduce an artificial temporal trend in the data. Appendix B documents one such particular square and the efforts that were made to correct this situation.

II.5 Notation and Definition of Data Quantities

It should be pointed out that in all figures presented in this document negative latitude indicates southern hemisphere and negative longitude indicates west of the Greenwich Meridian. Each of the 5° by 5° squares are referred to by the latitude and longitude of its southeast corner. (i.e. the square denoted by 5 and -30 in the Atlantic refers to the square from 5°N to 10°N and from 30°W to 35°W.) This notation will be used throughout this thesis whenever references are made to any particular grid point.

Several quantities are referred to often in this study and will be defined here formally:

The long term annual mean for any variable x at any geographical location i is defined as:

$$\bar{x}_i = \frac{1}{N \cdot M} \sum_{k=1}^N \sum_{j=1}^M x_{ijk}$$

where N is the number of years and M the number of months with available data at i . The long term monthly mean for any month j is defined as:

$$\bar{x}_{ij} = \frac{1}{N} \sum_{k=1}^N x_{ijk}$$

The standard deviation for the annual mean is

$$s_i = \left[\frac{1}{N \cdot M} \sum_{k=1}^N \sum_{j=1}^M (x_{ijk} - \bar{x}_i)^2 \right]^{1/2}$$

and the same quantity for the monthly mean is

$$s_{ij} = \left[\frac{1}{N} \sum_{k=1}^N (x_{ijk} - \bar{x}_{ij})^2 \right]^{1/2}$$

The monthly anomaly is defined as the departure from the monthly mean:

$$x'_{ijk} = x_{ijk} - \bar{x}_{ij}$$

CHAPTER III STATISTICAL PROPERTIES OF SST

In this chapter we present some statistical properties of the global SST field derived from CDS. The long term annual and monthly mean and standard deviations of SST are presented. The histograms of the global SST and the autocorrelation of SST are also calculated to give an indication of the nature of the statistical distribution and the persistence in SST.

III.1 Annual Mean and Variance

To characterize the long term behavior of the SST field, the long term annual mean and annual standard deviations for the three oceans are calculated and presented in Figures 3.1 to 3.3 . A plot of the annual mean SST is presented in Figure 3.4. As can be seen in Figure 3.4, the distribution of the annual SST pattern is latitudinal in general except for regions where boundary processes such as upwelling and the western boundary currents dominate. Although the 5° by 5° resolution is perhaps too coarse to absolutely define the Gulf Stream and the Kuro-Shio current, this analysis does show that the temperature gradient in the Gulf Stream is much higher than its counterpart in the Pacific. One can see the influence of the Gulf Stream all the way to 60° N. Upwelling is another important feature. The clearest example is along the South American coast where the 26° isoline bends northward from the 20° S latitude line over the Pacific to the 5° S latitude line near the Peruvian coast. A weaker but still obvious example is the upwelling off

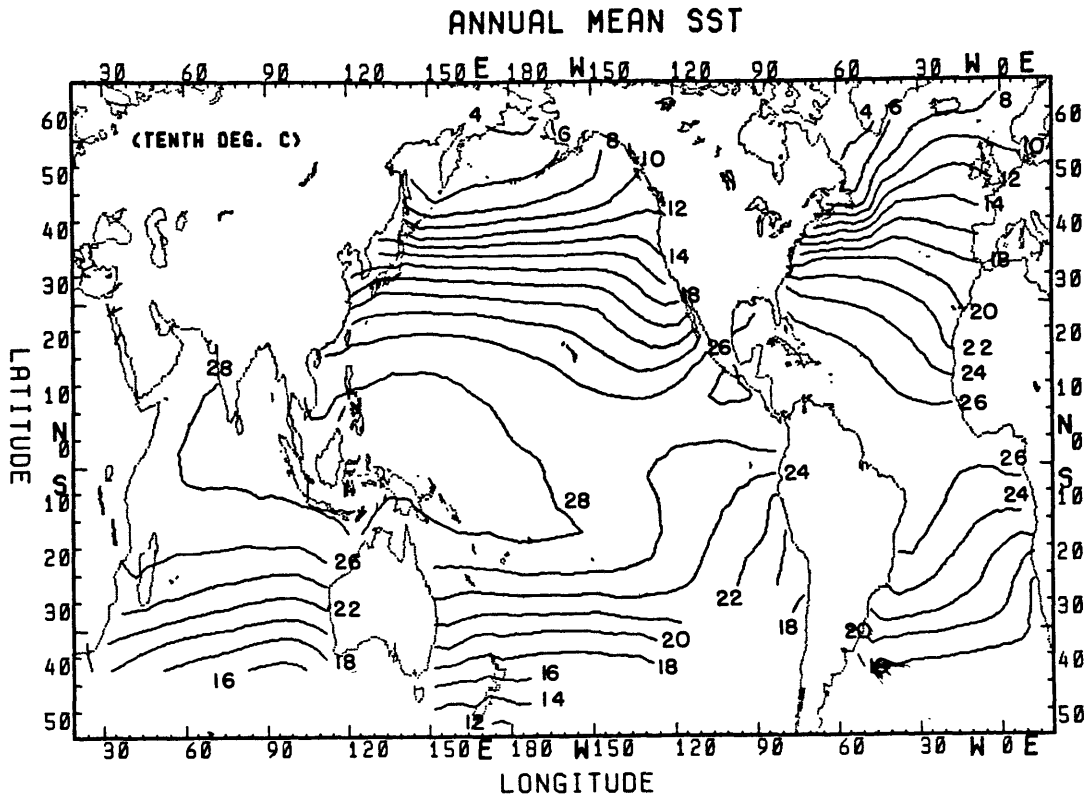


Figure 3.4 Long term (1949-1979) annual mean SST

the African coast. The western Pacific and the eastern Indian Ocean along the equator have a large body of $>28^{\circ}$ temperature, the highest SST observed. Other features include the cool California current and upwelling off Baja California.

Since the annual variance contains seasonal variation, the variances at extratropical regions are obviously larger than those in the tropical region (see Figures 3.1 through 3.3). The largest observed variance occurs, not surprisingly, in western boundary current regions. Water influenced by the Kuro-Shio and the Gulf Stream both have standard deviations larger than 6°C . The Pacific Ocean contains more grids with greater than 3°C standard deviations in mid-latitude than the Atlantic.

Atlantic Ocean Long Term Mean (1949-1979) Using New Filled Data for Atlantic_SST

	-100	-95	-90	-85	-80	-75	-70	-65	-60	-55	-50	-45	-40	-35	-30	-25	-20	-15	-10	-5	0	5	10	15	20	
65---	0	0	0	0	0	0	0	0	0	0	0	0	0	0	0	0	61	48	0	0	59	72	81	86	0	0
60---	0	0	0	0	0	0	0	0	0	0	21	21	47	63	74	83	85	92	88	89	94	93	90	0	0	0
55---	0	0	0	0	0	0	0	0	0	0	47	52	63	75	87	99	108	109	111	100	98	97	99	0	0	0
50---	0	0	0	0	0	0	0	0	0	0	36	72	96	95	108	118	125	128	128	122	121	113	105	0	0	0
45---	0	0	0	0	0	0	0	60	67	66	56	66	128	145	144	143	143	144	141	139	131	0	0	0	0	
40---	0	0	0	0	0	123	110	128	147	139	146	175	177	175	171	166	160	160	154	0	179	177	187	165	0	
35---	0	0	0	0	174	188	213	218	217	213	210	205	201	196	191	188	186	181	178	186	191	191	0	0	0	
30---	0	0	0	0	250	237	232	231	229	227	225	223	220	216	212	207	200	195	193	0	0	0	0	0	0	
25---	248	251	262	261	263	253	252	249	249	246	243	239	235	230	226	219	207	200	0	0	0	0	0	0	0	
20---	257	264	273	271	272	271	269	265	261	258	254	250	245	241	235	227	202	0	0	0	0	0	0	0	0	
15---	0	0	280	279	279	278	275	273	270	266	262	257	251	246	243	237	231	0	0	0	0	0	0	0	0	
10---	0	0	0	279	277	272	275	276	276	274	269	264	260	258	257	255	254	0	0	0	0	0	0	0	0	
5---	0	0	0	0	0	0	0	0	0	277	276	275	270	269	270	270	273	277	0	0	0	0	0	0	0	
0---	0	0	0	0	0	0	0	0	0	0	276	275	273	271	272	270	267	272	271	272	275	275	0	0	0	
-5---	0	0	0	0	0	0	0	0	0	0	0	274	271	268	264	260	256	254	255	260	259	0	0	0	0	
-10---	0	0	0	0	0	0	0	0	0	0	0	0	272	272	268	264	260	254	251	246	246	254	0	0	0	
-15---	0	0	0	0	0	0	0	0	0	0	0	0	269	269	262	257	249	243	235	233	224	223	238	0	0	
-20---	0	0	0	0	0	0	0	0	0	0	0	0	261	262	254	245	238	232	224	217	210	203	182	0	0	
-25---	0	0	0	0	0	0	0	0	0	0	231	237	252	244	241	238	230	227	221	214	205	195	172	0	0	
-30---	0	0	0	0	0	0	0	0	0	0	222	238	234	229	225	223	219	212	209	207	199	193	178	0	0	
-35---	0	0	0	0	0	0	0	0	186	209	195	0	0	0	193	190	190	191	187	184	183	181	172	0	0	
-40---	0	0	0	0	0	0	0	0	0	0	0	0	0	0	0	0	0	0	0	0	0	0	0	0	0	
-45---	0	0	0	0	0	0	0	0	0	0	0	0	0	0	0	0	0	0	0	0	0	0	0	0	0	
-50---	0	0	0	0	0	0	0	0	0	0	0	0	0	0	0	0	0	0	0	0	0	0	0	0	0	

Atlantic Ocean Long Term Standard Deviation (1949-1979) Using New Filled Data for Atlantic_SST

	-100	-95	-90	-85	-80	-75	-70	-65	-60	-55	-50	-45	-40	-35	-30	-25	-20	-15	-10	-5	0	5	10	15	20																
65---	11	11	11	11	11	11	11	11	11	11	11	11	11	11	11	11	15	18	11	20	20	19	21	11	11	11															
60---	11	11	11	11	11	11	11	11	11	11	11	11	11	11	11	11	18	17	22	19	17	15	17	16	16	15	17	25	24	11	11	11	11	11							
55---	11	11	11	11	11	11	11	11	11	11	11	11	11	11	11	11	22	22	21	19	18	18	16	16	16	19	24	32	41	11	11	11	11	11							
50---	11	11	11	11	11	11	11	11	11	11	11	11	11	11	11	11	28	26	18	21	19	18	18	19	20	26	30	38	47	11	11	11	11	11							
45---	11	11	11	11	11	11	11	11	11	11	11	43	55	53	46	38	28	21	20	20	20	21	22	24	28	11	11	11	11	11	11	11	11	11							
40---	11	11	11	11	11	11	11	11	11	11	11	57	47	50	45	45	37	28	27	27	26	26	25	23	21	11	11	40	37	39	42	11	11	11	11						
35---	11	11	11	11	11	11	11	11	11	11	11	61	47	36	31	30	30	29	28	27	26	26	24	22	21	32	38	38	11	11	11	11	11	11	11						
30---	11	11	11	11	11	11	11	11	11	11	11	26	28	30	30	30	29	28	27	26	25	23	22	21	20	22	11	11	11	11	11	11	11	11	11	11					
25---	35	34	24	25	20	23	23	24	22	22	21	20	20	20	20	20	19	16	18	11	11	11	11	11	11	11	11	11	11	11	11	11	11	11	11	11					
20---	26	21	15	19	15	14	15	14	14	14	14	14	14	14	14	14	17	17	18	11	11	11	11	11	11	11	11	11	11	11	11	11	11	11	11	11	11				
15---	11	11	11	11	11	10	10	11	10	10	10	10	10	10	10	10	12	13	14	16	19	31	11	11	11	11	11	11	11	11	11	11	11	11	11	11	11	11			
10---	11	11	11	11	11	8	9	10	9	9	8	9	10	12	12	13	14	17	27	11	11	11	11	11	11	11	11	11	11	11	11	11	11	11	11	11	11	11			
5---	11	11	11	11	11	11	11	11	11	11	11	7	6	8	8	9	8	7	9	10	8	11	11	11	11	11	11	11	11	11	11	11	11	11	11	11	11	11	11		
0---	11	11	11	11	11	11	11	11	11	11	11	6	4	5	6	6	10	13	13	13	15	16	15	14	11	11	11	11	11	11	11	11	11	11	11	11	11	11	11		
-5---	11	11	11	11	11	11	11	11	11	11	11	7	8	10	13	15	18	18	19	20	22	11	11	11	11	11	11	11	11	11	11	11	11	11	11	11	11	11	11		
-10---	11	11	11	11	11	11	11	11	11	11	11	11	9	10	12	14	14	17	18	11	11	11	11	11	11	11	11	11	11	11	11	11	11	11	11	11	11	11	11		
-15---	11	11	11	11	11	11	11	11	11	11	11	11	11	11	11	11	11	11	13	14	17	18	20	24	27	11	11	11	11	11	11	11	11	11	11	11	11	11	11		
-20---	11	11	11	11	11	11	11	11	11	11	11	11	11	11	11	11	11	11	13	15	16	15	14	15	17	18	20	21	24	11	11	11	11	11	11	11	11	11	11		
-25---	11	11	11	11	11	11	11	11	11	11	11	11	11	11	11	11	11	11	11	11	11	11	11	11	11	11	11	11	11	11	11	11	11	11	11	11	11	11	11	11	
-30---	11	11	11	11	11	11	11	11	11	11	11	11	11	11	11	11	11	11	11	11	11	11	11	11	11	11	11	11	11	11	11	11	11	11	11	11	11	11	11	11	
-35---	11	11	11	11	11	11	11	11	11	11	11	11	11	11	11	11	11	11	11	11	11	11	11	11	11	11	11	11	11	11	11	11	11	11	11	11	11	11	11	11	
-40---	11	11	11	11	11	11	11	11	11	11	11	11	11	11	11	11	11	11	11	11	11	11	11	11	11	11	11	11	11	11	11	11	11	11	11	11	11	11	11	11	
-45---	11	11	11	11	11	11	11	11	11	11	11	11	11	11	11	11	11	11	11	11	11	11	11	11	11	11	11	11	11	11	11	11	11	11	11	11	11	11	11	11	11
-50---	11	11	11	11	11	11	11	11	11	11	11	11	11	11	11	11	11	11	11	11	11	11	11	11	11	11	11	11	11	11	11	11	11	11	11	11	11	11	11	11	11

Figure 3.1 Atlantic Ocean SST: Long term annual mean and standard deviation

The variance in the tropical region varies typically from $.7^{\circ}\text{C}$ to 1.0°C . The exception is in the eastern tropical Pacific where standard deviations of 2.7°C are observed. The upwelling region off the coast of North Africa is also of note. Standard deviations as high as 3.1°C are observed. In the Indian Ocean, the Adria Sea is where the largest variance (4.1°C) occurs.

III.2 Monthly Mean and Variance

The long term monthly means of SST are calculated and the results for one month in each season are illustrated from Figures 3.5 to 3.8 . In general, the variations in higher latitudes are mostly zonal with the exception of the Gulf Stream region and upwelling areas. The longitudinal variation is most evident in the Atlantic ocean. The mean temperature gradient in the southwest Pacific and south Indian ocean stays fairly constant throughout the year. In the tropical oceans, the most pronounced feature is the migration of the $>28^{\circ}$ body of water. It expands from January to April and moves northward in July. The location changes relatively little from summer to fall. The mean temperature gradient in the eastern Pacific has large seasonal variations. In January, it is at a minimum. In April, the intensification starts at the Peruvian coast when the expansion of the 28° C water pushes the gradient southeastward. By July, its value is about twice that of January. The gradient gradually starts decreasing in the fall. Similar movement is observed off the south African coast in the Atlantic and at the 20° S region in the Indian Ocean.

When the seasonal component is removed by calculating the standard deviation with respect to individual monthly means, the scenario changes somewhat from the annual standard deviations. Figure 3.9 to 3.11 presents the standard deviations of the three oceans. Months January and July are selected to illustrate the standard deviations representative of the winter and the summer seasons. In Figures 3.10 and 3.11, the Gulf Stream and the Kuro-Shio still dominate the variance

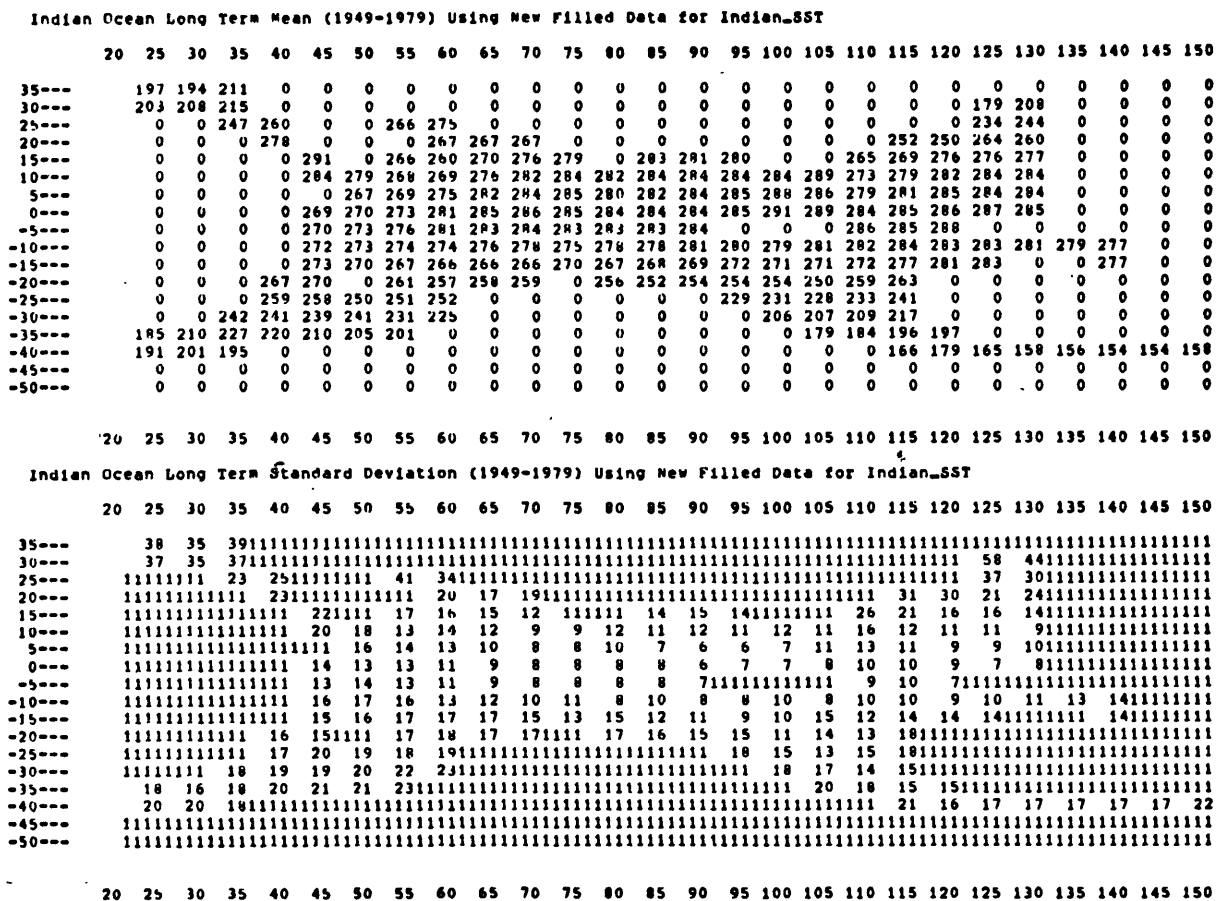


Figure 3.3 Indian Ocean SST: Long term annual mean and standard deviation

pattern of the global ocean although their magnitudes are much smaller than the annual case (maximum of 2.5°C is observed in the Kuro-Shio in winter.) The variances in upwelling regions of the oceans become comparable to the western boundary current regions. There is not a great deal of difference among the standard deviation of different months, although summer standard deviations seem to be slightly larger. The southern hemisphere generally exhibits larger variance than northern hemisphere at the same latitude. In general, our long term statistics of the global sea surface temperature do not show any unexpected features except for the more extensive coverage in the Southern Hemisphere.

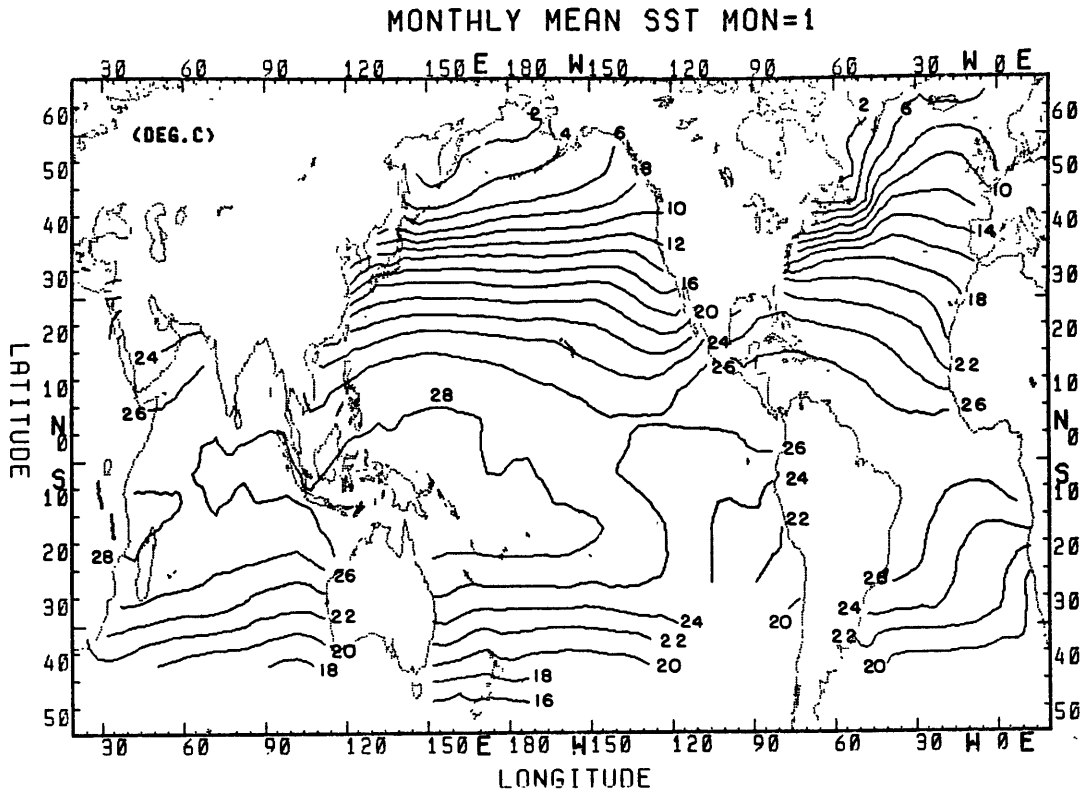


Figure 3.5 Long term monthly mean of SST for January

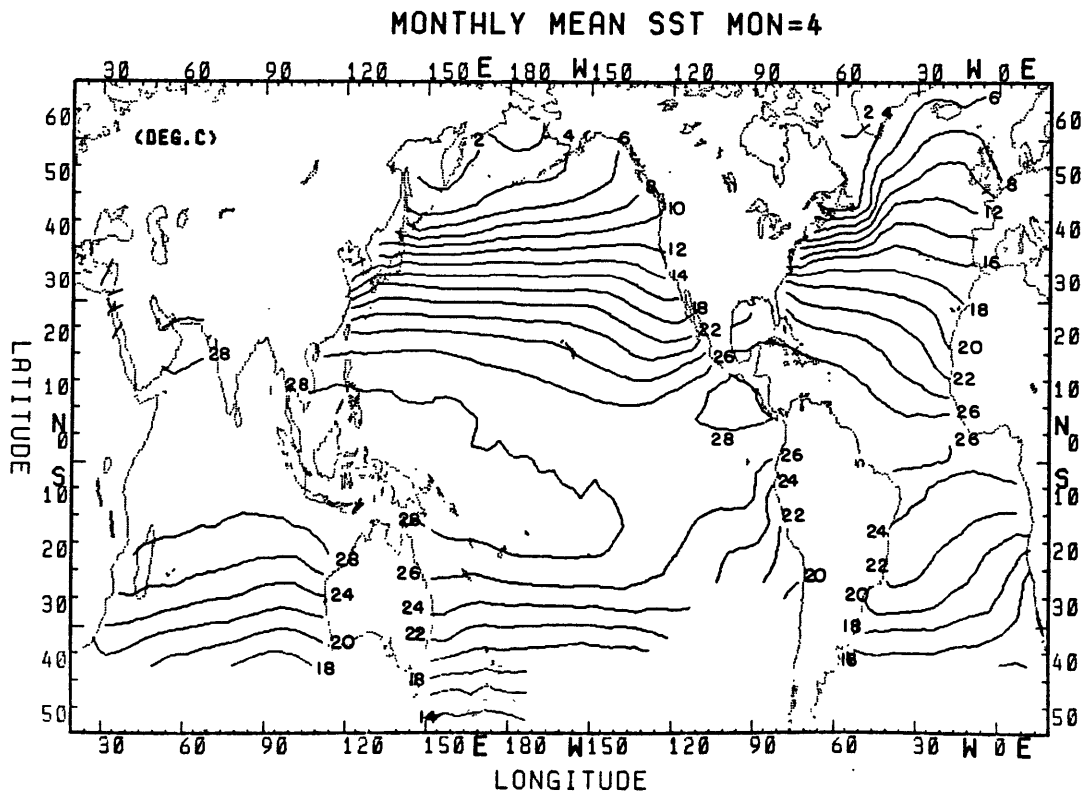


Figure 3.6 Long term monthly mean of SST for April

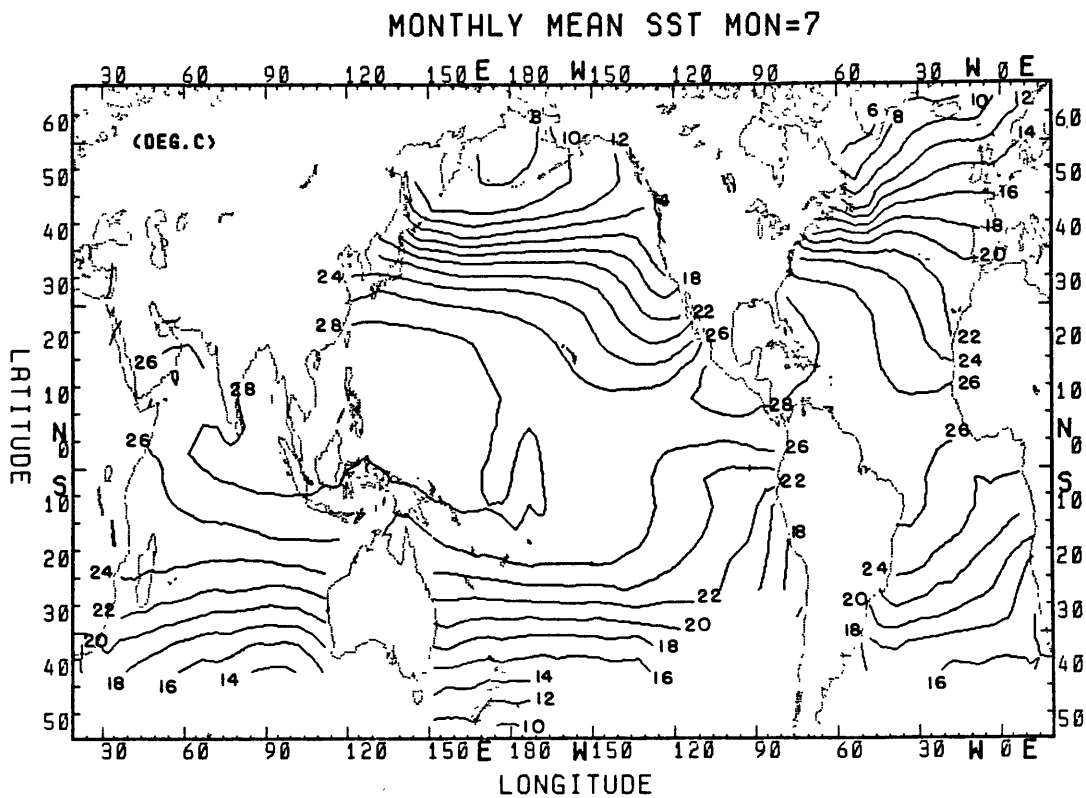


Figure 3.7 Long term monthly mean of SST for July

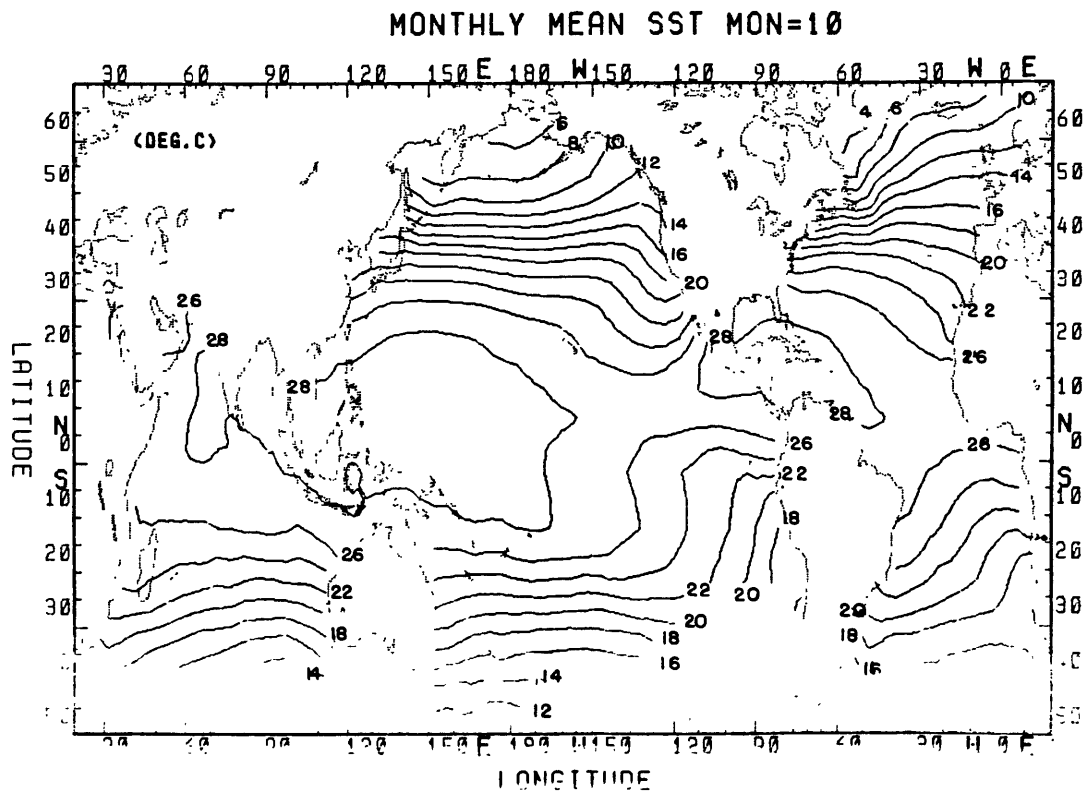


Figure 3.8 Long term monthly mean of SST for October

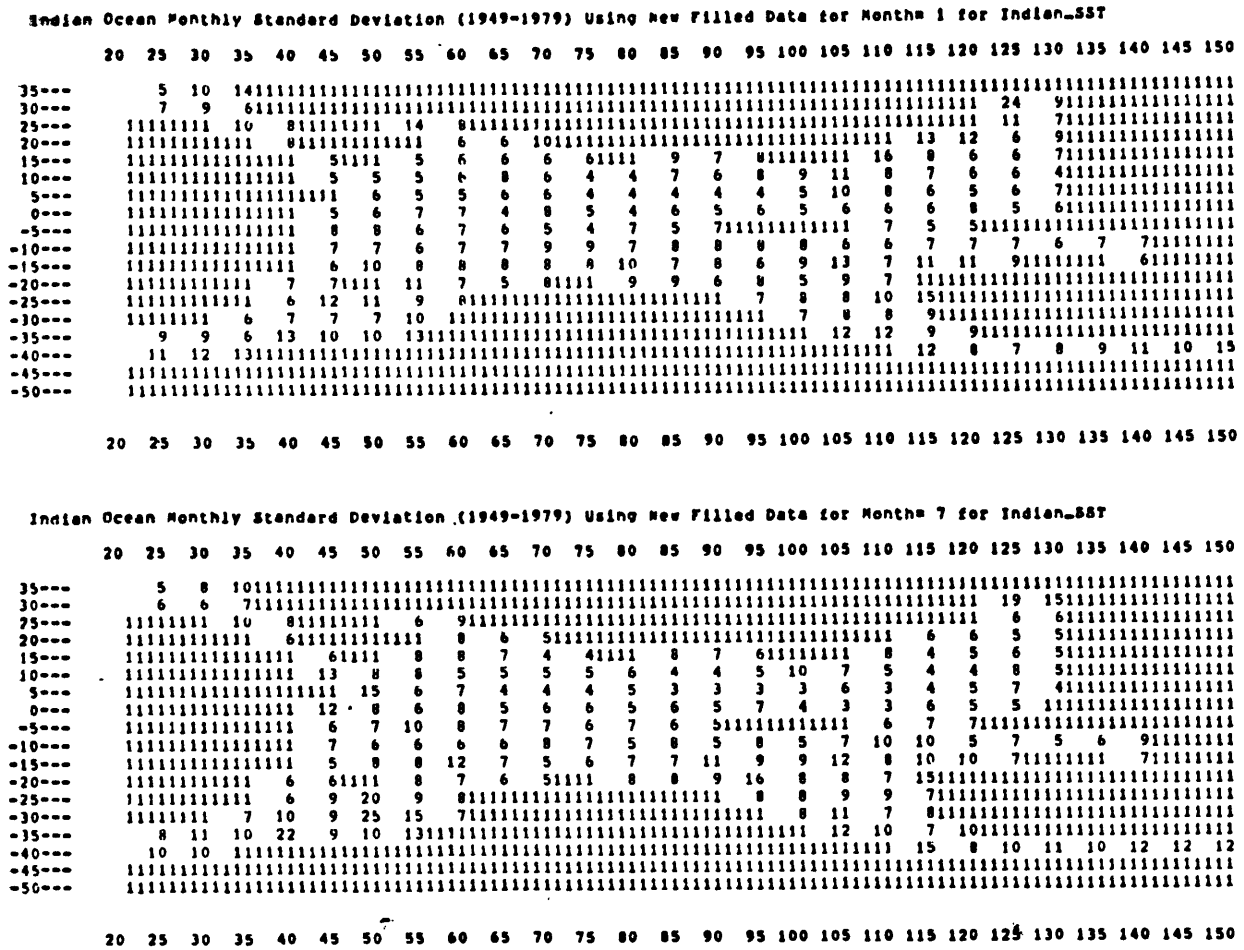
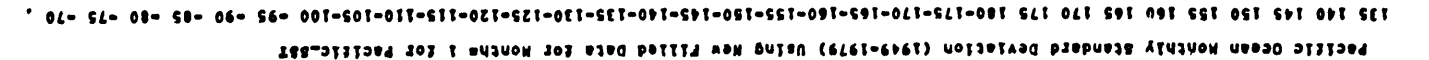
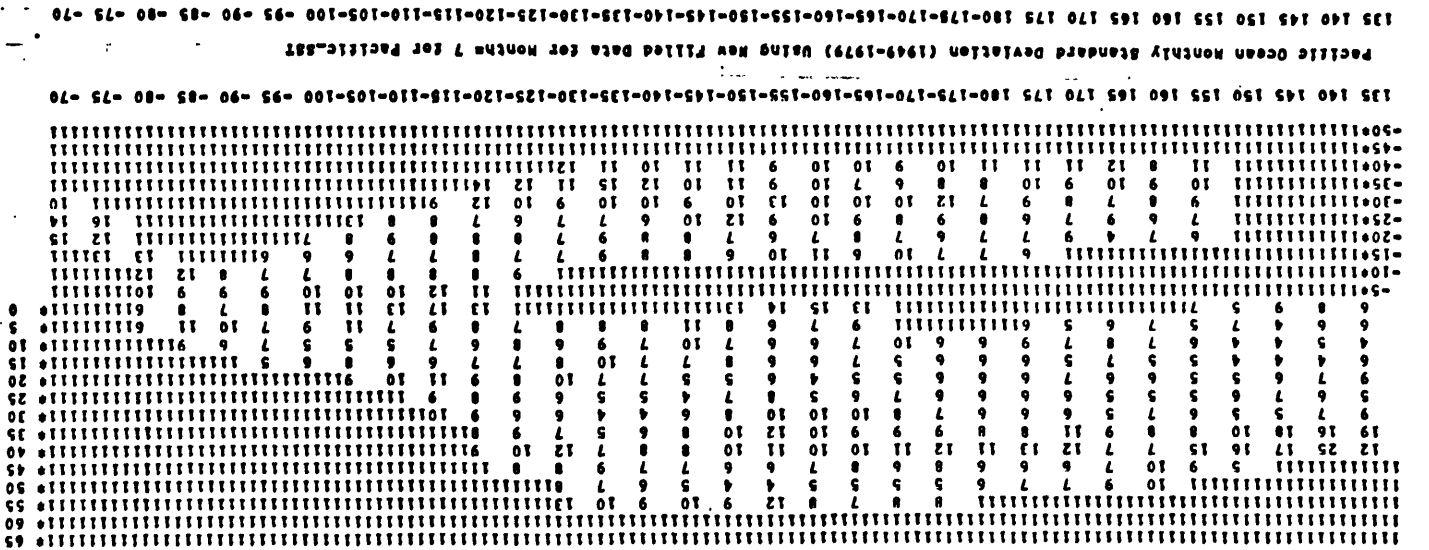
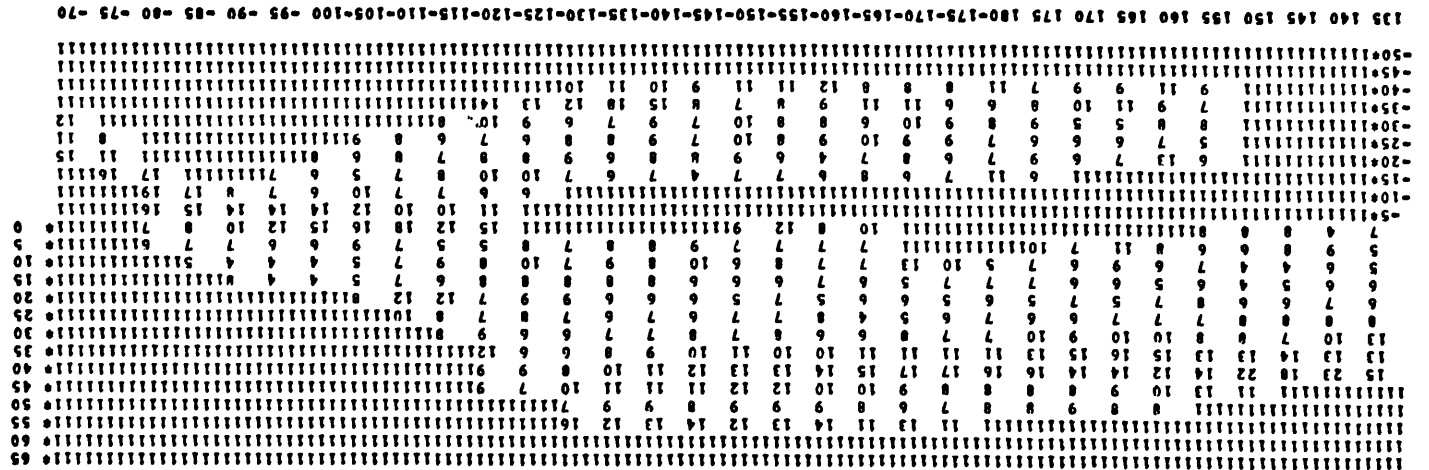


Figure 3.9 Indian Ocean SST: Long term monthly standard deviation for January and July

III.4 Frequency Distribution

The variance field give us an idea of how variable the oceans are and the mean field tells us the expected value at any given month. It would be of interest to know how the SST is distributed from a statistical point of view. If we have a normally distributed variable,

Figure 3.10 Pacific Ocean SST: Long term monthly standard deviation for January and July.



4.5% of the time and anomalies three times its standard deviation should not occur more than .2% of the time if a given variable is normally distributed. We have calculated histograms for every grid point of the ocean and applied the normality test (p.121 Bendat and Piersol) to check whether SST's are normally distributed. The result is overwhelmingly negative. Less than 2% of the total possible 1100 grid squares can be considered to have a normal distribution and there is no spatial coherence to those grid squares that do indicate a normal distribution.

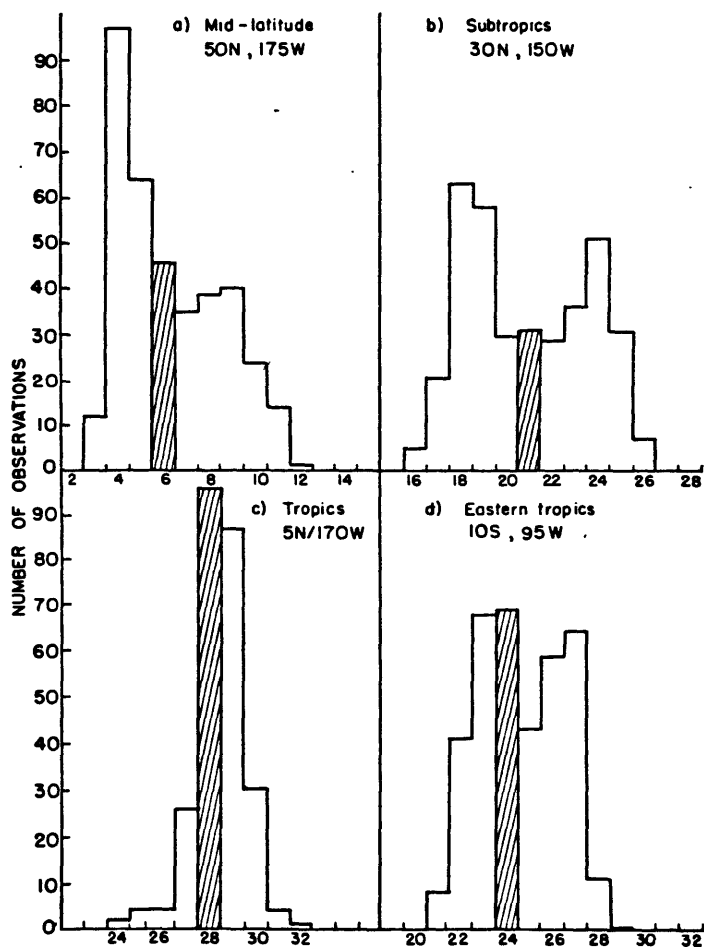


Figure 3.12 Typical frequency distribution of SST at selected grid squares

The results of the histograms from this analysis are too voluminous to present completely. Figure 3.12 illustrates some of the typically observed distributions of SST. Figure 3.12a is the typical pattern of the northernmost high latitude locations. It is a skewed distribution. Figure 3.12b is the typical distribution for regions from 20°N to 45°N in the Pacific and from 25°N to 55°N in the Atlantic. It is clearly a bimodal distribution. Initially, we suspected this might be due to the result of the nonstationarity of the time series with two different long term means for two different periods. The data set was then divided into two subsets: 1949-1964 and 1965-1979. Similar results are observed from both subsets. In addition, a similar bimodal distribution is also observed at mid-latitudes in the southern hemisphere. The monthly mean maps of SST in Figures 3.5 to 3.8 indicate that in these regions the sea surface temperatures tend to have a summer mean and a winter mean, even for the transitional seasons of spring and fall. This led us to conclude that the bimodal structure is from the seasonal cycle at these latitudes.

In the tropics, the distributions become centered around narrower temperature ranges. The exception to this is again in upwelling regions in the tropics where a more 'squatter' distribution is noted. In some squares there is even evidence of another bimodal distribution such as the one shown in Figure 3.12d. This type of distribution might be a result of the frequent occurrence of El Nino which gives the time series a secondary peak that is warmer than the mean. However, the bimodal structure is not observed in all grid squares in the eastern tropical boundary region.

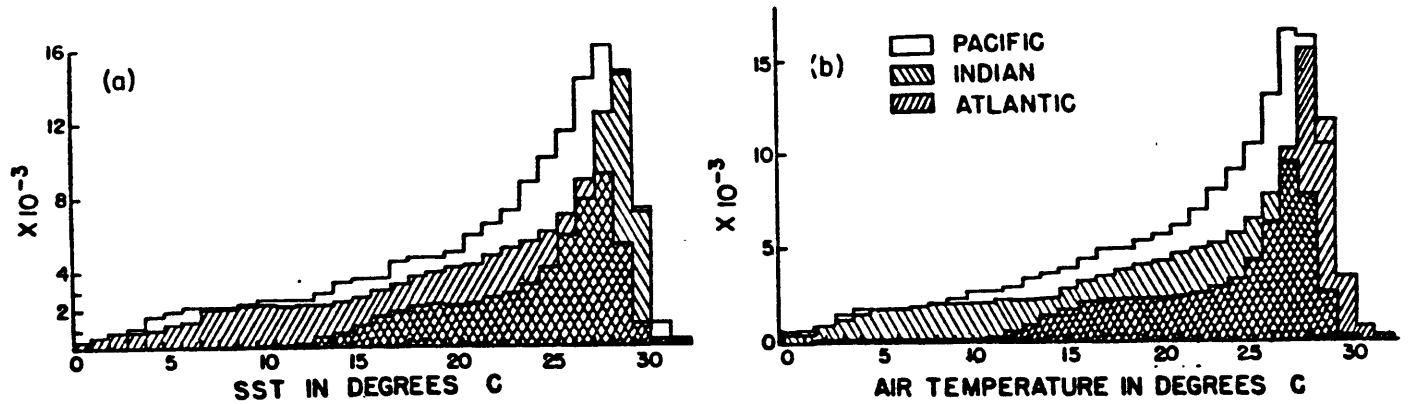


Figure 3.13 Histograms of frequency distribution of SST and air temperature for three oceans

Frequency histograms of SST for each of the three oceans are presented in Figure 3.13 . Together on the same figure is the frequency histograms of air temperature in the data set. As can be seen from the figure, the distributions of SST, and air temperature are almost identical. The SST distributions in the Pacific Ocean and the Indian Ocean both have their maximum at 28°C while the Atlantic peaks at 29°C . One feature worth noting here is that almost no SST (or air temperature) is observed to be larger than 31°C . This fits precisely with the evaporation buffering limit that was proposed by Newell and Dopplick(1979).

CHAPTER IV. ENERGY BUDGETIV.1 TheoryIV.1a Energy Balance of the Surface Layer

The equation governing the change of sea surface temperature can be derived from the second law of thermodynamics (conservation of enthalpy) as:

$$\frac{DT}{Dt} = q \quad (4.1)$$

where T is the sea surface temperature; $D()/Dt$ the total derivative operator and q the rate of heating. Expanding this equation further, we have:

$$\frac{\partial T}{\partial t} = - \mathbf{V} \cdot \nabla T + q \quad (4.2)$$

Here $\partial T/\partial t$ is the local time derivative operator. The term $-\mathbf{V} \cdot \nabla T$ represents the advective processes.

When we consider the sea surface temperature change over a finite mixed layer of uniform temperature with depth D and over a finite time period t , the integral form of the above equation can be written as

$$\int_0^t \int_{-D}^0 (\rho C_p \frac{\partial T}{\partial t}) dz dt = \int_0^t \int_{-D}^0 (Q_v + Q) dz dt + \int_0^t \int_{-D}^0 Q_d dz dt \quad (4.3)$$

where ρ = water density

C_p = specific heat capacity of water

Q = total energy transfer across air-sea surface

Q_v = horizontal advection of heat into the layer

Q_d = vertical flux of heat into the layer at depth D

Theoretically, the local rate of the temperature change over a finite layer can be estimated from Equation (3.3). In practice, this is rarely done because of the following reasons:

- 1) $\partial T/\partial t$ has to be estimated from finite difference schemes,
- 2) Q has to be inferred from empirical formulas,
- 3) the depth of the mixing layer D is not well known,
- 4) the current data needed to estimate Q_v and Q_d are not available directly.

Each of the above factors contributes to the uncertainties of the estimates. In this study, we will not attempt to specify the individual terms in equation (2) directly. However, we do have data available to perform a detailed calculation of the second term in the equation - the total energy flux across the sea and air interface. It is hoped that from this calculation we will see how much of the local SST change is accounted for by this term.

IV.1b Energy Flux Formulations

The total energy flux Q can be separated into four components:

$$Q_{net} = Q_{in} - Q_{out} - Q_h - Q_l \quad (4.4)$$

Here we are using Q_{net} to denote the total energy flux. Q_{in} is the incoming solar radiation; Q_{out} is the outgoing longwave radiation; Q_h is the sensible heat flux and Q_l is the latent heat flux.

The following sections describe the formulations used to estimate each of the components of the energy transfer fluxes.

The formulas applied by most researchers to calculate sensible and latent heat fluxes are the so-called bulk formulas:

$$Q_h = C_p \rho_a C_e |v| (T_s - T_a) \quad (4.5)$$

$$Q_l = L_e \rho_a C_e |v| (q_s - q_a) \quad (4.6)$$

where the meteorological variables are:

$|v|$ = wind speed in m/s

T_s = sea surface temperature in deg. K

T_a = air temperature in deg. K

q_s = specific humidity corresponding to T_s

q_a = specific humidity of air in g/kg

and the constants are:

C_p = specific heat of air ($= 1.0048 \times 10^3 \text{ J kg}^{-1} \text{ K}^{-1}$)

L_e = latent heat of evaporation ($= 2.5008 \times 10^6 \text{ J kg}^{-1}$)

ρ_a = air density in $\text{kg/m}^3 = (RT_a/p_s)$

R = ideal gas constant ($= 287.04 \text{ J kg}^{-1} \text{ K}^{-1}$)

p_s = sea level pressure in mb

C_e = transfer coefficient; function of $|v|$ and $(T_s - T_a)$

These formulae are finite difference approximations of the equation for the vertical flux of a property x :

$$F_x = -\kappa_x \frac{\partial x}{\partial z} \quad (4.7)$$

Here κ_x is the eddy transfer coefficient and turbulent exchange is assumed to be the dominant mechanism affecting the vertical distribution.

The choice of the transfer coefficient is a perplexing problem. Budyko (1963) in his estimate of the annual mean energy transfer over the world ocean used constant transfer coefficients. Bunker (1976) estimated the energy balance over the North Atlantic ocean using an update of the transfer coefficients. He determined values of the coefficients as a function of stability and wind speed from results by other researchers and data of experiments at sea and in laboratories. He ignored the difference between the coefficients of latent heat and that of sensible heat. Since sensible heat flux is an order of magnitude smaller than latent heat, this difference is negligible. Liu et al (1977) developed an iterative method for estimating the transfer coefficients using boundary layer theory.

These are just a few of the available formulations for estimating the transfer coefficient C_e . Although the methods of various estimates of the coefficients are different, the results for most meteorological conditions are quite similar. We decided to use Bunker's formulation of C_e as a function of wind speed and atmospheric stability (defined by the difference between the sea surface temperature and air temperature.) The coefficients are easily calculated with the data on hand.

The meteorological data required to calculate the energy fluxes are $|v|$, T_s , T_a , q_a , q_s , and p_s . All are available from the consolidated data set except q_s and q_a . These are calculated by:

$$q = \frac{.622 \cdot e}{p_s - .378 e} \quad (4.8)$$

where e is the saturation vapor pressure. It is computed using a polynomial approximation as a function of temperature (Lowe, 1977). For q_a , e is calculated using dew point temperature. For q_s , e is calculated using sea surface temperature.

In this study, when $|v|$ is missing, none of the heat fluxes are calculated. When T_a or T_s are missing, sensible heat flux is not calculated. When q_a or q_s are missing, latent heat flux is not calculated. When p_s is missing, air density is assumed to be 1.2 kg/m^3 and p_s is set to 1000 mb in the formulation for q .

The outgoing radiative flux is calculated according to the formula:

$$Q_{\text{out}} = 4 \epsilon \sigma T_a^4 (.39 - .05 \sqrt{e}) \cdot (1 - a_{\text{out}} C^2) + \epsilon \sigma T_a^3 (T_s - T_a)$$

where

Q_{out} = the outgoing long wave radiation

a_{out} = function of latitude; varying from 1. at the poles
to .5 and equator

ϵ = emissivity of water (ratio of radiation of the sea to that of
a black body) = .97

σ = Stefan-Boltzman constant = 5.6697×10^8 in $\text{watt/m}^2 \cdot \text{T}^{-4}$

C = cloud cover in tenths

The notation of meteorological variables are the same as before.

Finding the appropriate formulation for the net radiation received at the surface is an extremely difficult task. First of all, one needs the total radiation (direct and diffuse) received at the ocean surface under clear sky. The direct radiation received at the top of the atmosphere is fairly well known and can be calculated given present day astronomical parameters and a solar constant. To estimate the radiation at the surface, one needs a knowledge of the climatological mean of the transmissivity of the atmosphere, and this is not well known. Secondly, the cloudiness affects the amount of the solar radiation received and its effect is usually included with an empirical relationship. Thirdly, the albedo of the ocean surface has to be taken into consideration. There are uncertainties involved at each stage of the estimation and there are many formulations available in the literature. For comparison sake, one would like to use the same formulation used by most other researchers. Budyko's formulation seemed to be a good choice.

$$Q_{in} = Q_0 (1 - a_{in}C - .38 C^2) (1 - A) \quad (4.10)$$

He used values from Berliand's (1960) estimate as the total radiation received at the surface under clear sky (Q_0), and a quadratic function of cloudiness to correct for the effect of clouds. For oceanic albedo A , he used an empirical estimate of values from .06 to .23 . Application of this formulation gave results that are unrealistically low. For example, in the tropics values of solar radiation received at the

surface are less than 200 watt/m². At the suggestion of Simpson and Paulson (1979), we used a formulation given by Reed (1977) for estimating the insolation over the oceanic surface :

$$Q_{in} = Q_o (1 - .62C + .0019\alpha) (1 - A) \quad (4.11)$$

Here α is the solar noon altitude (in degrees) and is calculated by

$$\sin\alpha = \sin\ell \sin(23.45 \sin(t-82)) + \cos\ell \cos(23.45 \sin(t-82)) \quad (4.12)$$

where ℓ is the latitude and t is the day of the year. Q_o is the total radiation received at the surface. To estimate Q_o , Reed (1977) used a formulation given by Seckel (1970) which, at low latitudes, should be the same as the direct radiation at the top of the atmosphere with a transmissivity of .7 . Since Seckel only gave formulae for low latitudes and we also need values for high latitudes, we decided to use the direct radiation received at the top of the atmosphere calculated by Ledley (1983) using present day astronomical parameters. We then adjusted this for the transmissivity of the atmosphere . It took many experiments to arrive at an appropriate value for the transmissivity of the atmosphere. Values from .75 to .65 were considered as possible candidates. The final selection of .68 is based on the consideration of three constraints. First of all, the incoming solar radiation calculated at the surface using the chosen transmissivity should be comparable with independent calculations by others. For this we have used values

presented by Weare (1980) in the tropics and by Bunker (1976) and Clark (1967) in the mid-latitudes. This comparison ruled out any value greater than .7 because values of Q_{in} calculated were much too large. The second constraint considered was Wunsch's estimates of maximum and minimum transport values at $24^{\circ}N$ and $48^{\circ}N$ in the Atlantic Ocean (personal communication). He presented a range of 8 to 13×10^{14} watts at $24^{\circ}N$ and a range of 1 to 7×10^{14} watts at $48^{\circ}N$. Transmissivity values greater than and equal to .7 would all give transport values that are below the minimum values at these latitudes. The last constraint concerns the transport values at the southern boundaries. Since a north to south integration technique was used to calculate the transport values, the final transport at the southern most latitude ($40^{\circ}S$) should be in general agreement with independent estimates at the same latitude if our values are reasonable. Transport results from Georgi and Toole (1982) at $40^{\circ}S$ were used. They obtained a transport of -6.67×10^{14} watts at $40^{\circ}S$ (negative indicates a southward transport). Transport values calculated for three transmissivity values .7, .68 and .65 gave values of -16.58×10^{14} , -4.37×10^{14} and $+18.74 \times 10^{14}$ respectively. With the above three considerations, a final values of .68 was chosen as the most suitable value to use.

The values of Q_0 used are presented in Table IV.1 . The oceanic albedo (A) is taken from Payne (1972). It is a function of month and latitude, ranging from .4 around the edges of sea ice to .06 at the center of the ocean basin (see Table IV.2). These are climatological results derived from an experimental study of the albedo of the sea

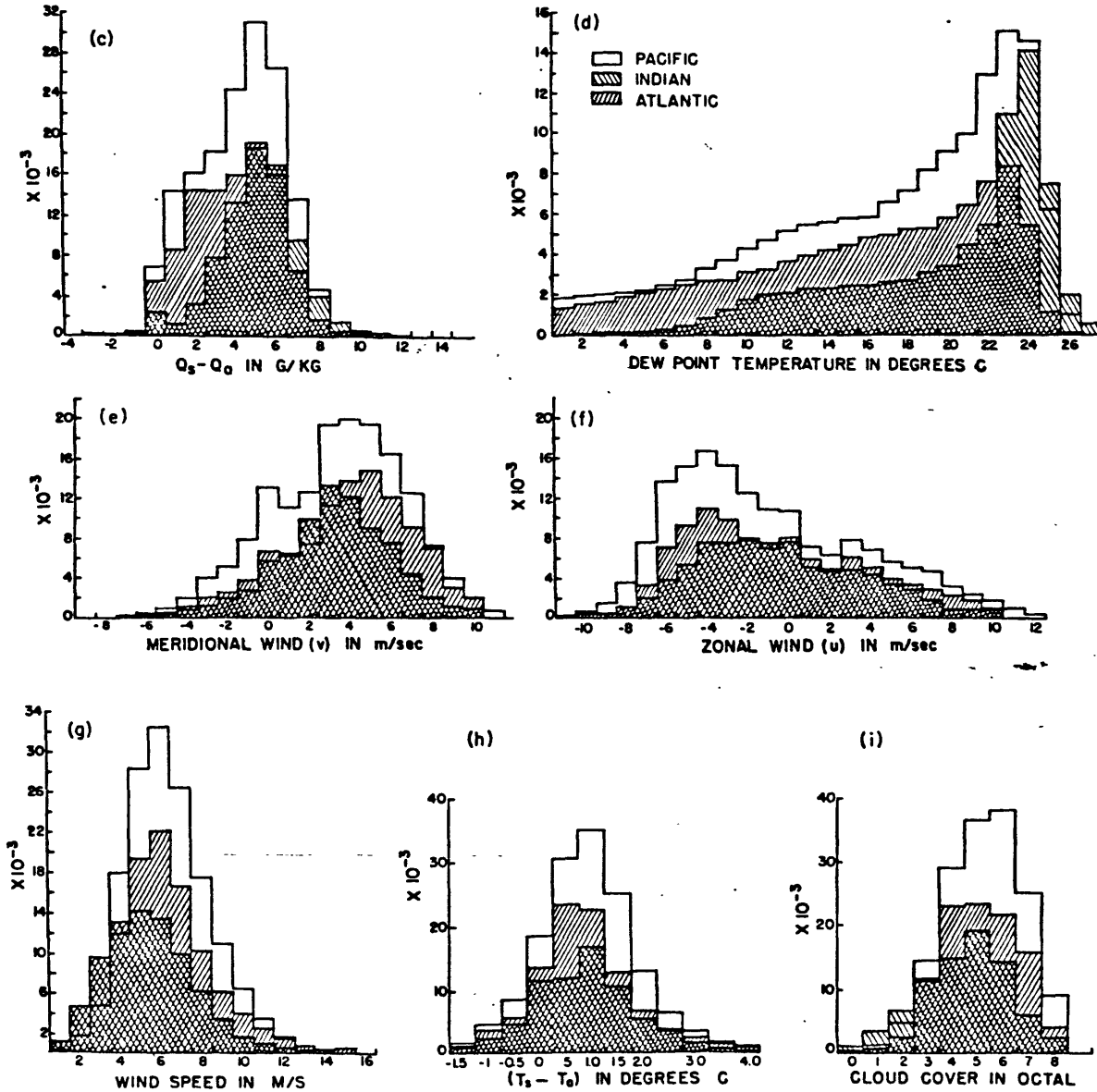


Figure 4.1 Frequency distribution histogram of the wind speed, zonal and meridional wind components, dew point temperature, cloud cover, and drag coefficients.

Table IV.2 Oceanic Albedo

Latitude	Jan	Feb	Mar	Apr	May	Jun	Jul	Aug	Sep	Oct	Nov	Dec
80N			0.33	0.14	0.10	0.09	0.08	0.08	0.12			
70N		0.41	0.15	0.10	0.08	0.07	0.07	0.09	0.11	0.25		
60N	0.28	0.12	0.09	0.07	0.07	0.07	0.06	0.07	0.07	0.10	0.16	0.44
50N	0.11	0.10	0.08	0.07	0.06	0.06	0.06	0.07	0.07	0.08	0.11	0.12
40N	0.10	0.09	0.07	0.07	0.06	0.06	0.06	0.06	0.07	0.08	0.10	0.11
30N	0.09	0.07	0.06	0.06	0.06	0.06	0.06	0.06	0.06	0.07	0.08	0.09
20N	0.07	0.06	-0.06	0.06	0.06	0.06	0.06	0.06	0.06	0.06	0.07	0.07
10N	0.07	0.06	-0.06	0.06	0.06	0.06	0.06	0.06	0.06	0.06	0.06	0.07
0	0.06	0.06	-0.06	0.06	0.06	0.06	0.06	0.06	0.06	0.06	0.06	0.06
10S	0.06	0.06	0.06	0.06	0.07	0.07	0.06	0.06	0.06	0.06	0.06	0.06
20S	0.06	0.06	-0.06	0.06	0.07	0.07	0.07	0.07	0.06	0.06	0.06	0.06
30S	0.06	0.06	-0.06	0.07	0.08	0.09	0.08	0.07	0.07	0.06	0.06	0.06
40S	0.06	0.06	0.07	0.08	0.09	0.11	0.10	0.08	0.07	0.07	0.06	0.06
50S	0.06	0.07	0.07	0.08	0.10	0.13	0.11	0.08	0.08	0.07	0.06	0.06
60S	0.06	0.07	0.08	0.11	0.13		0.27	0.07	0.08	0.07	0.06	0.06

surface. Payne (1972) expressed the albedo as a function of atmospheric transmittance and sun altitudes and found that the uncertainty in the measurement of albedo is greater at low sun altitudes (< 20%). The effect of wind (through surface roughness) was found to be small with decreasing albedo accompanying increasing wind. Simpson and Paulson (1979) performed an independent experiment and found that their results agreed with Payne's. It should be noted here that both of these experiments were performed over fairly open ocean and there might be significantly different ocean albedos along coastal regions, particularly where there is active marine biosphere.

IV.2 Sensitivity of the Flux Formulations

Once we have made the choice as to which formulations to use for the flux calculations, it is instructive to understand its sensitivity with respect to the input data set from which the fluxes will be computed. One should have a good idea of how changes in the input variables affect the output variables regardless of whether it is a real physical change or an error in observation. For example, in sensible heat flux calculations, we might want to ask the question of whether a change of 1 m/sec in wind speed has a greater effect on the heat flux

than a change of one degree in sea and air temperature difference ($T_s - T_a$). In most cases because of the nonlinearity of the formulas used, it is hard to find a definite answer. Nevertheless, we will show relationships that illustrate the importance of some meteorological variables in modulating the fluxes.

IV.1a Range and variations of the input parameters

The important meteorological variables used in the flux calculations are wind speed ($|v|$), zonal and meridional components of wind (u and v), air and sea temperatures (T_a and T_s), dew point temperature (T_d) and cloud cover (C). The frequency distribution histograms for these variables are presented in Figures 4.1 and 3.13. Following is a table listing the range of 90% of their values and the most frequently occurring value:

Table IV.3 Range of Input Parameters

Variable	Unit	Range	Most Frequent
T_a	°C	10 to 31	27
T_s	°C	10 to 31	28
$T_a - T_s$	°C	-2 to 2	-0.5
T_d	°C	4 to 26	23
$Q_s - Q_a$	g/kg	0 to 8	5
v	m/sec	0 to 10	6
u	m/sec	-8 to 8	-4
v	m/sec	-3 to 7	4
C	octal	0 to 8	5,6

Month:	1	2	3	4	5	6	7	8	9	10	11	12	Lat.
	0.00	0.00	14.22	218.61	423.29	515.71	479.38	324.56	87.75	0.00	0.00	0.00	89.50
	0.00	0.00	17.14	218.41	422.90	515.24	478.94	324.26	90.60	0.00	0.00	0.00	87.50
	0.00	0.00	39.22	219.18	419.68	511.31	475.29	321.80	109.45	5.20	0.00	0.00	82.50
	0.00	2.71	72.76	229.84	413.27	503.50	468.03	318.28	139.27	23.18	0.00	0.00	77.50
	0.00	17.22	108.46	251.80	404.89	491.86	457.21	322.71	172.01	53.01	2.37	0.00	72.50
	3.52	44.71	144.12	277.75	404.50	476.53	445.91	338.00	204.49	86.80	17.63	0.19	67.50
	23.69	77.26	179.03	303.72	413.96	470.90	447.05	356.50	235.88	121.60	44.98	14.98	62.50
	52.91	111.70	212.76	328.50	425.45	473.29	453.09	374.87	265.74	156.35	76.83	41.66	57.50
	85.08	146.75	245.00	351.45	436.50	476.91	459.60	391.92	293.73	190.46	110.74	73.07	52.50
	119.57	181.65	275.46	372.17	446.00	479.78	465.02	406.97	319.60	223.48	145.52	106.96	47.50
	154.92	215.84	303.88	390.39	453.34	480.99	468.57	419.64	343.11	255.06	180.39	142.12	42.50
	190.40	248.92	330.03	405.89	458.17	479.99	469.80	429.65	364.07	284.90	214.77	177.72	37.50
	225.45	280.51	353.71	418.50	460.24	476.46	468.41	326.82	382.31	312.73	248.23	213.17	32.50
	259.63	310.31	374.72	428.08	459.40	470.24	464.24	441.01	397.68	338.31	280.38	247.96	27.50
	292.55	338.03	392.91	434.55	455.58	461.22	457.22	442.15	410.05	361.43	310.88	281.69	22.50
	323.86	363.44	408.13	437.83	448.75	449.38	447.30	440.18	419.34	381.89	339.46	314.00	17.50
	353.28	386.31	420.27	437.90	438.90	434.74	434.52	435.11	425.46	399.55	365.84	344.57	12.50
	380.53	406.46	429.22	434.73	426.09	417.36	418.91	426.94	428.37	414.24	389.81	373.12	7.50
	403.38	423.72	434.93	428.36	410.40	397.36	400.59	415.74	428.04	425.86	411.15	399.41	2.50
	427.63	437.96	437.35	418.82	391.94	374.86	379.68	401.59	424.48	434.32	429.71	423.22	-2.50
	447.12	449.06	436.46	406.20	370.84	350.05	356.34	384.58	417.71	439.56	445.34	444.37	-7.50
	463.70	456.96	432.26	390.58	347.28	323.12	330.76	364.86	407.79	441.53	457.92	462.72	-12.50
	477.27	461.59	424.79	372.09	321.46	294.30	303.15	342.58	394.79	440.22	467.38	478.15	-17.50
	487.78	462.94	414.11	350.89	293.59	263.86	273.76	317.94	378.81	435.65	473.68	490.59	-22.50
	495.20	461.02	400.30	327.14	263.94	232.10	242.88	291.14	359.98	427.87	476.81	500.02	-27.50
	499.57	455.88	383.47	301.03	232.80	199.36	210.83	262.42	338.45	416.94	476.81	506.46	-32.50
	500.97	447.61	363.76	272.80	200.48	166.03	177.96	232.06	314.38	402.97	473.75	510.03	-37.50
	499.58	436.35	341.31	242.70	167.36	132.57	144.70	200.36	287.96	386.09	467.80	510.91	-42.50
	495.70	422.29	316.31	210.99	133.91	99.55	111.58	167.67	259.41	366.48	459.17	509.43	-47.50
	489.82	405.69	288.96	178.01	100.67	67.75	79.27	134.41	228.97	344.33	448.25	506.14	-52.50
	482.78	386.97	259.49	144.12	68.45	38.34	48.77	101.13	196.89	319.93	435.62	502.04	-57.50
	476.21	366.77	228.17	109.81	38.48	13.45	21.82	68.60	163.47	293.64	422.33	499.18	-62.50
	474.85	346.26	193.30	75.78	13.42	0.06	3.01	38.14	129.07	265.99	410.67	504.51	-67.50
	486.55	328.50	161.30	43.30	1.18	0.00	0.00	13.16	94.15	237.98	408.10	520.61	-72.50
	498.07	321.36	126.85	16.41	0.00	0.00	0.00	1.40	59.56	212.54	415.34	532.94	-77.50
	505.80	323.60	94.15	2.44	0.00	0.00	0.00	0.00	28.51	197.50	421.78	541.21	-82.50
	509.68	326.08	72.49	0.00	0.00	0.00	0.00	0.00	9.04	193.77	425.02	545.36	-87.50
	510.15	326.38	69.62	0.00	0.00	0.00	0.00	0.00	6.12	193.95	425.40	545.85	-89.50

Table IV.1 Total short wave radiation received at the top of the atmosphere (from Ledley, 1983)

The most frequently occurring value for specific humidity difference is 5g/kg while the same for wind speed is 6 m/sec. This is true for all three oceans. Since these are the two main parameters that make up the latent heat flux, it is interesting to note that the most observed values for these two terms make equivalent contributions towards the magnitude of the latent heat flux. In higher latitudes, however, the wind is typically much larger in magnitude than the specific humidity difference. This may explain why the distribution is skewed towards higher values in the distribution of wind speed and towards lower values in the distribution of specific humidity difference (Figure 4.1c and 4.1g). An inspection of the variance pattern also shows that the standard deviations for these two parameter are also about the same in magnitude, ranging from 1 to 3 g/kg and 1 to 3 m/sec.

The distribution of air-sea temperature difference shows that most of the time the sea is warmer than the air. The difference is not very large. Few observations have values greater than 3°C (Figure 4.1h). Together with wind speed, the temperature difference makes up the sensible heat flux. The small difference observed is the main reason for the small calculated values of sensible heat flux. The standard deviations of the temperature difference are also about the same as those of the wind speed (or a little smaller). Values with comparable magnitude to the mean are observed in high latitudes.

The distribution of zonal winds is dominated by the easterly winds in the tropics. For the meridional component of the wind, southerly winds cover a large part of the ocean. The long suspected bimodal distribution from the opposing westerlies and easterlies is not present in our calculations.

It should be pointed out that all the observed peaks in frequency distributions are from values observed in the large area covered by the tropical oceans. For instance, if the mean humidity difference in the tropics is 5 g/kg, the peak in the frequency histogram will also be 5 g/kg.

For reference, monthly mean maps from each season for these parameters are presented in Appendix C.

IV.2b Energy Budget Fluxes

Let us rewrite the flux formulae in terms of their meteorological variables:

$$\text{Sensible Heat } (Q_h) = \text{constant} \cdot f(|v|, T_a - T_s)$$

$$\text{Latent Heat } (Q_l) = \text{constant} \cdot f(|v|, q_a - q_s, T_a - T_s)$$

$$\text{Incoming Solar } (Q_{in}) = f(C) \cdot \text{constant}(f(\text{lat}, \text{month}))$$

$$\text{Outgoing Radiation } (Q_{out}) = f(C, T_s, T_d) \text{ and } f(T_s, T_a - T_s)$$

We will discuss each flux terms below.

From Bunker (1976), both sensible and latent heat flux are a function of the transfer coefficient C_e , which in turn is a function of the stability and wind speed. Stability is defined as the surface air-sea temperature difference. Figure 4.2 is a plot of C_e versus wind speed for seven different stability classes. C_e is greatest under unstable conditions, decreasing quadratically with wind speed. Under stable conditions ($T_s < T_a$), C_e increases quadratically with wind speed. The values converge for wind speed above 20 m/sec.

Since $T_s - T_a$ is small (over 95% of the time its value is between $-.2$ and $.2$ °C, more than an order of magnitude smaller than the

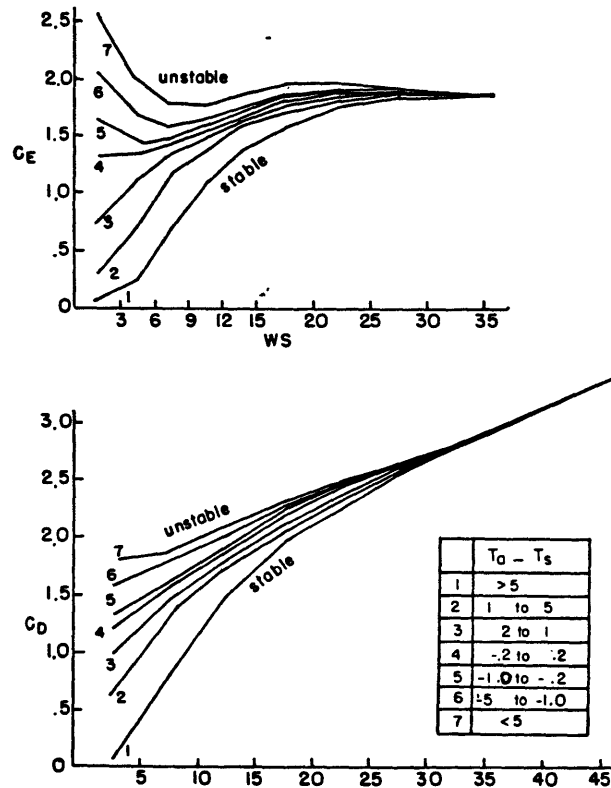


Figure 4.2 Transfer coefficients (C_e) and drag coefficients (C_d) versus wind speed for seven different stability classes

humidity difference), contribution to the total heat flux from sensible heat is small. A graph showing the latent heat flux as a function of $q_a - q_s$ and wind speed is presented in Figure 4.3. For latent heat flux, the dependence on wind speed is slightly larger than the dependence on specific humidity difference. A change of wind speed by 1.0 m/s (from 5 to 6 m/s) will give a 22% change in the flux while a 1 g/kg change (from 5 to 6 g/kg) in specific humidity will give a 20% change in the flux. The effects of wind speed on latent heat flux are more pronounced when the humidity difference is high.

Figure 4.3 LATENT HEAT IN WATT/M*2

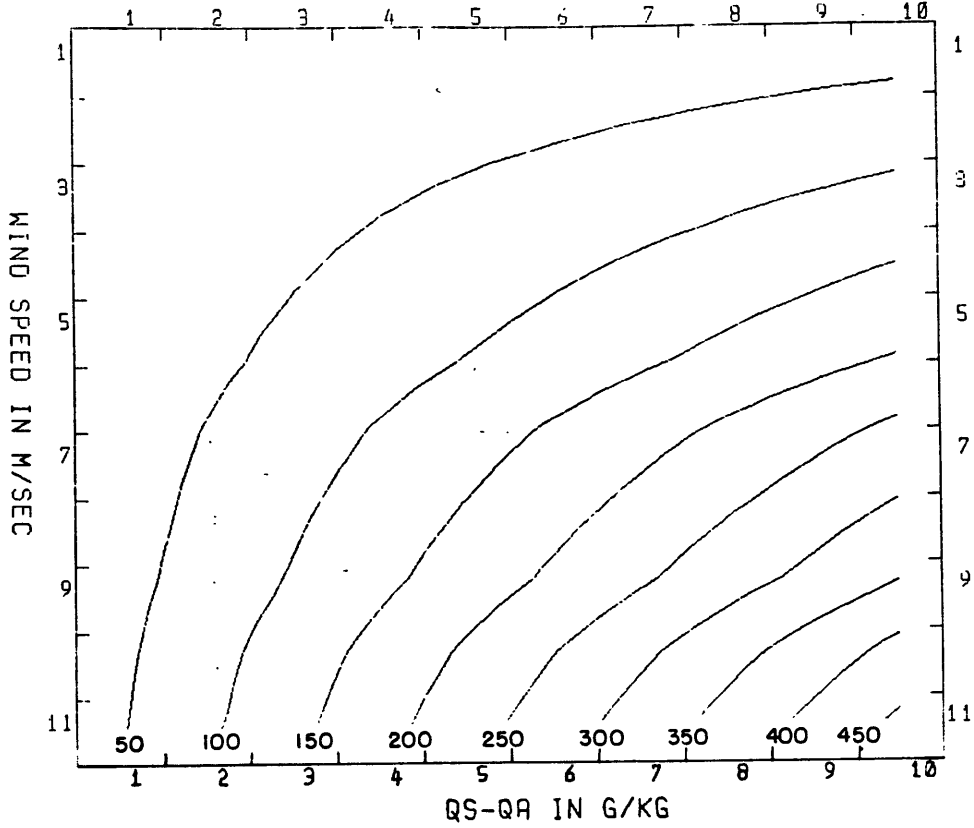


Figure 4.4 OUTGOING RADIATION

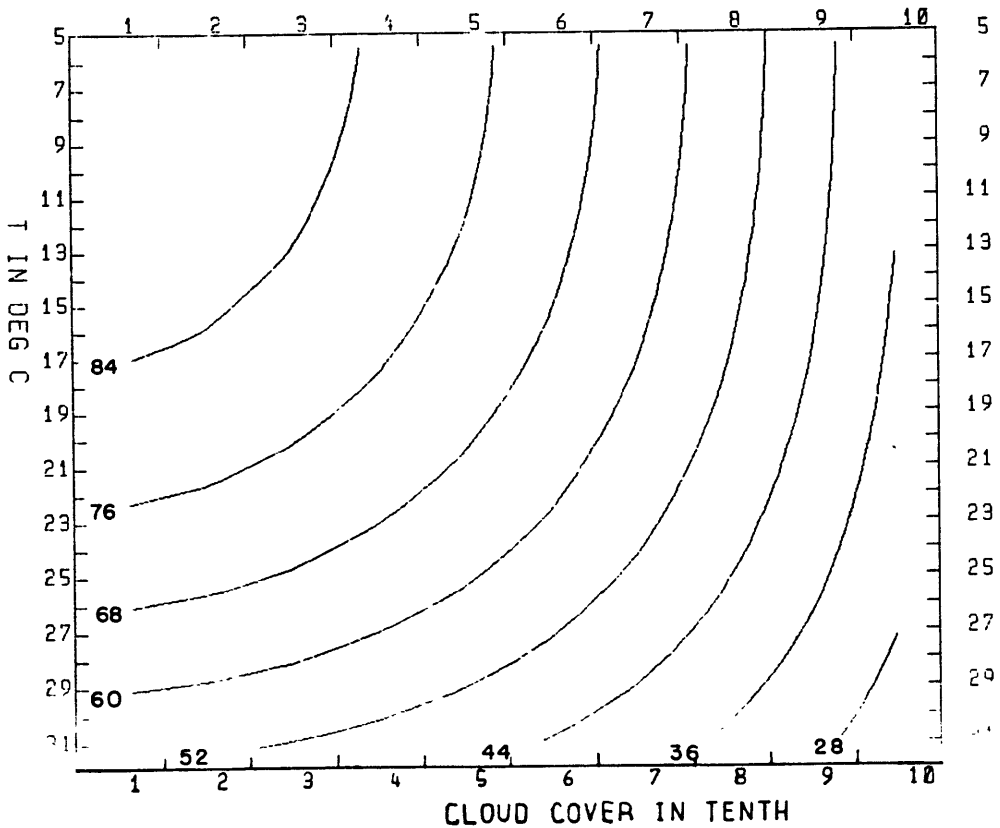


Figure 4.3 Latent heat flux as a function of $q_s - q_a$ and wind speed

Figure 4.4 Outgoing radiation as a function of cloud cover and air temp.

Once a formula is chosen for incoming radiation, the variation of this flux is principally from the variation of cloud cover. Given a time of the year and the latitude, the solar radiation is then a linear function of the cloud cover. The outgoing radiative flux consists of two terms: a black body formulation and a correction term for air-sea temperature difference. The black body radiation term is typically an order of magnitude larger than the second term. The change in vapor pressure in the first term contributes little to the flux. Its two biggest contributors are cloud cover and air temperature. Figure 4.4 gives the outgoing radiation flux as a function of cloud cover and air temperature. At temperatures below 17°C , the outgoing radiation is almost solely a function of cloud cover while at higher temperatures the dependence on cloud cover is less pronounced.

Recall from Eq.(4.4), the net energy flux is the sum of the four fluxes. Of the four fluxes, Q_h is typically an order of magnitude smaller than Q_{in} and Q_l . Q_{out} is about 25% of that of Q_{in} . Q_{net} is then mostly a balance between Q_{in} and Q_l . Q_{in} is determined mostly by Q_0 , the amount of radiation received under cloudless sky, modified by the amount of cloud cover. Q_l is mainly determined by wind speed and the humidity difference. Therefore, the meteorological variables that are most responsible for the net energy flux balance are the wind speed, cloud cover and the humidity difference.

To obtain an estimate of the percentage error introduced by the meteorological parameters, namely wind speed and specific humidity difference, we consider the formulation of the latent heat flux, the largest contributor to the net surface energy flux.

We may rewrite the flux formula as:

$$Q_1 = A \cdot f(V) \cdot V \cdot \delta q \quad (4.12)$$

Here a constant A is used to denote $L_e \cdot \rho_a$, V is wind speed, δq is the humidity difference at the surface, and $f(V)$ is a function to denote the dependence of the transfer coefficient (C_e) on wind speed.

Assuming δq and V are independent, changes in Q_1 can be related to changes in V and δq by the following expression:

$$\partial Q_1 = \frac{\partial Q_1}{\partial V} dv + \frac{\partial Q_1}{\partial \delta q} d(\delta q)$$

The magnitude of ∂Q_1 can be estimated by:

$$\Delta Q_1 = \left[\left(\frac{\partial Q_1}{\partial V} \Delta V \right)^2 + \left(\frac{\partial Q_1}{\partial \delta q} \Delta \delta q \right)^2 \right]^{1/2} \quad (4.13)$$

From (4.12),

$$\frac{\partial Q_1}{\partial V} = Q_1 \cdot \left(\frac{1}{V} + \frac{f'(V)}{f(V)} \right) \quad (4.14)$$

and

$$\frac{\partial Q_1}{\partial \delta q} = \frac{Q_1}{\delta q} \quad (4.15)$$

Substituting (4.14) and (4.15) into (4.13), we have

$$\frac{\Delta Q_1}{Q_1} = \left[\left(\frac{\Delta V}{V} \right)^2 + \left(\frac{\Delta(\delta q)}{\delta q} \right)^2 + \left(\frac{\Delta V \cdot f'(V)}{f(V)} \right)^2 + 2 \frac{f'(V) \cdot \Delta V^2}{V \cdot f(V)} \right]^{1/2}$$

The transfer coefficient's dependence on wind speed can be approximated by the following expression:

$$f(V) = a \cdot (1 - e^{-V/V_0}) + c$$

This would give us an expression for $\frac{f'(V)}{f(V)}$ as:

$$\frac{f'(V)}{f(V)} = \left(\frac{a/V_0 \cdot \exp(-V/V_0)}{a(1 - \exp(-V/V_0)) + c} \right)$$

With $a = .67$, $c = 1.0$ and $V_0 = 3$, this expression satisfies a neutral to weakly stable atmosphere, a condition that occurs most of the time.

Taking ΔV to be 1 m/s and $\Delta(\delta q)$ to be 1 g/kg (these values are typical standard deviations for V and δq in the tropics), together with $V = 5$ m/s and $\delta q = 5$ g/kg, we have

$$\frac{\Delta Q_1}{Q_1} = \left[\left(\frac{1}{5}\right)^2 + \left(\frac{1}{5}\right)^2 + \left(\frac{0.4}{1.46}\right)^2 + \frac{2 \cdot 0.4}{1.46} \cdot \frac{1}{5} \right]^{1/2}$$

$$\approx .30$$

If we assume ΔV to be 2 m/s (a typical standard deviation in the mid-latitudes), then

$$\frac{\Delta Q_1}{Q_1} = \left[\left(\frac{2}{5}\right)^2 + \left(\frac{2}{5}\right)^2 + \left(\frac{0.8}{1.46}\right)^2 + \frac{2 \cdot 0.4}{1.46} \cdot \frac{4}{5} \right]^{1/2}$$

$$\approx .50$$

It should therefore be kept in mind that 30% to 50% are the possible percentage error in the flux estimates due to uncertainties in the meteorological parameters.

IV.3 Results

IV.3a Seasonal Means

To see how the seasonal pattern of observed SST is related to the seasonal patterns of the components of the energy budget, the long term monthly means of Q_{net} , Q_{in} , Q_{out} , Q_h , and Q_l are calculated and results for one month in each season (January, April, July, and October) are presented in Figures 4.5 to 4.24 .

In January (Figure 4.5), there is net loss of energy in the Northern Hemisphere and a net gain of energy in the Southern Hemisphere. The regions with the largest loss are the Gulf Stream and the Kuro-shio region. By April (Figure 4.6), the pattern has changed considerably. In the Northern Hemisphere, the only significant energy loss region is confined to the Gulf Stream in the Atlantic. There is energy gain everywhere in the tropics and energy loss south of $20^{\circ}S$. The maximum energy gain occurs in the North Indian Ocean. In July (Figure 4.7), the pattern is the reverse of that in January (Figure 4.7) - a net gain in the Northern Hemisphere and a net loss in the Southern Hemisphere. In October (Figure 4.8), the pattern reverses again towards the direction of the winter pattern.

All the non-latitudinal spatial variation in incoming solar radiation is from the variation in cloud cover. The monthly mean maps of the incoming solar radiation (Figure 4.9 through Figure 4.12) therefore resemble that of the cloud cover (see Appendix C). In January, the distribution in the Northern Hemisphere is mostly zonal.

NET HEAT BALANCE MON=1

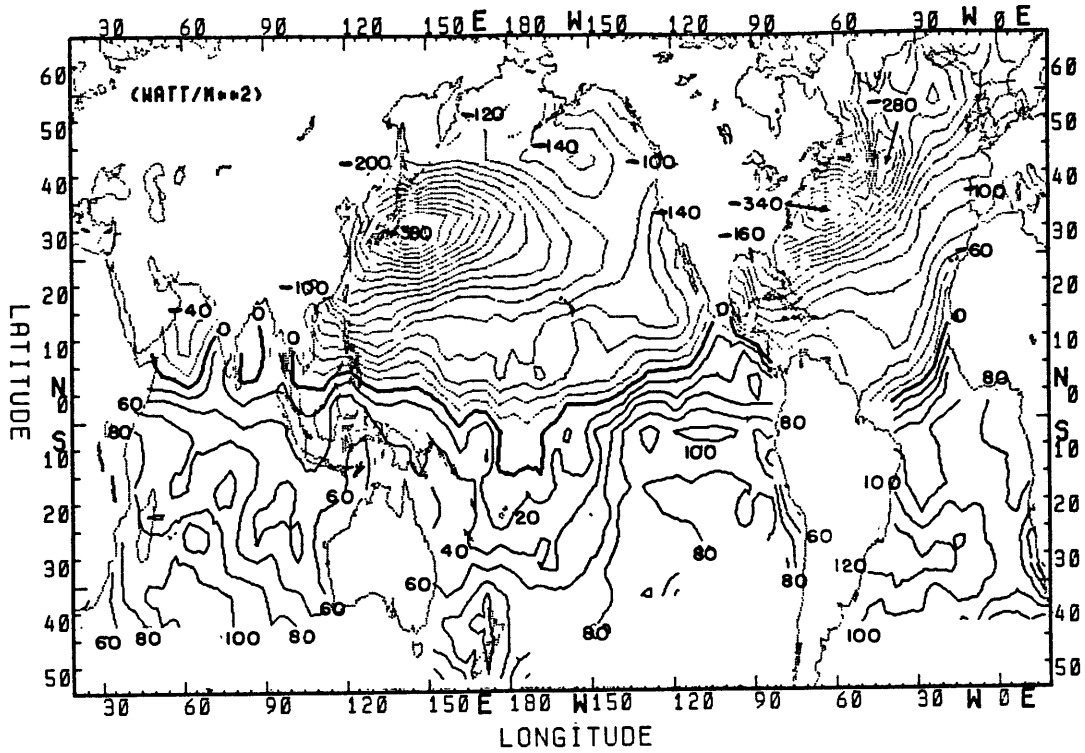


Figure 4.5 Long term monthly mean of net heat flux for January

NET HEAT FLUX MON=4

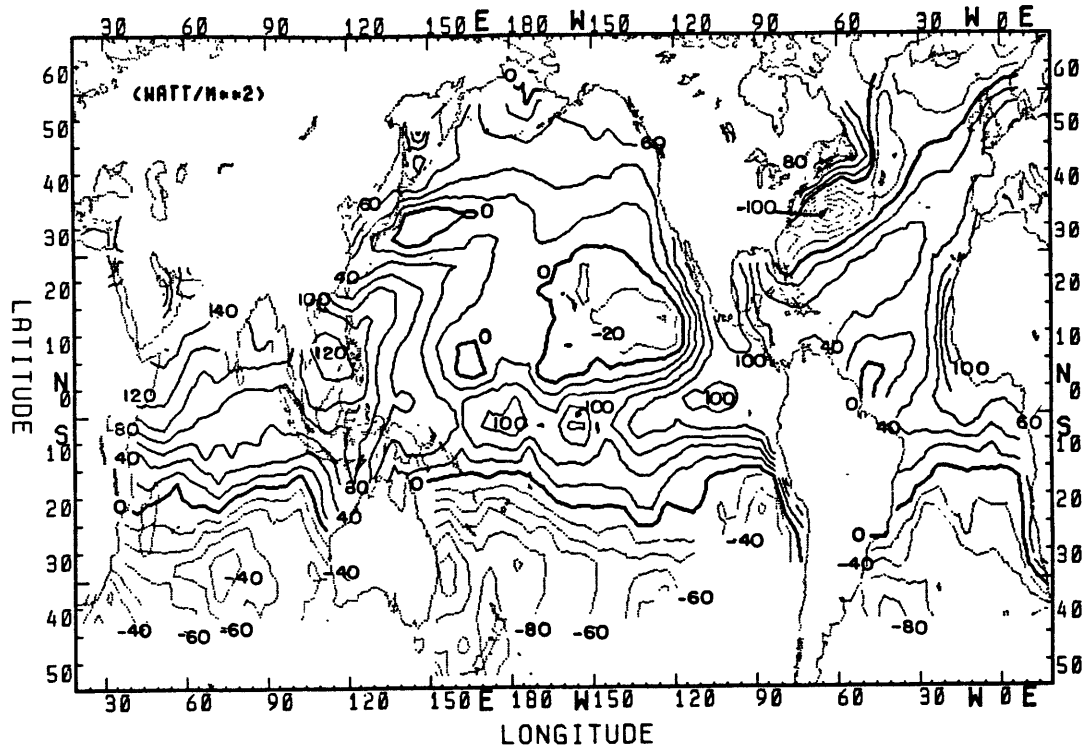


Figure 4.6 Long term monthly mean of net heat flux for April

64a

NET HEAT FLUX MON=7

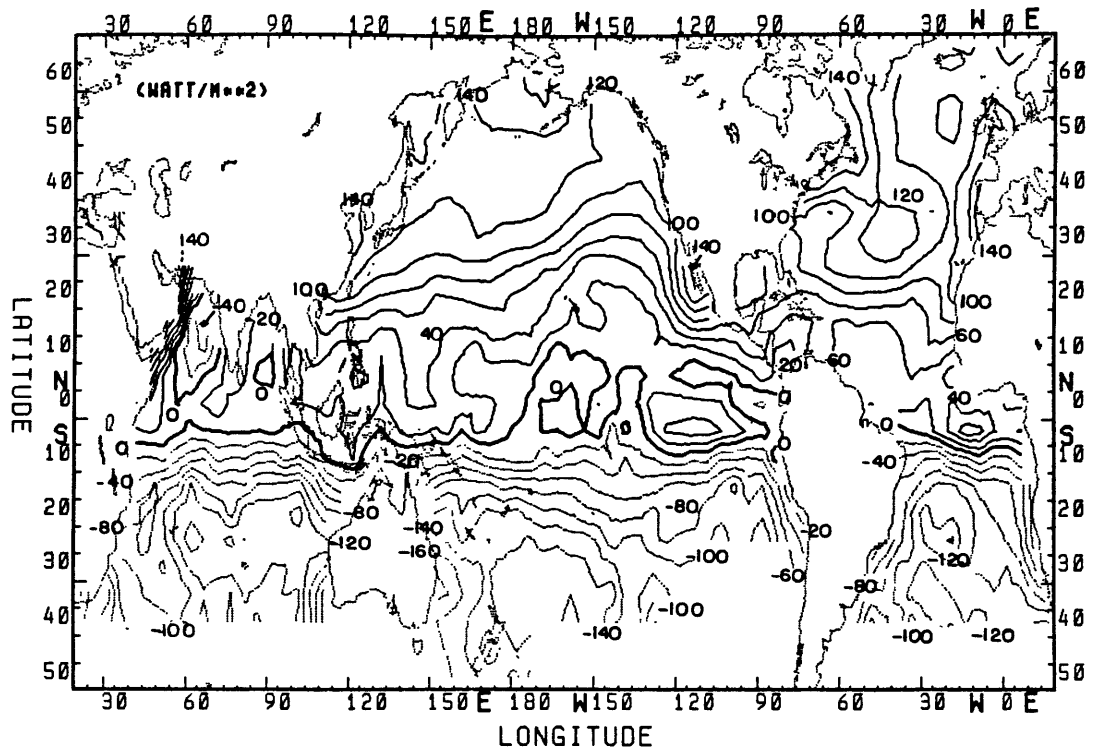


Figure 4.7 Long term monthly mean of net heat flux for July

NET HEAT FLUX MON=10

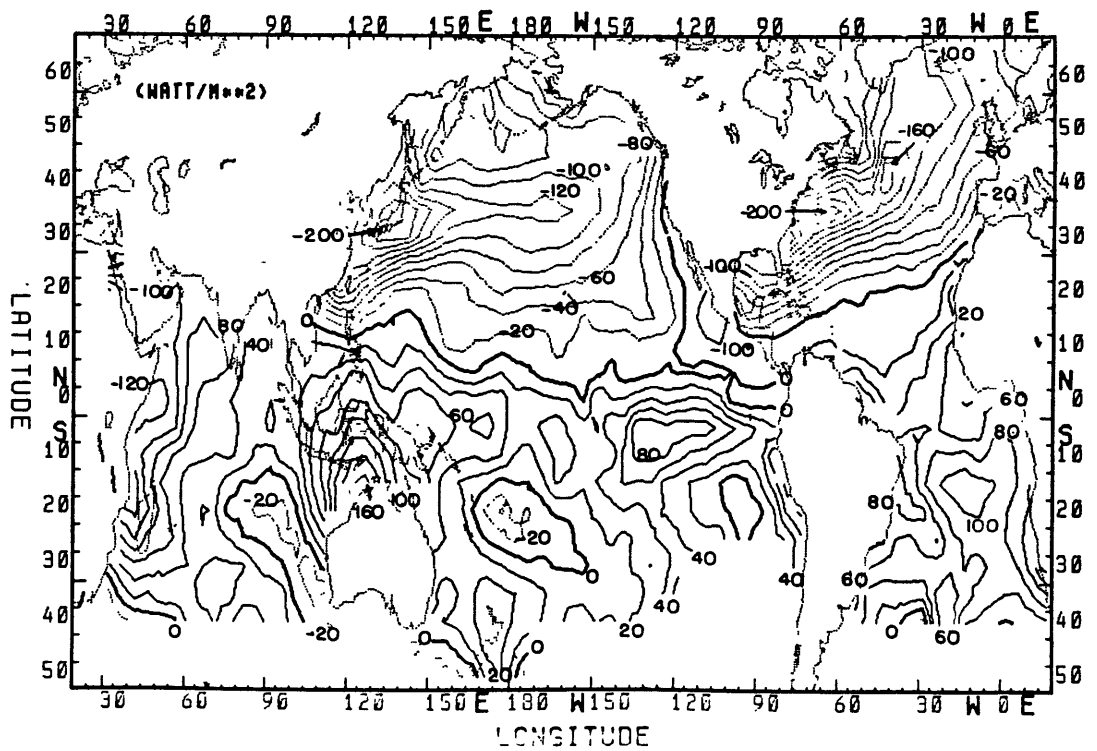


Figure 4.8 Long term monthly mean of net heat flux for October

INCOMING SOLAR RADIATION MON=1

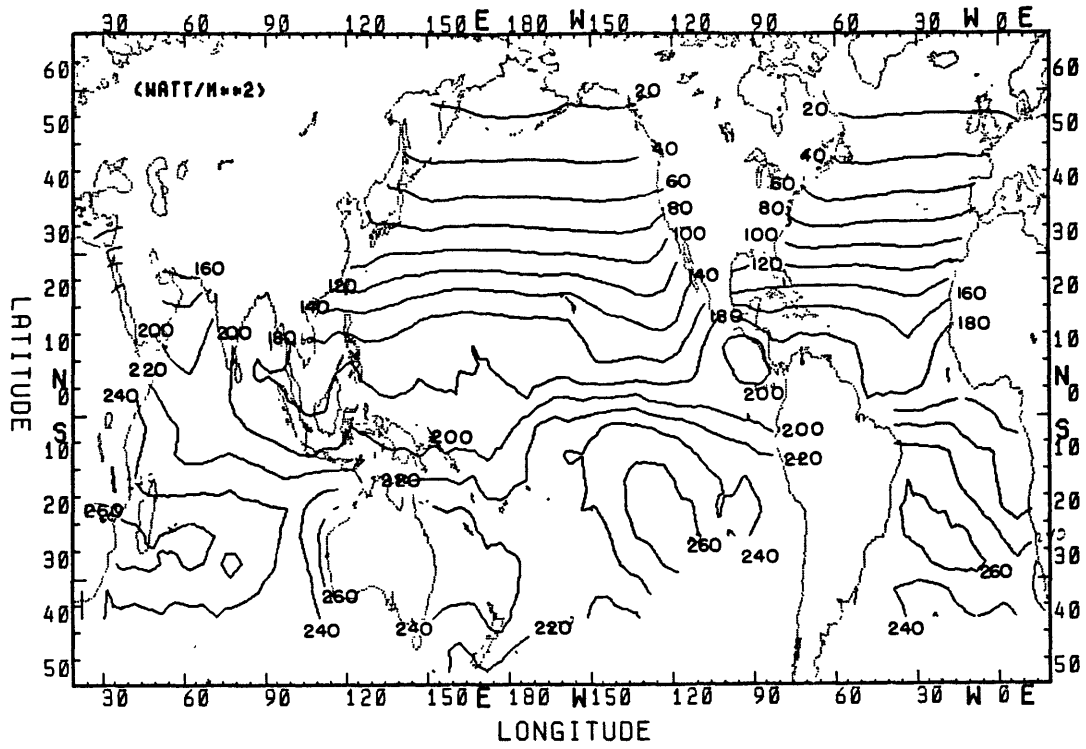


Figure 4.9 Long term monthly mean of incoming solar radiation for January

INCOMING SOLAR RADIATION MON=4

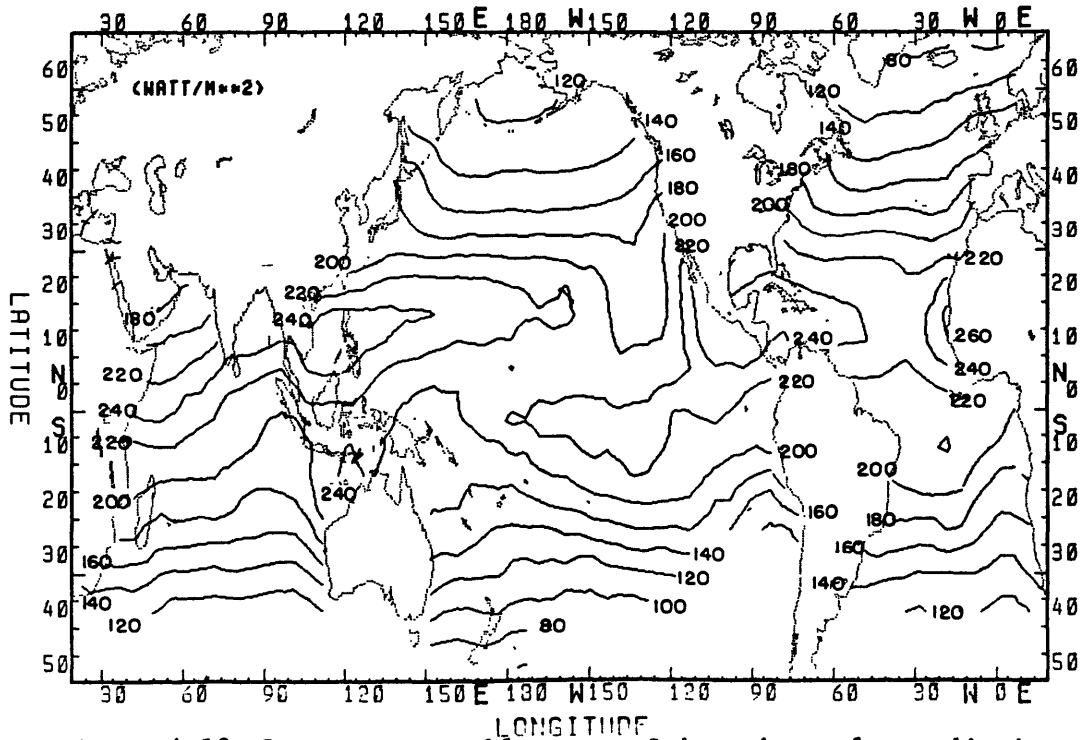


Figure 4.10 Long term monthly mean of incoming solar radiation for April

65a

INCOMING SOLAR RADIATION MON=7

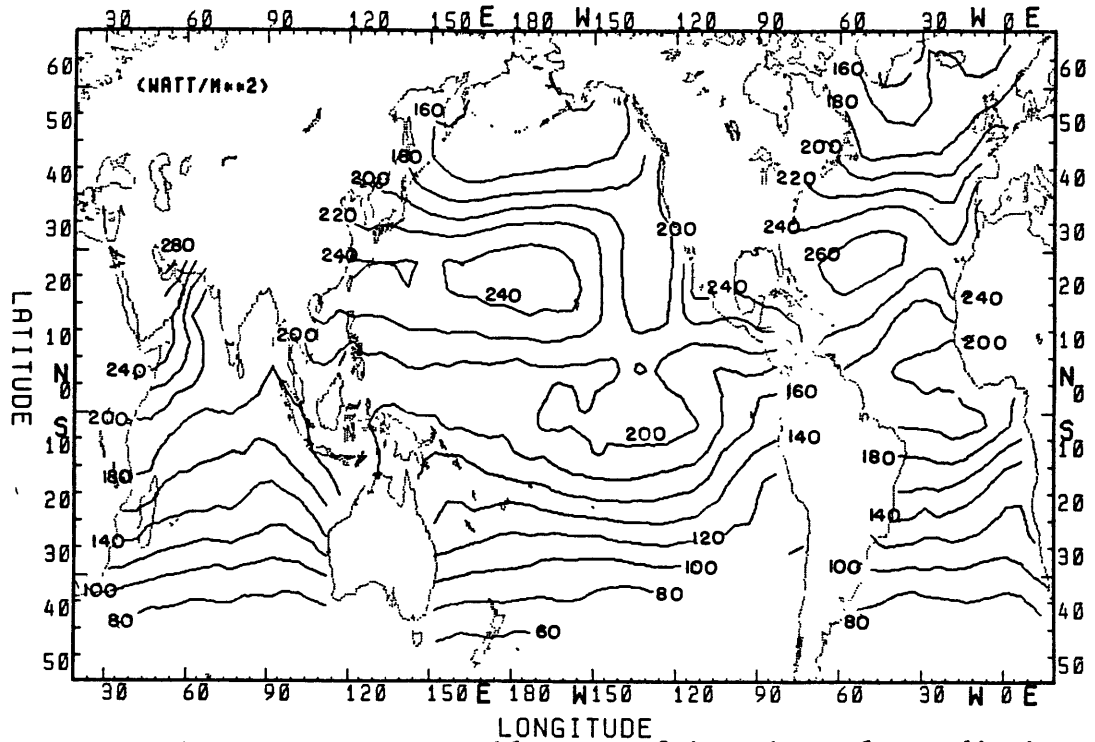


Figure 4.11 Long term monthly mean of incoming solar radiation for July

INCOMING SOLAR RADIATION MON=10

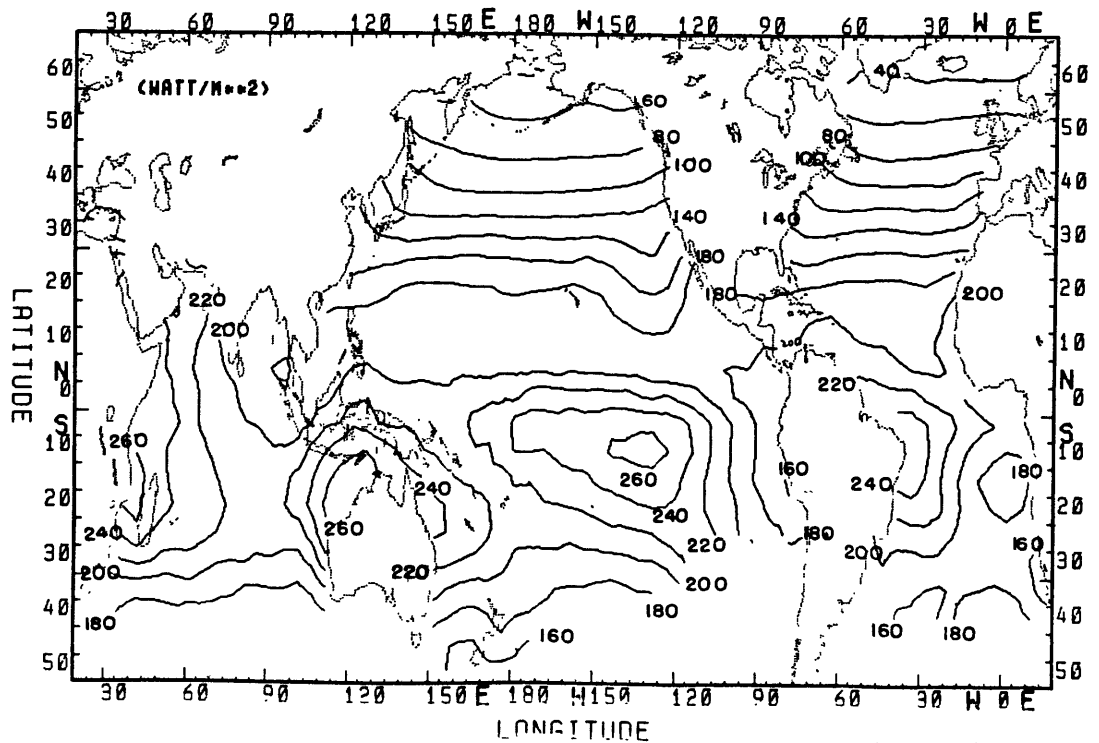


Figure 4.12 Long term monthly mean of incoming solar radiation for October

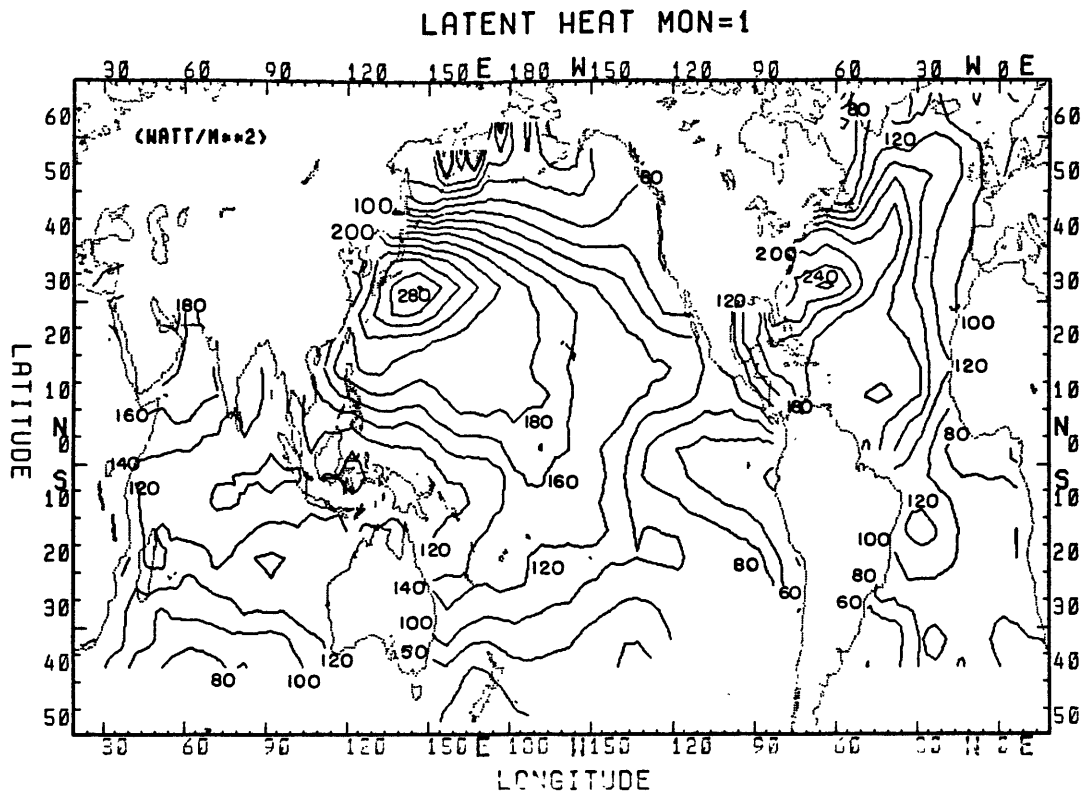


Figure 4.13 Long term monthly mean of latent heat for January

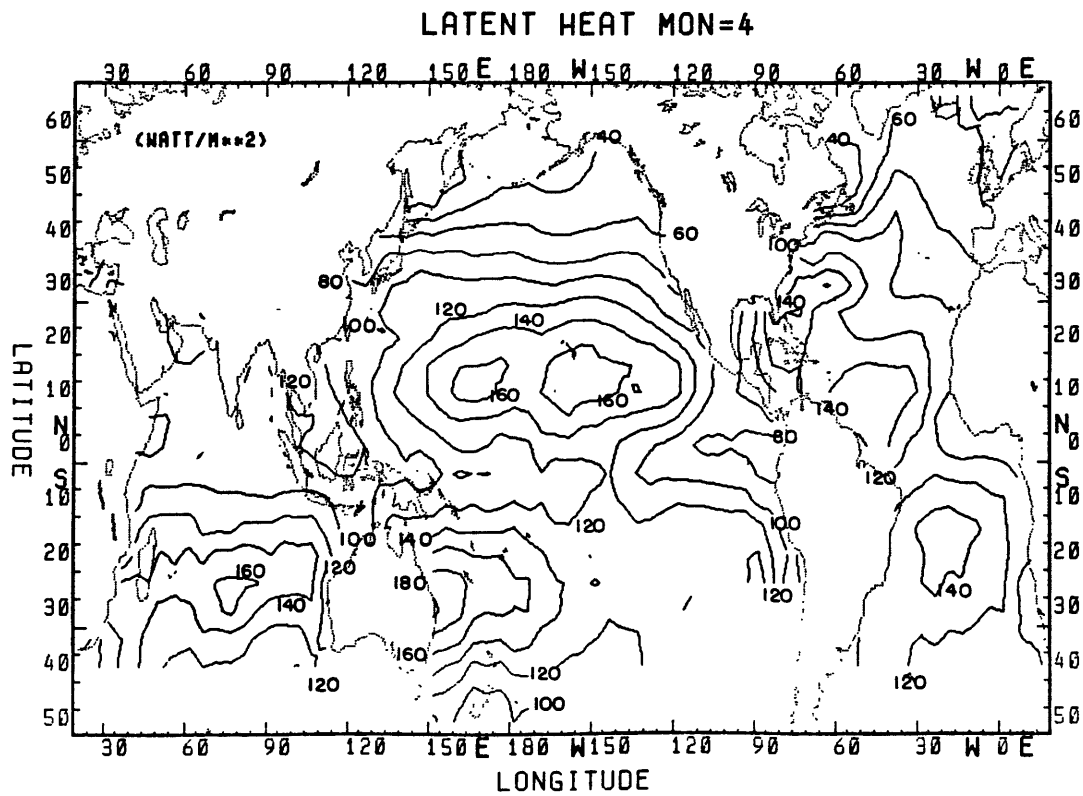


Figure 4.14 Long term monthly mean of latent heat for April

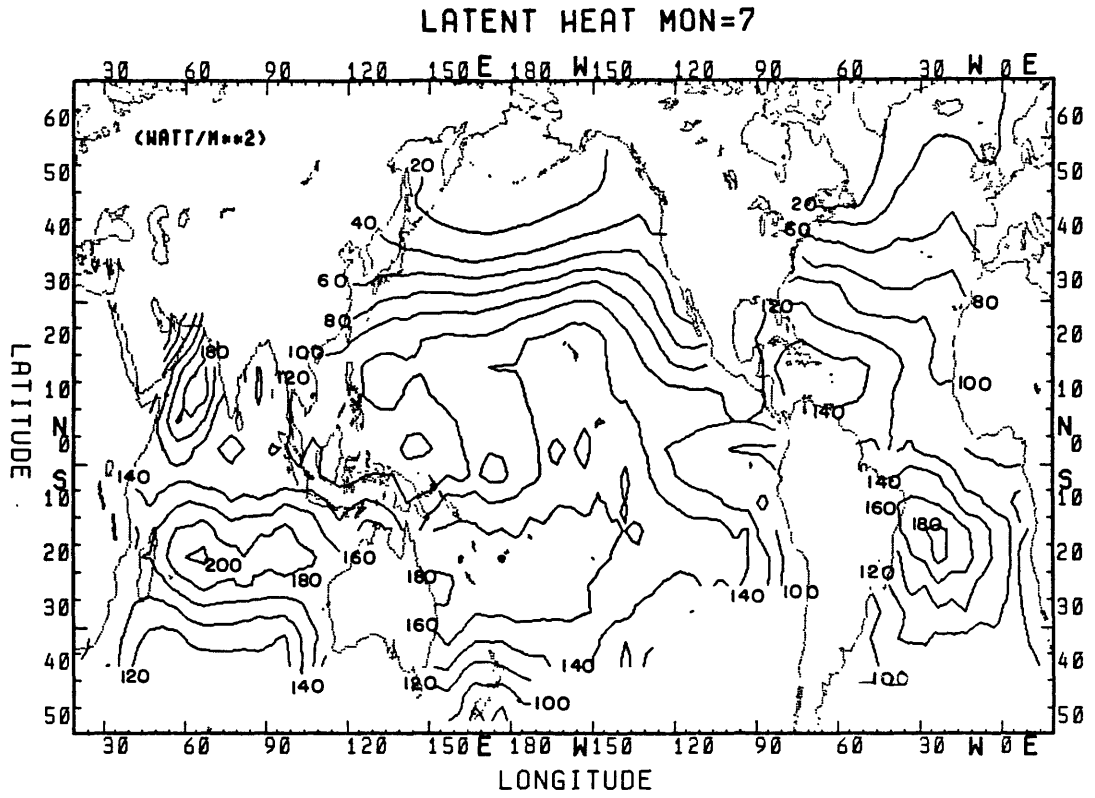


Figure 4.15 Long term monthly mean of latent heat for July

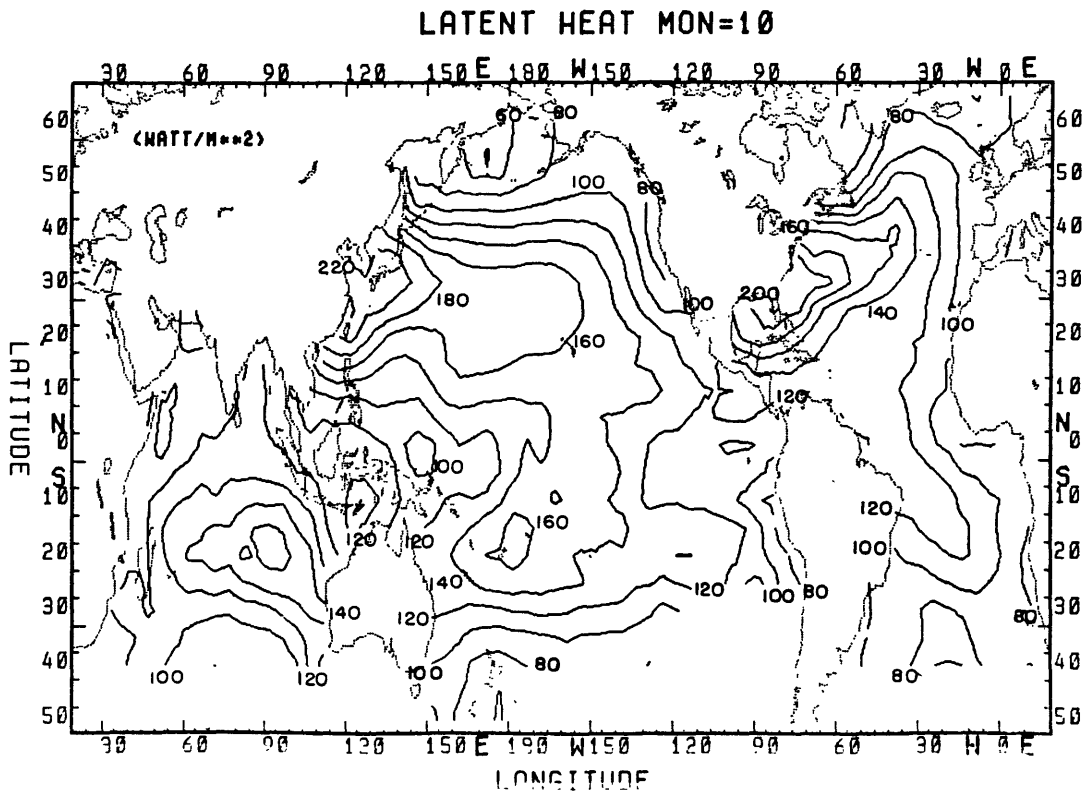


Figure 4.16 Long term monthly mean of latent heat for October

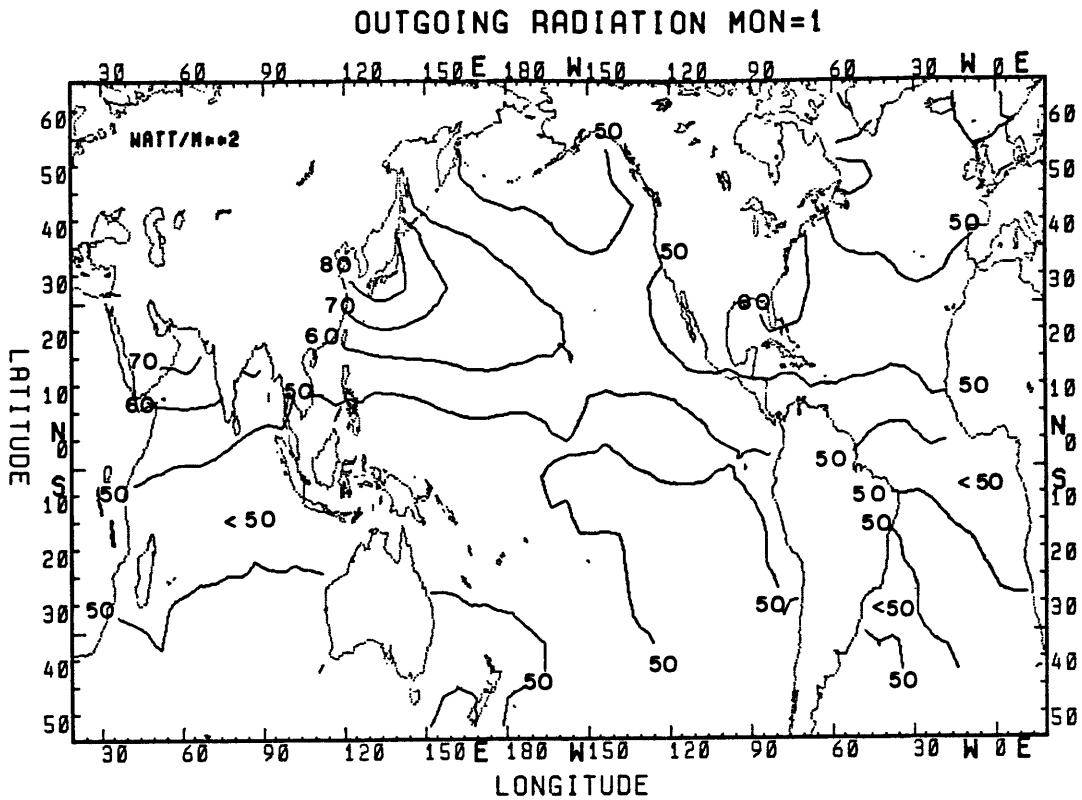


Figure 4.17 Long term monthly mean of outgoing radiation for January

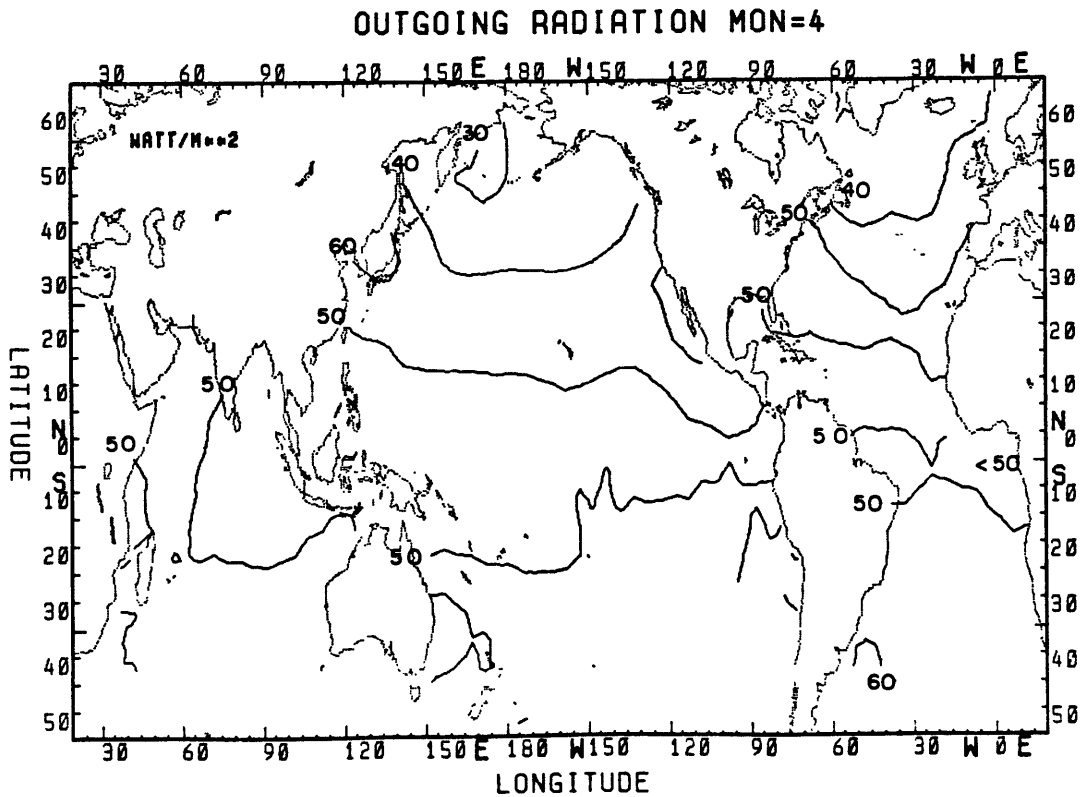


Figure 4.18 Long term monthly mean of outgoing radiation for April

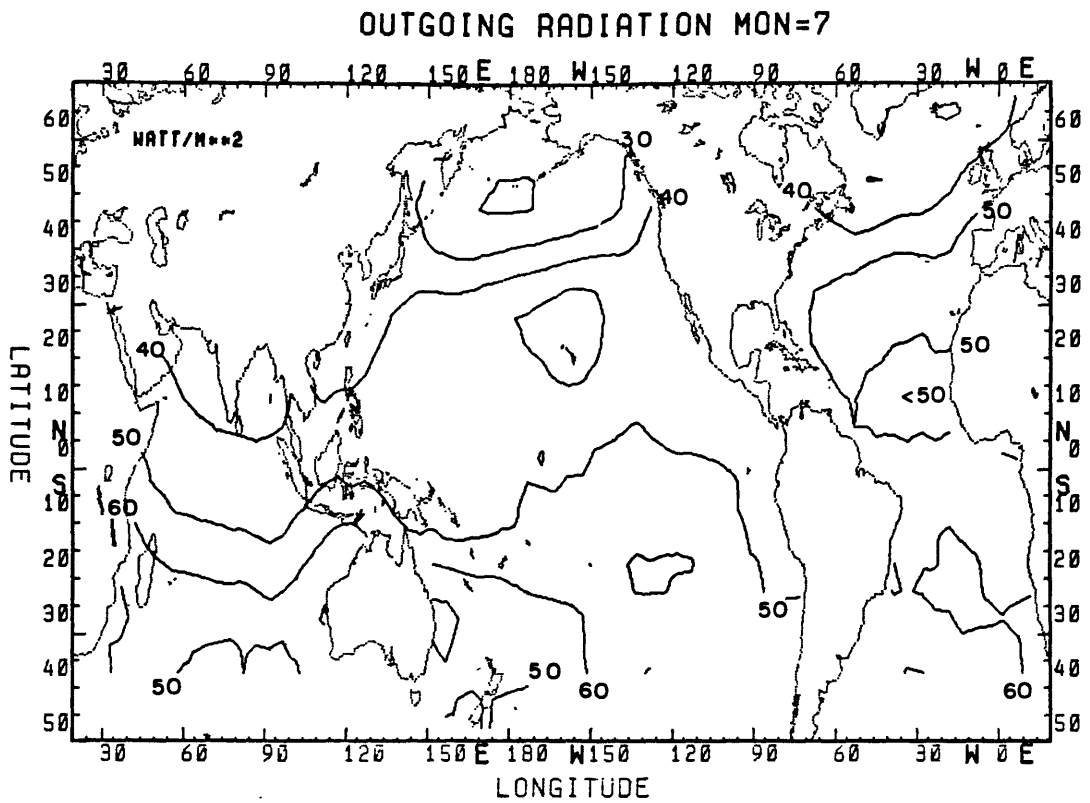


Figure 4.19 Long term monthly mean of outgoing radiation for July

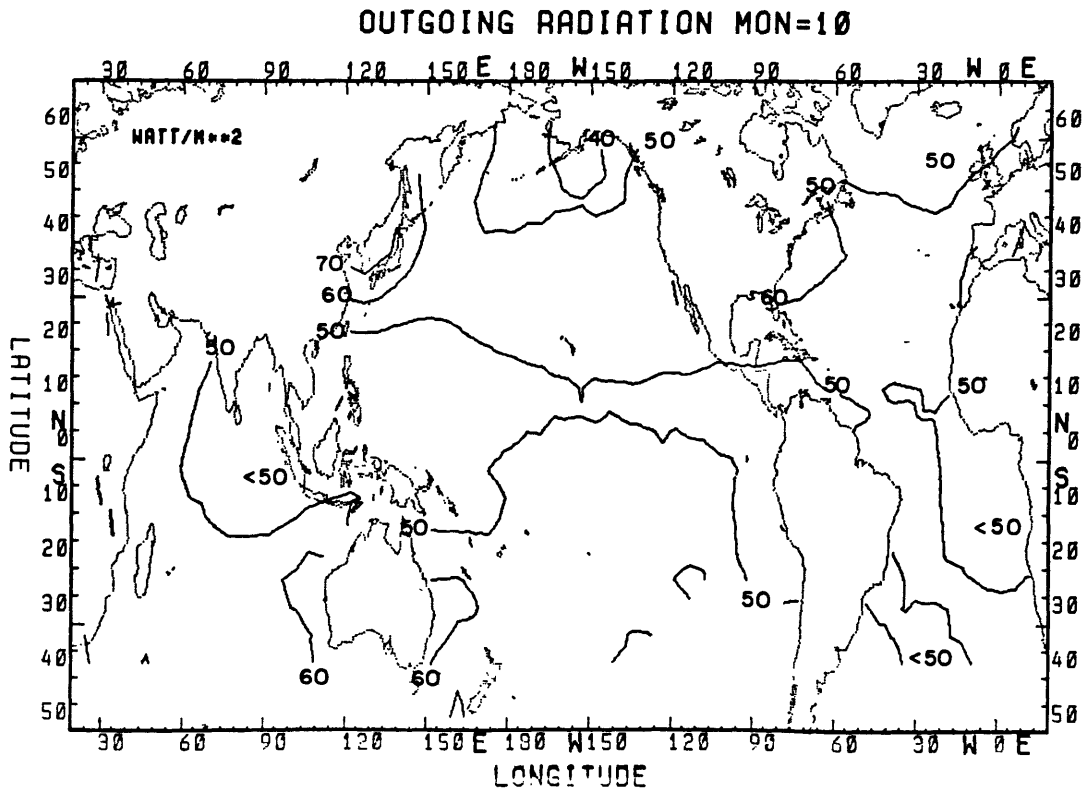


Figure 4.20 Long term monthly mean of outgoing radiation for October

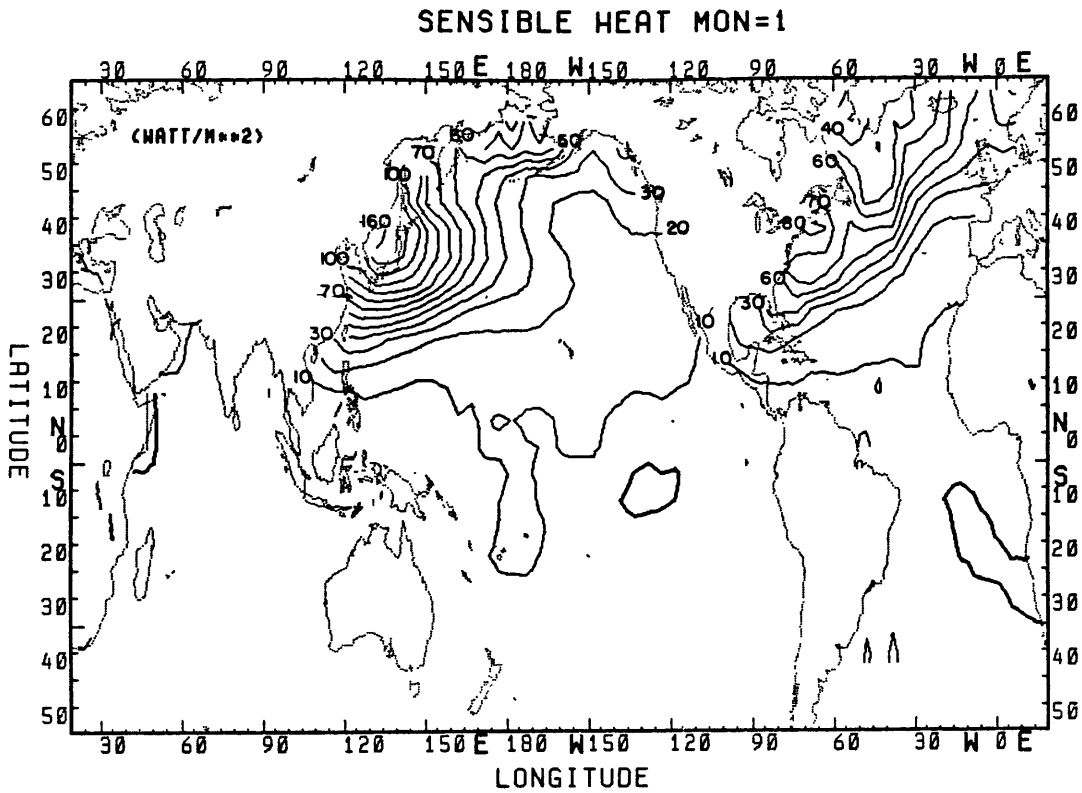


Figure 4.21 Long term monthly mean of sensible heat for January

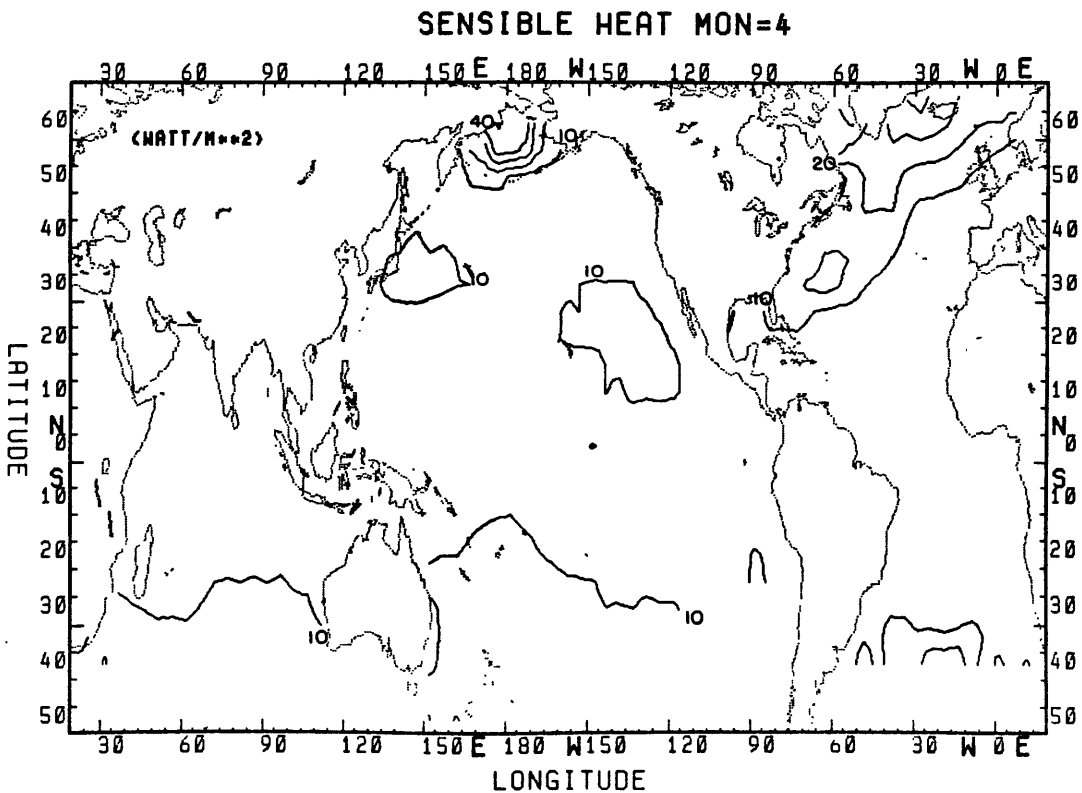


Figure 4.22 Long term monthly mean of sensible heat for April

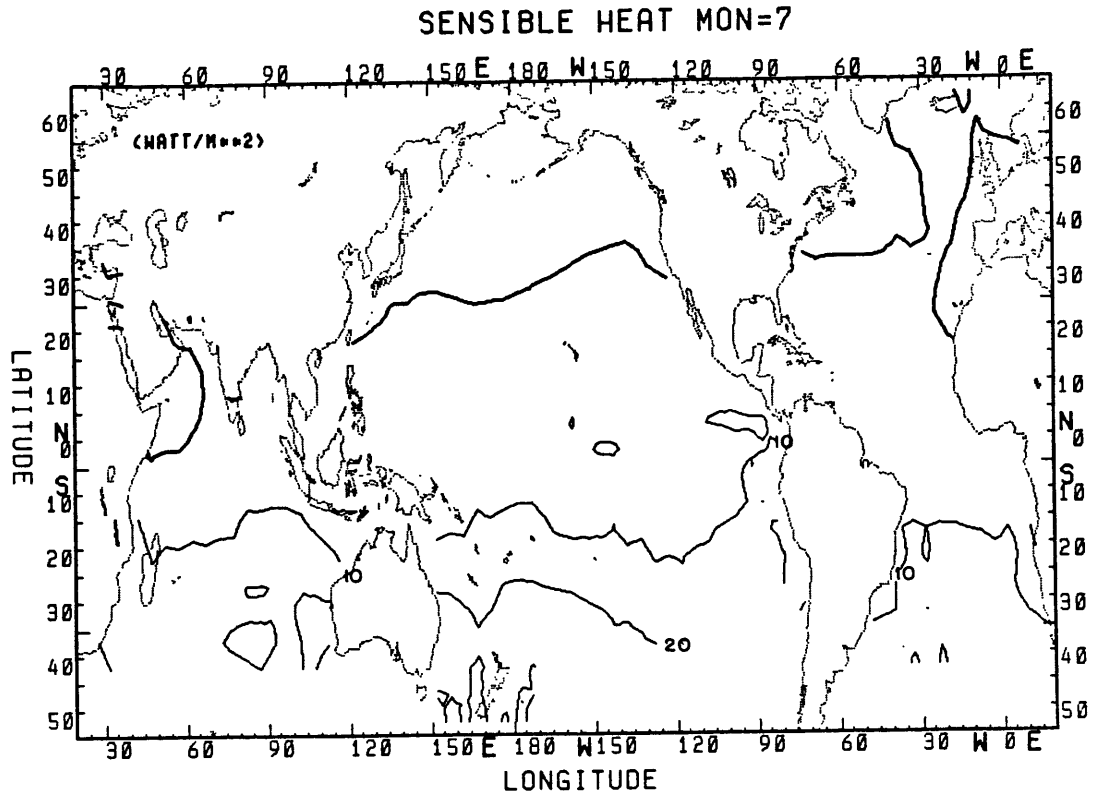


Figure 4.23 Long term monthly mean of sensible heat for July

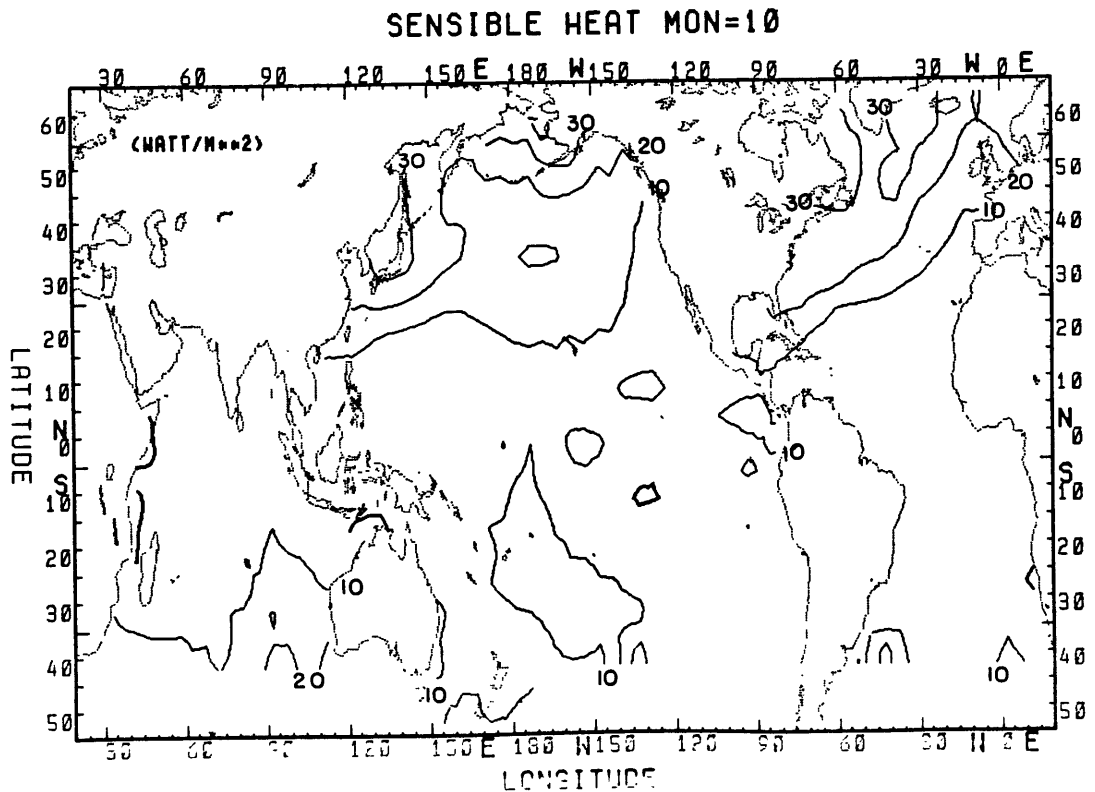


Figure 4.24 Long term monthly mean of sensible heat for October

There is large longitudinal structure in the Southern Hemisphere with maximum incoming radiation at 20°-30°S. In April, values at higher latitudes in both hemispheres are zonally distributed with the maximum in the equatorial region. In July, the maximum shifts north to the 20°-30°N latitude belt. In October, the maximum is centered around 10°S. There is considerable similarity between the spatial pattern of mean SST and mean incoming solar radiation, indicating that the solar energy is the primary driving force responsible for the mean SST pattern.

There is very little variation in outgoing radiation from season to season (Figures 4.17 to 4.20). Most of the values range from 40 to 50 watt/m². The only location where there is any gradient is along the coast of China where the calculated maximum value is 80 watt/m².

There is large seasonal variation in the distribution of latent heat flux (Figure 4.13 to 4.16). In January and October, the western ocean loses a large amount of heat through evaporation while the upwelling areas show minima. In April, the area of maximum loss moves to the central subtropical Pacific and southern Atlantic and southern Indian Ocean. Except in parts of the Indian ocean, the same pattern prevails in July where with the summer Monsoon season, there is a pronounced latent heat maxima in the Arabian Sea and in the western Bay of Bengal.

Contrary to latent heat fluxes, the sensible heat (Figures 4.21 to 4.42) has little spatial variation except in January when the warm western boundary currents in both the Pacific and the Atlantic oceans

set up a large temperature gradient between the cold air in the atmosphere and the warm ocean. This, together with the stronger winds in January, produces a large amount of energy loss through sensible heat flux.

To compare seasonal cycles of the energy flux components of the three oceans more closely, plots of seasonal energy flux cycles of selected grid points are presented from Figure 4.25 through Figure 4.28. In Figures 4.25 and 4.26, grid points in the central oceans at latitudes 45°N , 20°N , 0° , 15°S and 30°S were chosen to demonstrate the differences (if any) of annual cycles of energy fluxes among three oceans at the same latitude. In Figures 4.27 and 4.28, grid points in the boundary regions of the three oceans were selected. Along with the components of energy fluxes, seasonal zonal and meridional wind stress are also presented to indicate the possible effects of upwelling or advection. The grid points presented here are chosen mostly because they illustrate different characteristics of energy balance throughout the year, and also because the number of observations for these squares are good.

Figure 4.25a and 4.25b shows the energy balance for central north region (45°N) in the Pacific and Atlantic oceans. There is substantially more energy loss in the north Atlantic than in the north Pacific in the same latitudes. This is a direct result of much greater latent heat loss in the Atlantic due to warmer water in the Atlantic than in the Pacific at the same latitude. (See Figure 12 in Newell et al (1981), reproduced here as Figure 4.29.) In northern hemisphere winter

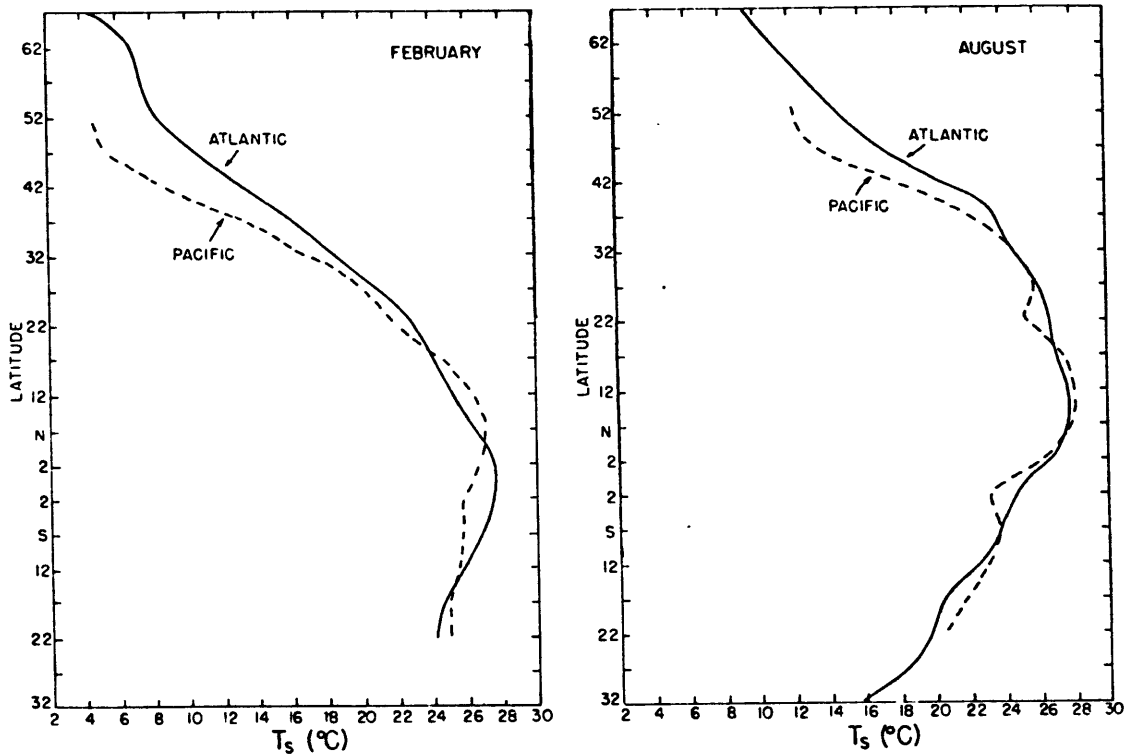


Figure 4.29 February and August zonal mean SST for the Atlantic and Pacific Oceans (From Newell et al, 1981)

months, the latent heat loss in the Atlantic can be three times greater and has a much larger annual cycle than that in the Pacific. The other components of the energy balance are comparable for these two regions. Newell et al (1981) have argued that the warmer water in the Atlantic is caused by the wind field carrying warm Gulf water further north than in the Pacific. The wind stress component shows a more northerly component in the Atlantic during the first part of the year. In the Pacific ocean, the largest latent heat loss and the largest meridional wind stress occurs in the Northern Hemisphere late fall and early winter.

This suggests that warmer water is carried there during these months and it gives off large amounts of latent heat.

Warren (1983) recently put forth an argument that the cold water is responsible for the absence of deep water formation in the North Pacific. In a simple salinity budget box model, he demonstrated that higher salinity in the North Atlantic surface water resulted from higher evaporation loss through warmer sea surface temperatures. This is in accord with our result that the latent heat loss is much greater in the North Atlantic than in the North Pacific at the same latitude. The denser water with higher salinity in the North Atlantic sinks to the ocean bottom while the fresher surface water in the North Pacific stays close to the surface.

In Figures 4.25c, d, and e, central ocean regions at 20°N from three oceans are compared. The Pacific and Atlantic profiles are much more alike than they were at 45°N. Note this is also the latitude where the zonal temperature of these two oceans are the same (Figure 4.29). The grid point in the Indian Ocean is from the eastern Arabian sea and it shows a completely different profile. It has two peaks in

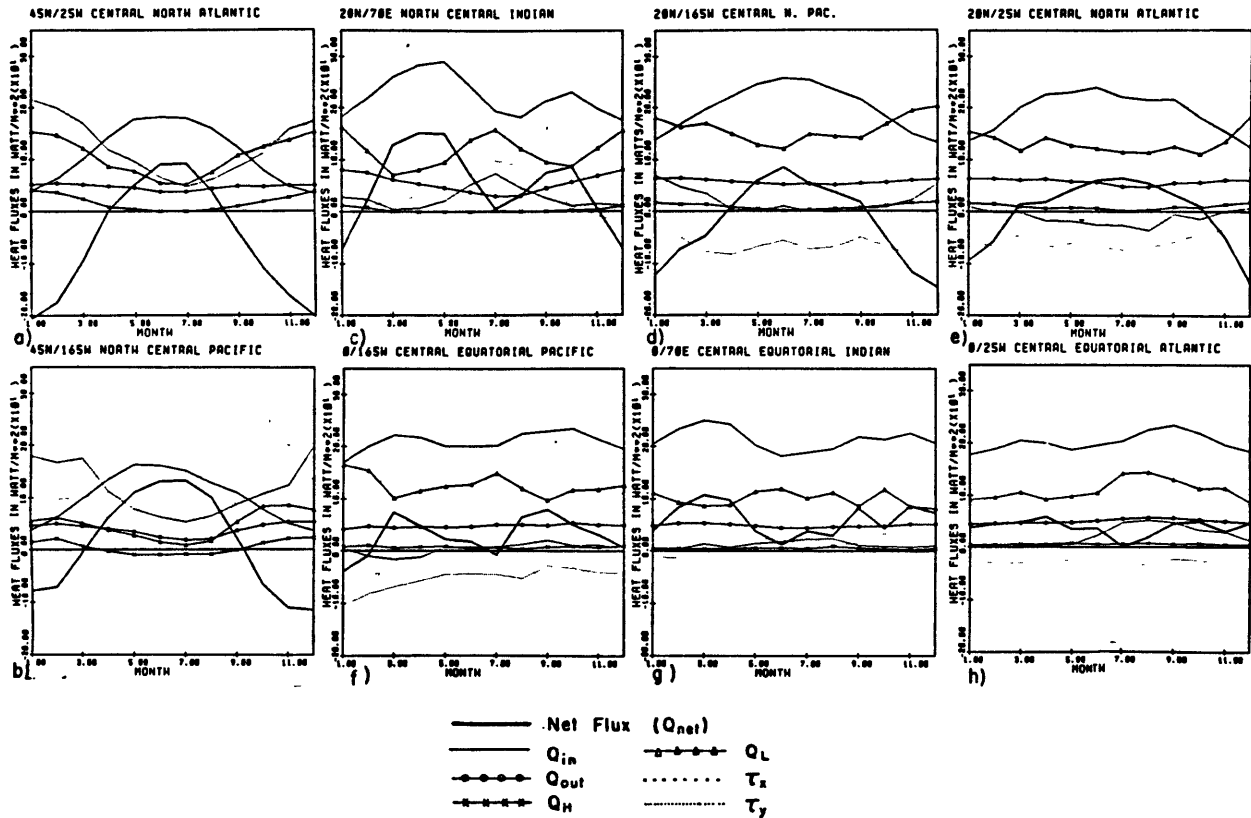


Figure 4.25 Seasonal cycle of energy flux components at selected grid squares

the annual net energy gain: one in the spring and another in the fall. These are the two seasons when there is the least latent heat loss and the most incoming solar radiation. In July, the minimum in heat gain is associated with the summer monsoon and its stronger winds. In northern hemisphere winter, the larger latent heat loss is from large humidity difference between the air and the sea. In July and January, a decrease in incoming radiation is observed due to enhanced cloudiness.

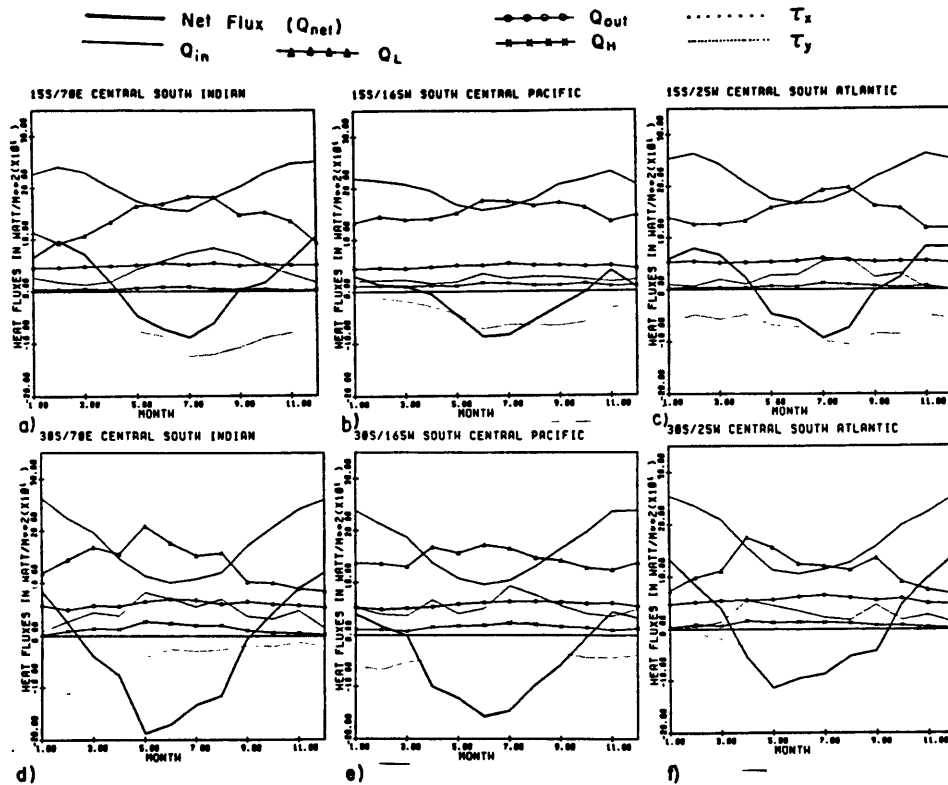


Figure 4.26 Seasonal cycle of energy flux components at selected grid squares

At the equator, the seasonal cycle disappears in all oceans as is evident in Figure 4.25f, g and h. The monsoon cycle is still present in the Indian Ocean at this latitude. The peak in the latent heat in the Atlantic is from the higher level of zonal wind stress from June to November. In the Pacific, the annual variation is again due to variation in the latent heat flux. It is greatest in January with a secondary peak in July. In the Southern Hemisphere, points along 15°S and 30°S were selected and presented in Figure 4.26. At 15°S, the seasonal cycle is evident again with its variation weakest in the Pacific where the incoming solar radiation balances all other components in January. In the Atlantic and the Indian oceans, the peaks in latent heat during the southern winter (July) are brought about by increased

winds. Coupled with less solar radiation, this results in a energy deficit in the winter season for all oceans. The winds in the Pacific are weaker but the latent heat loss is comparable in magnitude with the other oceans. This indicates the specific humidity difference there is greater than it is for the other two oceans at the same latitude.

Further south at 30°S, the seasonal swing is greater. Here again, the profile of latent heat loss follows that of the zonal wind stress. In the Atlantic and the Indian oceans the seasonal variation in latent heat brings about a energy surplus in the summer and a deficit in winter. In the Pacific, latent heat loss stays high throughout the year, eliminating any significant energy surplus in the Southern Hemisphere summer months. Thus, for most of the central southern hemisphere in the Pacific there is a significant annual energy loss while in the Atlantic and the Indian oceans there is a balance between the energy gains in the summer and energy losses in the winter.

The outgoing radiation and sensible heat loss stay constant throughout the year. Their magnitudes are almost identical for all three oceans at almost all latitudes in central oceans. The sensible heat loss also has a slight annual cycle in the higher latitudes in the Atlantic and in the Pacific.

The energy balance for western boundary current regions in the Atlantic and the Pacific are shown in Figure 4.27a and 4.27b. These are regions where maximum energy loss are observed. In the Northern Hemisphere winter months, the warm current from the south sets up a tremendous sea-air temperature difference and therefore large amounts of

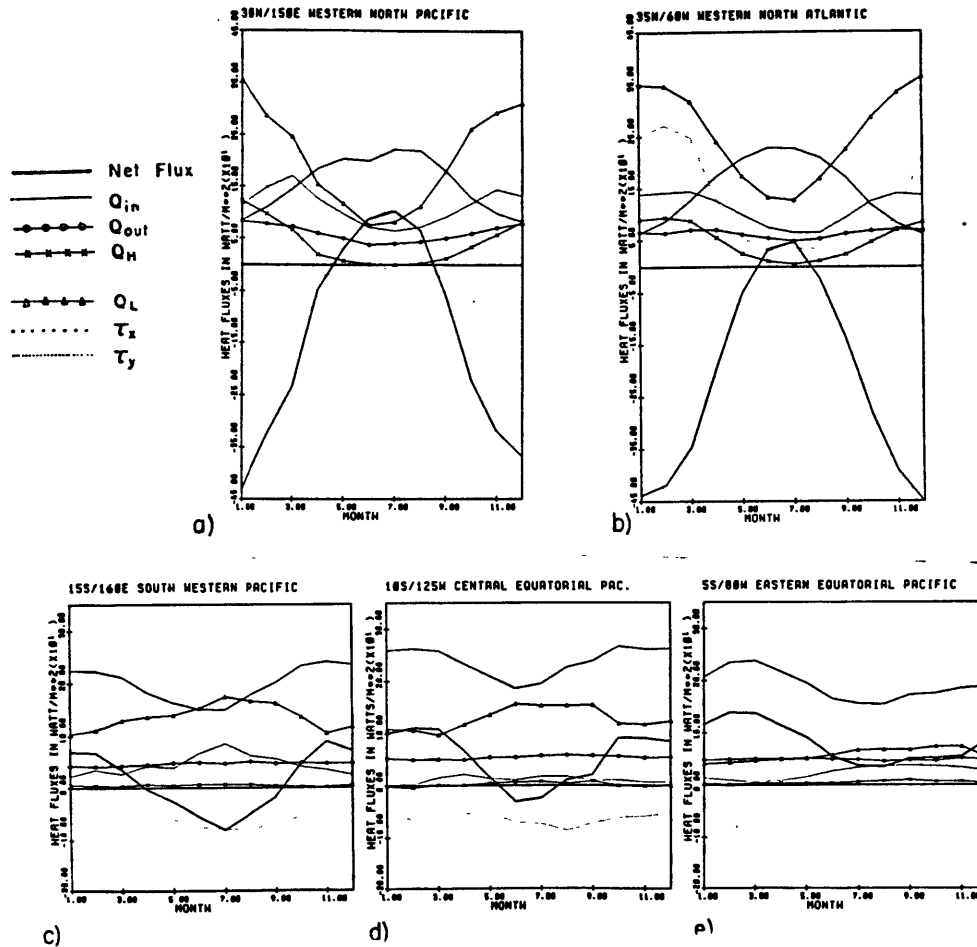


Figure 4.27 Seasonal cycle of energy flux components at selected grid squares

sensible heat loss to the air. The strong winds in the winter together with high humidity difference bring about latent heat flux in excess of 350 watt/m^2 . The larger northward meridional wind stress in the Atlantic might also help to advect warmer water further north than in the Pacific. This in turn causes larger latent heat loss in the Atlantic than in the Pacific so that the annual net energy loss is greater in the northwestern Atlantic than it is in the northwestern Pacific.

To contrast the different characteristics in the energy balance profile between eastern and western coast in the tropical Pacific, Figure 4.27c, d, and e are presented. The eastern coast Pacific is a region where there is large energy gain observed all year. There is very little energy loss through evaporation due to weaker winds and small humidity differences. In the central equatorial region, there is a slight energy deficit in May to August. The higher humidity difference causes greater latent heat loss and cloudiness decreases the incoming radiation received. There is greater meridional wind stress in the central region than in the eastern region, but the larger latent heat flux is mostly from the high humidity difference there. In the

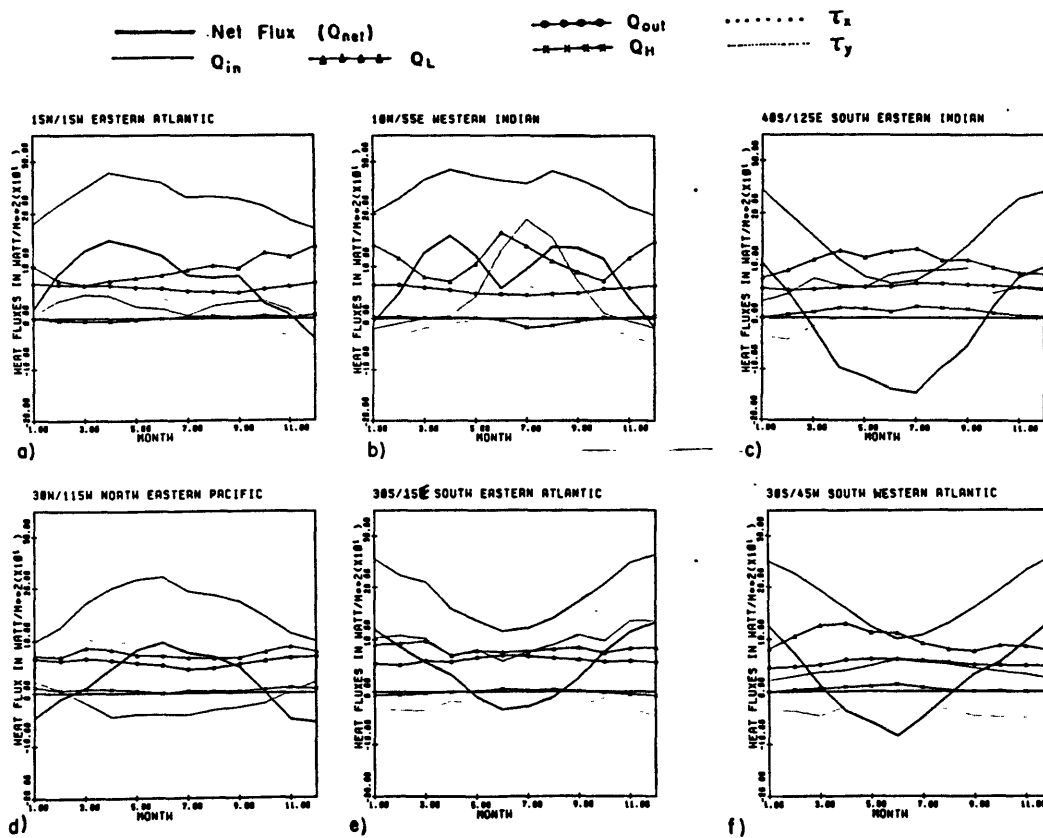


Figure 4.28 Seasonal cycle of energy flux components at selected grid squares

western equatorial region the wind and the humidity difference are both greater, therefore, there is a much larger energy deficit in the winter months.

The difference between the southwestern Atlantic and the southeastern Atlantic is not as great as the east-west difference observed in equatorial Pacific (Figure 4.28e and 4.28f). The zonal wind stress is greater off the southern African coast than it is off Brazil. However, latent heat loss is greater near Brazil due to warmer sea water.

Two additional grid points from the Indian ocean are shown in Figure 4.28b and 4.28c. One is from the western Indian ocean at 10°N and the other is south of western Australia at 40°S . The point at 10°N is north of the Somali Republic. Here the effect of the summer monsoon is clearly evident. In most of the northern Indian Ocean, there is a large net heat gain throughout the year similar to the balance shown here.

Heat balance in the southeastern Indian ocean is not much different from the central south Indian ocean (see Figure 4.27d) with the exception of smaller latent heat loss in the eastern part of the ocean due to drier air there. The total heat loss is therefore smaller than in the central region. This is true despite the fact that it is further south and hence receives less incoming radiation.

Two grid points off the eastern coast in the Atlantic and the Pacific oceans are shown in Figure 4.27a and 4.27d . One is off the Sahara desert in the Cape Verde Island region, the other is off the Baja California coast. The eastern subtropical Atlantic is a major heat gain

area. Maximum annual heat gain is observed there. This is a region where major upwelling is observed. Under the influence of the Bermuda-Azore high, lack of clouds due to the subsidence allows radiation close to 300 watt/m^2 to come through. The cool water also keeps the dew point depression small, hence less latent heat loss. Similar mechanisms operate in the eastern Pacific region.

IV.3b Annual Mean Fluxes

In this section we present the results of the 31-year annual means of the heating terms and the pertinent meteorological parameters used to calculate these means. Ultimately we would like to see how much of the observed SST pattern is explained by the net energy flux.

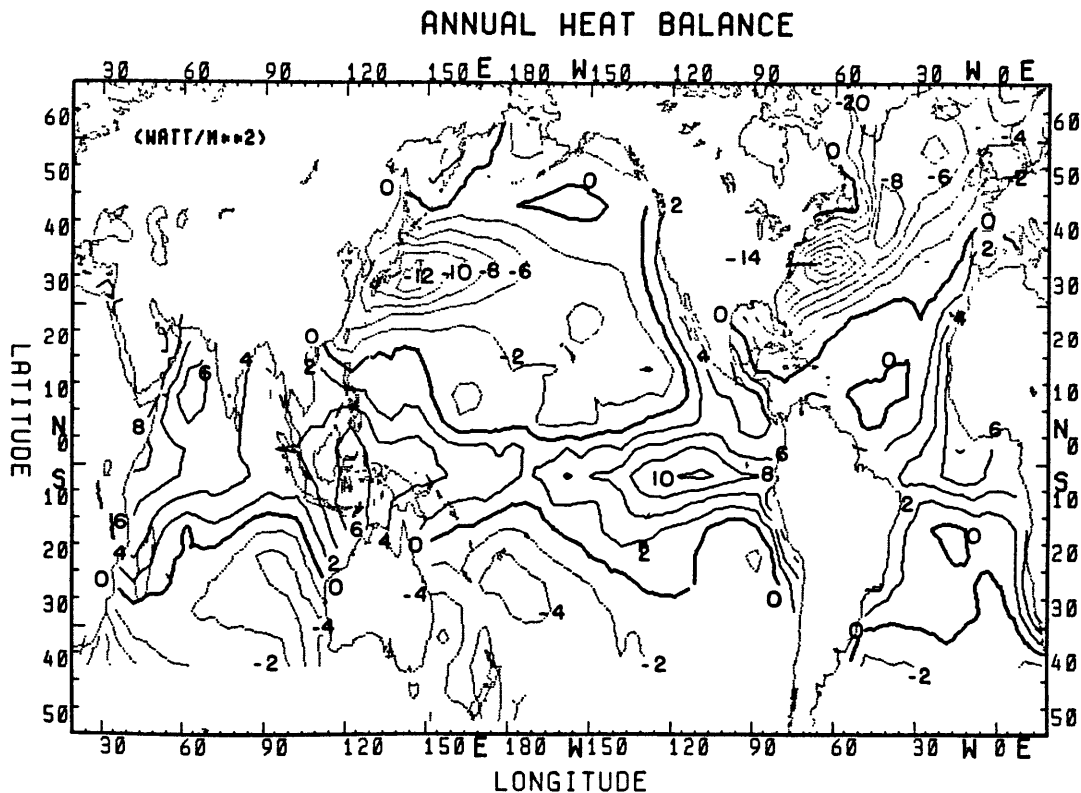


Figure 4.30 Long term annual mean of net energy flux

The annual net energy balance (Q_{net}) is presented in Figure 4.30. In general, there is a net surplus of energy in the equatorial Pacific region, most of the Indian Ocean, and in the eastern tropical Atlantic Ocean. The largest energy surplus occurs in the upwelling region along the South American coast, and in a small region off eastern Africa. The Gulf Stream and the Kuro-Shio are the two regions where there are large energy losses to the atmosphere, the Gulf Stream having the largest of the two. There are small areas of energy gain north of these western boundary currents, and a positive strip exists along the coast of North America where the cool California current travels. Similarly, energy gain is observed along the upwelling region off the African coast. There are calculated energy losses in the Pacific and Indian oceans south of 20°S . Most of the balances in the south Atlantic are probably too small to be significantly different from zero. In general, there is a nice gross relationship between observed SST patterns and the net energy balance: Areas with warm currents give off energy to the atmosphere and areas with cool water (such as upwelling regions) take in energy from the atmosphere. To see which component is responsible for this net energy pattern, we present the annual mean values of Q_{in} , Q_{out} , Q_{l} , and Q_{h} separately in Figures 4.31 through 4.34 .

Incoming solar radiation is the largest energy input into the oceans. The long term mean annual pattern shows that most of the Indian and tropical Pacific oceans are dominated by values greater than 200 watt/m^2 . The Atlantic has a smaller tropical region with the same

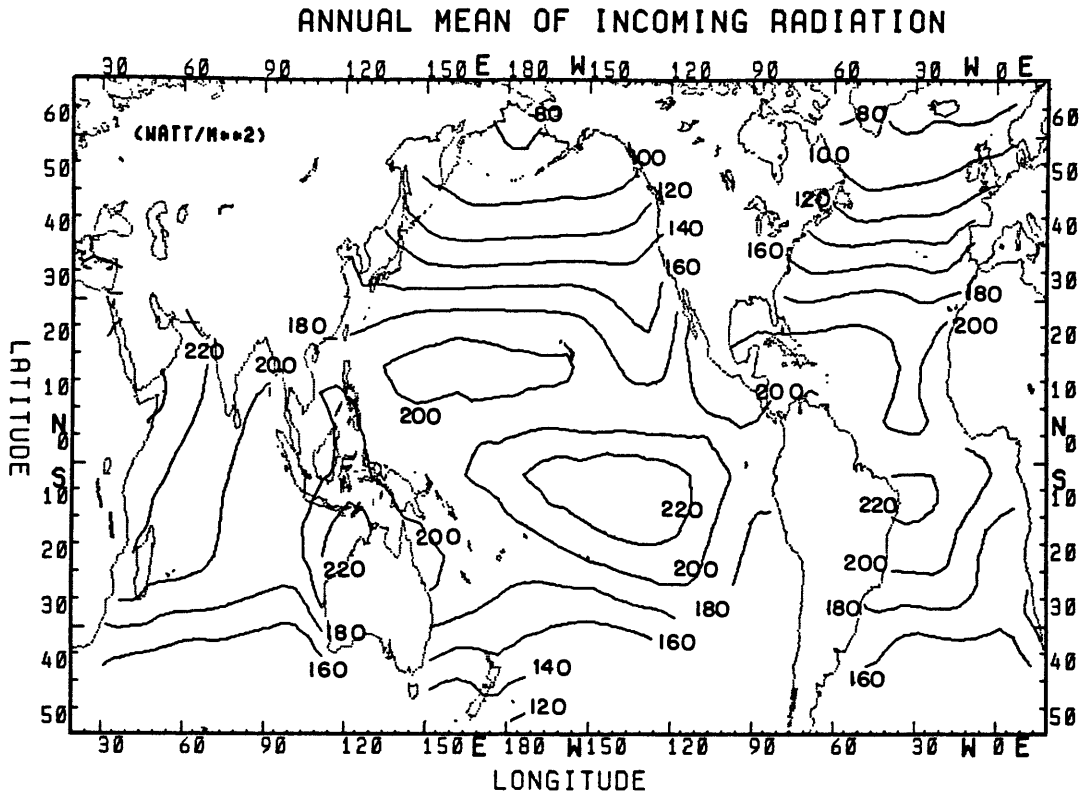


Figure 4.31 Long term annual mean of incoming radiation

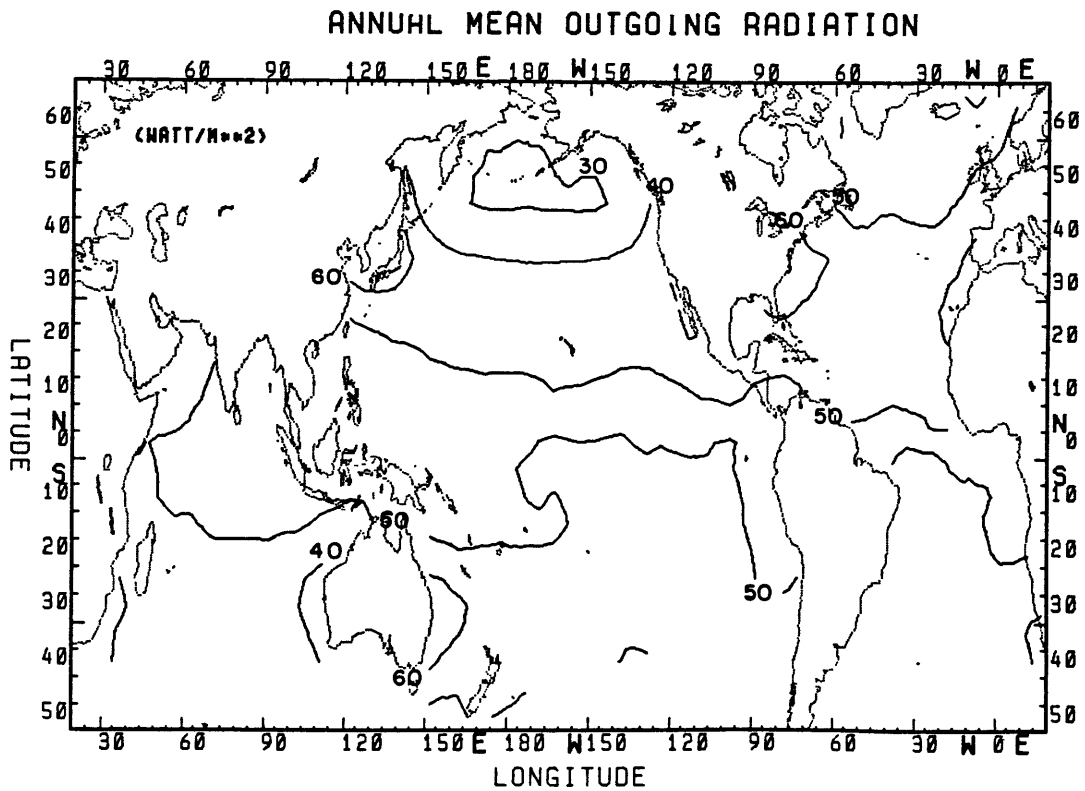


Figure 4.32 Long term annual mean of outgoing radiation

values. The deviation between the zero line and the 180 watt/m^2 line comes from the interplay between other components of the total flux. Since all of the variation in the incoming solar radiation comes from the cloudiness data, one would expect the annual mean cloud cover to explain most of the observed distribution of absorption of incoming solar radiation. Figure 4.35 illustrates the annual mean pattern of cloudiness. One can clearly see the similarity of annual mean cloud cover to that of the incoming solar radiation. The absorption is high where the mean cloud cover is low and vice versa.

Another radiative flux is outgoing radiative flux from long wave radiation (Figure 4.32). This term is a function of air temperature, cloud cover and humidity. The magnitude of this term is about 25% of the incoming solar radiation and its latitudinal variation is much less pronounced than other components of the energy budget. One feature worth noting is that the mean value of outgoing radiative flux is less in the North Pacific than it is in the North Atlantic at the same latitude. Presumably this is due to the surface water being colder in the North Pacific than it is in the North Atlantic (see Figure 4.29).

Of the two heat fluxes (latent and sensible), latent heat is overwhelmingly the dominant flux (Figure 4.33). One might say that the net energy is mostly a balance between the incoming radiation and the latent heat flux. The largest evaporative loss regions are the Indian Ocean, the subtropical western Pacific, the Gulf Stream and the southwestern Atlantic. Regions where there is a minimum of evaporative

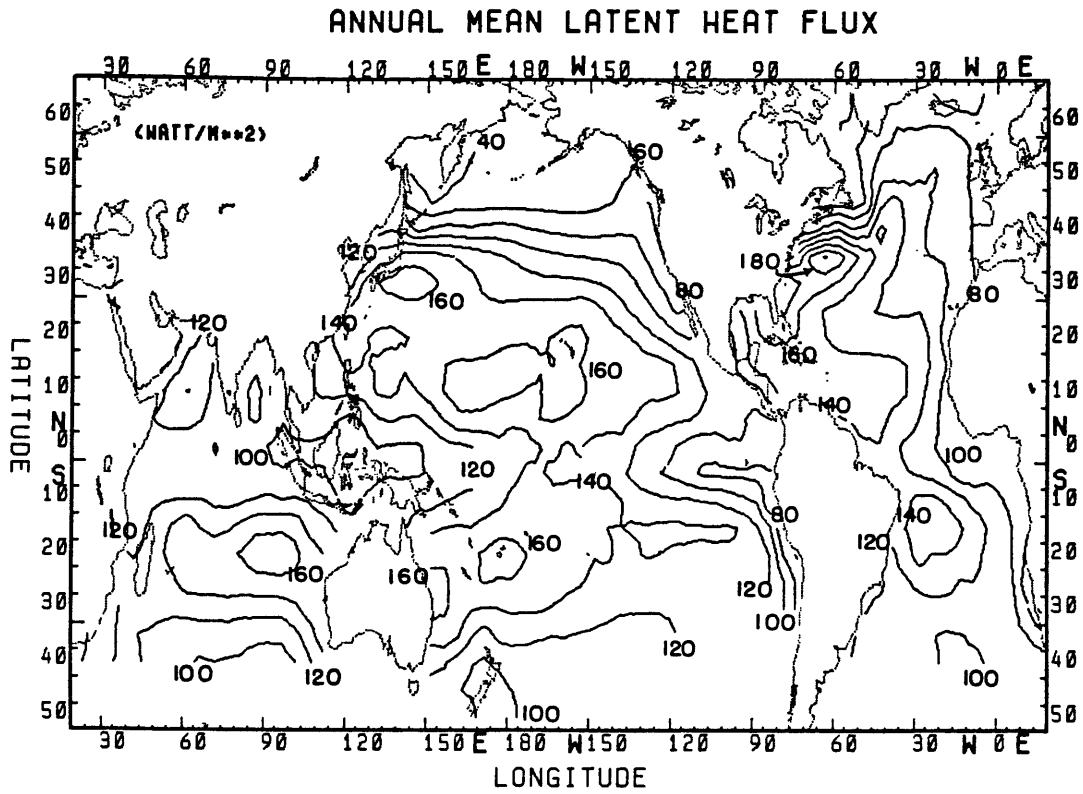


Figure 4.33 Long term annual mean of latent heat flux

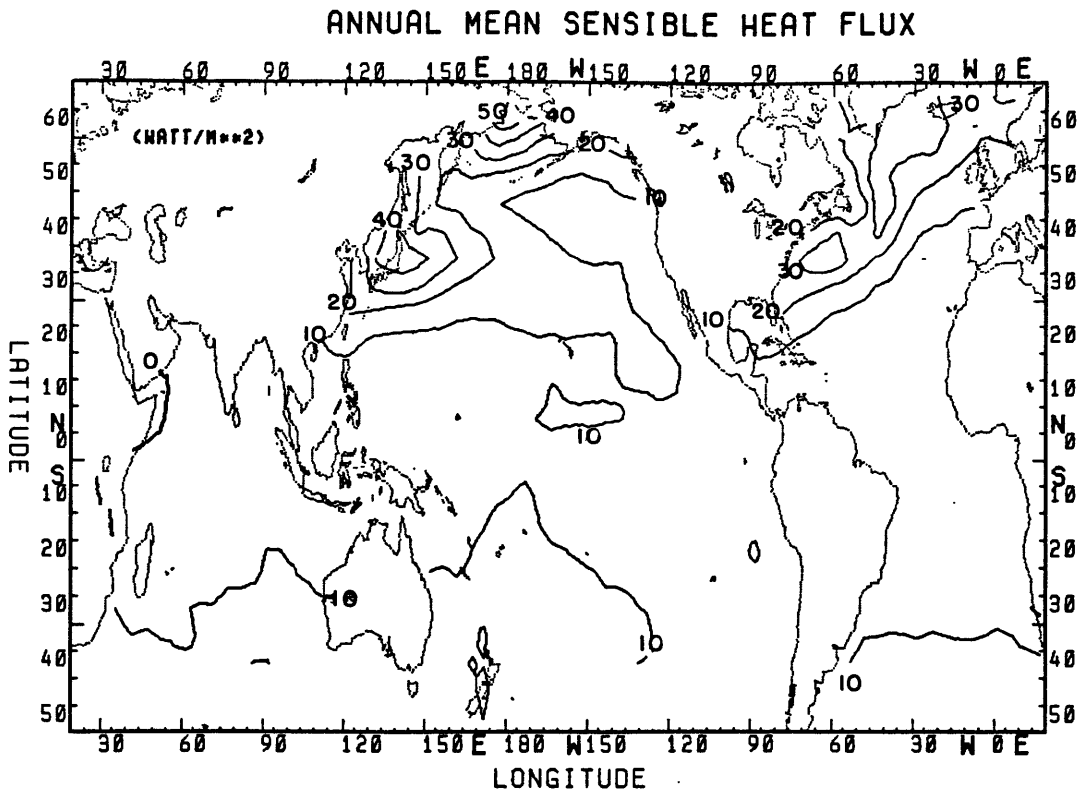


Figure 4.34 Long term annual mean of sensible heat flux

loss are also areas of large net heating. These are mostly regions where there is cooler surface water. Three factors contribute to the calculation of latent heat flux: wind speed, specific humidity difference and the bulk transfer coefficient (C_e). The annual mean value of C_e is shown in Figure 4.36. The values vary from 1.1 to 1.6. Spatially, C_e does not vary much. The area with the most variation is the area above Australia where the lowest C_e is observed. The low value of C_e explains why low latent heat flux is observed there. Off the south American coast, the low value of C_e also contributes to the low latent heat flux.

Humidity difference and wind speed are about equally important in the variation of latent heat flux. The latent heat flux is essentially a product of these two fields. Their annual mean patterns are shown in Figures 4.37 and 4.38. The humidity difference roughly follows the pattern of temperature: it is high where the oceans are warm and low where they are cold. The wind speeds are greater in high latitudes than in low latitudes. There are minima along regions of upwelling and in the north Indian Ocean. In general, there is a negative correlation between wind speed and the humidity difference. The wind is strong where the humidity difference is low and vice versa.

The sensible heat flux is the smallest of all terms contributing to the net heating term (Figure 4.34). Its maximum is the same in magnitude as the mean of the outgoing radiation (about 50 watt/m^2). This is observed in the regions of western boundary currents. The spatial pattern shows little or no variations outside the boundary currents. Like latent heat, sensible heat flux is a product of three

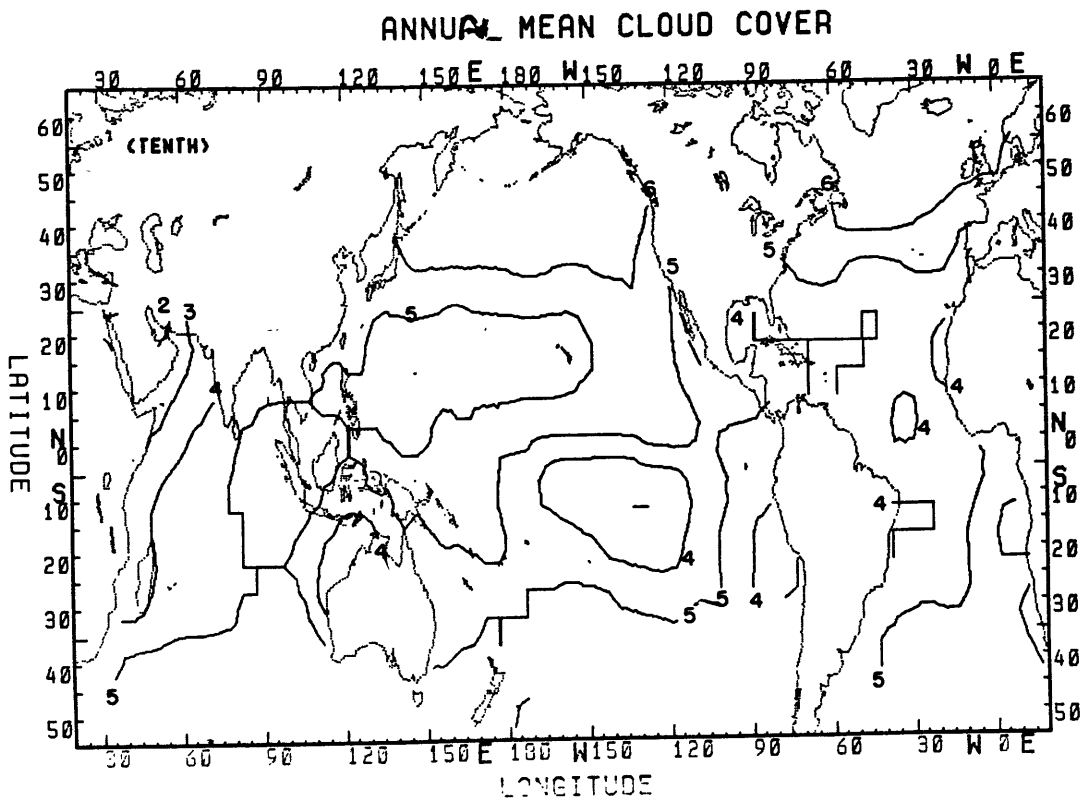


Figure 4.35 Long term annual mean of cloud cover

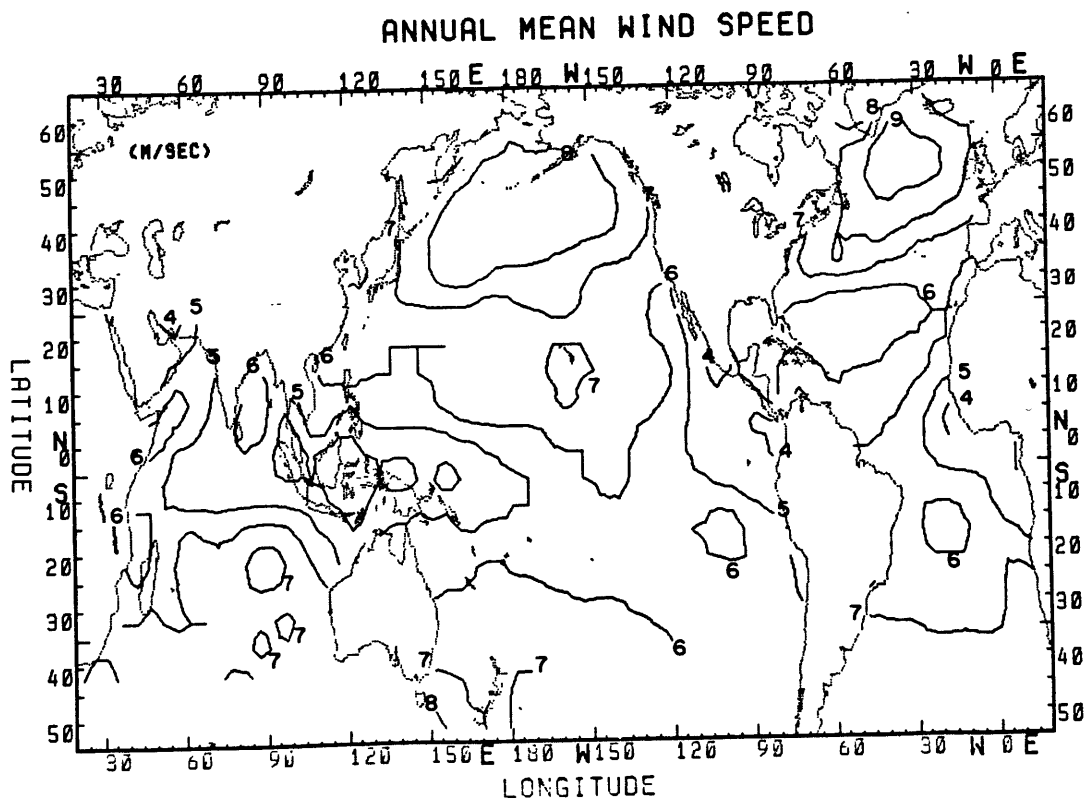


Figure 4.36 Long term annual mean of wind speed

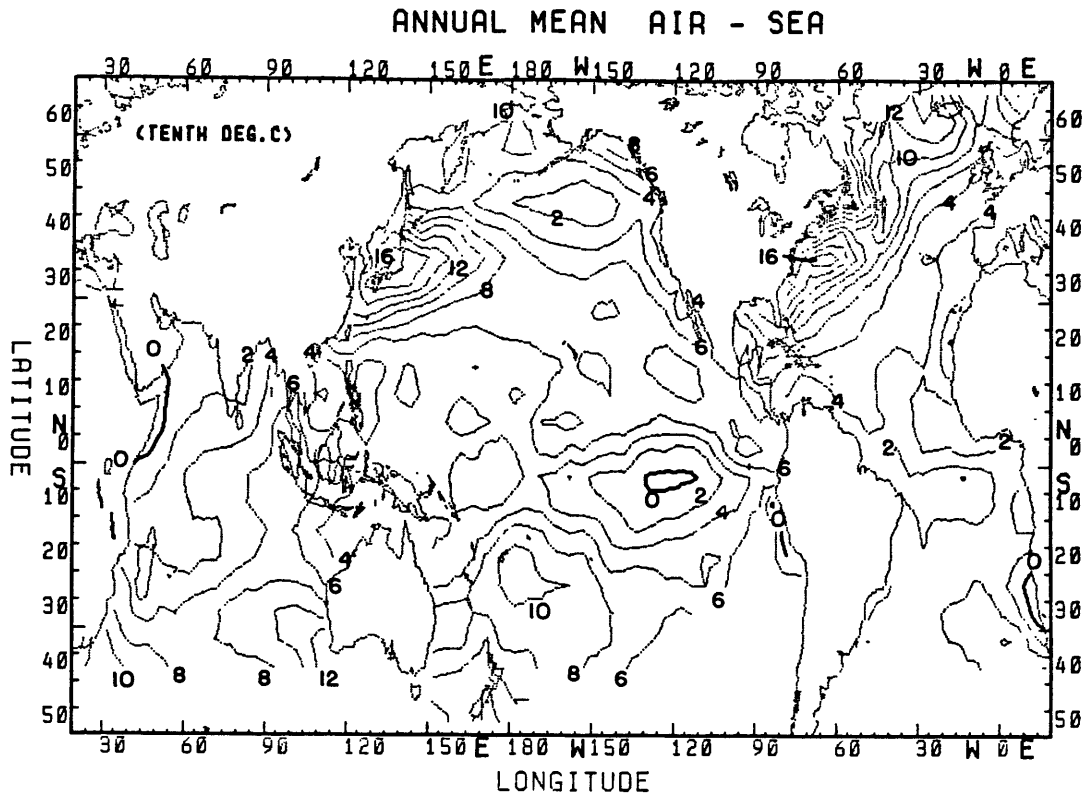


Figure 4.37 Long term annual mean of air-sea temperature diff.

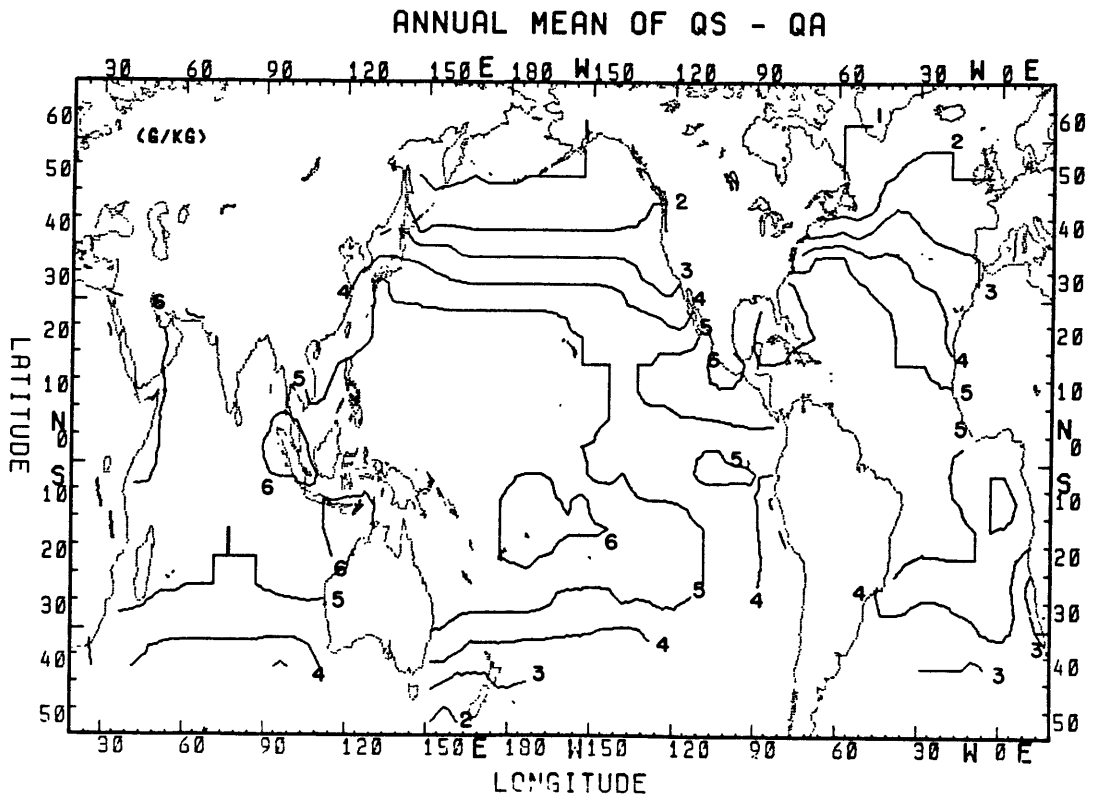


Figure 4.38 Long term annual mean of specific humidity difference

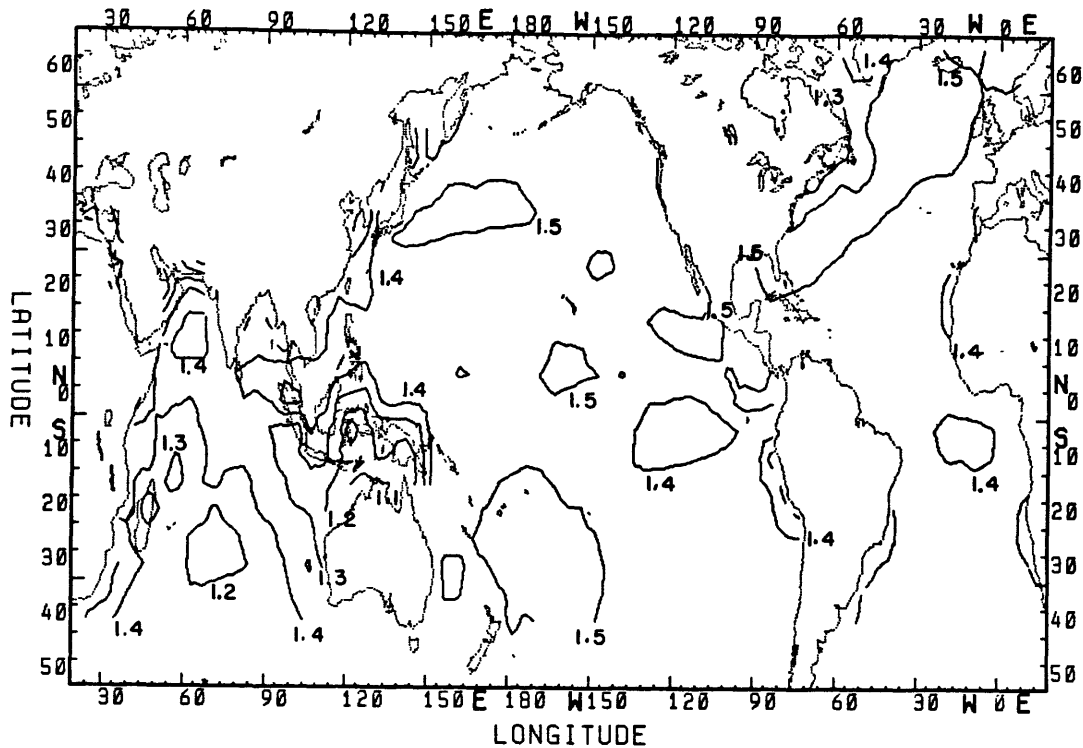
ANNUAL MEAN C_e 

Figure 4.39 Long term annual mean drag coefficient (C_e)

terms: C_e , wind speed and air-sea temperature difference. The annual mean pattern of air and sea temperature difference is illustrated in Figure 4.39. Clearly the spatial variation can be attributed mostly to that of air-sea temperature difference. Note the only regions where the sea is cooler than the air are in areas of intense upwelling.

Zonal averages of all three oceans are computed for each of the terms that make up the net energy term and these are presented in Figure 4.40. The same quantity is also calculated for the meteorological variables that contribute to these fluxes. They are presented in Figure 4.41. There is an obvious inverse relationship between Q_{in} and cloud cover. The zone of ITCZ is visible at $5^\circ N$ and it has a corresponding local minimum for Q_{in} at that latitude. Q_1 is a

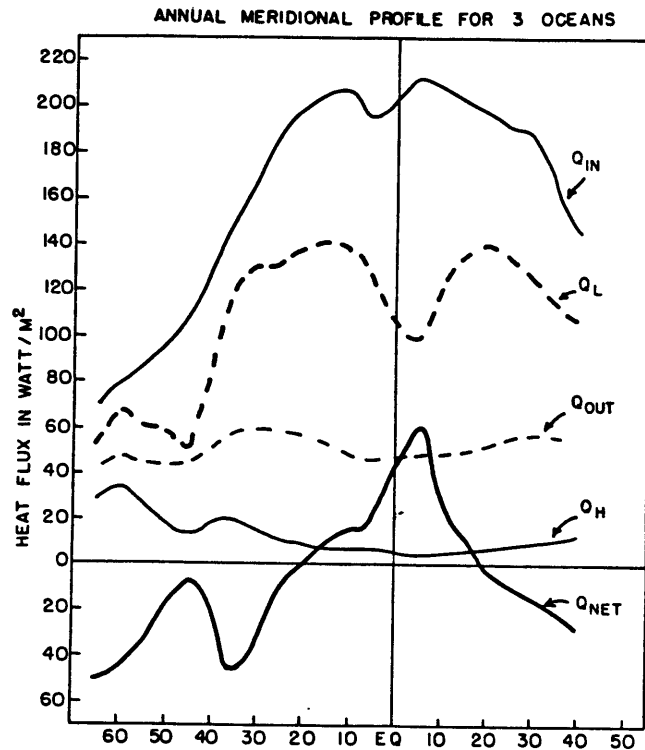


Figure 4.40 Zonal average of energy flux components for the three oceans

product of the profiles for C_e , wind speed and humidity difference with a minimum at 5°S and 45°N. Profiles of Q_h follow that of air-sea temperature difference with a minimum around 45°N. Q_{out} exhibits little or no latitudinal variation. The latitudinal profile of Q_{net} has a local maximum at 45°N and a local minimum at 35°N. This is mostly from the variation in Q_l . The minimum in Q_{in} around 5°N and the minimum in Q_l at 5°S gave Q_{net} its variations in the tropics. Comparing these profiles to that of SST, one can see clearly latitudinal zones where large dynamical processes are necessary in order to explain the observed profile of SST. There is almost a symmetry of SST profiles around the equator (The actual maximum is skewed slightly to 5°N.)

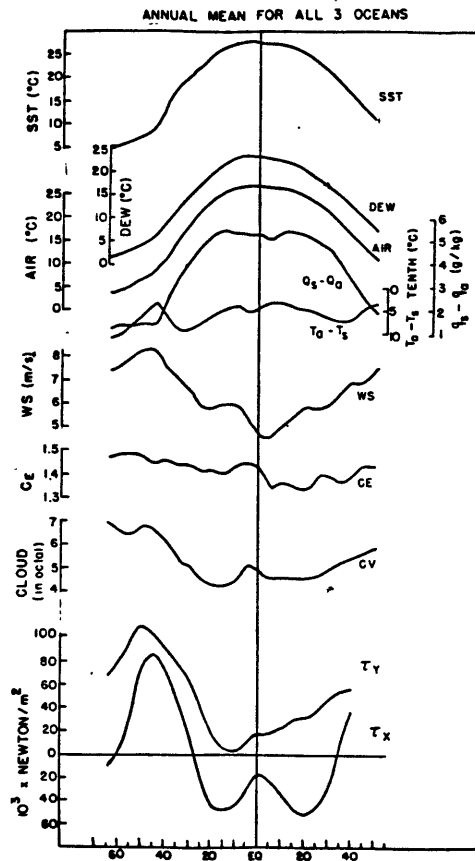


Figure 4.41 Zonal average of SST, air, dew point, $q_s - q_a$, $T_a - T_s$, wind speed, C_e , cloud cover, and wind stress

The profile of Q_{net} has a maximum at 5°S and lacks the symmetric property that the SST exhibits. In order to understand the dynamic processes that maintain the observed SST, subsurface data are needed.

The meridional profiles of annual energy budget for the three oceans separately are presented in Figure 4.42. The energy surplus latitudes are north of 20°S in the Indian Ocean; south of 5°N and north of 15°S in the Pacific ocean and south of 25°N in the Atlantic ocean. Clearly, if no latitudinal trend is observed, there should be a transport of energy from the surplus regions to regions with a deficit. With the constraint imposed on by the configuration of the ocean basins,

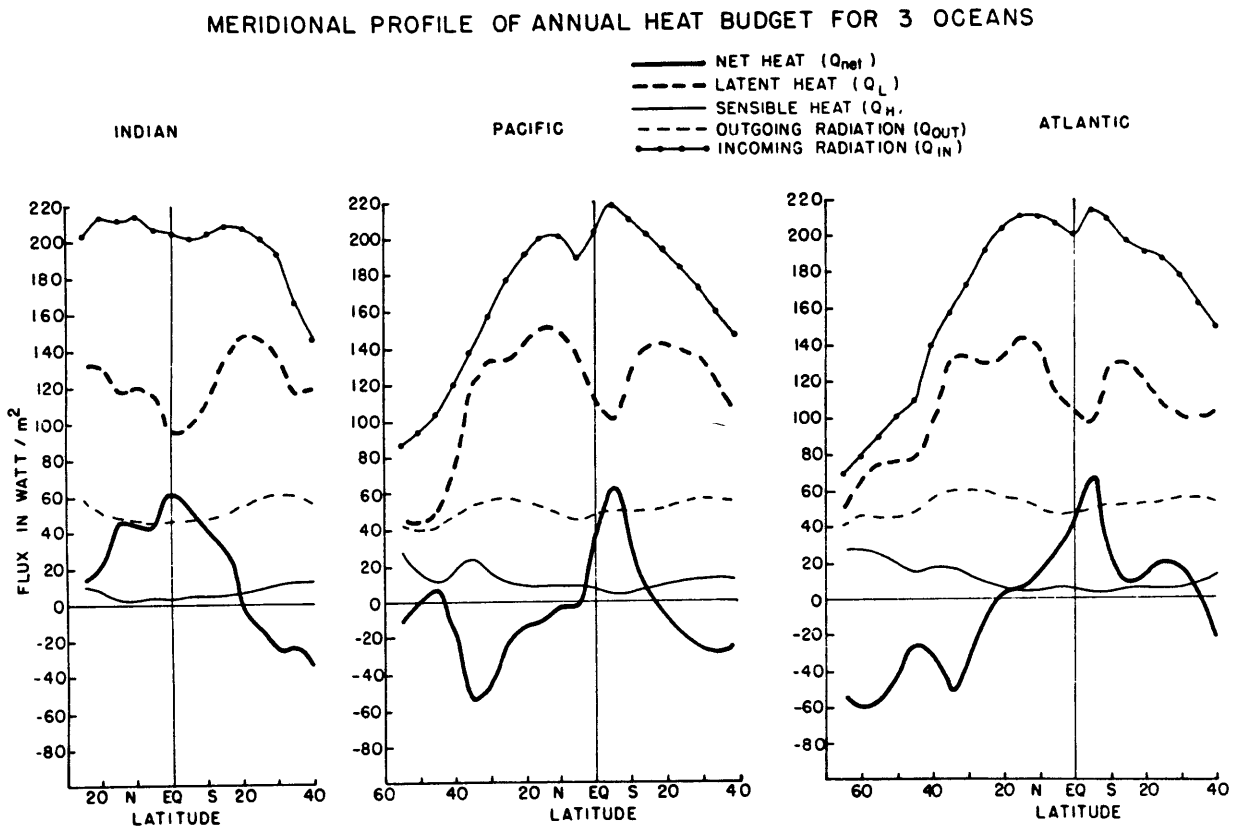


Figure 4.42 Meridional profile of annual energy budget for the the three oceans

this would imply a northward transport in the Atlantic; a southward transport in the Indian; a northward transport in the northern Pacific and a southward transport in parts of the south Pacific. The calculation of this energy transport will be discussed in detail in Chapter V.

IV.3c Comparison with Other Results

In this section we will compare our calculations of annual mean energy budget terms with those of other researchers. It is extremely difficult to make a straightforward comparison of various estimates due to several reasons: First of all the data processing criterion are usually different. Secondly, different formulae are used to derive the

same quantity. Thirdly, the spatial and temporal resolution of the calculations vary. However, it is often instructive to compare estimates of the same quality to see how variations from the above mentioned sources contribute to the differences observed. We will restrict our comparisons to those estimates that have the same data sources and whose method of computation are closest to ours. Namely, studies that use ship observations and make the calculations with bulk formulae. Hastenrath and Lamb (1978, 1979) have published an atlas of oceanic energy budgets for the Indian Ocean, the tropical Atlantic and the eastern Pacific oceans. Bunker (1976) has results for the North Atlantic and Clark (1965) has estimates for the North Pacific. Weare et

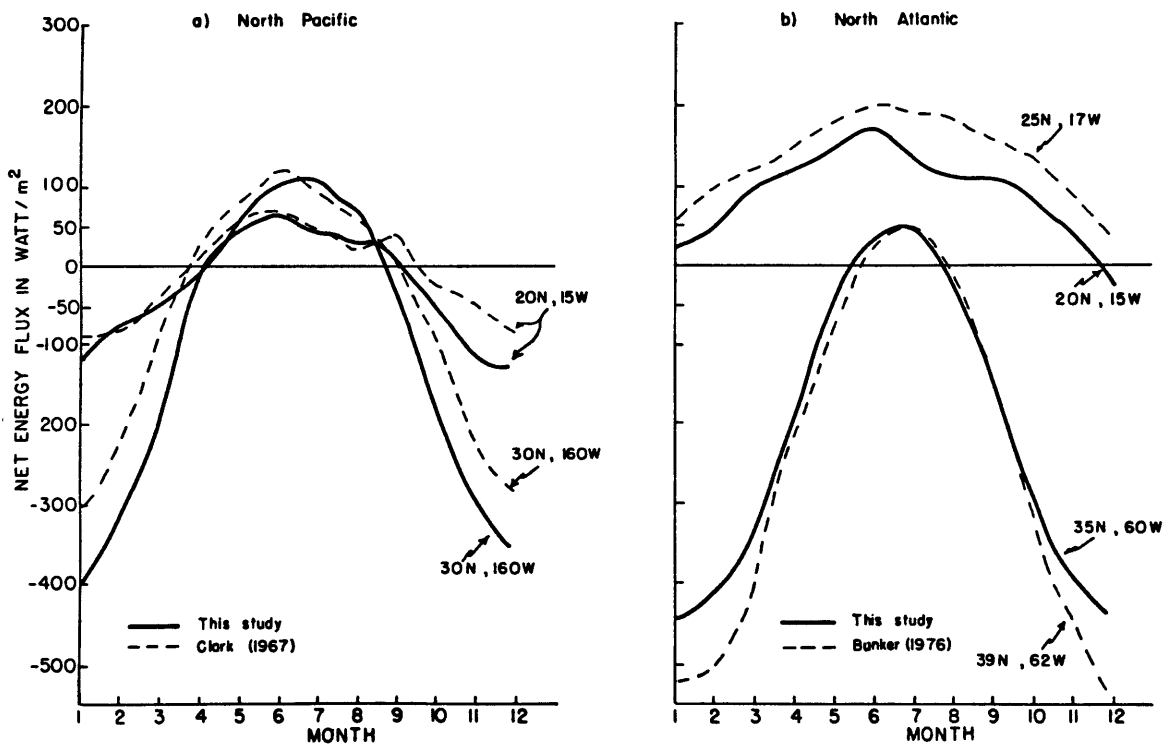


Figure 4.43 Comparison of seasonal cycle of net energy flux estimates for a) North Pacific, and b) North Atlantic

al (1980) has also published values for the tropical Pacific. We will compare results region by region.

In the North Atlantic, our net energy term agrees fairly well with Bunker's estimate. The long term monthly mean values of Q_{net} at two grid squares in the North Atlantic are presented in Figure 4.43b. The zero line that divides the surplus area from the deficit coincide almost exactly but the magnitudes of the net energy flux are different, especially in the Northern Hemisphere winter seasons. Bunker's estimate in regions of maximum energy loss in the Gulf Stream are approximately 10% higher than ours. The same discrepancy is found (not shown) in upwelling regions where there is a maximum energy gain. His values for the sensible heat flux is about 5 watt/m^2 higher in regions of maximum loss (again in the Gulf Stream.) Radiative fluxes and latent heat fluxes also exhibit the same general distribution pattern, but our values are about 10% higher than his. These differences could be attributed to the fact that he calculated individual fluxes from each observation and then applied monthly averages to the fluxes whereas we computed our fluxes from monthly averaged variables. It is pleasing to see that our error estimate of about 10% (Chapter IV.4) verifies in comparison here.

In the north Pacific, our results are most comparable with Clark's (1967) estimate. Comparison of long term monthly means are presented for two representative squares are given in Figure 4.43a. Again, there are differences observed between the two estimates of the net energy flux. The agreement is much better at subtropical region than that at higher latitudes. In general, our estimate of net heat loss is higher than his. This is a direct consequence of the fact that our estimates

of the latent heat flux is higher than his. His latent heat has a constant transfer coefficient (C_e) while ours is a function of wind and stability. With higher wind speed in the winter at higher latitudes,

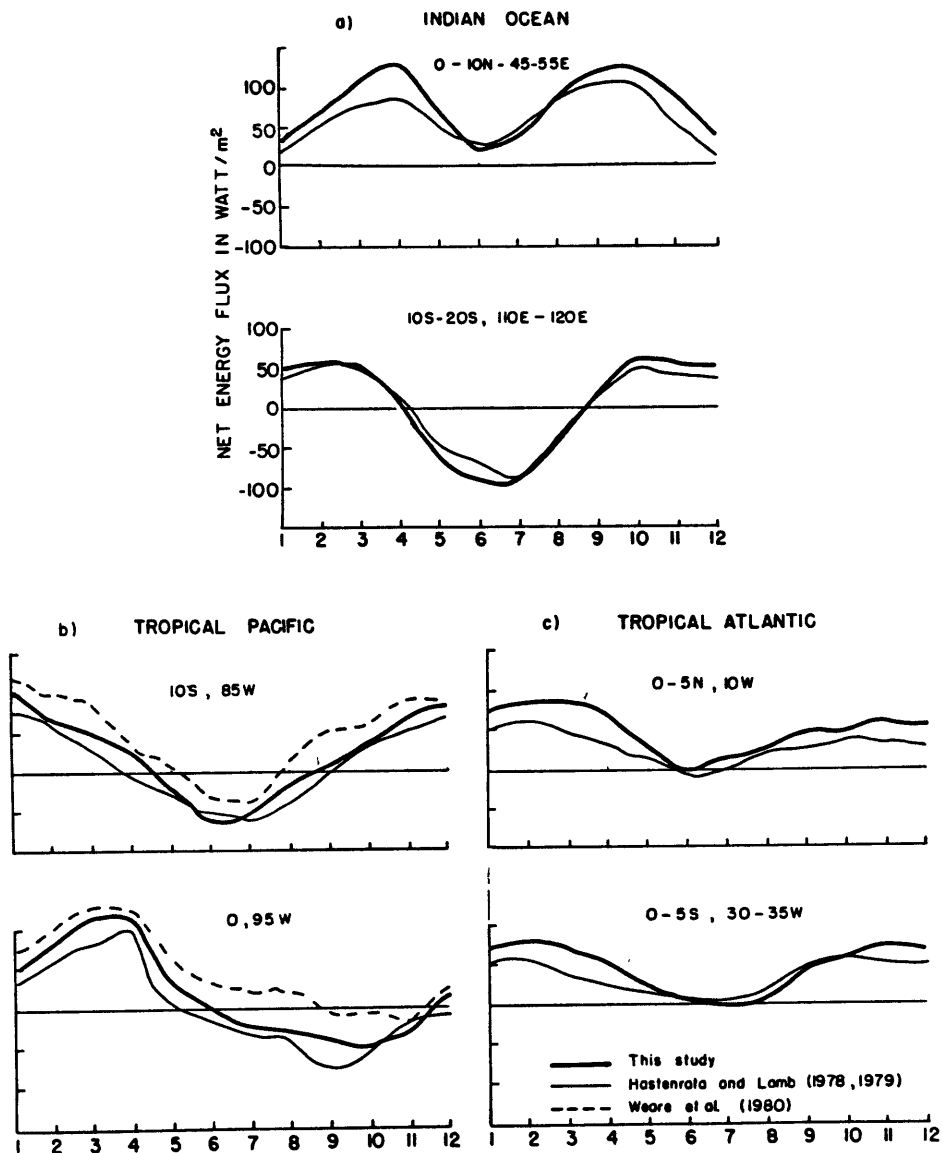


Figure 4.44 Comparison of net energy flux estimates for the tropical oceans: a) Indian Ocean, b) Pacific Ocean and c) Atlantic Ocean

this can cause a significant difference in the estimate of latent heat flux. Our incoming radiation estimates are also different due to different formulae used. Clark used Budyko's formulation while in this study we used Reed's formulation. Estimates of sensible heat and outgoing radiation are in better agreement.

In the tropical region, our results are directly comparable with those of Weare et al (1980) and Hastenrath and Lamb (1978, 1979). In the Pacific Ocean (Figure 4.44b), our net energy term agree well with Weare's estimate although our maximum energy gain is about 10% lower. However, it is higher than Hastenrath and Lamb's estimate (1978). In the Indian Ocean (Figure 4.44a), our results differ from Hastenrath and Lamb's estimate with ours generally higher than theirs, and in some areas the differences are quite significant. In the tropical Atlantic (Figure 4.44c), our net heat flux is again in between Weare's estimate and Hastenrath and Lamb's estimate. As for other components of the energy budget (not shown), our incoming solar radiation is low compared with Weare's ($\approx 10\%$) and high compared with Hastenrath's ($\approx 5\%$). Our longwave radiation compares well with Hastenrath and Lamb but Weare has values $\approx 10\%$ lower. Our latent heat values are, again, higher than Hastenrath's in general. The exception is in regions of maximum evaporative loss, where it agrees well with his. Weare's estimate is greater than both ours and Hastenrath's estimates.

As can be seen, significant discrepancies exist among various estimates of the same quantity. Comparison among them does not tell us whether one estimate is better than others. Rather, it serves the purpose of giving us an idea of how variable some of these quantities

can be. Basically all of the estimates are made from the same set of ship observations - some have better coverage than others. The differences are from different data periods, different processing methods, and different methods of computation. The general feature of all estimates agree in spite of the differences observed in magnitudes.

IV.4 Error Analysis

IV.4a On monthly fluxes

No energy budget calculations are complete without an analysis of errors. In addition to errors associated with meteorological parameters, there are four major areas that may cause additional errors in our flux computations:

- 1) Inadequacy of the bulk flux formulae as an approximation to the true fluxes,
- 2) Observation, reporting, and archiving problems,
- 3) Bias from inadequate data sampling, both spatially and temporally.
- 4) Calculation of the monthly mean fluxes from monthly averaged input variables.

We will address these four problems separately in the following sections.

The amount of uncertainty of calculated fluxes associated from using bulk flux formulas is hard to assess. There is a serious lack of verification of fluxes calculated over open ocean. In addition, marine

reports do not give sufficient information on the condition over the lower atmosphere and/or the upper ocean necessary for more detailed calculation of the fluxes. The determination of the transfer coefficients is a derived empirical relationship from data which may or may not be suitable for all areas of the ocean. Their values vary from one study to another, sometimes differing by as much as a factor of two. As can be seen from the previous section on sensitivity of the flux formulas, a factor of two change in the transfer coefficients can cause a factor of two change in the heat fluxes. The transfer coefficient is especially important for latent heat flux because it is one of the most important components in the total energy budget. Radiative fluxes, especially the incoming shortwave radiation, also suffer from uncertainties in their formulation. Simpson and Paulson (1979) compared some mid-ocean observations of atmospheric radiation to the calculated fluxes using various available formulations and suggested that Reed's (1979) formula is probably the most suitable one to use. Compared with observation results, they obtained an error of 6% with Reed's formulation and an error of 1% with Berliand's formulation for the longwave radiation. Even with perfect observational data and the best available formulation, we probably have an uncertainty of accuracy in the range of 10%. This translates to be about 10 watt/m^2 at high latitudes and about 20 watt/m^2 in low latitudes. It should be noted that errors associated with formulations are fixed for all regions and all times and are therefore time invariant. This means that this systematic error will not affect comparison studies among different areas of the ocean or among different time periods. However, it will dominate errors associated with long term mean calculations.

The second source from which error may arise is from sampling errors associated with observation, reporting and archiving method. For example, take latent heat flux and radiative flux. Since latent heat is a function of C_e and wind speed and C_e is a function of wind speed, an error in wind speed observation could give substantially different results in the latent heat flux calculation. Weare and Strub (1981) have estimated that a 1 m/s error would lead to about a 1% error in the variance of the latent heat flux estimation. Similarly, since radiative flux is a function of cloud cover, and ships observations of cloud cover have been shown to be less reliable than other parameters (Bunker, 1976), the error introduced here may be a serious one. Presumably this type of error is random and will decrease with increasing number of observations. Averaging over space and time increases the number of observations and therefore long term means over large areas of the ocean should be relatively free of this type of error. However, it would dominate the fluctuations on a short term time scale.

Weare and Strub (1981) have done a detailed study of the error associated with sampling bias from inadequate sampling both spatially and temporally. By this we mean the error introduced from an uneven sampling throughout the month and from a narrow ship route within the five by five degree grid square. This type of error varies greatly both in time and in space. For instance, in areas where there is a large gradient within the grid area, a narrow ship route could introduce a large bias (See Appendix B). In areas where there are large diurnal

variations, the time of the day a report is taken becomes critical. In regions of frequent cyclonic activity, a large number of observations is necessary to capture the large fluxes over short periods of time associated with storm activities. Weare and Strub (1981) gave an estimate of about 10% of the longer term mean being affected by this bias and a much greater percentage for individual monthly means.

Finally, we should consider errors introduced from calculating monthly mean fluxes from monthly mean meteorological variables rather than calculating the fluxes from individual observations and then averaging the fluxes. This type of error arises from the fact that the flux formulas are non-linear in nature and the error is high when the variables in the formula are highly correlated on a daily basis. Clark (1965) computed monthly averaged flux values both ways: first daily values were averaged over the number of days, secondly the variables were averaged and the flux terms computed from these averaged values. He found a difference in the long term monthly mean flux between the two methods of 10% to 17% for the net energy flux, with the largest contribution from sensible heat flux and latent heat flux. This is due to the fact that daily values of surface wind, $T_s - T_a$ and $q_s - q_a$ are strongly correlated. Weare and Strub (1981) did a similar study on latent heat flux and radiative flux and found similar results. Esbensen and Reynolds (1981) in a more recent work using boundary-layer similarity theory for the formulation of the transfer coefficients, obtained a relative error of approximately 10% for sensible and latent heat fluxes. It should be noted that all of the estimates on the

difference of two types of methods of calculation are based on mid-latitude areas. This is because these are the only regions where there are sufficient frequency of daily observations to enable this type of comparison studies. There is reason to believe, however, that similar results should be obtained in tropical regions where the Bowen ratio (ratio of sensible heat to latent heat) is small and the wind speeds are also lower.

IV.4b On annual mean estimates

As mentioned before, in taking the long term mean averaged over a 31-year period, most of the error is probably from systematic sources. Two of the major systematic errors are from the bias in data observations and from bias from flux formulations. As mentioned in the previous section, 10%-20% may be a reasonable estimate for errors arising from the methods of calculation for Q_{in} and Q_l . The accuracy of Q_{out} is hard to estimate in the absence of published observations. Although the magnitude of Q_{out} is small compared to Q_{in} and Q_l , it is comparable to the magnitude of Q_{net} . Q_h is small and any error associated with it probably will not alter Q_{net} significantly.

Experiments with various formulations for Q_{in} and Q_l have shown that Q_{in} is the most sensitive component of the four. Q_l , on the other hand, is quite insensitive to any reasonable estimates of C_e (in the annual mean.) Weare et al (1981) have made estimates for significance level of various terms for the tropical Pacific region. They found a 95% confidence level for solar, infrared and latent heat

fluxes to be 29, 14, and 39 watt/m² respectively if one assumes these fluxes are normally distributed. They also indicated that this would correspond to a 49 watt/m² as the 95% confidence level for Q_{net} . Because our fields in the high latitudes have different means and standard deviations, we cannot apply these error estimates to our findings directly. However, our error in the tropical region will probably be around the same range as their estimates. In higher latitudes, the values would be larger due to larger standard deviations of these fluxes.

We should note here that the approximately 20% error mentioned in this section is in addition to the large errors (30% to 50%) associated with uncertainties in the meteorological parameters discussed in section IV.2b. If we assume these two errors are independent, then the total error associated with the flux estimates is anywhere from $((.2)^2 + (.3)^2)^{1/2} = .34$ to $((.2)^2 + (.5)^2)^{1/2} = .54$, or from 34% to 54%. In the worst case, the total error can be as large as 70% (20%+50%).

CHAPTER V. OCEANIC MERIDIONAL ENERGY TRANSPORT

In this chapter, we will present estimates of oceanic meridional transport of energy using the surface energy balance method. The theory and method used will be discussed first and the results will be presented.

V.1 Theory

We may write the energy equation of the earth-atmosphere system as

$$R_{net} = R_{in} - R_{out} = S_n + S_c + S_o + S_a + \text{Div}(F_a + F_o)$$

where

R_{net} = net radiation received at the top of the atmosphere

R_{in} = radiation received at the top of the atmosphere

R_{out} = radiation lost at the top of the atmosphere

S = storage terms

F = flux terms

Div = horizontal divergence

Subscripts are :

o = ocean

a = atmosphere

n = land

c = ice

Figure 5.1 (adopted from Newell et al (1981)) illustrates this balance schematically.

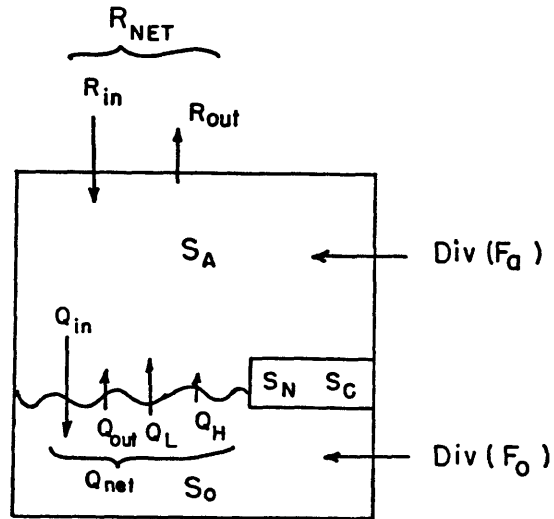


Figure 5.1 Schematic representation of the energy balance of the earth-atmospheric system

In the annual mean, as long as no long term temperature change is observed, the storage terms vanish and the energy balance equation becomes:

$$R_{net} = \text{Div} (F_a + F_o)$$

In other words, there must be a transport of energy from areas with a surplus of energy to areas with a deficit of energy. This can be accomplished by either the atmosphere or by the oceans. The role that the ocean plays in maintaining the temperature field relative to that of the atmosphere is one of the critical problems in understanding the present climate and its potential changes. The various mechanisms that accomplish this transport may be summarized into the following categories: (Chiu,1978)

- 1) transport associated with the net meridional volume flow.
- 2) transport associated with the mean meridional cell.
- 3) transport associated with the horizontal gyres.
- 4) transport associated with Ekman drift
- 5) transport associated with eddy motions in the ocean.

Considerable literature has been collected on the estimate of energy transport accomplished by the oceans. Generally, the methods used to estimate this transport can be separated into three categories: the residual method, direct estimates, and the surface energy balance method. The following sections describe briefly each method and the results from various estimates.

One way to compute the oceanic transport is from the residuals in balancing the energy atmosphere-ocean system. The ocean flux is calculated as the difference between the net radiation at the top of the atmosphere and the atmospheric flux, i.e.

$$\text{Div } F_o = R_{\text{net}} - \text{Div } F_a$$

Vonder Haar and Oort (1973) applied this method to the Northern Hemisphere and found a northward transport at all northern latitudes. Using the same method, Newell et al (1974) calculated the flux from 90°N to 30°S and found a poleward transport in both hemispheres. The maximum transport is found to be at 30° in both hemispheres.

The errors associated with the residual method are large because the residual is the difference between two large terms. In addition,

the transport for individual oceans cannot be resolved from this approach. However, it does give us an estimate of the relative magnitude of the oceanic transport compared to the transport by the atmosphere

The oceanic transport of energy can be calculated directly. This is done by vertically integrating the meridional velocity and temperature fields. However, due to a lack of continuous measurements of the variables needed for the calculation, this method has only been applied to particular areas with oceanographic stations and for limited time periods. Bryan (1962) and Bennett (1978) have made direct estimates of energy transport using hydrographic data from 12 sections taken within the period from March to October. Their results indicate that there is a northward transport in both hemispheres in the Atlantic, a southward transport in both hemispheres in the Pacific, and a northward transport in the southern Indian Ocean. Roemmich (1981), Wunsch (1980) and Fu (1981) applied an inverse method to estimate the transport in the Atlantic Ocean and found northward transport in the Atlantic ocean in both hemispheres. They also found small southward transport in the southern Pacific Ocean.

The disadvantage of direct estimates is that the time periods and locations for which data are available to make such an estimate are limited. It is hard to infer an **average** value of transport from one or two years data for a given season. Without a knowledge of seasonal variability and the interannual variability of the transport, it is

difficult to compare results from direct estimates to the annual mean values inferred from both the residual method and surface energy balance method. However, these estimates do give us a feeling of the possible ranges of oceanic transports for certain locations.

The surface energy balance method uses, as the name implies, balance at the surface of the ocean-atmosphere interface. From Figure 5.1, the balance at the surface of the ocean can be written as

$$Q_{\text{net}} = S_0 + \text{Div } F_o = Q_{\text{in}} - Q_{\text{out}} - Q_l - Q_h$$

The notation used here are the same as before:

Q_{net} = net energy flux at the ocean surface

Q_{in} = radiation received at the surface

Q_{out} = radiation lost at the surface

Q_l = latent heat flux

Q_h = sensible heat flux

Again, in the long term mean, S_0 vanishes as long as no long term temperature change is observed. We would then have

$$Q_{\text{net}} = \text{Div } F_o$$

The above equation indicates that the annual mean net energy balance at the ocean surface can be used as an estimate of the oceanic flux divergence. The meridional energy transport could then be

calculated using Green's theorem by integrating the energy flux divergence with respect to area. An appropriate boundary condition has to be assumed. The most common assumption (and perhaps the safest) is to assume the flux vanishes at the northern or the southern boundary of the ocean basin.

Sverdrup(1957) did the first calculation of oceanic energy transport using this method. Bryan (1962) used Budyko's (1956) data and made similar calculations. Emig (1967) recalculated the oceanic transport using updated values of Q_{net} from Budyko (1963). The results from these studies generally indicate a poleward transport of energy in both hemispheres with a maximum at $30^{\circ}N$ in the Northern Hemisphere and $20^{\circ}S$ in the Southern Hemisphere. Hastenrath (1980) performed an updated calculation using satellite measurements of radiation at the top of the atmosphere and estimated the transports for individual oceans. In the Pacific, the energy transport is directly from the tropics into both hemispheres. In the Atlantic, it is northward in all latitudes, including the Southern Hemisphere. In the Indian Ocean, it is directed southward in all latitudes. He found a maximum transport at $30^{\circ}N$ and $25^{\circ}S$ for all oceans combined. The disadvantage of using this balance method is that it is essentially an estimate of flux divergence as the difference between the two largest components of the energy budgets, namely Q_{in} and Q_1 . The error associated with this may be large. In addition, only the long term annual mean value of the transport can be calculated since only in the long term can one safely assume that the storage term is zero. One would need additional subsurface data to calculate the seasonal variations of the flux values.

V.2 Computation and Results

In this section we present the estimates of oceanic energy transport from our annual mean net energy flux at the oceanic surface using the surface energy balance method. The annual mean net energy balance (or equivalently, the energy flux divergence) from the previous chapter is integrated to yield the energy transport across each 5° latitude circle. For each ocean, the net energy transport across each 5° latitude band is computed by multiplying the appropriate annual mean flux divergence (Q_{net}) and the corresponding ocean area in that latitude belt. This value is then integrated to yield the transport across that latitude. The integration can be done from either the northern boundary or the southern boundary depending on which boundary condition is available.

To illustrate how transport across each latitude is calculated, we take the transport across 65°N in the Atlantic Ocean as an example. Since we do not have flux divergence data for the southern end of the ocean basin, we will perform the integration from the north to the south. In this case, we need a boundary condition at 70°N. If we assume a flux of zero at 70°N and if no long term change for that latitude belt is observed, then the deficit of $.54 \times 10^{14}$ watts (Table V.1) for the 65°-70°N belt must be made up from a transport of the same magnitude from the south (since no energy flux is transported from the north). So a northward transport of $.54 \times 10^{14}$ watts is obtained for 65°N. At 60°N, to take care of the total deficit in these two five

degree latitude belts, the deficit of 1.02×10^{14} watt must be added to the flux at 65°N to give us a net northward flux of 1.56×10^{14} watts across 60°N . This process is repeated for all latitudes.

The transport for the Indian Ocean and the Pacific Ocean is calculated in the same way. We assume a zero net flux at 30°N in the Indian Ocean and a zero net flux at 60°N in the Pacific. The integration is performed from north to south. The presence of continents in northern boundaries makes it relatively safe to assume a zero flux for the northern boundary conditions. Of course, one could also integrate from south to north. Since we only have data down to 40°S and reliable energy transport flux across this latitude is not easily obtained, we choose to use a north to south integration. The transport values are calculated for each 5° latitude for each oceans. This transport value, the flux divergence and the area for each of the latitude belts in each ocean are presented in Table V.1. The total transport accomplished by all three oceans combined is also computed by assuming a zero flux across the 70°N latitude. The results for this computation are presented in Table V.2. To help ease the digestion of the data, the net flux divergence (weighted by the area) for each 5° latitude belt and for each ocean is presented schematically in Figure 5.2 . The calculated transport directions at selected latitudes are indicated by arrows. Figure 5.3 presents a plot of the estimated meridional energy transport for each ocean and for all oceans combined.

Our results indicate a northward transport at all latitudes in the Atlantic with a maximum of 9×10^{14} watts at 20°N . The Pacific Ocean transports energy northward north of 10°S and southward from 10°S to

TABLE V.1 Annual Mean Heat Flux and Heat Transport
 *Error bars on the flux estimates are approximately 35% to 70%

Lat.	Indian Ocean				Pacific Ocean				Atlantic Ocean			
	Flux watt /m ² *	Area m ² 10 ¹²	F*A watt 10 ¹²	Trsprt watt 10 ¹⁴	Flux watt /m ² *	Area m ² 10 ¹²	F*A watt 10 ¹²	Trsprt watt 10 ¹⁴	Flux watt /m ² *	Area m ² 10 ¹²	F*A watt 10 ¹²	Trsprt watt 10 ¹⁴
72.5												0.0
67.5									-50.2	1.07	-54	.54
62.5									-59.4	1.72	-102	1.56
57.5					-11.2	2.37	-27	0.0	-54.5	2.2	-120	2.76
52.5					-0.4	3.54	-1	.27	-39.1	1.98	-86	3.62
47.5					5.8	4.31	25	.28	-25.1	2.3	-58	4.20
42.5					-17.0	5.10	-87	.03	-32.2	3.18	-102	5.22
37.5					-54.2	5.24	-284	.90	-51.0	3.58	-183	7.05
32.5					-46.5	5.83	-271	3.74	-32.7	3.51	-167	8.72
27.5	13.1	.93	12	0.0	-22.8	6.29	-143.	6.45	-8.1	4.53	-37	9.09
22.5	22.4	1.76	39	-.12	-12.9	7.08	-91	7.88	5.4	4.51	24	8.85
17.5	45.5	3.10	141	-.51	-9.1	7.80	-71	8.79	5.5	4.23	23	8.62
12.5	43.8	3.94	173	-1.92	-3.4	8.71	-30	9.50	14.9	3.9	58	8.04
7.5	42.3	4.68	198	-3.65	-1.6	9.15	-15	9.80	29.2	2.8	82	7.22
N2.5	60.6	4.41	267	-5.63	36.5	9.22	337	9.95	43.3	3.75	152	5.70
S2.5	53.9	5.38	290	-8.30	63.2	7.95	502	6.58	66.7	3.37	225	3.45
7.5	40.6	6.1	248	-11.20	26.5	7.93	210	1.56	24.0	2.86	69	2.76
12.5	19.7	6.08	120	-13.68	5.3	8.11	43	-.54	8.4	3.02	25	2.51
17.5	1.1	4.98	5	-14.88	-7.4	8.22	-61	-.97	13.7	2.94	40	2.11
22.5	-12.5	4.21	-53	-14.93	-18.3	7.97	-146	-.36	20.1	3.25	65	1.46
27.5	-27.1	4.23	-115	-14.40	-27.5	7.66	-211	1.10	15.9	3.55	56	.90
32.5	-23.6	5.0	-118	-13.25	-27.8	7.19	-200	3.21	0.3	3.61	1	.89
37.5	-32.8	6.0	-197	-12.07	-25.1	6.66	-167	5.21	-21.5	3.82	-82	1.71
				-10.10				6.88				

TABLE V.2 Total Oceanic Heat Transport
 Error bars are approximately 34% to 70%

Lat.	Flux watt /m ² *	Area m ² 10 ¹²	F*A watt 10 ¹²	Trsprt watt 10 ¹⁴
				0.0
67.5	-50.2	1.07	-54	.54
62.5	-44.4	2.3	-102	1.56
57.5	-32.1	4.57	-147	3.03
52.5	-17.4	5.52	-96	3.99
47.5	-6.9	6.61	-46	4.45
42.5	-23.9	8.28	-198	6.43
37.5	-46.5	10.03	-466	11.09
32.5	-35.5	10.71	-380	14.89
27.5	-11.3	11.74	-133	16.22
22.5	-0.6	13.40	-8	16.30
17.5	9.4	15.13	142	14.88
12.5	14.8	16.55	242	12.46
7.5	17.5	16.63	291	9.55
N2.5	45.0	17.38	782	1.73
S2.5	60.3	16.73	1009	8.36
7.5	31.4	16.89	530	13.66
12.5	11.2	17.21	193	15.59
17.5	-0.6	16.14	-10	15.49
22.5	-8.1	15.45	-125	14.24
27.5	-15.9	15.44	-245	11.79
32.5	-18.9	15.83	-299	8.80
37.5	-27.5	16.48	-453	4.27
42.5				

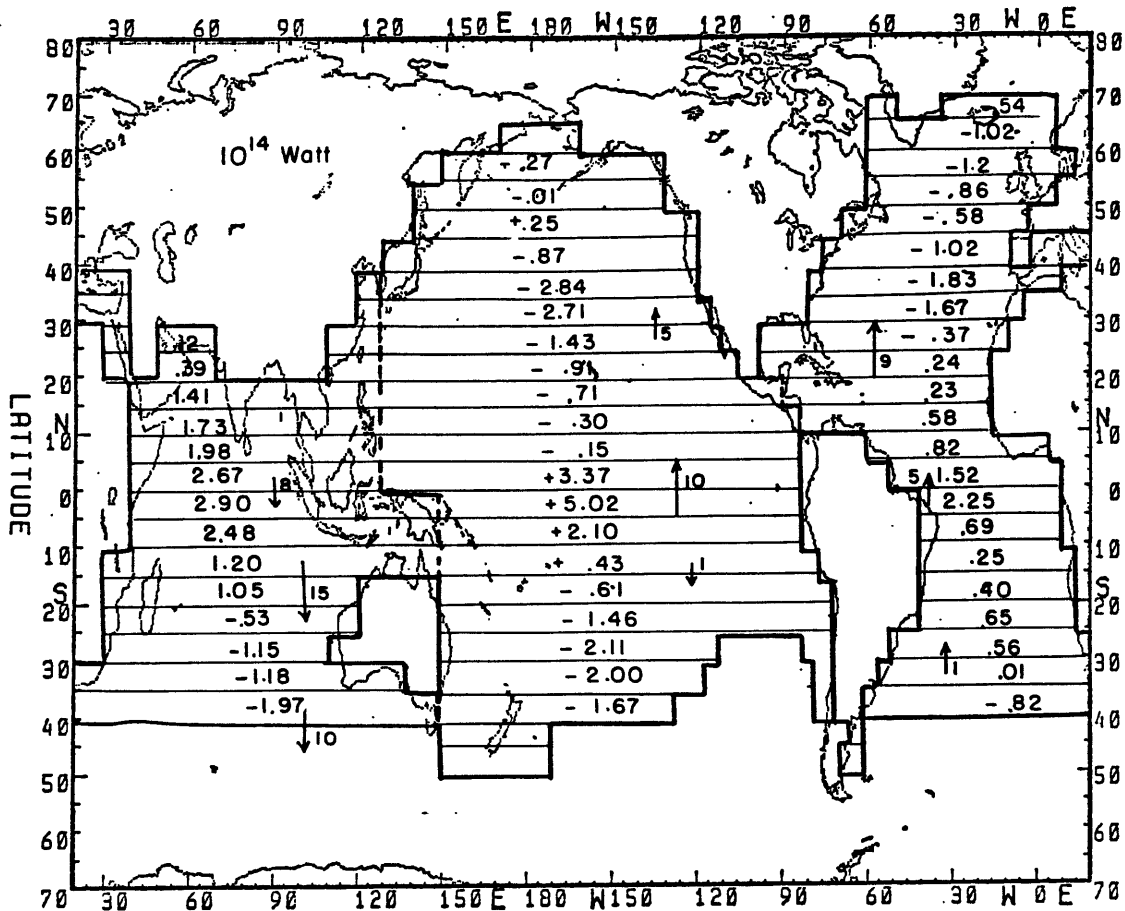


Figure 5.2 The net energy flux divergence for each 5° latitude belt and the direction of the purposed meridional transport of energy

25° S. South of 25° S, the transport becomes northward again. The maximum northward transport is at 5° N with a magnitude of 10×10^{14} watts. In the Indian Ocean, the transport is southward for all latitudes with a maximum of 15×10^{14} watts at 20° S. When data for all three oceans are combined, the total oceanic energy transport is northward in the Northern Hemisphere and southward in the Southern Hemisphere with a maximum of 16×10^{14} watts at 25° N and 16×10^{14} watts at 15° S.

For comparison purposes, the results of the oceanic energy transport from this study and other estimates are presented together in Table V.3 for each of the three oceans separately and in Table V.4 for

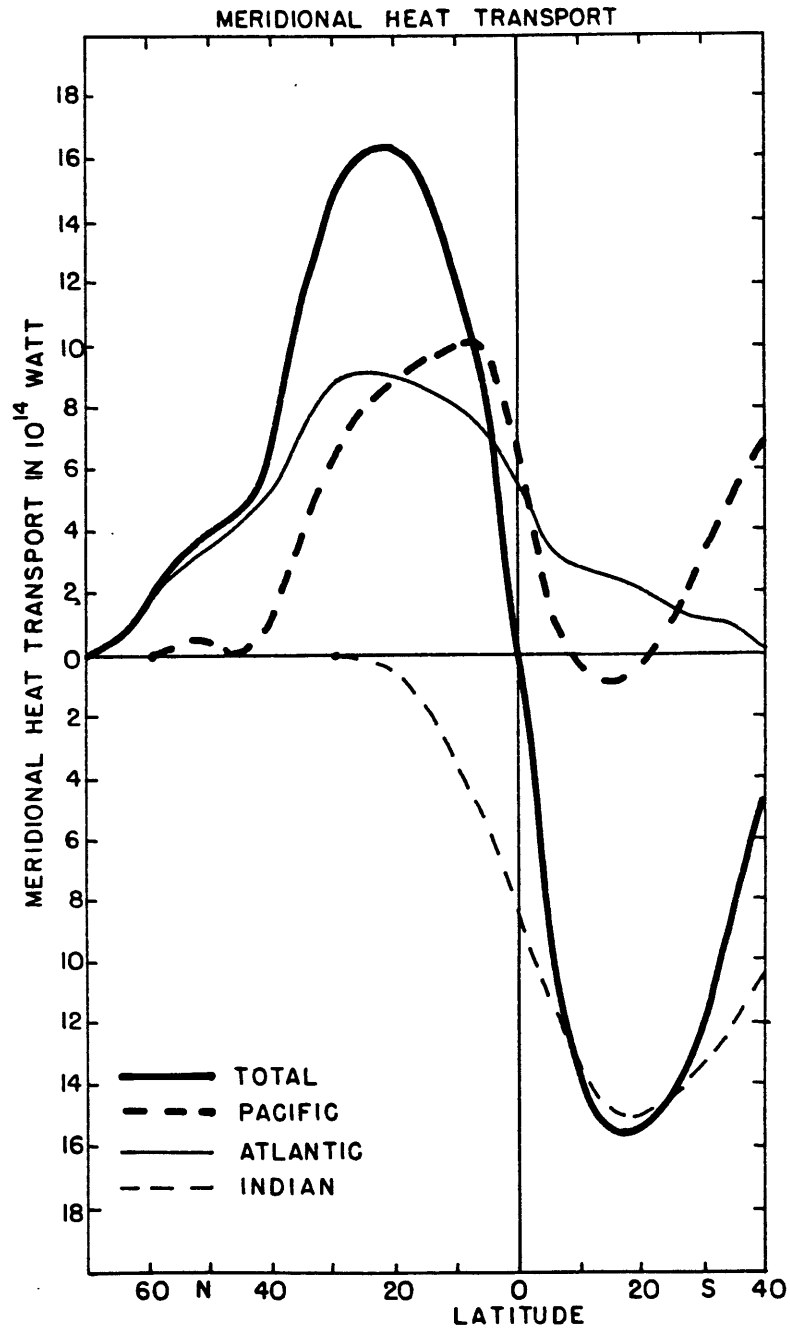


Figure 5.3 Meridional energy transport for three oceans separately and combined

all oceans combined. Two estimates under one study represent estimates using different assumptions and usually imply the possible ranges of the transport values. For example, the two estimates from Bennett(1978) are the ranges using different width assumption for the western boundary current. Georgi and Toole (1982) obtained different estimates using different reference levels.

TABLE V.3c Comparison of Various Estimates for Atlantic Ocean

Meridional Heat Transport in 10^{14} Watts

Latitude	This Study*	Hastenrath 1980,1982	Fu 1982	Bunker 1976	Bennett 1978	Bryan 1962	Wunsch 1980	Roemmich 1981
60N	1.56	2.6,2.6		1.8				
50N	3.62			4.1				
40N	5.22			6.3		0.		
36N						7.	7.5	8.
30N	8.72	15.5,10.7		9.7				
25N	9.09						12.	12.
15N	8.62	15.8,11.1				13,6		
10N	8.04		4.2, 1.8	8.2				
0	5.70	14.4, 9.8		6.6				
10S	2.76			3.9				
15S	2.51		8.6,7.3					
20S	2.11		5.4	3.9				
25S	1.46				3,6.5	3.		
30S	.90	11.5, 6.9	8.3,5.4	4.1				
32S			7.7		1.6,1.8	4.		
40S	1.71	1.7,.67(Georgi & Toole, 1982)						

*Errors on these estimates are from 34% to 70%

V.3 Discussion

As can be seen from Figure 5.3, the nature of the transport differs remarkably for the three oceans. The Atlantic ocean as a whole loses energy and needs to have energy imported from other oceans in order to maintain its temperature. There is significant energy loss in the mid-latitudes of the north Atlantic, particularly at latitudes under the influence of the Gulf Stream. Although the energy surplus area in the tropical region has one of the largest values per square meter, the total area with this surplus is small. Therefore, the total available energy for the tropical region is not large enough to make up for the energy loss in the Northern Hemisphere. Hence the estimated energy transport is northward at all latitudes of the Atlantic Ocean.

The most estimates of energy transport exist for the Atlantic Ocean (Table V.3c). It is also where most of the estimates are in agreement with each other. In Bunker (1976) and Hastenrath (1980,1982), estimates are obtained by surface energy balance methods. The Hastenrath 1982 estimate is an update of his 1980 estimate using a different boundary condition at 30°N. Lamb (1981) made transport estimates using the same data set as Hastenrath's. He also made estimates of the annual variation of meridional heat transport in the Atlantic Ocean with the addition of subsurface data and found that from November to December the transport is southward, opposite to that for the rest of the year. The Roemmich (1981), Wunsch (1980) and Fu (1981) data are direct estimates obtained using inverse methods. Results from Bryan (1962), Bryden and Hall (1980) and Bennett (1978) are also direct estimates using hydrographic data. Wunsch (personal communication) has calculated the maximum and minimum values of energy transport using linear programming

techniques. He found a range of $8-13 \times 10^{14}$ watt for the energy transport at 24°N and a range of $1-7 \times 10^{14}$ watts at 48°N . Most estimates fall within this range. In the Southern Hemisphere, the magnitudes of various estimates are quite variable although the directions are the same. Our estimates are uniformly lower than others. This is probably due to the assumed boundary condition of zero flux across 70°N . Aagaard and Greisman (1975) have estimated the energy budget for the Arctic Basin and found a small transport northward into the Basin from the Atlantic Ocean. Hastenrath (1980,1982) used a 1×10^{14} watts at 66.5°N as his boundary condition. With a correction of the northern boundary value at 70°N , our values would be in better agreements with others. Note, however, our final flux across 40°S of 1.7×10^{14} watts is in good agreement with values from Georgi and Toole (1982) where they estimated the energy and fresh water balance for the Antarctic circumpolar current.

Energy Transport in the Indian Ocean is the opposite of that in the Atlantic. The direction of the transport is southward in all latitudes. With the exception of higher latitudes in the Southern Hemisphere, most of the Indian Ocean has a surplus of energy. The

TABLE V.3a. Comparison of Various Estimates for Indian Ocean

Meridional Heat Transport in 10^{14} Watts

Latitude	This Study*	Hastenrath 1982	Georgi & Toole 1982	Bennett 1978
0	-8.30	-4.8		
15S	-14.88	-7.7		
30S	-13.25	-4.9		
32S				4.6-6.4, 15.5-17.6
40S	-10.10		-8.77,-6.35	

excess energy cannot be transported northward into the continent and if we assume not much energy is transported laterally into the Pacific Ocean, then the excess energy has to be transported southward. The deficit in the Southern Hemisphere is much smaller than the energy surplus at the northern ocean so that the Indian Ocean as a whole exports energy to other areas of the oceans.

Our estimates of a southward transport in the Indian Ocean is in agreement with Hastenrath's estimate but the magnitude of our estimate is about twice as large. (See Table V.3a) Part of this difference is from the way our Pacific Ocean and Indian Ocean is divided. Both our estimate and Hastenrath's estimate differ from those obtained by direct estimate by Bennett (1978). He obtained a significant **northward** transport at 32°S. This difference may indicate that there are large interannual variations in the energy balance in the southern Indian Ocean. Again, our southward flux of approximately 10×10^{14} watts agrees rather well with estimates of Georgi and Toole (1981) of 9×10^{14} watts at 40°S.

Energy transport in the Pacific ocean is more complicated and more uncertain than in the other two oceans. The tropical Pacific ocean, especially the eastern part, has the largest observed energy surplus. Together with the large area covered by the tropical Pacific Ocean, this region has the highest surplus energy of any latitude belt. However, because of the Kuro-shio current, the north Pacific requires a large amount of energy to be imported to make up for the large energy loss there. With no significant transport from the Bering Strait (Aagaard

TABLE V.3b. Comparison of Various Estimates for Pacific Ocean

Meridional Heat Transport in 10^{14} Watts

Latitude	This Study*	Hastenrath 1982	Bennett 1978	Bryan 1962	Georgi & Toole 1982	Wunsch 1983	Roemmich 1980
60N	0	.1					
32N				-12.			
30N	6.45	11.4					
0	6.58	-2.3					
20S	-.36	-20.7					
28S			-11.6, -1.7			-1.8+2.2	-2.5
30S	3.21	-19.2					
40S	6.88	-18.0			0.4, -8.9		
43S			-1.5, 4.2			-.3+3.5	-2.

*Errors on these estimates are from 34% to 70%

and Greisman, 1975), the transport in the north Pacific would have to be northward. The region between 40°N - 50°N has a small surplus of energy but it is not large enough to change the direction of the transport. Also any other reasonable boundary condition at 60°N (other than the zero value used) would not alter the direction in the Northern Hemisphere. Higher latitudes in the Southern Hemisphere also experience a large energy loss and energy also has to be imported to maintain the temperature field. The surplus energy in the tropics can either be transported north and/or south. The energy surplus in the tropical Pacific from this calculation is not large enough to take care of all the energy deficits in both hemispheres. Therefore in our estimates there is a northward transport in the higher southern latitudes.

The Pacific Ocean is also the place where there are large differences among the results from various estimates (Table V.3b). Most estimates, with the exception of Hastenrath (1982) have small energy transports for the southern Pacific Ocean. Wunsch et al (1983) have some estimates indicating a small transport northward at 43°S. Georgi and Toole (1982) also found a small northward flux at 40°S. It should be noted that all the discrepancy amongst various estimates in the southern Pacific may indicate that it is a region that is highly variable and that the transport may be too small to have a definite

TABLE V.4 Comparison of Various Estimates for World Oceans

Meridional Heat Transport in 10^{14} Watts

Latitude	This Study*	Hastenrath 1982	Oort & Von der Haar 1976	Vonder Haar & Oort 1973	Emig 1967	Newell et al.	Atmo. Newell
70N	0.0		-1.±4	+1.	0.	-.48	14.5
60N	1.56	2.5	-2.±5	1.	1.84	0.	27.1
50N	3.99		10.±7	11.	4.38	6.29	32.4
40N	6.43		18.±12	21.	6.98	15.5	30.
30N	14.89	22.5	20.±15	25.	9.74	20.8	23.2
20N	16.30		29.±17	34.	8.58	18.4	16.4
10N	12.46		11.±19	19.	.42	9.2	8.2
0	1.73	1.0	-7.±21	3.	-13.59	-1.45	-1.4
10S	-13.66				-25.0	-9.69	-12.6
20S	-15.49	-20.0			-27.87	-16.9	-21.3
30S	-11.79	-17.5			-25.43	-23.2	-24.7
40S	-4.27				-17.29		

*Errors on these estimates are from 34% to 70%

direction. As a matter of fact, the tropical regions are the most sensitive to perturbations in our solar radiation estimation and the amount of surplus energy in the tropical region is crucial to the transport in the Southern Hemisphere. Our estimate of approximately 7×10^{14} watts across 40°S seems large. Part of this is due to the fact that we only have data for the western part of the higher southern latitudes in our estimates for the latitudinal mean. The southeastern Pacific would presumably have smaller deficits (since the water is colder there) and inclusion of all the area in these latitudes would bring our transport values down.

When three oceans are taken together as a whole, the transport becomes northward in the Northern Hemisphere and southward in the Southern Hemisphere with a maximum at 20°N and 15°S (Table V.4). The direction of our estimates agree with those of Hastenrath but the magnitudes are different. In both hemispheres, our estimates are smaller than his and the latitudes where the maximums occur are slightly different. Our northern hemisphere estimates agree fairly well with those made by Emig (1978) using Budyko's flux data. Again, her values are higher than ours in the Southern Hemisphere. Newell et al (1974) obtained the oceanic transport value using the residual method. Their transport values are about twice ours in the Northern Hemisphere mid-latitudes and higher latitudes in the Southern Hemisphere. The agreement is much better for the subtropical regions and for the tropics. Estimates of the atmospheric transport from Newell et al is also presented in Table V.4. As can be seen, energy transport accomplished by the atmosphere is much greater than those by the oceans in the mid-latitudes, especially in the North Hemisphere where it is

about twice to five times the oceanic energy transport. In regions between 30°N and 30°S , the transport values much more comparable.

In summary, our results indicate a northward transport at all latitudes in the Atlantic with a maximum of about 9×10^{14} watts at 25°N . The Atlantic Ocean as a whole experiences a net energy deficit. It would require transport from other ocean areas to maintain its temperature field. The Indian Ocean transports energy southward in all latitudes with a maximum of 15×10^{14} watts at 20°S and it has a energy surplus for this 31-year period. It needs to export energy to other areas to avoid a increase in its temperature field. The Pacific transports energy northward in the Northern Hemisphere with a maximum of 10×10^{14} watts around $5\text{-}15^{\circ}\text{N}$. The data coverage in the South Pacific is too sparse to make any definite statements on transports there.

It should be pointed out here that the error bars on these estimates due to uncertainties in the fluxes can be large. One might want to ask the question of whether there would be a significant change in the transport estimates with the possible errors. If we consider a more or less systematic change in all latitudes, the answer to that question is that in the Indian Ocean, the North Pacific and the North Atlantic, the direction of the transport will remain the same (the magnitudes of the transport will obviously change with a change in the flux estimates) while the transport estimates in the South Pacific and the South Atlantic would have a different direction as well as a different magnitude from the estimates presented. We should perhaps be reminded of a point Wunsch (1980) stressed. In his opinion, due to the large error bars associated with estimates from bulk formulas, there is no real discrepancy among various estimates and that any agreements found are fortuitous.

One should also be careful when comparing annual mean estimates from bulk formulas to direct estimates. This is because direct estimates do not give us a true average transport. In addition, we do not yet have a good enough knowledge of the seasonal or interannual variation of the transport value to make a good comparison. To obtain long term mean estimates, bulk formulas, although inadequate are the only viable means so far. In this study, it is the first time global data coverage is available to estimate the oceanic transports. With net energy flux data available only in limited regions, one has to assume a boundary condition that is crucial to the transport. The importance of correct boundary conditions, as evident in Hastenrath's case when he needed to update his transport values due to incorrect boundary condition used at 30°N, becomes a smaller problem when data is available up to the northern boundary of the ocean basin as we have in this study.

V.4 Difference in Transport between Two Periods

In our EOF analysis of non-seasonal SST, we found a cooling trend in the North Atlantic and in the North Pacific (Chapter VI.1). The time series associated with this pattern indicated that most of the cooling occurred in the 1965-1979 period. In order to investigate the pattern of the cooling further, we performed the EOF analysis for two periods separately: one from 1949 to 1964 and another from 1965 to 1979. We found the cooling to be most evident in the latter period. The pattern tells us that the strongest cooling occurred along 30-40°N in the Pacific and along 40-45°N in the Atlantic - both at the northern edge of the warm western boundary current (Figure 6.6). Note there is also slight warming in the Southern Hemisphere in both oceans.

In order to investigate the underlying cause for this cooling further, we calculated the annual mean values of the four components of the energy budget separately for these two periods. We would like to know whether there is any significant difference among the means for these two periods. If there is, we need to know which components are responsible for the differences as well as where these differences occur.

The annual mean energy balance for the periods 1949-1964 and 1965-1979 are calculated separately. The values are then zonally averaged to produce zonal means for each ocean. The results for both periods and their differences is presented in Table V.5. Each component of the energy balance are presented separately for each ocean. The number of grids that made up the zonal means are also presented in Table V.5a. This table indicates that because of the poor data coverage in the first period, it is impossible to compare the results from the two periods for some latitudes. For instance, the difference between the two periods is artificially high in the 5-10°S latitude belt in the Pacific. This is primarily due to the fact that most of the central and western Pacific have virtually no useable data in the first period.

A brief inspection of the differences tells us there is negligible difference in Q_{out} , Q_h and Q_{in} . Q_l accounts for most of the differences shown in the net energy budget (Q_{net}). Referring to Table V.5b, we can see that the biggest difference occurs in the Indian Ocean. It has a much larger energy surplus in the first period than in the second period.

TABLE V.5a Difference in Net Heat Flux

Units in watt/m²

Latitude	Indian Ocean			Pacific Ocean			Atlantic Ocean		
	1949-1964	1965-1979	Diff.	1949-1964	1965-1979	Diff.	1949-1964	1965-1979	Diff.
65N							-37(5)	-50(11)	13
60							-55(12)	-62(14)	7
55				-26(8)	-5(16)	-21	-53(15)	-53(15)	0
50				-10(14)	4(18)	-6	-43(14)	-33(14)	-10
45				5(18)	9(20)	-4	-28(14)	-22(14)	-6
40				-19(22)	-13(22)	6	-38(19)	-26(18)	-12
35				-60(22)	-48(22)	-12	-55(18)	-47(18)	-8
30				-50(23)	-41(23)	-10	-35(15)	-31(15)	-4
25	29(6)	2(9)	27	-30(24)	-17(24)	-13	-5(18)	-11(18)	6
20	29(8)	8(8)	21	-20(25)	-6(25)	-14	7(17)	4(17)	3
15	51(15)	39(16)	12	-15(28)	-3(28)	-12	7(15)	4(15)	3
10	47(18)	40(18)	7	-8(29)	1(29)	-9	16(14)	14(14)	2
5N	48(17)	36(17)	12	-6(30)	2(30)	-4	22(8)	33(13)	-11
0	69(18)	53(18)	16	35(26)	36(30)	0	41(9)	46(13)	-5
5S	65(17)	46(22)	19	90(11)	63(26)	27	68(9)	67(10)	1
10	59(20)	31(22)	28	43(13)	26(26)	17	22(10)	28(10)	6
15	42(21)	10(22)	32	9(26)	5(22)	4	7(11)	9(11)	-2
20	8(15)	-7(20)	15	-12(26)	-4(28)	-8	16(10)	15(11)	1
25	-9(13)	-18(18)	11	-18(24)	-16(28)	-2	28(10)	16(13)	12
30	-20(15)	-32(17)	12	-26(21)	-26(22)	0	8(10)	16(13)	12
35	-22(20)	-26(24)	4	-35(20)	-21(10)	-14	2(15)	0(15)	2
40	-34(12)	-32(26)	-2	-29(18)	-22(18)	-7	7(13)	-23(16)	30

TABLE V.5b Difference in Latent Heat Flux

Units in watt/m²

Latitude	Indian Ocean			Pacific Ocean			Atlantic Ocean		
	1949-1964	1965-1979	Diff.	1949-1964	1965-1979	Diff.	1949-1964	1965-1979	Diff.
65N							54	54	0
60							67	70	-3
55				60	39	21	80	73	7
50				51	39	12	82	70	12
45				49	47	2	81	75	6
40				78	73	5	104	93	11
35				125	115	10	136	127	7
30				137	129	8	136	132	4
25	124	136	-12	138	129	7	129	131	-2
20	122	138	-16	149	136	13	135	134	1
15	113	121	-7	155	146	9	145	145	0
10	119	123	-4	154	145	9	140	140	0
5N	113	120	-7	139	133	6	118	110	8
0	90	99	-9	111	112	-1	107	102	5
5S	90	103	-13	71	102	-31	98	96	2
10	100	119	-19	113	129	-16	131	127	5
15	119	142	-23	139	140	-1	132	130	2
20	141	153	-13	146	138	8	116	120	-4
25	141	150	-9	140	137	8	116	120	-4
30	132	142	-10	133	133	0	108	101	7
35	114	199	-5	125	115	10	100	100	0
40S	109	108	1	108	103	5	102	107	-5

TABLE V.5c Difference in Incoming Radiation

Units in watt/m²

Latitude	Indian Ocean			Pacific Ocean			Atlantic Ocean		
	1949-1964	1965-1979	Diff.	1949-1964	1965-1979	Diff.	1949-1964	1965-1979	Diff.
65N							76	69	7
60							82	80	2
55				97	86	11	92	90	2
50				98	94	4	103	101	2
45				106	104	2	116	114	2
40				121	120	1	141	140	1
35				139	138	1	160	158	1
30				158	157	1	175	172	3
25	218	202	16	178	176	2	194	189	5
20	209	218	-4	194	192	2	205	202	3
15	214	210	4	206	200	0	212	209	3
10	215	213	2	262	260	2	212	209	3
5N	209	206	3	188	188	0	198	197	1
0	208	204	4	204	202	2	202	200	2
5S	204	201	3	213	219	-6	217	214	3
10	207	203	4	210	211	-1	208	207	-1
15	212	208	4	205	202	3	197	197	0
20	207	207	0	196	195	1	193	191	2
25	200	200	0	186	185	1	189	186	3
30	181	181	0	174	174	0	178	179	-1
35	165	165	0	161	160	1	165	162	3
40	145	146	-1	147	146	1	169	148	21

TABLE V.5d Difference in Sensible Heat Flux

Units in watt/m²

Latitude	Indian Ocean			Pacific Ocean			Atlantic Ocean		
	1949-1964	1965-1979	Diff.	1949-1964	1965-1979	Diff.	1949-1964	1965-1979	Diff.
65N							26	29	-3
60							27	29	-2
55				21	21	0	25	25	0
50				12	13	-1	20	19	1
45				8	8	0	15	13	2
40				16	14	2	19	17	2
35				21	19	2	19	17	2
30				17	15	2	14	12	2
25	9	9	0	12	10	2	10	10	0
20	7	8	-1	10	8	2	8	8	0
15	3	3	0	9	7	2	6	6	0
10	3	3	0	9	7	2	5	5	0
5N	2	4	2	11	9	2	8	6	2
0	3	4	1	8	7	1	7	5	2
5S	3	5	2	3	5	-2	2	2	0
10	3	6	3	4	6	-2	4	4	0
15	2	6	4	9	8	1	6	5	1
20	5	7	-2	11	9	2	5	5	0
25	7	9	-2	12	11	1	5	5	0
30	16	11	5	14	12	2	7	6	1
35	12	12	0	15	12	3	8	9	-1
40	13	13	0	15	13	2	13	13	0

TABLE V.5e Difference in Outgoing Radiation

Units in watt/m²

Latitude	Indian Ocean			Pacific Ocean			Atlantic Ocean		
	1949-1964	1965-1979	Diff.	1949-1964	1965-1979	Diff.	1949-1964	1965-1979	Diff.
65N							43	43	0
60							47	47	0
55				46	43	3	46	46	0
50				40	41	-1	47	46	1
45				41	41	0	49	48	1
40				48	47	1	58	57	1
35				54	53	1	61	60	1
30				57	55	2	61	60	1
25	58	56	2	57	56	1	60	60	0
20	52	54	-2	56	54	2	57	57	0
15	49	48	1	52	51	1	55	55	0
10	47	47	0	49	48	1	51	51	0
5N	46	46	0	46	45	1	50	48	2
0	46	47	-1	49	48	1	49	48	1
5S	45	47	-2	51	50	1	49	50	-1
10	46	48	-2	51	50	1	51	52	-1
15	48	50	-2	52	50	2	52	52	0
20	53	55	-2	53	52	1	52	53	-1
25	57	59	-2	56	55	1	53	54	-1
30	59	60	-1	57	57	0	56	56	0
35	59	60	-1	58	56	2	56	55	1
40	56	56	0	56	54	2	57	54	3

Having found the regions with the largest difference, one might want to check and see if the difference observed in latent heat flux is truly significant. If the standard deviations for this area is high, then the difference shown may be part of the natural random fluctuation. The significance test can be done by a simple hypothesis testing the difference of the means for these two periods. One would have to make sure the frequency of ship observations for these two periods are not drastically different in areas compared. Four representative grids with similar number of observation per month for the two periods are chosen and the hypothesis that there is no real difference between the means is tested. The results imply that there **is** a significant difference and are given in Table V.6. Most of the other areas with similar differences are presumably also significant if we believe that this pattern of difference is a large scale phenomenon.

TABLE V.6 Hypothesis Testing of Difference in Latent Heat Flux

Units in watt/m²

Location	Latent Heat 1965 - 1979			Latent Heat 1949 - 1964			$Z = \frac{\bar{X}_1 - \bar{X}_2}{\sqrt{S_1^2/N_1 + S_2^2/N_2}}$
	\bar{X}_1	S_1	N_1	\bar{X}_2	S_2	N_2	
40E/20S	135	49	180	112	63	175	3.8
45E/20S	117	48	180	103	57	180	2.5
115E/10N	136	44	180	118	51	180	3.6
120E/15N	138	56	180	125	53	180	2.3

Reject the hypothesis $\mu_1 = \mu_2$ if $Z > 1.625$ at 5% significance level. μ_1 and μ_2 are the population mean for these two periods, \bar{X}_1 and \bar{X}_2 are the sample means, S_1 and S_2 are the sample standard deviations, and N_1 and N_2 are the number of observations.

In the calculation of the annual mean values, most of the uncertainties arise from the formulation of the fluxes or from fixed bias in ship observations. This systematic error should disappear when one compares the difference between two values calculated using the same formulation. If we are sure that random errors do not override the differences, we can place more confidence in interpreting the results of the differences. From the results presented in the previous section, it seems that the difference in our latent heat estimates between these two periods are indeed significant in the Indian Ocean (where the largest differences are observed). We will be speculative and infer a little further on the possible relationship between this difference in the net energy flux and the cooling of the sea surface in the Northern Hemisphere.

If we consider the first period as a base year where not much cooling occurred and assume that most of the cooling occurred in the second period, there must be a larger Q_{net} in the first period than in the second period. However, the only place that has such a significant difference is in the Indian Ocean. The two areas where the major cooling occurred (the North Pacific and the North Atlantic) actually have a slightly smaller surface loss in the second period than in the first.

In the previous section we deduced that the Atlantic transports energy northward, the Pacific transports energy in both directions, and the Indian Ocean transports energy southward. From this we can offer the following explanation of the Northern Hemisphere cooling: During the first period, the surplus in the Indian Ocean not only made up for

the deficit in the southern Indian Ocean, but it also supplied energy northward to the Atlantic to maintain its temperature. The Pacific Ocean, on the other hand, must have relied on the tropical ocean to maintain the temperature in the Northern Hemisphere. The south Pacific takes some energy from the tropical region and some from latitudes south of 40°S. Due to the larger latent heat loss, the energy surplus in the Indian Ocean is not as great during the second period. There may be just enough energy surplus to make up for the deficit in the southern part of the Indian Ocean. The southern Atlantic ocean normally gets a northward influx of energy from the southern oceans. It would therefore not experience this expected input of surplus energy from the Indian Ocean. The northern Atlantic ocean, not having enough energy from the southern ocean, cooled in response to this net loss of energy. The tropical Pacific probably transported its energy surplus entirely southward when no energy was imported from the 40°S or higher latitudes. The northern part of the ocean therefore cools in response to a deficit that is not quite made up by the usual transport from the tropical region.

The above argument is based on qualitative reasoning given the estimated SST and energy flux variations. We have not estimated the actual magnitudes of the transports for these two periods because the assumption that the storage term vanishes in the long term mean probably requires a time period larger than the 15-year period we have here. More data, especially storage information using subsurface data are needed to have a better understanding of the observed behavior of long term SST variations. The differences of the fluxes between the two periods shown in this section does illustrate the importance of the time

period used when estimating energy transport values. We have assumed in the previous section that 31 years is a long enough period for the storage term to be neglected. It is entirely possible that a different 31 year period might give us different transport values. One needs more careful assessment as to exactly how long a period is required to neglect the storage term and to use the net surface flux as a valid estimate for the oceanic flux divergence.

CHAPTER VI. NONSEASONAL VARIATIONS OF SSTVI.1 EOF Analysis of SSTVI.1a The Analysis

The method used to characterize the nonseasonal variation of global SST is commonly referred to as empirical orthogonal function (EOF). This technique decomposes the time series at geographical locations into separate space and time functions that are orthogonal to each other. The functions are the eigenvectors of the variance-covariance matrix of the original data field. This method was pioneered for use in meteorology by Lorenz (1956) and by Gilman (1957). In this study, the theorem of singular value decomposition (SVD) is used to find the eigenvectors and the associated eigenvalues. The calculation of the single value decomposition is different from that of the conventional EOF. No covariance matrix needs to be constructed explicitly for SVD. Rasmussen et al (1981) have applied this method to surface temperatures of the United States, and pointed out the advantages of its use over the conventional calculation of eigenvectors from the covariance matrix. It is more accurate than most matrix inversions, especially when the data is highly correlated. In cases where the number of grid points in space exceeds the length of the time series (as is the case here when 876 grid points are available over a period of 372 months), considerable computer time and storage requirement can be saved. The numerical method used here follows that of Businger and Goulb (1969). Further

information on single value decomposition may be obtained from the text by Goulb and Reinsch (1970). A brief derivation of EOF and SVD and the relationship between the two are given in Appendix C. Using long term monthly mean SST's of the 1949-1979 period (see Chapter III), the monthly anomalies with respect to the monthly means were computed. 372 monthly anomalies at 876 grid square were used. 234 grid squares were eliminated from the original 1100 grid squares due to excessive number of months without data. Data for November and December of 1977 are deleted because there are large areas with no data for these two months. Interpolated values between October, 1977 and January, 1978 were used instead.

VI.1b The main results

After performing the analysis on the SST anomaly data set, one needs to find out whether the eigenvectors obtained are physically meaningful. First of all, there is the problem of degeneracy where the consecutive eigenvectors may not be independent of each other and the 'true' eigenvector may be a linear combination of the calculated eigenvectors. Secondly, one needs to know whether the eigenvectors are sufficiently different from random noise. Two separate formulae are used to determine whether the eigenvalues are distinct and significantly different from random noise. The first method is to apply a formula derived by Kendall (1980) to estimate the sample error associated with each eigenvalue. North et al (1982) recommended using the same procedure recently. The formula used is:

$$\partial\lambda = \lambda \cdot (2/N)^{1/2} \quad (6.1)$$

where N is the number of independent time samples used to calculate the EOF. If the sampling error for a particular eigenvalue λ is larger than the spacing between λ and a neighboring eigenvalue, then the eigenvector associated with λ will not be distinguishable from its neighboring eigenvectors. The first twenty eigenvalues and their sample errors are illustrated in Figure 6.1. The sample errors for the first five eigenvalues all show values smaller than the spacing between their neighboring values.

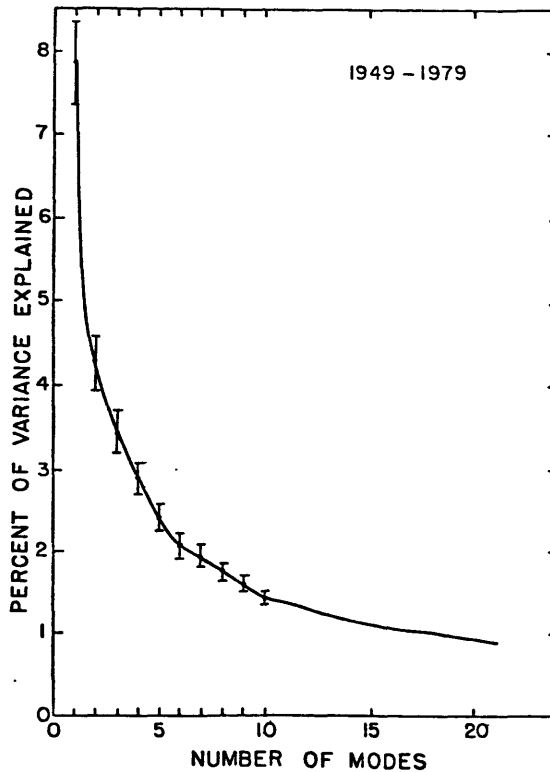


Figure 6.1 The eigenvalues and the associated sampling errors for the first twenty modes of the nonseasonal SST EOF analysis.

In the second method, we use one of the testing procedures suggested by Preisendorfer and Barnett (1977) to separate the noise from the signal in the data. The procedure chosen involves calculating the autocorrelation function of the time series of a particular EOF and forming the 'Q-statistic':

$$Q = \sum_{\ell=1}^k \frac{r^2(\ell)}{\text{var}[r(\ell)]} \quad (6.2)$$

where $r(\ell)$ is the sample autocorrelation at lag ℓ . The Q-value is used to perform a χ -square test against the hypothesis that the time series is a random sample from a Gaussian population. The Q-statistic of the first ten time series associated with the first ten eigenvectors are calculated. Their values are all exceedingly large, indicating a strong non-noise signal in these modes.

To further test the significance and the stability of the principal eigenvectors, eigenvector analysis was performed on various partitioning of the 31-year data set. The data was first divided into two separate 15-year periods, one from 1949 to 1964 and another from 1965 to 1979. The first period denotes a period where the number of observations per month was small compare to the second period. Seasonally stratified data (December-February, March-May, June-August, September-November) were also used to see if the principal patterns (modes) are different from season to season. The fraction of variance explained by the first five eigenvectors are given in Table VI.1 for the various combinations analyzed. The sample error ($\partial\lambda$) for the eigenvalues of the smaller

TABLE VI.1 Percentage of Variance Explained for Separate EOF Analysis

#	1949-1979	1949-1964	1965-1979	Dec-Feb 1949-1979	Mar-May 1949-1979	June-Aug 1949-1979	Sept-Nov 1949-1979
1	7.67	9.42	8.26	10.42	8.96	7.90	9.53
2	4.29	4.62	5.78	5.50	4.59	6.06	5.76
3	3.44	4.05	3.49	4.73	4.18	4.28	4.44
4	2.84	3.53	3.37	4.50	4.02	3.90	3.79
5	2.37	2.90	3.07	3.49	3.58	3.69	3.11

partitioned data sets may not be small enough to render the modes higher than three to be independent of each other. Therefore, we will limit our discussion to the first three modes of the EOF analysis (which are clearly distinct from each other) in the following sections.

VI.1c Discussion

A. The First Mode (The El Nino Mode)

The first eigenvector pattern is shown in Figure 6.2. This pattern explains between 7.7 and 10.4% of the total variance of the global SST field. As can be seen from Figure 6.2, this mode is almost identical to the first eigenvector found by Weare et al (1976) for a data set covering the Pacific Ocean alone from 20°S to 55°N but omitting the western tropical Pacific. This was termed the El Nino mode because of the presence of the warm body of water in the eastern equatorial

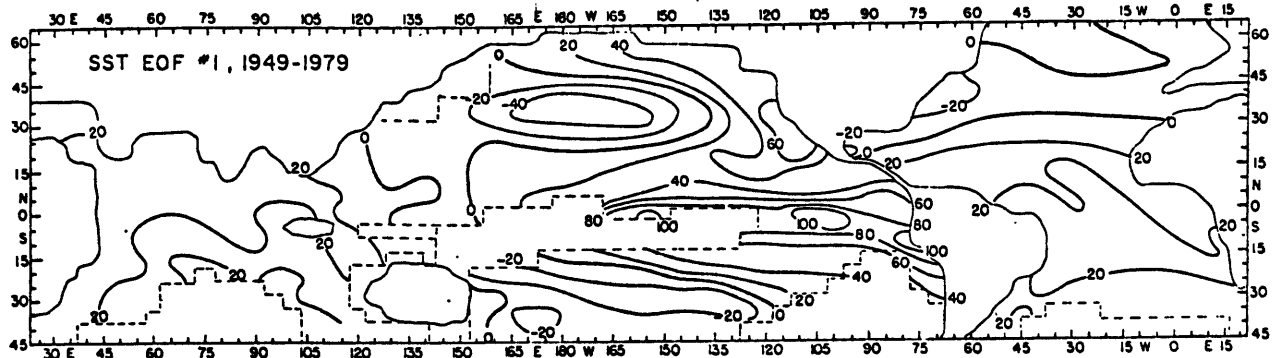


Figure 6.2 First nonseasonal SST eigenvector pattern for 1949-1979 (7.67% of total variance explained)

Pacific. When temperatures are high in the eastern equatorial Pacific, they are also high in the tropical Atlantic, the tropical Indian and north eastern Pacific. At the same time, they are low in the north middle latitude and the western Pacific. We should point out here that the name El Nino may be misleading because both studies show a large region in the mid-latitude central Pacific to be an integral part of this mode, as noted by Weare et al (1976). Time series of the first eigenvector is presented in Figure 6.3a for the analysis covering 1949-1979.

It has been shown that an eigenvector analysis of zonal mean SST data evaluated for the global oceans (Chiu and Newell, 1983) is also dominated by this mode. The El Nino is strongly related to the Southern Oscillation and to subsequent tropical troposphere free air temperature changes (Newell and Weare, 1976a,b and Walker (1923,1932)). Kidson (1975) has shown by eigenvector analysis that the Southern Oscillation explains the largest fraction of the variance of the nonseasonal global pressure field. It seem reasonable to find this El Nino mode also dominates the variability of the global SST pattern.

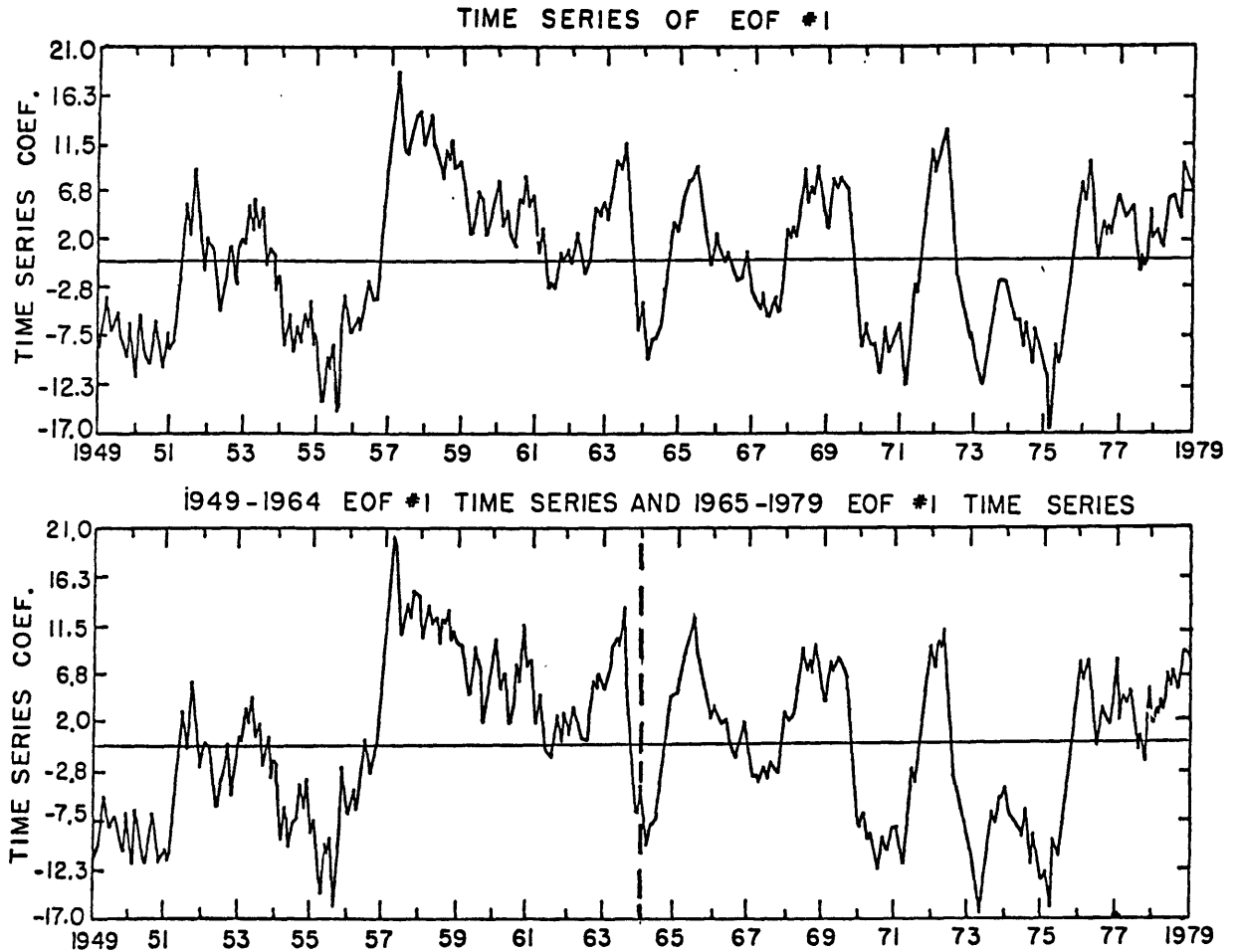


Figure 6.3 Time series of the first eigenvector patterns for
a) 1949-1979 and b) 1949-1964 and 1965-1979

The first mode obtained from various partitioning of the data set are very similar to the one obtained from the entire period. There are minor differences, mostly in the Atlantic and the Indian Ocean. This indicates that perhaps these regions are not dominated by the El Niño mode. The time series for the two half periods separately show the same fluctuations as the time series for the whole data set, as

illustrated in Figure 6.3b. Even though the error bar of this analysis is increased due to decreased sample size for the two half periods, this mode is still separated from the second mode (as indicated in Figure 6.1).

Time series of the first mode from the four seasonally stratified analysis are presented in Figure 6.3c. The global pattern of the eigenvectors are essentially the same as before. The time series show the same characteristics as Figure 6.3a but with different relative amplitude of the extremes.

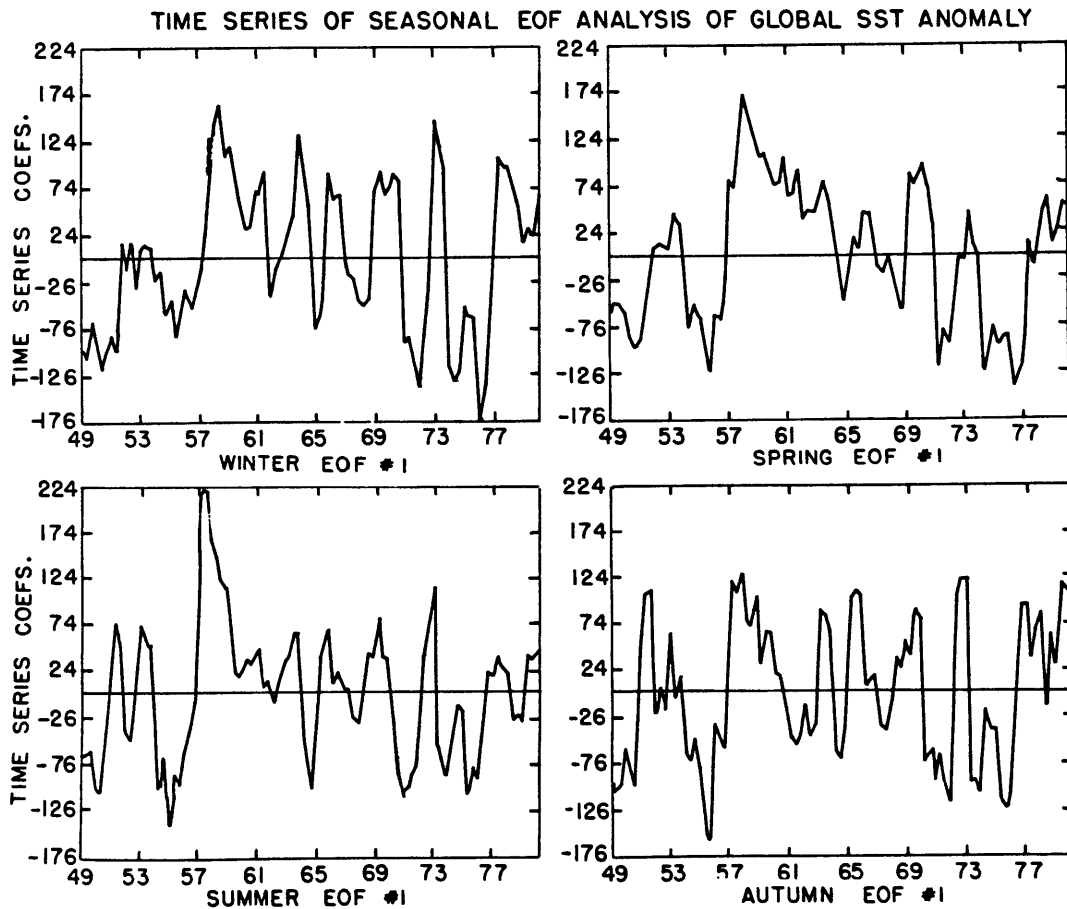


Figure 6.3c Time series of first eigenvectors for seasonally stratified analysis.

Note that the fraction of variance explained by the first mode is smaller than the 23% obtained by Weare et al (1976). This is mostly due to the addition of the rest of the global ocean. This addition of the Atlantic Ocean, the Indian Ocean, and the tropical western Pacific has apparently increased the variance without a proportional increase in the signal.

Since we have calculated the eigenvector analysis on the nonseasonal anomalies without first normalizing them according to their standard deviations, one might wonder whether the eigenvectors are merely a result of the regions with high variance. The standard deviations based on the entire nonseasonal data set are shown in Figure 6.4. We can see that the equatorial Pacific dominance of the first eigenvector is not simply due to standard deviations of SST being larger than elsewhere. There are large values in the vicinity of the Kuro-Shio and Gulf Stream. A situation that also prevails if standard deviations for separate months are considered. (See Chapter III.)

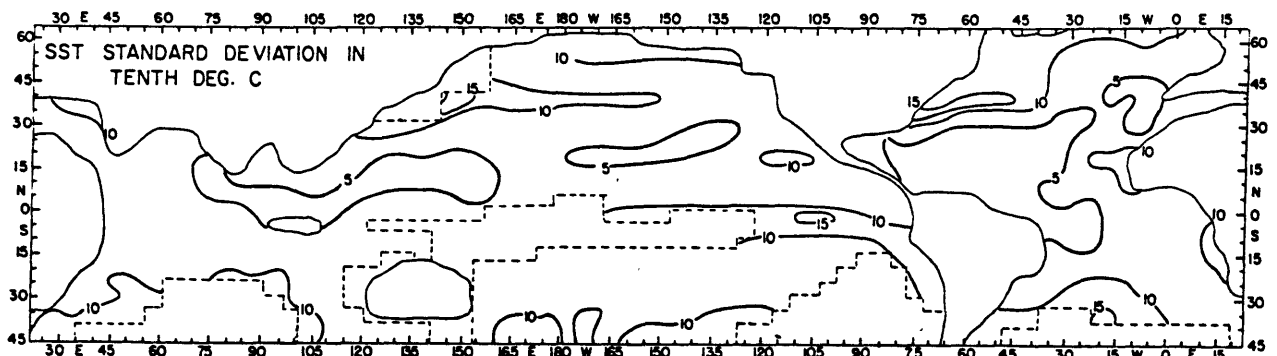


Figure 6.4 Standard deviation of SST for the period 1949-1979

In order to investigate the relationship between the El Niño mode and other areas of the ocean, the correlation coefficient between the time series of the first EOF and the time series of SST anomalies in each 5° by 5° grid region was calculated. The global pattern of this correlation coefficient, shown in Figure 6.5, is quite similar to that of the first eigenvector, but the relative values are different. For example, the tropical Indian Ocean and the tropical Atlantic Ocean are quite highly correlated with the first EOF time series, whereas in the eigenvector pattern itself these areas show relatively low weight.

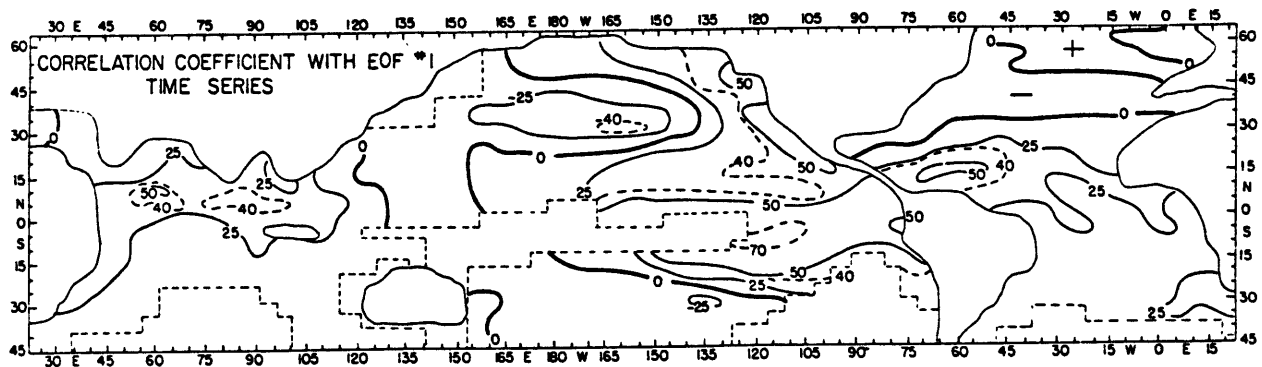


Figure 6.5 Correlation coefficients of EOF #1 time series and each 5° by 5° grid squares

Cross-correlation were performed between EOF #1 time series and selected points over the global ocean to see if the contemporary correlations found in Figure 6.5 are the maximum correlations if all lags are considered. The results are displayed in Figure 6.6 for squares that are significantly related to El Niño variations. The correlation between this mode and tropical Atlantic have their maximum at three month lag and the same is true for tropical Indian Ocean. In both cases, the eastern tropical Pacific leads the temperatures in other

tropical areas. There is also a high positive contemporary correlation between areas off the north American coast and contemporaneous negative correlation with the north central Pacific (this is to be expected from the pattern of the first eigenvector.) The exact lag at which peak correlation occurs between tropical oceans varies slightly depending on which grid points are used, but the general result, evident in all squares considered, is that the tropical Atlantic and Indian lags the eastern tropical Pacific.

The matrix of the correlation coefficients between zonal mean temperatures in the three separate oceans has been presented by Newell and Chiu (1981) and shows high values between the tropical Pacific and tropical Indian Ocean. The coherence between the nonseasonal SST variation in the tropical Atlantic and eastern tropical Pacific has previously been pointed out by Covey and Hastenrath (1978) and Hastenrath (1978). As for the physical link between the regions, they suggested that the trade wind appear to be stronger or weaker in both regions at the same time, and the increased wind stress and evaporational loss occur at the same time in these regions. Thus a general finding from Figure 6.5 is that the tropical oceans vary in phase.

It has been known since Walker's early work (Walker, 1932) that the Indian Ocean temperatures vary with an index of the Southern Oscillation. Newell (1979) and Weare (1979) pointed out that the physical reasons for the temperature changes are different in the Indian Ocean and the equatorial Pacific. The eastern equatorial Pacific is

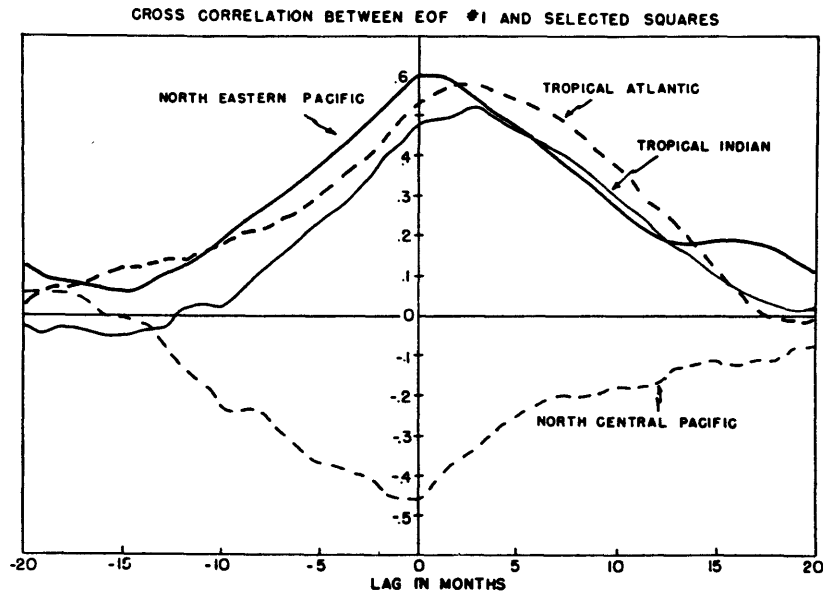


Figure 6.6 Cross correlation between time series of EOF #1 and selected grid squares

colder due to enhanced upwelling from higher than average pressure in the south-east Pacific. On the other hand, the water over the northern Indian Ocean is colder due to enhanced cloud cover from lower than average pressure, and therefore less radiation available to heat the ocean (see Newell (loc cit); Weare (loc cit); Hastenrath and Wu (1982) and Newell et al (1982)).

Empirical orthogonal functions were calculated for nonseasonal variations in incoming solar radiation (see Chapter VI.3). The first eigenvector is a time series whose behavior is similar to the El Nino mode. The pattern of the first eigenvector shows large positive values in the eastern and western tropical Pacific, North Indian Ocean and tropical Atlantic. This indicates that the physical parameters that link the SST in tropical oceans during El Nino episodes might be the variations in cloudiness.

While the first EOF pattern in the Pacific closely mirrors individual situations with the eastern equatorial Pacific out of phase with the central North Pacific, the other parts of the global ocean do not follow a unique pattern linked to El Nino. If actual monthly anomaly patterns are examined, it is seen that for the same conditions in the eastern equatorial Pacific there are quite different conditions in the Gulf Stream region off the northeastern United States. Figures 6.7 and 6.8 illustrate the behavior of global ocean temperature anomalies during El Nino episodes in 1957, 1972 and more recently, in 1982. The only consistent pattern in these episodes of El Nino is the north central Pacific and eastern tropical Pacific oscillation.

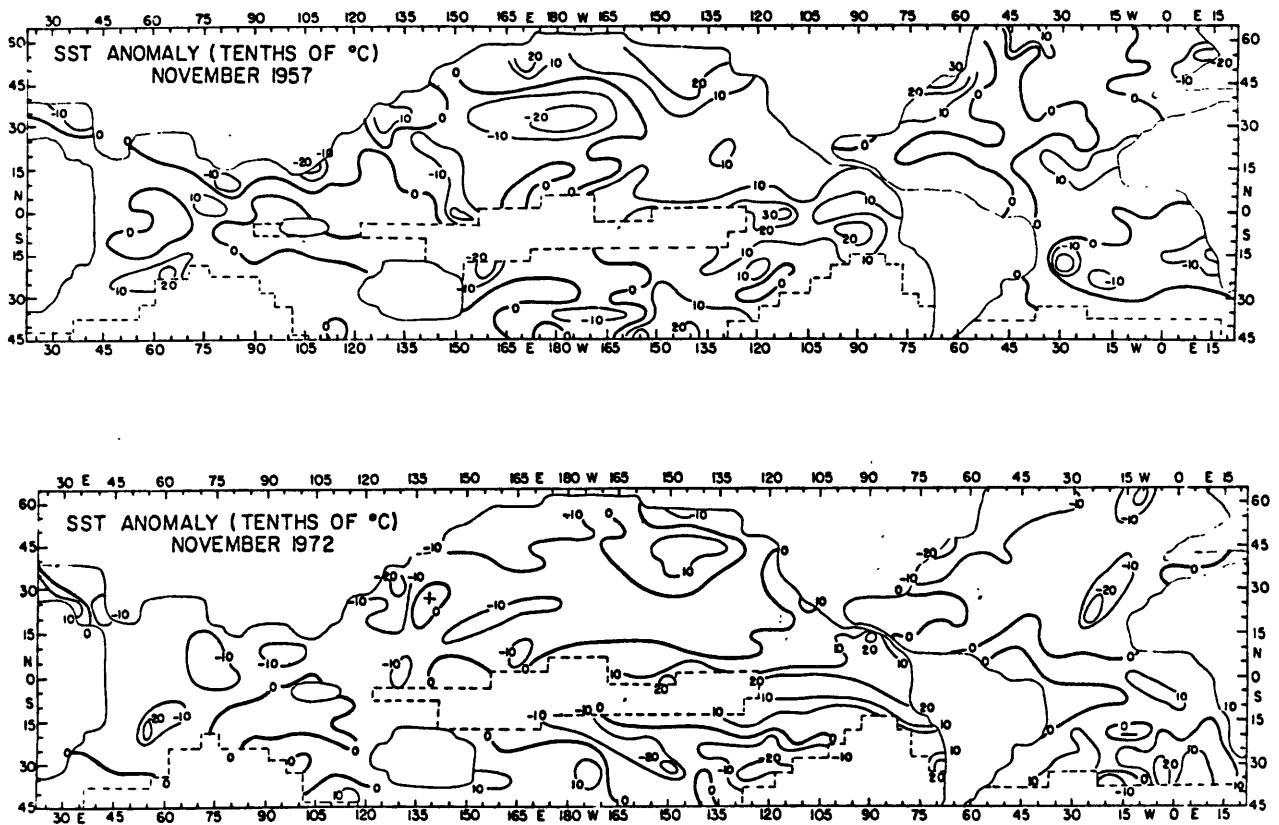


Figure 6.7 Global SST anomaly pattern for November, 1957 and for November, 1972

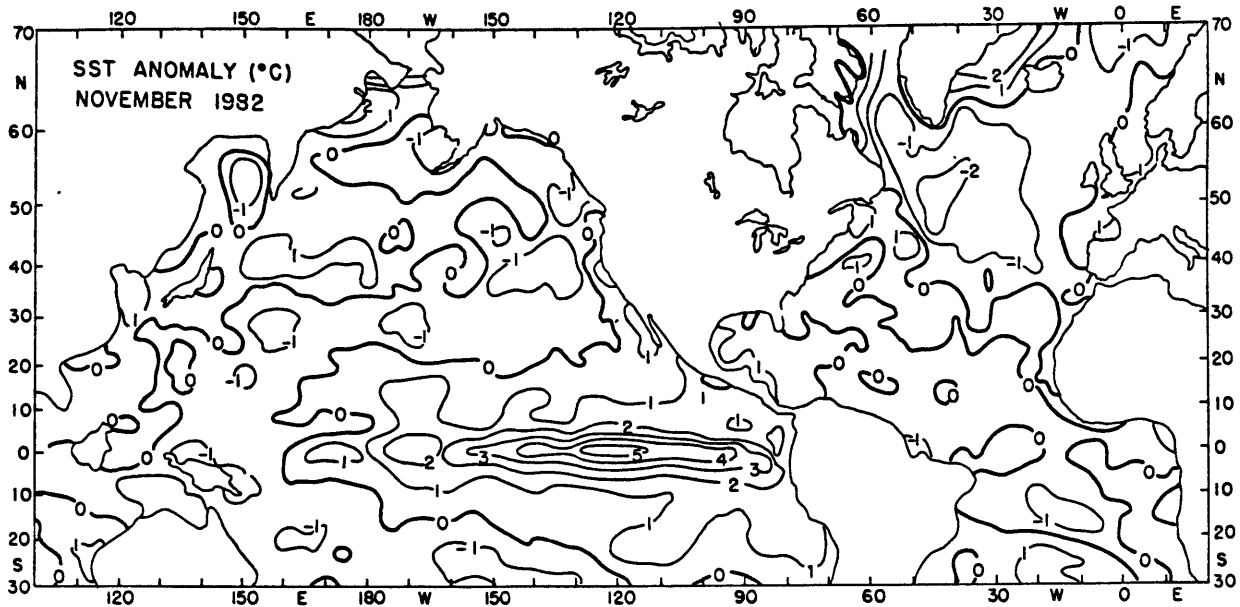


Figure 6.8 Global SST anomaly pattern for November, 1982

Since the north central Pacific and eastern tropical Pacific oscillation is the strongest feature in all El Niño episodes, one might want to raise the question as to why the water of the central North Pacific are cold while the equatorial water are warm. There are three possible reasons: there could be oceanic energy loss due to increase evaporation from enhanced northerly flow; there could be weaker advection of warm water from the south from a weaker subtropical gyre; and there could be reduced solar radiation reaching the sea surface from more cloud cover.

The first hypothesis is supported by Kidson (1975). He showed that when the eastern equatorial Pacific was warm the middle latitude north-south pressure gradients were enhanced in both hemispheres. One could argue that either stronger winds produced greater evaporational cooling in the central mid-latitudes or carried drier air to the ocean

there, which would have the same effect. Correlation studies between anomalous SST and anomalous zonal wind tends to support this hypothesis (see Chapter VI.4). A significant negative relationship was found at the northern branch of the subtropical gyre suggesting that colder SST is associated with stronger wind.

There is little data on ocean current velocities to test the second hypothesis, although Reiter (1978) has suggested that the Pacific gyre is modulated by trade wind changes and these would operate to produce colder water at the equator and warmer water at 30°N at the same time.

The third hypothesis is that the subtropical gyres are weaker in the El Nino mode as suggested by Newell et al (1982). Computation of solar energy flux at the surface using observed mean monthly cloud amounts obtained from the same data set has been made and this flux has been correlated with SST anomalies (see Chapter VI.4b). There are regions of significant positive correlation in the North Central Pacific suggesting that more cloud cover lowers the SST. The solar flux at the surface and the actual SST anomalies are shown for 30°N/165°W and 0°/80°W in Figure 6.9. The correlation between this flux and SST is 0.41 (with a maximum of .61 in the summer season) at 30°N and 165°W and the association between the curves is evident. For the eastern equatorial Pacific, the association is not so clear (the correlation coefficient is -0.02). Changes in the parameters are clearly related in some periods. 1957 is a good example. A similar check of the evaporation anomalies shows no significant correlation between SST and

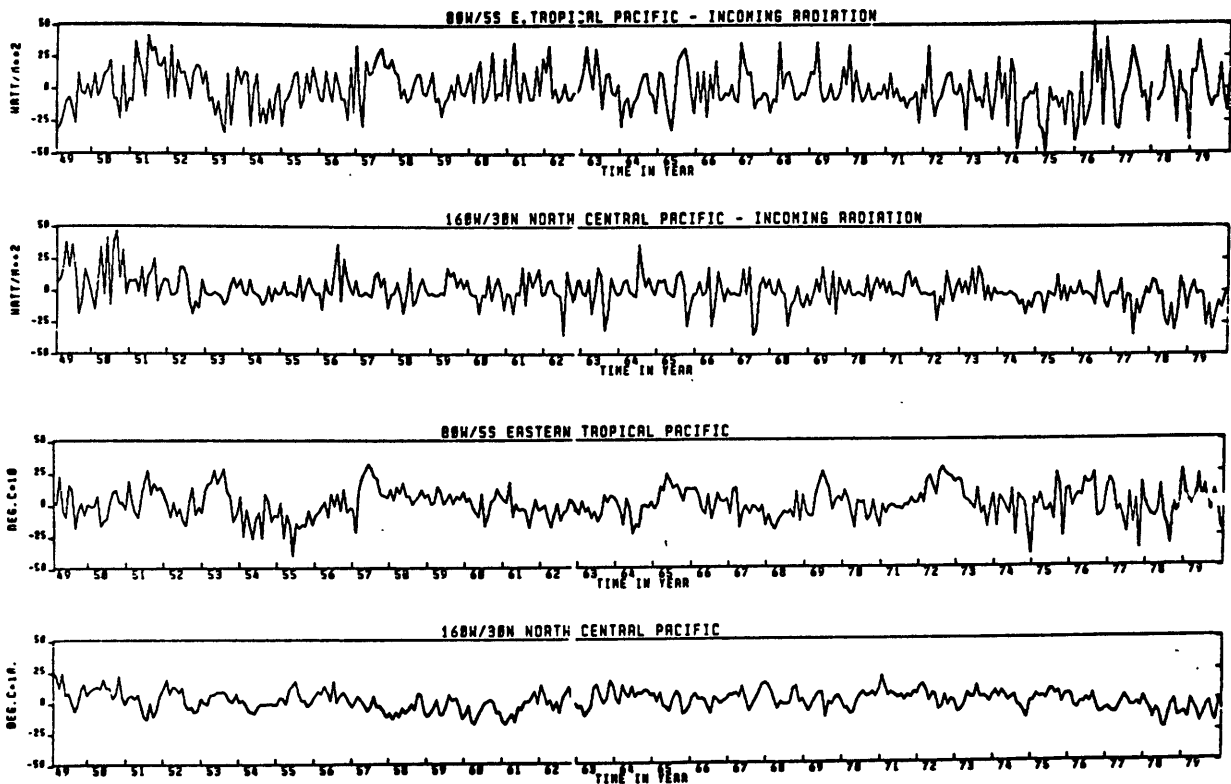


Figure 6.9 Nonseasonal time series of SST and incoming solar radiation at two selected grid squares

evaporation in mid-latitudes. Hence the third possibility, that enhanced cloudiness explains the lower sea temperature in the middle latitude seems the most likely explanation. Another point evident from Figure 6.9 is that enhanced solar flux is sometimes associated with warmer water in the tropics. It has been argued that the warm water is generally a response to decreased upwelling with solar radiation supplying a constant heat source (Newell et al,1982). If there is increased solar flux at the same time as decreased upwelling, as apparently occurred in 1957, the positive anomalies would be expected to be sharp. Further studies need to be made of factors controlling cloudiness change.

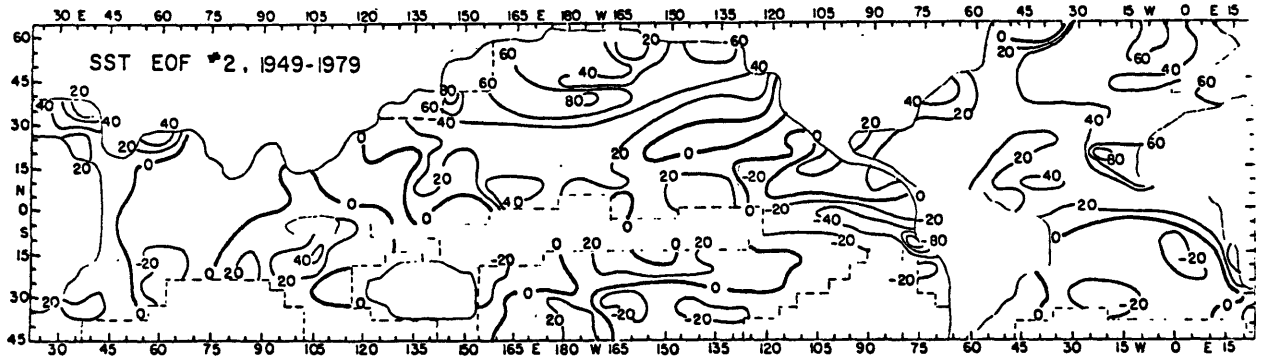


Figure 6.10 Second nonseasonal SST eigenvector pattern for 1949-1979 (4.29% of the total variance explained)

B. The Second Mode (The Cooling Mode)

The second eigenvector is shown in Figure 6.10 with the associated time series shown in Figure 6.11a. Large positive values occur in the north Atlantic, north Pacific, the Mediterranean and the eastern equatorial Indian Ocean. They are negative values in the eastern equatorial Pacific, the south Atlantic, south Pacific and a good part of the western Indian Ocean. The second mode from the eigenvalue analysis of the two separate half periods shown somewhat different patterns (Figure 6.12). A substantial negative region appearing in the the west Atlantic at 40-50°N and in the subtropical north Pacific in 1949-1964. Positive values in the northeast and southwest Indian Ocean were enhanced and positive values appeared in the western equatorial region. The 1965-1979 period, however, yielded a similar pattern to that for the 1949-1979 period. The time series of this mode is shown in Figure 6.11b. It is apparent that the cooling trend occurred mostly in the second half of the 31-year period. The pattern from the eigenvectors shows that the north Atlantic and the north Pacific dominated the cooling. This cooling trend was also evident in a previous

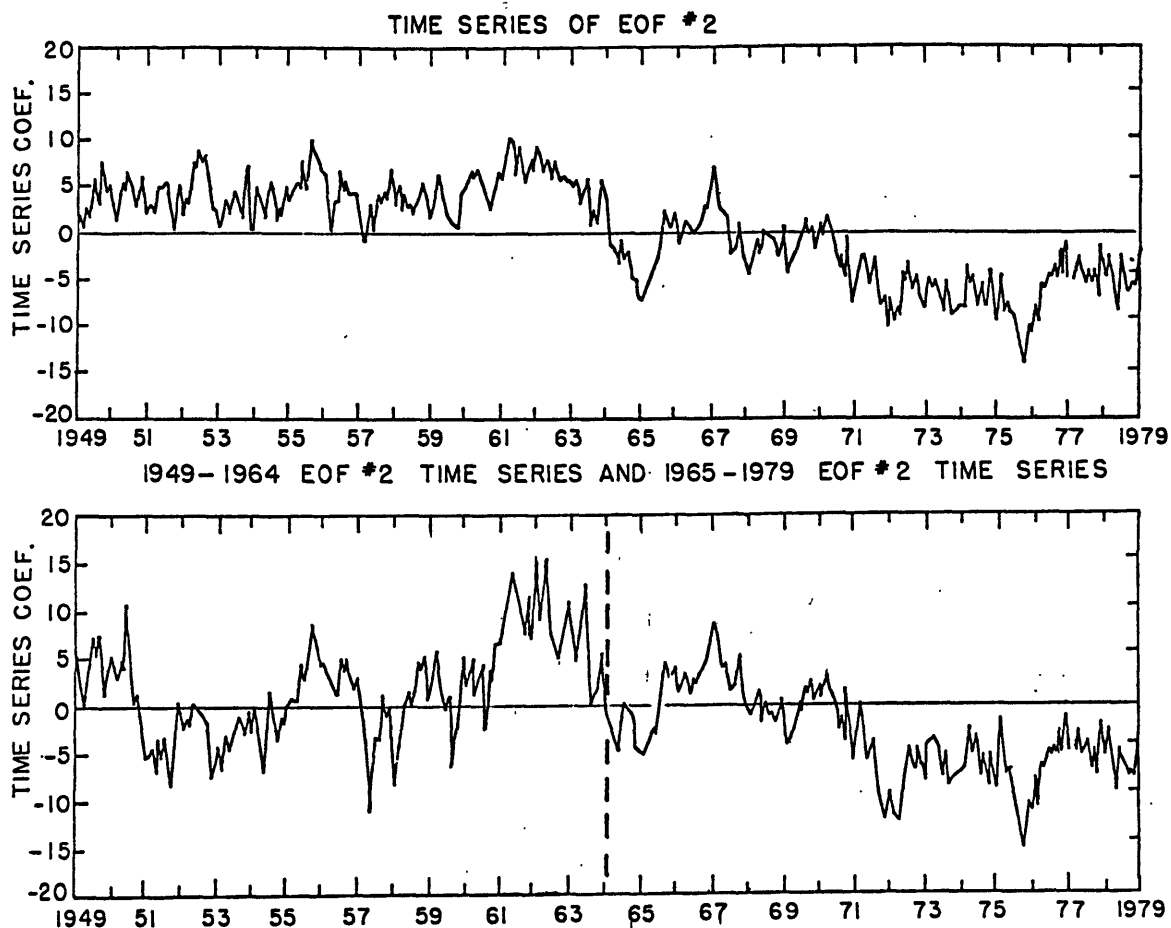


Figure 6.11 Time series of second eigenvector for the periods
 a) 1949-1979 and b) 1949-1964 and 1965-1979

investigation of zonal mean SST changes (Newell and Hsiung, 1979), in the third non-seasonal eigenvector of the Pacific SST reported by Weare et al (1976) and the first non-seasonal eigenvector of the Atlantic SST reported by Weare (1977). This interpretation also leads to the inference that the south Atlantic and part of the south Pacific are warming at the same time that the northern oceans are cooling.

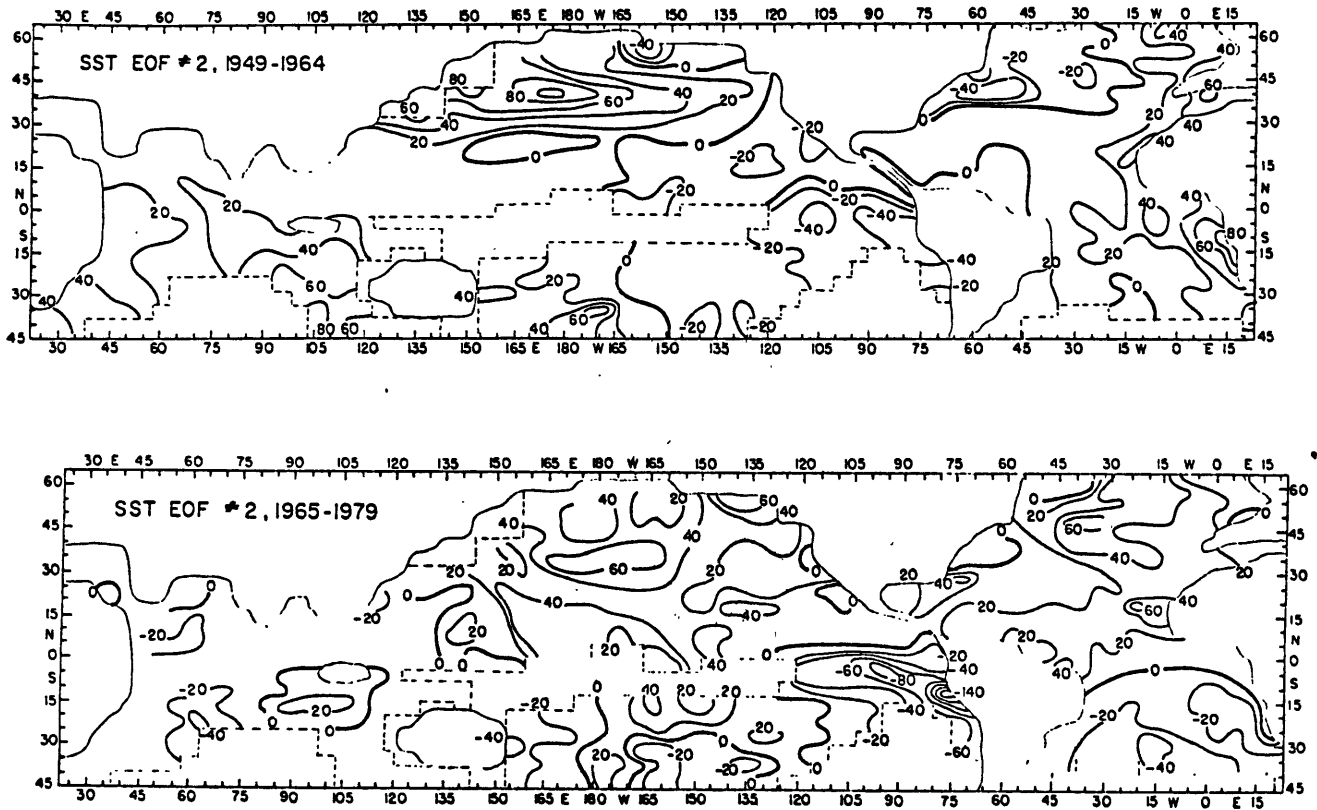


Figure 6.12 Second nonseasonal SST eigenvector pattern for
 a) 1949-1979 (4.62% of total variance explained)
 b) 1965-1979 (5.70% of total variance explained)

The observed cooling is intriguing and calls for an explanation. Is this an effect of the Mt. Agung volcanic eruption of 1963 or is this just another natural mode of variation of the ocean? One could safely rule out the argument of bucket versus engine intake method as an explanation of this trend because the data set covers a period which we believe is free of this bias. Most of the conversion from bucket to engine intake took place in the mid-1940's. At any rate, the switch to engine intake method would have given us a warming trend, rather than the cooling trend observed. Douglas et al (1982), in a recent contribution, reported that the cooling SST trends between the 1947-1966 and 1969-1980 periods are matched by 700 mb height changes in the Pacific sector. They make a good case for a relationship between SST

and 700 mb height - a relationship that has been frequently pointed out by Namias. In a previous paper on global SST (Newell and Hsiung, 1979), a cooling trend was also found to be present in the north Atlantic (as found by others; see for example Kukla et al, 1977). Boer and Higuchi (1980) also showed that the zonal mean 1000-700 mb thickness (geopotential difference) of the polar cap showed a cooling trend after 1964. Douglas et al ascribe the cooling to stronger winds, and greater than normal southward Ekman drift, at least for the winter season.

C. The Third Mode

The third eigenvector (Figure 6.13) shows a general sign alternation between the northern hemisphere and the southern hemisphere

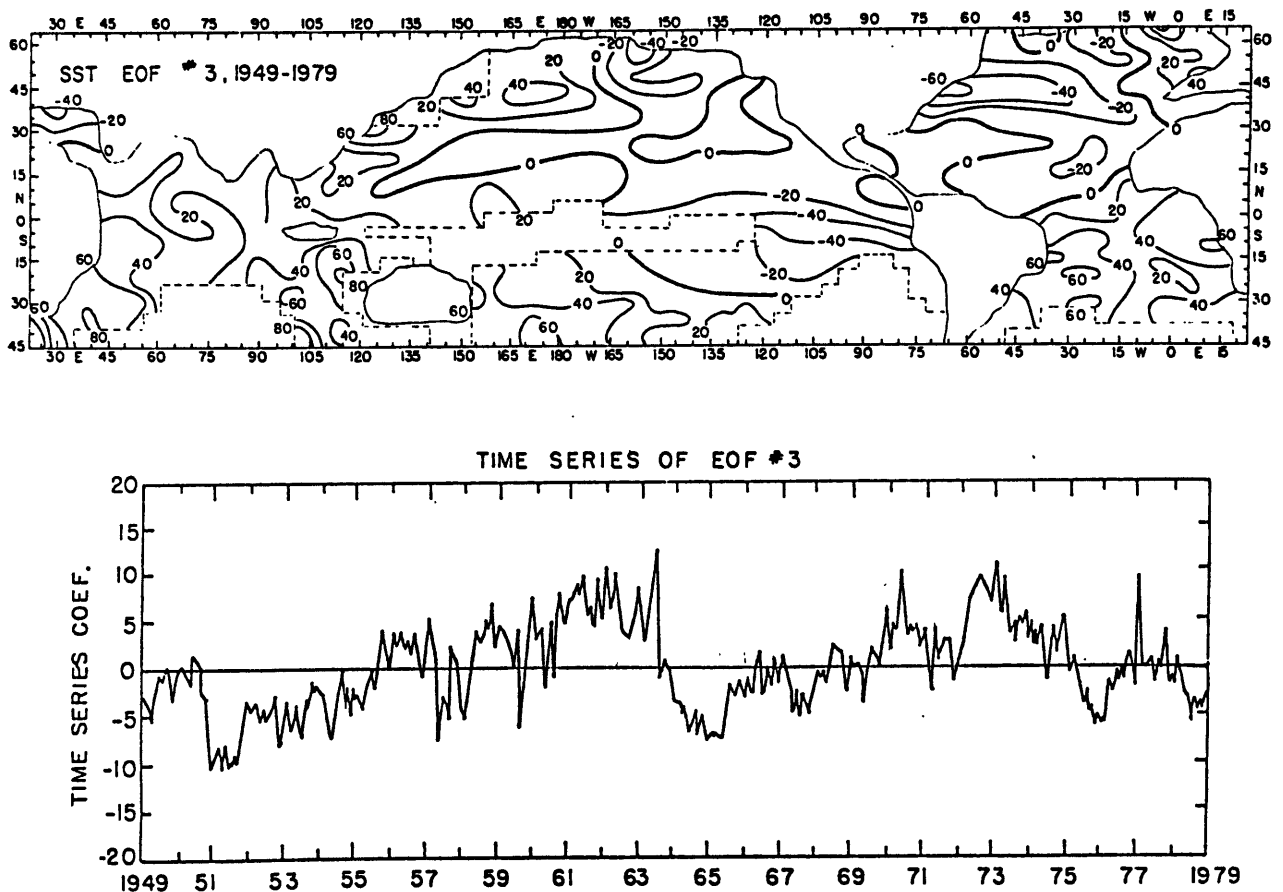


Figure 6.13 a) Third nonseasonal SST eigenvector pattern for 1949-1979 (3.44% of the total variance explained) and b) time series of the eigenvector

in the Atlantic, and a general east-west sign change in both the north and south Pacific. The latter is not present for the 1949-1964 period.

The third global mode seems to reflect a shorter-term fluctuation of some type as well as trends, making the interpretation complex and difficult. Once the data is divided into two to try to examine the trends separately, the error bars on the eigenvalues increase to the point where the third and fourth modes may not be resolved. We therefore do not pursue this further.

Autocorrelation functions were computed from the eigenvector time series for the entire period and for the two halves separately in order to provide further information on the differences in the patterns (Figure 6.14). For the first eigenvector, the period 1965-1979 exhibits a typical recent El Nino characteristic and the 1949-1964 results seem to reflect the fact that the rather large event, the 1957 El Nino dominated the period. The second eigenvector time series shows unmistakable evidence of a trend occurring in the second half and dominating the entire period. Autocorrelations for the third eigenvector show evidence of a trend in the 1949-1964 period.

VI.2 Statistical Properties of Δ SST: Autoregressive Models

The time series of SST anomaly at the two centers of action of our first global EOF analysis - the north central Pacific (NCP) and the eastern tropical Pacific (ETP) - are investigated next in more detail. We examine how SST anomalies in these two key regions behave.

blank page

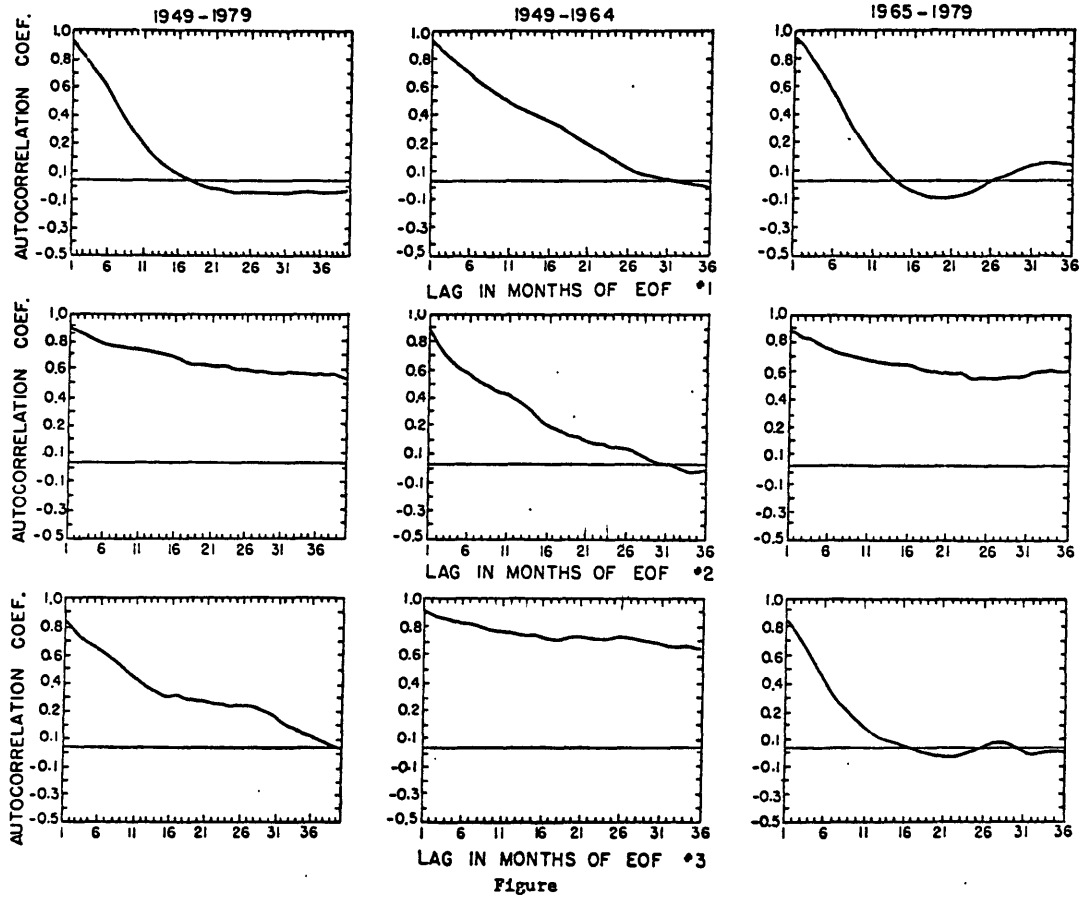


Figure 6.14 Autocorrelation functions for the first three eigenvector time series computed for the entire period and for the two half periods separately

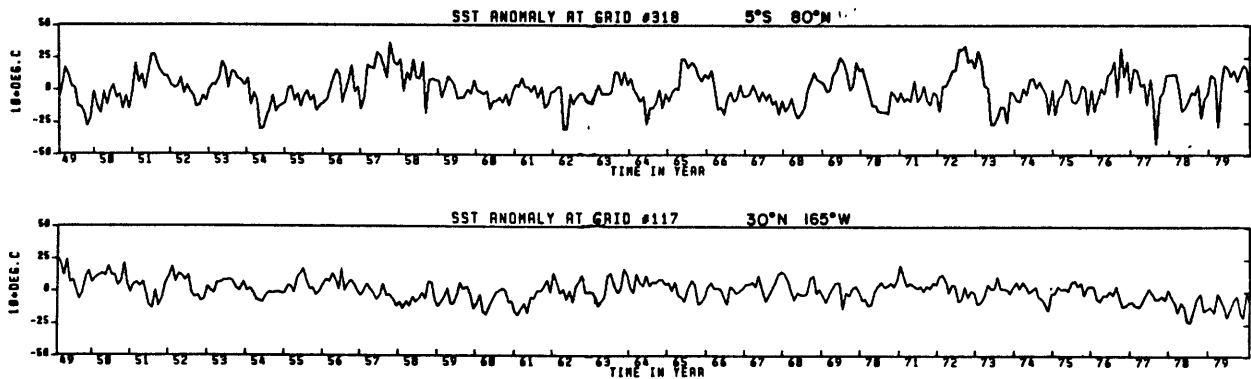


Figure 6.15 Nonseasonal time series of SST at 5°S , 80°W and 30°N , 165°W

The time series plots at two representative grid points from NCP and ETP are presented in Figure 6.15. In ETP, the grid point at 5°S and 80°W is selected and in NCP the grid point at 30°N and 165°W is selected. The time series at ETP mimic the time series of the first EOF - the El Niño mode. The amplitude of the fluctuations is larger than that in the NCP. The anomaly in ETP also seem to have more high frequency component than that in the NCP. The difference observed in the behavior of SST anomaly at these two areas can perhaps best be explained by the observed mean mixing layer depth at these two areas. Mixing depth at NCP has a large seasonal variation ranging from as deep as 300 meter in the winter to about 50 meter in the summer time, while at tropical regions the mixing depth is shallow (ranging from 10 to 50 meters) all year round (Levitus, 1982). The energy that is required to change the temperature of the layer is larger when it is deep than when

it is shallow. Therefore, we observed the slow-varying SST anomaly in NCP while the adjustment in the tropics is much faster. During episodes of El Nino, however, the behavior of SST anomaly in eastern tropical regions seems to switch to a different mode - one that is more similar to SST anomalies in the NCP region. As expected, the observed thermocline during El Nino is also much deeper than usual (Wyrcki, 1975).

VI.2a Autoregressive model fitting

Here we assume that the two time series considered in the previous section can be represented as autoregressive processes for some unknown order p . A p^{th} order autoregressive process (Box and Jenkins, 1976) denoted by AR(P) can be expressed as

$$\sum_{k=0}^p \phi_k (x_{t-k} - \mu) = a_t, \quad t=p+1, p+2, \dots \quad (6.3)$$

with $\phi_0 = 1$, μ the mean, and the other autoregressive coefficients ϕ_k , $k=1, 2, \dots, p$ being the unknown parameters to be estimated from the time series. In (6.3), it is required that the a_t 's constitute a white noise process with zero mean and constant variance. Of course, more complicated process can also be considered. Nevertheless, low-order autoregressive models are adequate to explain these time series and it is easier to interpret these simple models physically.

One good way to estimate the order of the autoregressive model for the time series is to examine the autocorrelation functions. The autocorrelation function for these two points are estimated from the time series by:

$$r_k = \frac{b_k}{b_0} \quad (6.4)$$

where

$$b_k = \frac{1}{N} \sum_{t=1}^{N-k} (x_t - \bar{x})(x_{t+k} - \bar{x}) \quad (6.5)$$

Here \bar{x} is the mean for the time series x_i , $i=1,2,\dots,N$. The results are presented in Figures 6.16. As can be seen, these two autocorrelation plots indicate that the SST anomalies for these two regions are probably the results of different mechanisms: NCP exhibits an autocorrelation function that is similar to a first order autoregressive process while the ETP has the characteristics of a second order process (see Box and Jenkins, 1976).

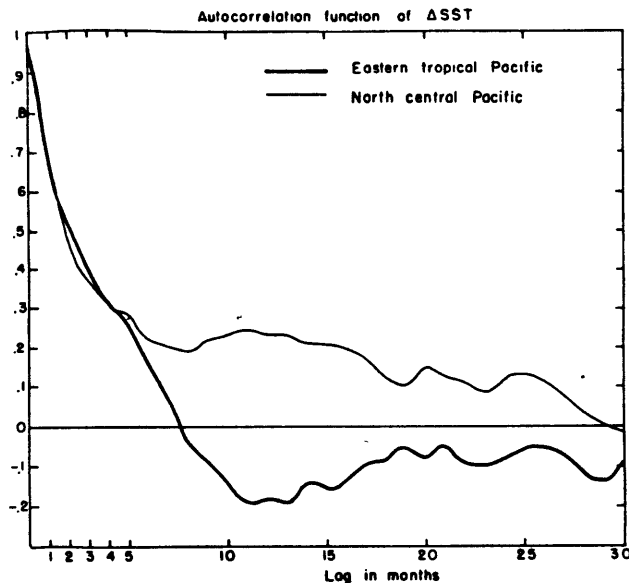


Figure 6.16 Autocorrelation function of nonseasonal SST at eastern tropical Pacific and north central Pacific

Autocorrelations of SST anomalies were also calculated for the global ocean and the coefficients at lag=1 are presented in Figure 6.17. This coefficient is the parameter estimate of a simple Markov process and gives an indication of how persistent the SST anomaly is. Note both north central and eastern tropical Pacific are areas with high persistence, but the behavior of their autocorrelation function are quite different in higher lags. Figure 6.17 also indicates that the SST anomalies are much more persistent in the northern hemisphere than in the tropics or in the southern hemisphere (with the exception of upwelling regions in the tropics.) This is the opposite of the autocorrelation function of the air temperature anomalies at higher levels. Newell et al (1983) have found that for air temperature

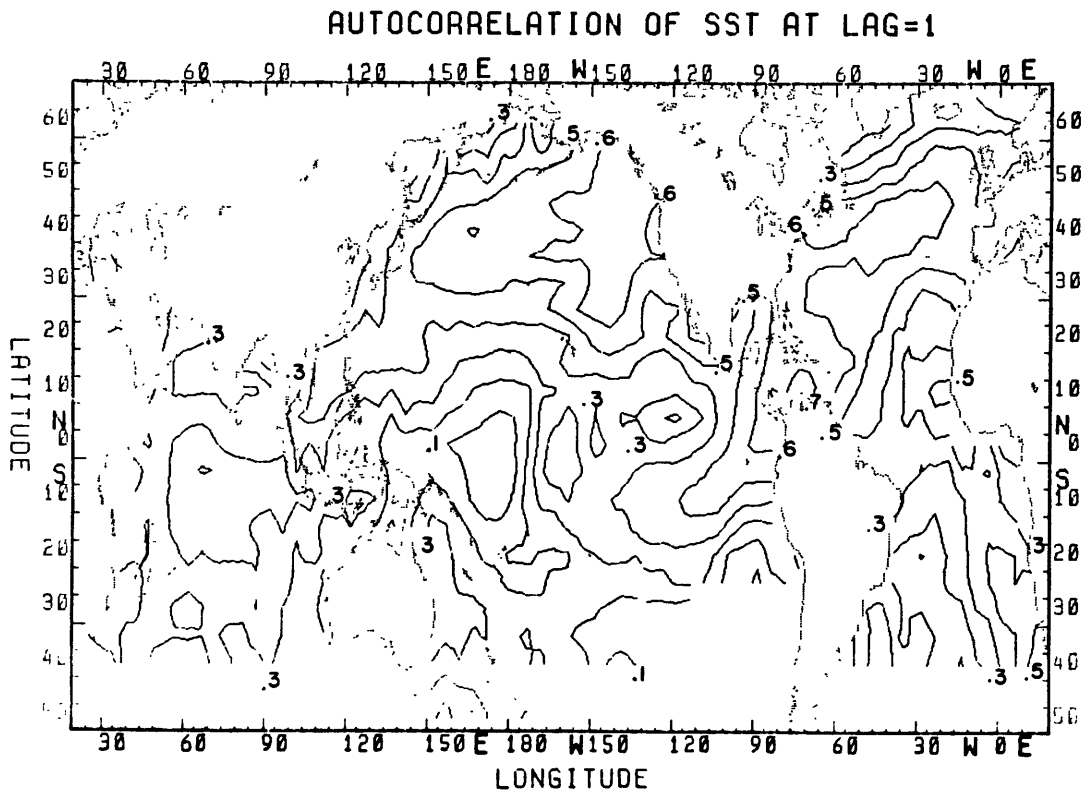


Figure 6.17 Autocorrelation coefficient at lag=1

fluctuations the areas with highest persistence (as measured by the autocorrelation at lag=1) are in tropical regions and decreasing towards higher latitudes.

To determine the optimal order of an autoregressive model for these SST fluctuations, we calculated the autoregressive coefficient of orders from one to five using Yule-Walker recursive method (see Box and Jenkins, 1976, p.82) and used the Bayesian information criterion (BIC) suggested by Katz (1982) to select the appropriate order of an autoregressive fit to the time series. The procedure requires that all possible orders p , $p=0,1,\dots,p$ be fitted to the data. Then the value of p is selected that minimizes the quantity

$$\text{BIC}(P) = N \cdot \ln[\hat{\sigma}^2(p)] + (p+1) \cdot \ln[N], \quad p=0,1,\dots,p \quad (6.6)$$

where

$$\hat{\sigma}^2(p) = \frac{N}{N-p-1} \sigma^2(p) \quad (6.7)$$

Here $\hat{\sigma}^2(p)$ is an unbiased estimator of the white noise variance for an AR(P) process and can be calculated by:

$$\hat{\sigma}^2(p) = \frac{1}{N-p-1} \sum_{t=1}^N [x_t - \bar{x}_t(p)]^2 \quad (6.8)$$

where $\bar{x}_t(p)$ denotes the fitted value of x_t obtained by substituting the estimated autoregressive coefficients. Thus, the first term on the right hand side of (6.6) can be thought of as a measure of how well an AR(P) process fits the data and the second term on the right hand side

of (6.6) is a penalty function for the $p+1$ parameters that needs to be estimated. The results of the criterion testing for models AR(1) to AR(5) are calculated and the results presented in Table VI.2 together with the parameter estimates for each model.

There are other test selection rules available such as Akaike's information criterion (AIC). However, the BIC procedure is more parsimonious and would select as low order a model as possible. As we can see, for the north central Pacific, a first order autoregressive model gives the best fit. For the eastern tropical Pacific, a second order proved to give the best fit.

TABLE VI.2 Autoregressive Model Identification

Baysian Information Criterion

North Central Pacific(30°N/165°W)			Eastern Tropical Pacific(5°S/80°W)		
Model Order	Parameter Estimates	BIC	Model Order	Parameter Estimates	BIC
1	.67	1339.0*	1	.64	1725.7
2	.644,.038	1342.0	2	.52,.187	1699.9*
3	.641,0.010,.075	1341.6	3	.517,.178,.017	1700.9
4	.639,-0.01, .055,.031	1343.7	4	.517,.178, .017,-.001	1702.3
5	.637,-.014,.056 -.010,.064	1343.8	5	.517,.177,.008 .028,.052	1703.2

*Minimum

As an additional check, the order of autoregressive models can be obtained from looking at the residuals from the selected order. The residuals are plotted in Figure 6.18. The autocorrelation function of the residuals from a first order fit and a second order fit for both NCP and ETP are calculated to see if additional information can be gained. The results are presented in Figure 6.19. For NCP, the residual for a first order and a second order fit are similar and close to the autocorrelation of a white noise process. For ETP, the residual from a

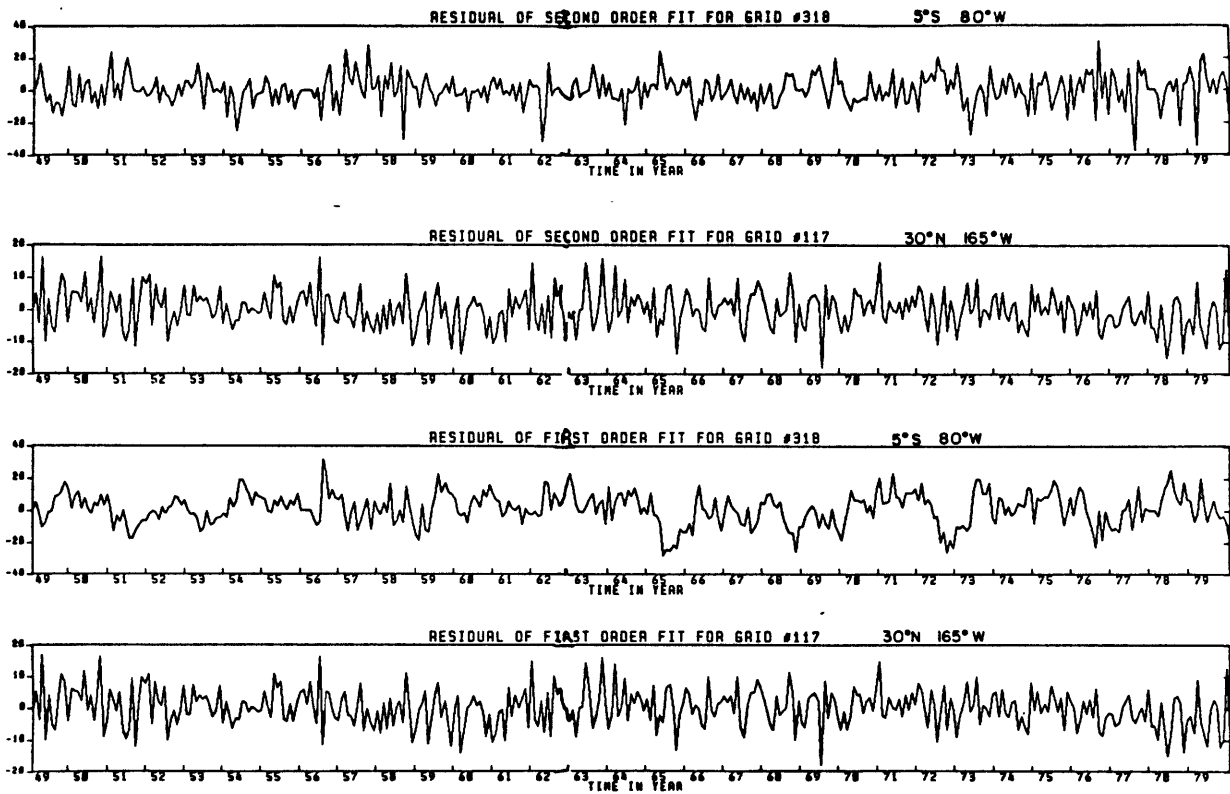


Figure 6.18 Residual plots of the first order and second order fit for eastern tropical Pacific and north central Pacific

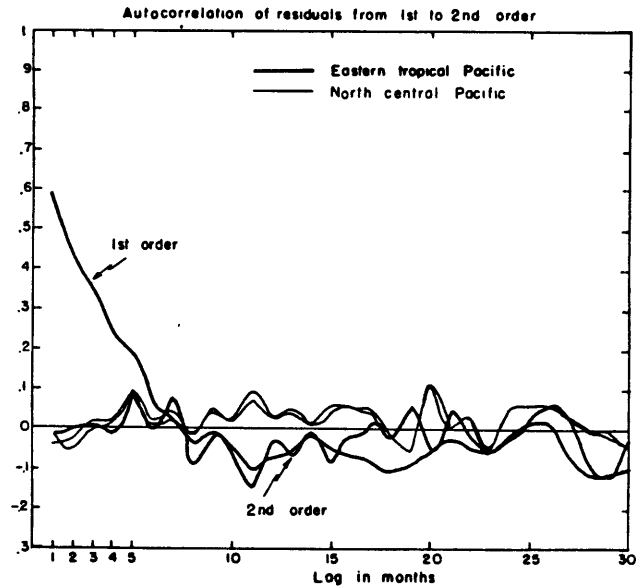


Figure 6.19 Autocorrelation of residual from first and second order fit for eastern tropical Pacific and north central Pacific

first order fit clearly shows a non-white noise behavior, suggesting a higher order fit is desirable. When a second order model is applied, the residuals show a behavior much more similar to that of a white noise series.

VI.2b Discussion

Having identified the order of the autoregressive model for SST fluctuations at two key regions in the Pacific, we might want to ask ourselves what kind of physical mechanisms are operating to give us the results we observed. In this section, we investigate the possibility of some physical parameters as candidates for the parameters in the statistical models proposed in the previous section.

The autoregressive equation of any given order is the finite difference form of a differential equation of the same order. For a

first order autoregressive model, we have the equivalent differential equation of the form:

$$\frac{dX}{dt} + AX = Y \quad (6.9)$$

where Y is a white noise forcing function. If Y is not a white noise but instead is forced by another white noise, Z, then we have

$$\frac{dY}{dt} + BY = Z \quad (6.10)$$

substituting (6.7) into (6.8), we have

$$\frac{d^2X}{dt} + (A+B)\frac{dX}{dt} + AB \cdot X = Z \quad (6.11)$$

which is the equivalent of a second order autoregressive equation.

Frankingoul (1978) has shown that the observed SST anomaly in the North Pacific can be explained using a first order model forced by the anomalous net heat flux, the heat flux being a white noise process (i.e. Y). In the eastern tropical Pacific, the process is more complex. We showed in the previous section that it is a second order model rather than a simple first order. It would probably be modeled better by equation (6.11) rather than (6.7). The forcing function Y, be it the wind or another parameter, should be a parameter that is in turn forced by another white noise process. The zonal wind anomaly and the anomaly of net heat fluxes can be considered as possible candidates for the forcing functions Y and Z. Figure 6.20 gives a plot of the zonal wind and net heat flux anomalies at these two regions. The zonal wind

anomaly at NCP show a higher amplitude and frequency fluctuation than those at ETP. The anomalies for the net heat fluxes, however, seems to exhibit similar characteristics in both regions.

Autocorrelation functions for these anomaly time series are calculated to determine whether they are indeed similar to the behavior of a white noise time series. We applied the test suggested by Box and Pierce (1970) in their studies of the residual of ARIMA time series by forming the Q-statistics (see Eq. 6.2). The statistic Q is approximately distributed as a χ^2 variate with k degree of freedom. Applying a χ^2 test to the autocorrelation functions of zonal wind anomalies and the net heat flux anomalies, we found that zonal wind anomalies at both regions is a random noise time series at 99% confidence level. The same

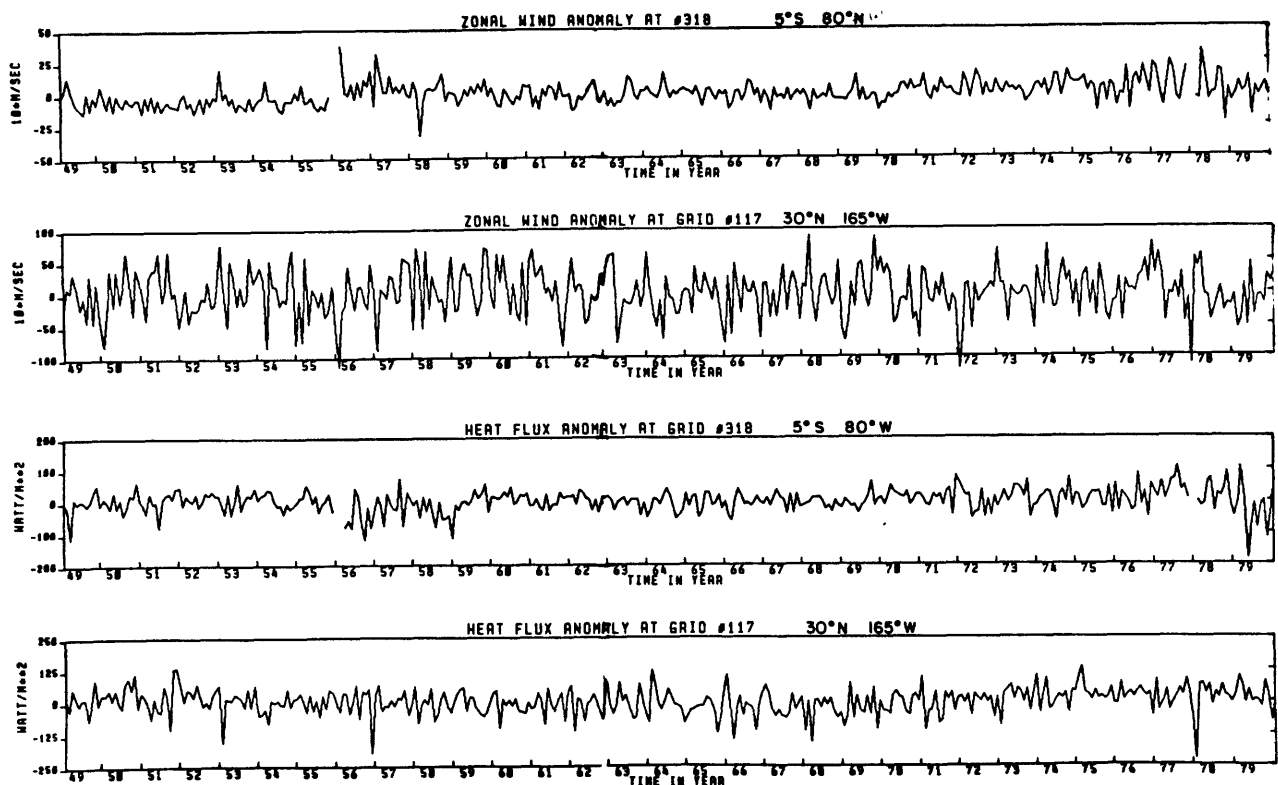


Figure 6.20 Time series plots of the net heat flux anomaly and zonal wind anomaly at eastern tropical Pacific and north central Pacific

is true for the heat flux anomaly in NCP. The heat flux anomaly at ETP however, shows non-random behavior according to the Q-statistic test and resembles a first order autoregressive process.

In summary, the above results show that the SST anomaly in ETP is the result of a more complex dynamic than that in NCP. While the latter can be explained fairly well by a first order model forced by a random noise time series, SST anomalies in ETP would require one order higher model to explain its fluctuations. For SST anomalies in the north central region in the Pacific, a simple first order model forced by the zonal wind anomalies would be sufficient to explain its variations. For the eastern tropical Pacific, a possible scenario to explain its SST fluctuations may be in the form of equation 6.11. Since the net heat flux anomaly in ETP has more structure to it than a simple random noise

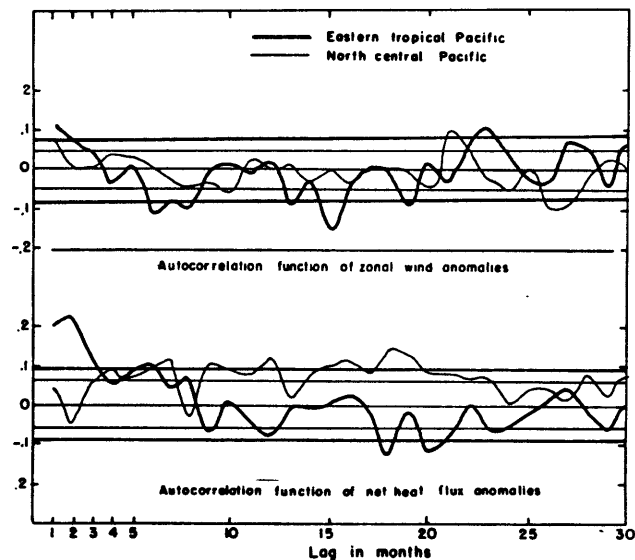


Figure 6.21 Autocorrelation function of zonal wind anomalies and net heat flux anomalies at eastern tropical Pacific and north central Pacific

series, it might be a possible forcing function for SST (as Y in Eq.6.10). This is in turn forced by the white noise function of the zonal wind at the same area. Of course, the forcing functions could be other parameters that satisfy the required statistical properties rather than the net flux and zonal wind anomalies considered here.

It should be noted that here we are only considering linear models of different orders. Presumably the process that involved the interaction between the atmosphere and the ocean is a highly non-linear process and could be a lot more complex than the model we are proposing here.

VI.3 Empirical Orthogonal Functions of Heat Flux Anomalies

In order to characterize the non-seasonal variations of components of the heat fluxes, we performed an EOF analysis on the anomalies of the net heat flux and two of its major components: the incoming radiation and the latent heat flux.

VI.3a Data and Analysis

The analysis procedure used to calculate the EOF is identical to that used on SST anomalies (see Chapter VI.1a). There were numerous months with missing data in the calculated flux data (especially the net heat flux) due to missing input parameters. Efforts were made to retain the maximum amount of available data and a preliminary run was done using all 1110 grid points in the 31-year data period. Missing values

were replaced by zeros (meaning zero departures from the monthly means). This method of filling in missing data would be justified if there is sufficient signal in the nonseasonal data set so that the variation introduced by the artificial zero anomalies would appear in higher modes of the EOF analysis. Unfortunately, there was so much missing data in the grid points for the first half of our data set (1949-1964) that the principal eigenvectors from this preliminary analysis were merely measures of variations in the number of observations missing. In view of the results from this preliminary analysis, another EOF analysis was made using only data from 1965-1979 period and grid squares with incomplete time series were deleted from the analysis altogether. Although this reduction has eliminated many valuable grid squares in the central tropical Pacific and a good part of Indian Ocean, there are still enough data to give us an approximate picture of what process, if any, dominates the nonseasonal variations in heat flux components.

VI.3b Results and Discussion

As stated in the previous section, EOF analysis was applied to Q_{net} , Q_{in} , and Q_1 . The percentage of total variance explained by the first five components of EOF are listed in Table 6.3 below.

TABLE VI.3. Percentage of Total Variance Explained

Mode	Q_{net}	Q_{in}	Q_1
1	5.0857	3.3115	5.6787
2	2.8830	2.2456	2.7949
3	2.8131	1.9636	2.5008
4	2.2607	1.8550	2.2634
5	2.1624	1.7881	2.0637

To see whether the eigenvalues from the EOF analysis are sufficiently separated from each other, we calculated the sampling error bar associated with the first five eigenvalues for the three EOF analyses. The method used is the same as those described in Chapter VI.1a. The first mode from all three EOF analyses are distinct from the other modes. Beyond the first eigenvalue, the eigenvalues were too close to be clearly separated from each other. The time series and the pattern of the first mode from Q_{net} are shown in Figure 6.22. The same for Q_{in} are shown in Figure 6.23. The time series from Q_1 is shown in Figure 6.22 together with the first time series from Q_{net} .

The time series from the first eigenvector of Q_{net} shows an unmistakable trend in the period 1965-1979. Since the eigenvector pattern shows that most of the ocean has a negative weight, the trend in the time series should therefore be interpreted as being an **upward** trend - that there is more flux available in the latter half of the period. The exact opposite behavior was obtained in the time series of the first eigenvector of latent heat flux anomalies. The pattern itself is not shown here because it is identical to that of the net heat flux. Again,

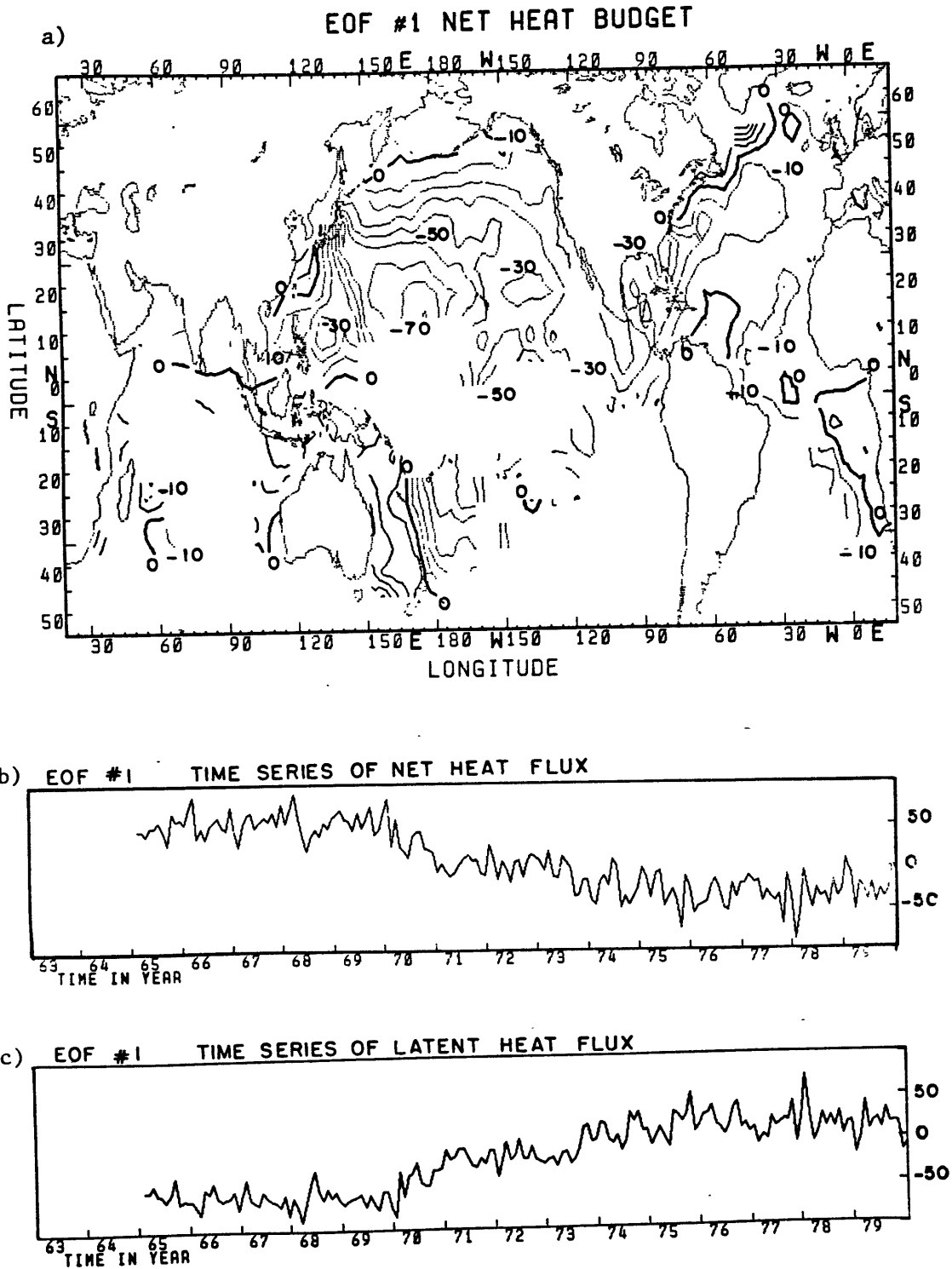
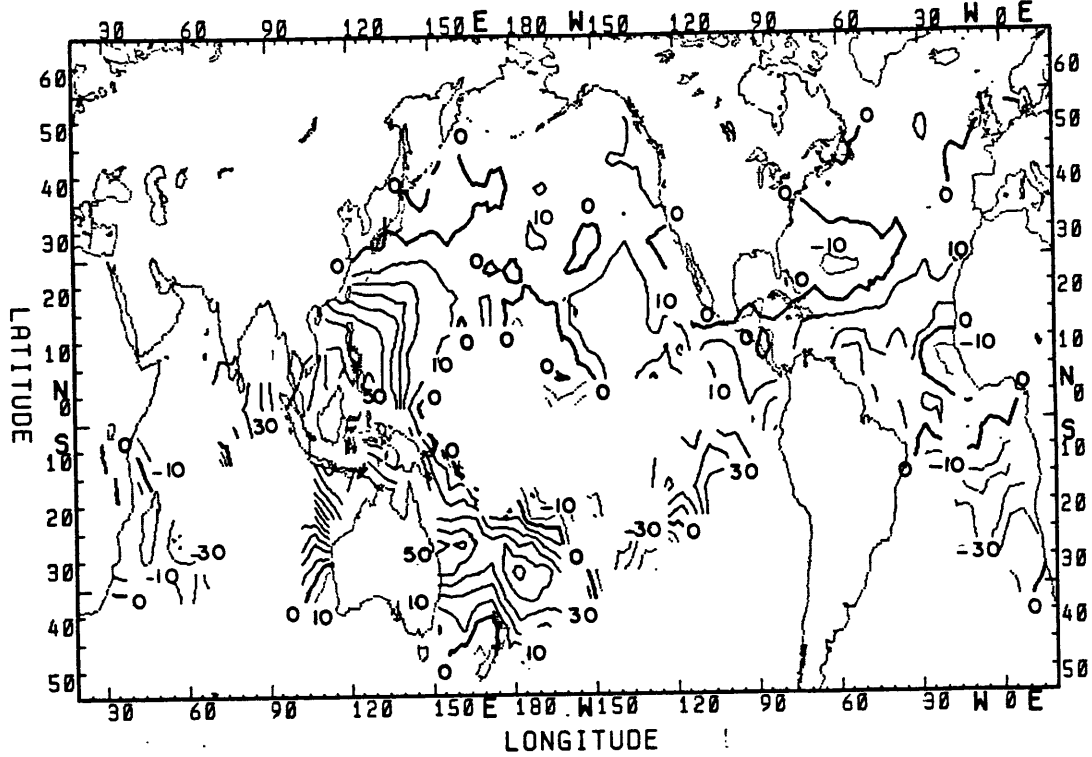


Figure 6.22 a) EOF #1 of net heat flux anomalies
 b) Time series of net heat flux anomalies EOF #1
 c) Time series of latent heat flux anomalies EOF #1

INCOMING RADIATION EOF #1



EOF #1 TIME SERIES

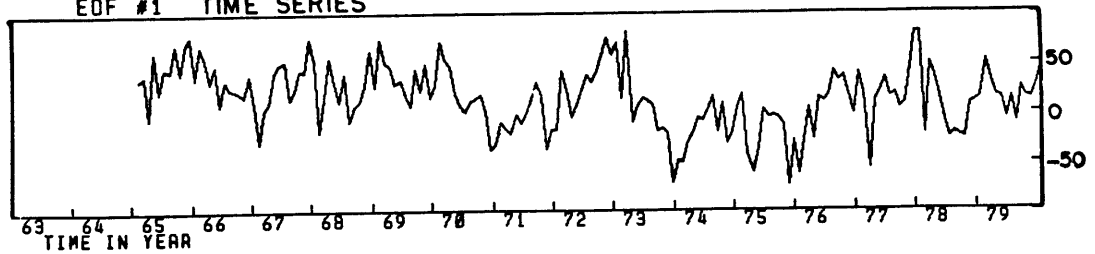


Figure 6.23 EOF #1 of incoming solar radiation anomalies and its associated time series

the negative sign in the pattern of the first eigenvector indicates that there is **more** latent heat loss in the first half of this analysis period than the second half. The identical fluctuations observed in the first eigenvectors of the net heat flux and the latent heat flux shows clearly that the nonseasonal variations in Q_{net} is completely dominated by variations from latent heat flux. Although the other components do contribute to the seasonal variation of the net flux, they play very small parts in modulating the nonseasonal variation.

Recall in our EOF analysis of global SST anomalies from Chapter VI.1a, the second major mode of nonseasonal variation was a cooling trend. The trend for the variations in latent heat revealed in this analysis is also a downward one. The implication here is that the variation in latent heat is controlled by variations in SST: the warmer the water, the more latent heat released to the atmosphere and vice versa.

The result from an EOF analysis of Q_{in} is intriguing. The time series associated with the first eigenvector (Figure 6.23) exhibits a behavior that is very similar to the behavior of the SST El Nino mode. The first EOF pattern in the same figure displays large positive weights in most of the tropical ocean except the central tropical Pacific. The largest values occurred off the coast of China and also in southwestern Pacific. This discovery may help us in understanding the reason why tropical oceans vary together during El Nino events. Here we found the principal mode of nonseasonal variation in incoming radiation is also associated with El Nino, supporting the theory proposed in Chapter VI.1c that cloud cover change is a major factor that ties the variations in tropical oceans together.

VI.4 Relationship between Nonseasonal SST and Other Nonseasonal Parameters

VI.4a Surface Sea and Air Temperatures

The relationship between the sea surface temperature and the surface air temperature (SAT) could give us an idea of how closely the upper ocean and the lower atmosphere are linked together. Here we present the results of relating contemporaneous sea and air temperatures over the global ocean. The results are based on the monthly anomalies from the long term monthly means.

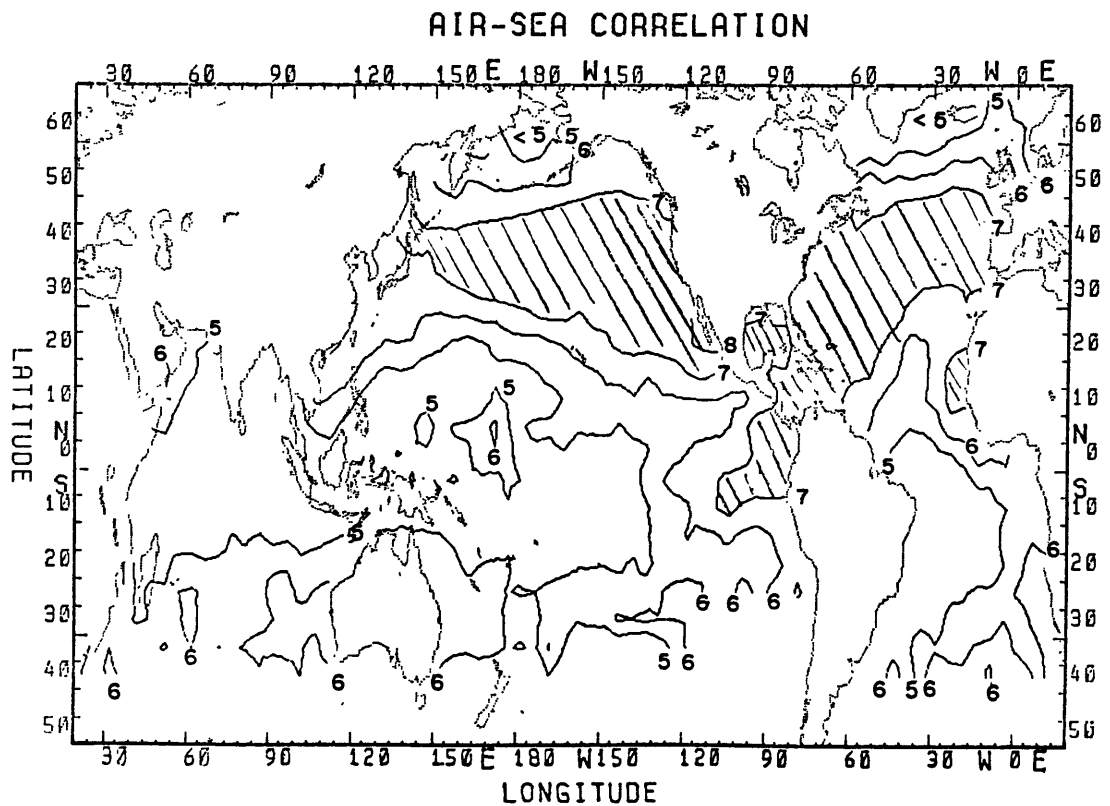


Figure 6.24 Global map of correlation coefficients between air temperature and sea temperature

There are substantial spatial variations in the relationship between sea and air temperature. Figure 6.24 shows a spatial distribution of the correlation coefficients between air and sea temperature variations. The correlations are generally very high (only a small part of the ocean has values below .5). Figure 6.25 illustrates their relationship through scattergrams of four selected squares with different correlation coefficients ranging from .22 to .8. For some areas, the relationship is a very well defined straight line the scatter is more or less random. The seasonal variation of this

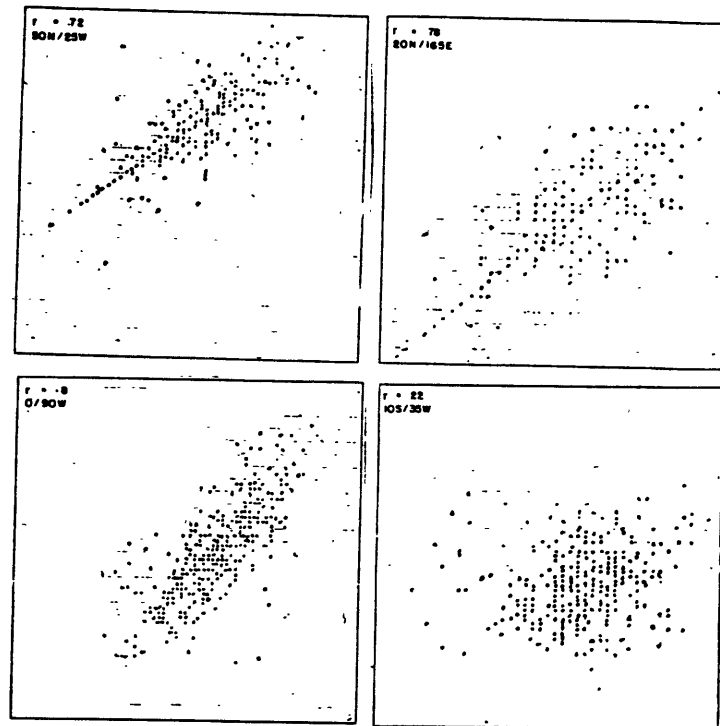


Figure 6.25 Scattergrams of surface air temperature vs. surface sea temperature at four selected grid squares

relationship (not shown) reveals that the correlation is highest in the summer season. This may be from the fact that other processes in winter (stronger advection, for example) may have hampered the thermal communication in the winter while the relatively quiet summer months allow more thermal communication between the upper ocean and lower atmosphere.

One special feature worth noting in Figure 6.24 is that in the Pacific the coefficients increase from west to east while in the Atlantic they decrease from west to east. One would expect the western boundaries of the ocean basins to behave the same way. Cayan (1980) observed the same pattern in a similar analysis for the North Pacific and North Atlantic. He claims that this difference might arise from different processing procedures done on the Atlantic and Pacific data. Since our data processing procedure is identical for all oceans, the above argument cannot be invoked to explain the difference. The autocorrelation study on the persistence of SST shows a map of the autocorrelation at lag=1 (see Figure 6.17). A surprising similarity is found between the areas with high autocorrelation coefficients and areas with high correlation coefficients between SST and SAT. It seems plausible that regions where SST anomalies have a larger time scale (large persistence) would have more 'time' to communicate with (or influence) the air above, therefore higher correlations are observed in regions with high persistence. One other feature worth noting is that in the eastern tropical upwelling regions of both the Pacific and the Atlantic, high correlation coefficients are also observed. Again, these

regions also show high autocorrelation of SST at lag=1. However, as was shown in the previous section, the statistical nature of the nonseasonal SST between the northern ocean and the eastern tropical ocean is very different despite the fact that both areas possess high autocorrelation at lag equal to 1. The results here seem to indicate that the strength of the correlation between air and sea temperatures is related only to the correlation between consecutive SST anomalies (i.e. the degree of persistence) regardless of other characteristics of the SST time series.

VI.4b Relationship between SST anomalies and Heat flux Anomalies

Anomalies of global SST and anomalies of components of heat fluxes are correlated to see if the observed SST departures from monthly means can be explained by that of the heat fluxes. Maps of the correlation coefficients between anomalies of SST, Q_{net} , Q_1 , Q_{in} , Q_{out} , and Q_h are presented in Figures 6.26 to 6.30. These coefficients are significantly different from 0 at the 95% confidence level if they are larger than .20. This is calculated using a fairly conservative estimate of a time scale of 4 months to reduce the number of degrees of freedom from N to an 'effective' degree of freedom of N/4. (See Davis, 1976)

The most striking result from the correlation map between SST and Q_{net} is that all the significant correlation coefficients are negative. This indicates that larger heat loss to the atmosphere is associated with high SST anomalies. Intuitively one would expect the opposite: that the SST would be lower if more heat is lost to the

atmosphere. The association between ΔQ_{net} and ΔSST is the strongest in the tropical oceans, especially in central Pacific where the highest SST are observed. Minimum correlation occur in the mid-latitudes along 25°N to 45°N.

The correlation map between anomalous latent heat and anomalous SST changes is almost identical to that in the previous Figure 6.26. This suggests that the nonseasonal fluctuation in the net heat flux is dominated by the fluctuation in the latent heat flux, as was evident in Chapter VI.3 through EOF analysis of the flux components. Again, we have high latent heat associated with high SST.

The outgoing radiation flux is a function of SST and the humidity of the air. Therefore it is not surprising to find that the highest correlation between Q_{out} and SST occurs where the SST is the warmest - namely the western and central tropical Pacific. Variations in sensible heat flux are from the wind and the sea-air temperature difference. Areas with strong positive correlations with SST are areas where the variation in SST dominates over the variation in the wind since anomalous wind speed is not significantly correlated with SST. Conversely, areas with low correlation imply that the variation in the wind there dominates over the variation in SST. It is then not surprising to find that the maximum correlation between SST and Q_{h} occur in regions of weaker winds. Nonseasonal variation in the incoming solar radiation is solely from the the variation in cloud cover. The only place with a significant correlation between Q_{in} and SST is located between latitude 20°N and 45°N in the central ocean and the

relationship is a positive one, meaning more cloud is associated with colder SST. There is a strong seasonal variation in the relationship between cloud cover and SST. The correlation coefficient, when calculated separately for each of the four seasons, shows the strongest relationship in the summer (maximum .61) and weakest in winter. This finding is somewhat contrary to expectations based on physical principal. One would expect to see the dependence being stronger in winter when there is more variation in the amount of cloud cover due to higher baroclinic activities. It should be noted that regions with maximum correlation between Q_{in} and SST are also regions where a minimum correlation between latent heat and SST are found.

Lag correlation up to 30 month were also calculated to see if there is a delay in the reponse of anomalous SST to the net surface flux anomalies. For a strip in the center of the subtropical gyre, significant positive correlation is found when the Q_{net} leads SST by one month (coefficients of .28 to .31). This is the same region where there is little or no contemporary relationship between ΔQ_{net} and ΔSST . Elsewhere the negative correlations drop off after the zero lag. This result implies that for a given area, there is a delay of about one month for ΔSST to respond to changes in the surface heat flux.

To further investigate the role of Q in affecting the observed changes in SST, we calculated the finite difference form of the term $\partial T / \partial t$, taking the difference of SST anomalies in month $i+1$ from SST anomalies in month i . This field is then correlated with anomalous Q . The results (Figure 6.31) show a highly significant **positive**

correlation with the maximum at the equatorial eastern Pacific between 0 and 10°S and 70°W to 130°W. In the Atlantic ocean, regions of maximum are off the coast of Africa in the tropics. This reveals that changes in surface heat flux affect the **rate** at which the SST anomaly is changing rather than the SST anomaly itself.

Correlation coefficients were also calculated between the wind stress anomalies and SST anomalies to see how advection or upwelling influences the changes in SST. The formulation of the wind stress is described and the results presented in Appendix E. The relationship between the zonal component of the anomalous wind stress and Δ SST found in the tropics is hard to interpret (See Figure 6.32). There is a significant **negative** correlation between the two in the eastern tropical Pacific with a maximum of .44 around 110°W in the equatorial region. Intuitively one would expect that when the wind is more easterly (negative anomaly of τ_x) more upwelling would occur and SST would be colder (negative anomaly of SST), resulting in a positive correlation. A negative relationship indicates that when the wind is stronger, the SST is warmer, a counter-intuitive relationship. However, the above argument is only applicable to regions close to the coast where upwelling is a major factor in controlling the SST variations. A negative coefficient would lead one to argue that a stronger easterly wind stress brings about a larger advection of warm water from the equator through the Coriolis force in the southern hemisphere and therefore resulting in warmer SST. (Of course, the relationship could also work the other way around - that warmer SST brings about a stronger easterly although this is hard to explain physically.)

Significant negative correlation of $\Delta\tau_x$ and ΔSST are also found in the north central oceanic region. This implies that weaker westerlies (negative τ_x) are associated with warmer SST (positive ΔSST) and stronger westerlies associated with colder SST. This could be accomplished through cold water advection: stronger westerlies in the northern hemisphere would advect colder water from the north and make the SST colder. Seasonal variation in the correlation coefficients show that this relationship is strongest in winter - the season when the mean SST gradient is the greatest in mid-latitudes. Results of the same study in the Atlantic ocean supports the above argument. There are significant negative correlations along the path where the mean SST gradient is greatest, indicating that advection is the link between τ_x and ΔSST . In the tropical Atlantic, positive coefficients are found along the coastal squares off Gabon, south of the Gulf of Guinea. Negative correlations are found in the tropical mid-ocean.

When ΔSST is correlated with the anomalous meridional component of the wind stress (τ_y), the only areas with significant correlations are in the eastern tropical oceans and the maximum correlation coefficient obtained is .44 (Figure 6.33). This is found in the equatorial tropical Pacific at 5°S from 100°W to 110°W. A similar relationship is found in the Guinea Basin in the Atlantic Ocean. One would expect the coefficient to be negative in sign right along the coastal regions, since more northward wind would bring about more upwelling (in the southern hemisphere) and hence colder temperature. Advection from higher latitudes would give a negative coefficient in the southern

hemisphere where the significant relationships are found. Further investigations in more detail are needed to explain the results obtained here.

The following points summarize the results obtained in this section:

- On the whole SST in the tropical oceans correlates much better with the heat fluxes than the middle latitude regions. The maximum relationship is found between the latent heat flux and SST. The positive coefficients indicate that warmer SST causes more latent heat to be released to the atmosphere, rather than colder SST resulting from a larger heat loss.

- The only region where there is a significant relationship between the ΔSST and ΔQ_{in} is in the middle latitudes between 30°N and 40°N . The sign of the coefficients indicates that more cloudiness leads to colder SST.

- A significant positive correlation is found between ΔQ_{net} and $\partial\Delta\text{SST}/\partial t$ in the eastern tropical regions. This implies that the net heat loss does affect the rate of change of ΔSST , but only in the tropical regions.

- Negative correlations between ΔSST and $\Delta\tau_x$ are found in two regions: the central mid-latitudes and eastern tropical Pacific indicating that colder temperature are associated with higher westerlies anomalies. This is an effect of cold water advection.

- The only place where significant correlation exists between ΔSST and $\Delta\tau_y$ is again the eastern tropical Pacific. The sign indicates stronger northward wind is associated with warmer temperature.

Note that the two key regions found in our EOF #1 of nonseasonal SST (Chapter VI.1) seem to be the regions where most of the significant correlations are found. This would imply that these are two areas with the strongest non-random signal and their SST variations are more readily explained with the given data we have while the dynamics associated with other parts of the ocean are more complex (or more random in nature) and needs further information to explain the observed variations.

Weare (1983) in a recent study analyzed the interannual variation in net heating at the surface of the tropical Pacific Ocean. In general, his results agree with ours. He found anomalously high heating to be associated with colder water in the tropical region. He also concentrated the analysis on composited El Nino periods and found the greater than average heating of the ocean occurred prior to periods of El Nino through the correlation of $\partial\Delta\text{SST}/\partial t$ with ΔQ_{net} . No literature is found on the nonseasonal relationship between SST and heat fluxes for other parts of the ocean.

It should be pointed out that the correlation studies done in this section are based on unsmoothed raw time series using all available months. It is not clear whether similar results would be obtained if we concentrated only on time periods associated with one particular

phenomenon such as El Nino. Spatial averaging with a given area and the application of a low-pass filter to remove the high frequency noise may give different results. Nevertheless, this is intended as a preliminary study to guide further research in the area of nonseasonal SST fluctuations, therefore no preselected space or time averages are used. The results, although crude, do give us an indication as to how Δ SST behaves in relation to the parameters studied.

SEA-NET HEAT BALANCE CORRELATION

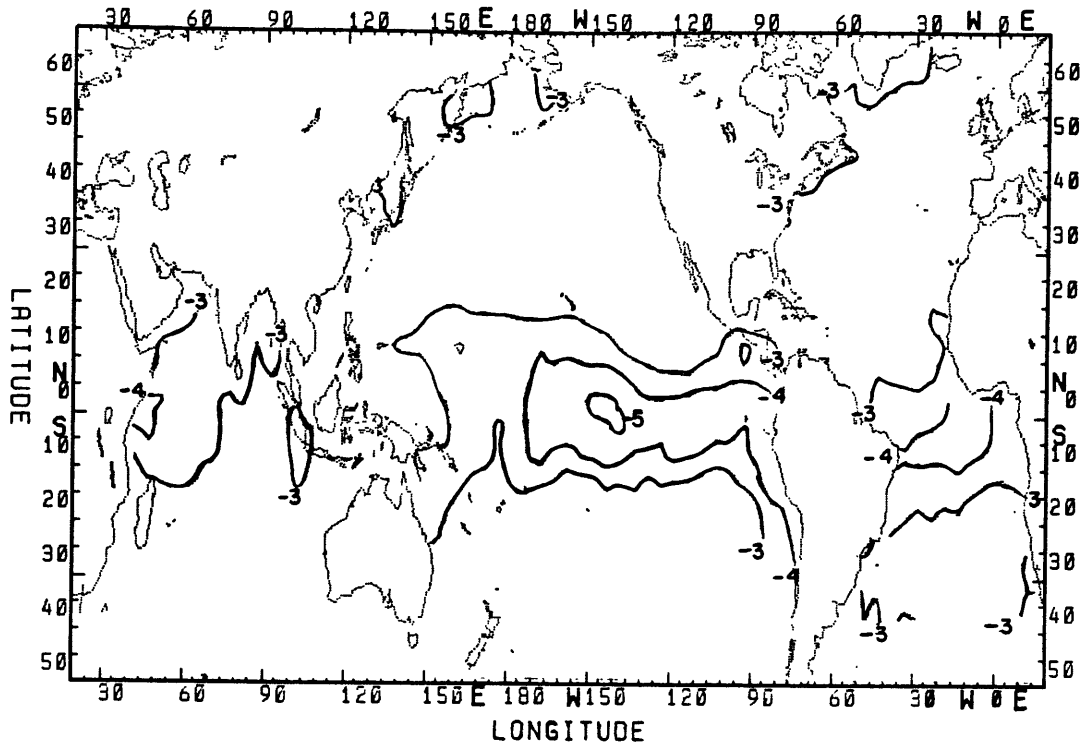


Figure 6.26 Correlation coefficients between anomalies of SST and net heat flux

SEA-INCOMING RADIATION CORRELATION

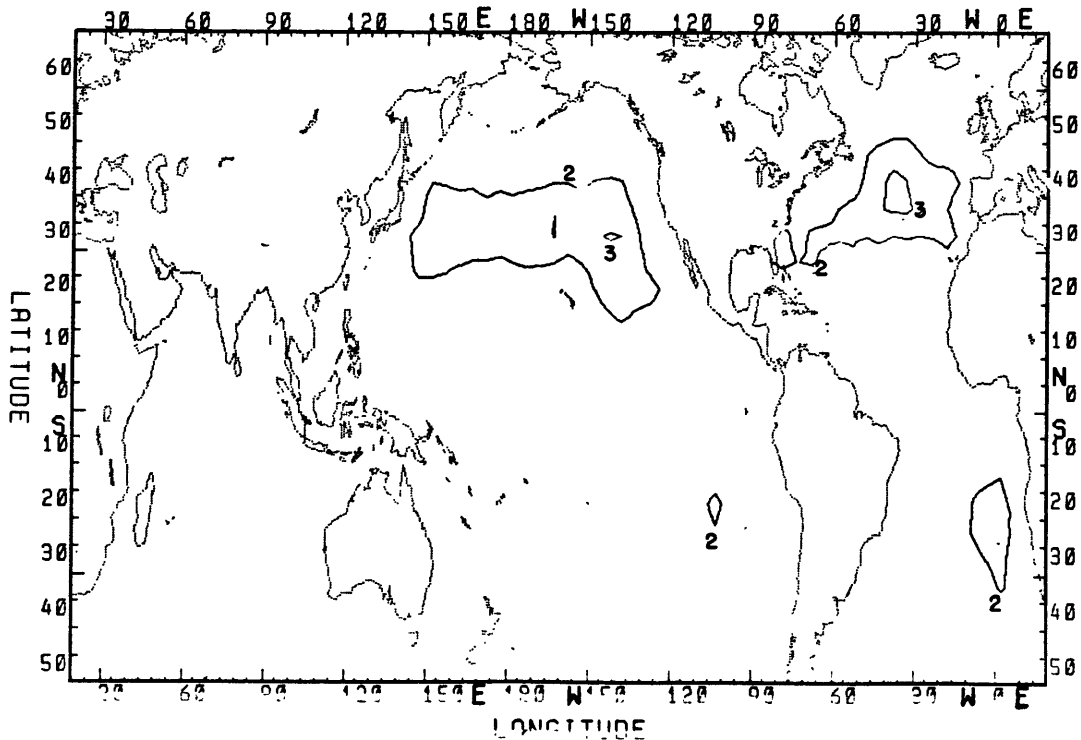


Figure 6.27 Correlation coefficients between anomalies of SST and incoming solar radiation

SEA-LATENT HEAT CORRELATION

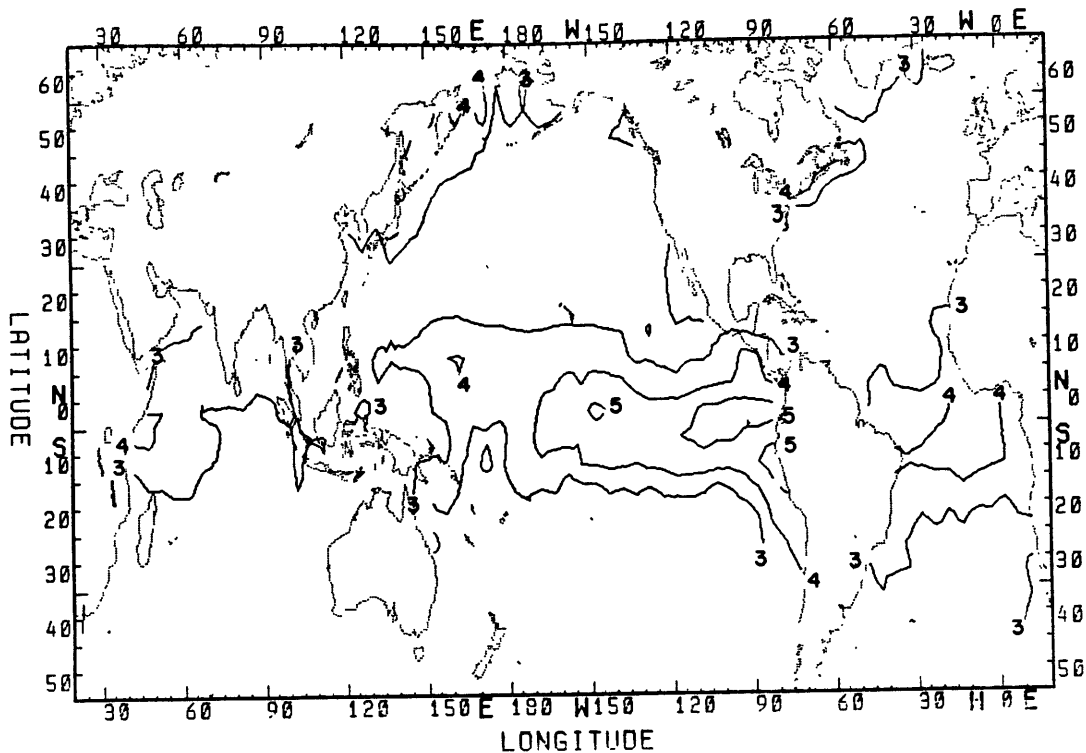


Figure 6.28 Correlation coefficients between anomalies of SST and latent heat flux

SEA-SENSIBLE HEAT CORRELATION

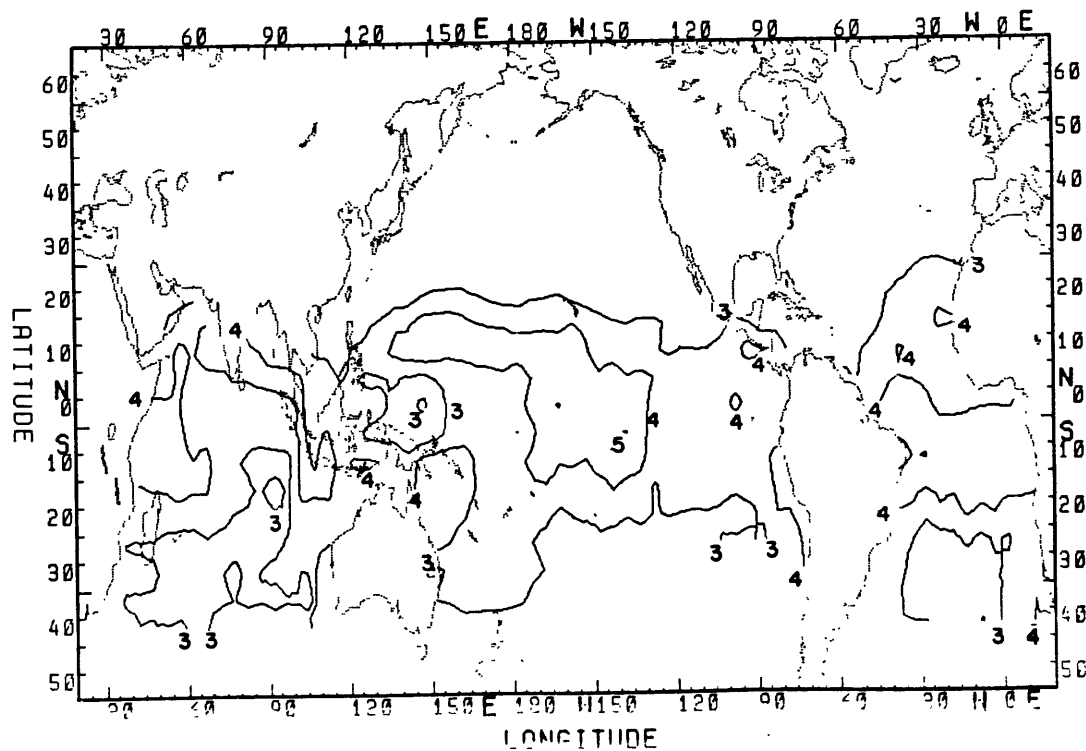


Figure 6.29 Correlation coefficients between anomalies of SST and sensible heat flux

SEA-OUTGOING RADIATION CORRELATION

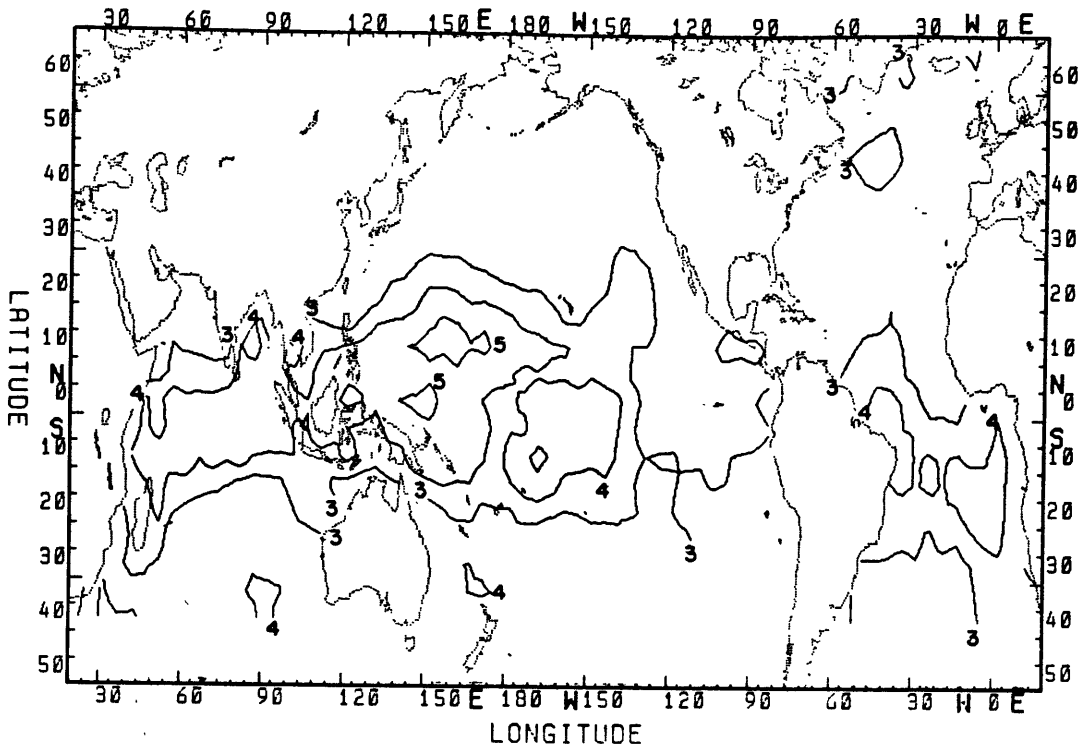


Figure 6.30 Correlation coefficients between anomalies of SST and outgoing radiation flux

Correlation bet. Q_{net} and dT/dt

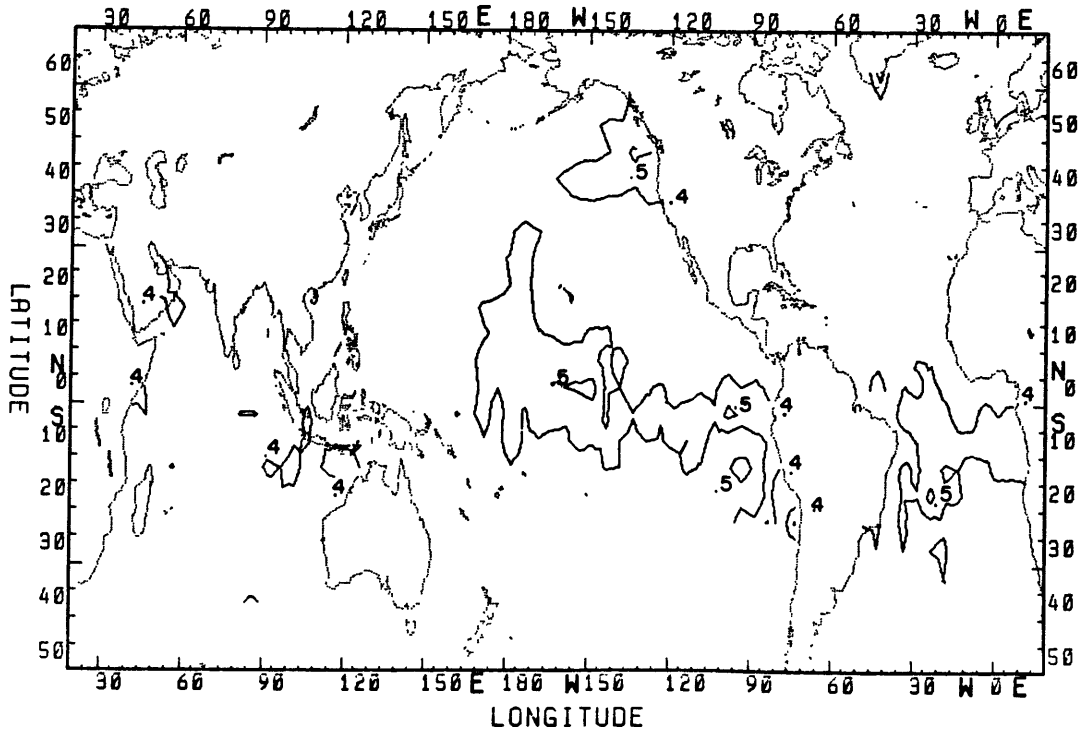


Figure 6.31 Correlation coefficients between anomalies of net heat flux and dT/dt

CORRELATION BETWEEN SST AND τ_x

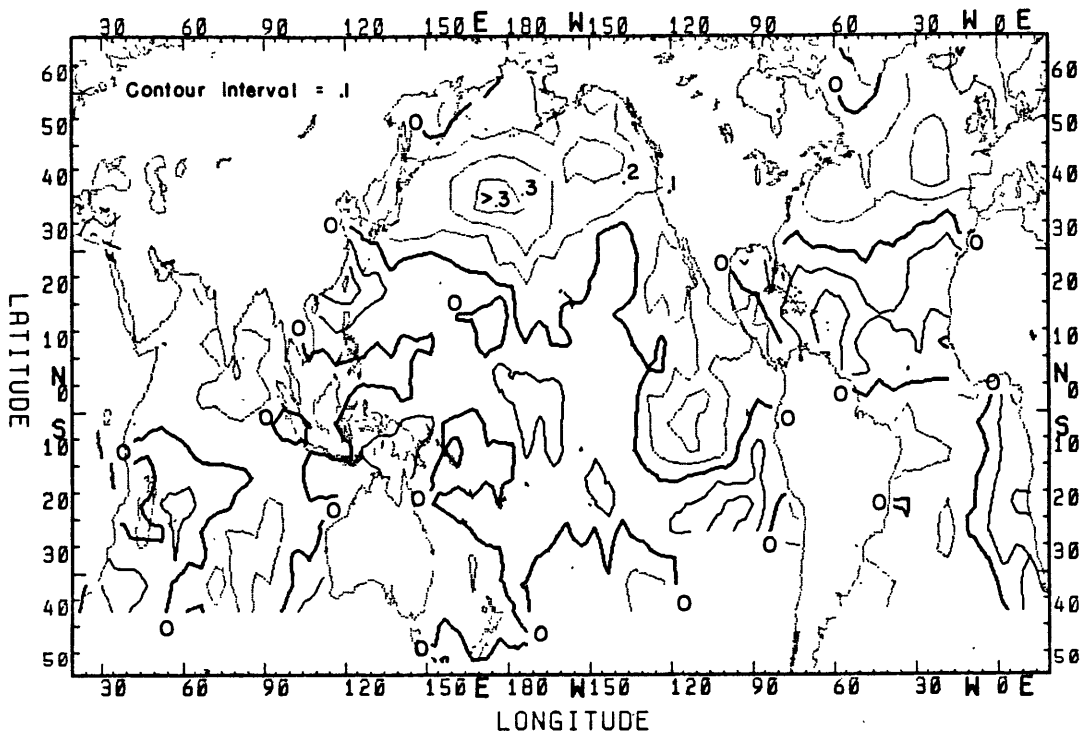


Figure 6.32 Correlation coefficients between anomalies of SST and zonal wind stress

CORRELATION BET. SST AND τ_y

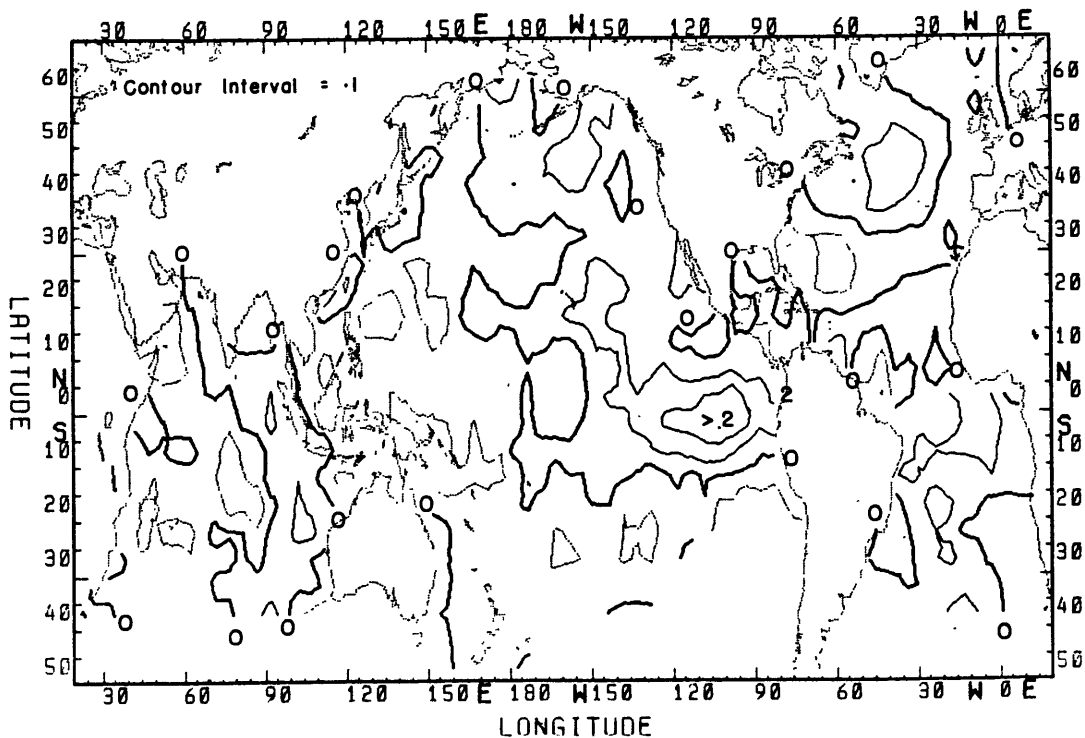


Figure 6.33 Correlation coefficients between anomalies of SST and meridional wind stress

CHAPTER VII. SUMMARY AND CONCLUSION

A newly available 31-year consolidated data set that spans from January, 1949 to December, 1979 was used to investigate the observed fluctuations of global sea surface temperature. In particular, the energy flux at the interface between the ocean and the atmosphere was calculated using surface observations from the data set. The purpose of this thesis is two fold: first of all, we would like to have a complete documentation of the global seasonal-nonseasonal variation of the sea surface temperature and the components of the surface heat flux. Secondly, we wanted to see what role the oceans play in maintaining the climate of the earth by calculating the meridional transport of heat by the oceans.

Specific conclusions and salient features from the calculations are summarized as follows:

- 1) The heat balance at the global ocean surface is calculated using bulk formulas. Of the four components that make up the net heat balance, the incoming solar radiation and the latent heat flux are the largest contributors. There is a large latitudinal variation in the incoming solar radiation with a maximum of 220 watt/m^2 near the equator and a minimum of 80 watt/m^2 at 60°N in the annual mean. The annual mean latent heat flux is more evenly distributed spatially with a maximum of 180 watt/m^2 in the Gulf Stream and a minimum of 40 watt/m^2 in the southern oceans. The sensible heat flux is about one quarter of the

latent heat flux in magnitude and the outgoing radiation is around a half to a third of the latent heat flux.

2) In the annual mean there is a net loss of heat in regions of the western boundary currents (up to 140 watt/m^2 in the Gulf Stream). The upwelling regions in both the Atlantic and the Pacific have the maximum heat gain with approximately 100 watt/m^2 found at eastern tropical Pacific. The northern Indian Ocean also has a substantial heat gain.

3) Ocean transport of heat in the meridional direction is estimated using annual mean net heat flux calculated. This is based on the theory that in the long term there must be a balance of surface heat components if no long term changes are observed. A northward transport is found at all latitudes in the Atlantic with a maximum of 1.0×10^{15} watts at 30°N . In the Indian Ocean, the transport is southward at all latitudes with a maximum of 1.5×10^{15} watt at 20°S . The Pacific transports heat northwards north of 10°S with a maximum of 1.0×10^{15} watt at 10°N . There is a small southward transport between 25°S and 10°S in the Pacific. The transport becomes northward again in the extreme southern Pacific Ocean. The transport at the southern Pacific Ocean is most uncertain due to the sparse data available in that region. When all three oceans are taken as a whole, there is a northward transport north of 15°S and a southward transport south of 15°S . The maximum northward transport is 1.6×10^{15} watt at 25°N and the maximum southward transport is 1.5×10^{15} watt at 15°S . The reader should be reminded here that the uncertainty associated with these estimates can be fairly large.

4) The annual mean heat flux difference between periods 1965-1979 and 1949-1964 was calculated. Significant differences were found for the Indian ocean where there was considerably greater latent heat loss in the 1965-1979 period than in the 1949-1964 period. There might be a possible link between this observed extra loss of heat in the Indian Ocean and the cooling of the north Pacific and north Atlantic. This link could be accomplished through less available heat transport southward in the Indian ocean and thus less available heat to be transported into the Northern Hemisphere of the Atlantic and Pacific oceans. To say anything more specific concerning the nature of the difference in heat transport, one would need transport values for these two separated periods. Unfortunately, 15 years may not be sufficiently long enough a period to calculate the specific transport values under the assumptions made using the surface energy balance method.

5) Global nonseasonal variation in SST is characterized through an analysis of empirical orthogonal functions. The first global mode is very similar to the El Nino mode found for the Pacific Ocean alone. This mode consist of an oscillation between the warm eastern tropical Pacific and the cold north central Pacific. Other areas of the global ocean have little or no correlation with this mode. The tropical regions in the Atlantic Ocean and the Indian Ocean are the only areas that vary concomitantly with the tropical region in the eastern Pacific. The North Atlantic seems to be completely detached from this mode. Physical mechanisms that connect this oscillation between remote

regions in the north central and eastern tropical regions in the Pacific Ocean are examined. One possible explanation is that the warm tropical ocean induces a stronger Hadley cell and this in turn strengthens the westerlies. This would bring about more cloudiness, and therefore cooling of sea surface temperature in the mid-latitudes.

6) The second mode of the global nonseasonal SST EOF analysis indicates a cooling trend in the north Pacific and in the north Atlantic. This cooling is especially evident in the northern branch of the subtropical gyres in both oceans. The cooling is more pronounced in the second half of the data period (1965-1979). The reason for this cooling is puzzling. The onset of the cooling in 1964 suggest that it may be related to the Mount Agung eruption in 1963. However, it is hard to verify this theory from one incident. If there indeed is a relationship between the two, further examination of volcano related cooling needs to be updated with the recent El Chichon explosion in 1982.

7) Nonseasonal SST fluctuations at two key regions, the eastern tropical and north central Pacific depicted in the global EOF analysis, are investigated in further detail through autoregressive modeling approach. It is found that the SST anomaly in the eastern tropical Pacific exhibits a more complex character than that in the north central Pacific. A simple first order autoregressive model (a Markov process) is sufficient for the north central region while a higher order (second

order) is more desirable for the SST fluctuations in the eastern tropical region.

8) EOF analysis were also performed on the nonseasonal net heat flux and two of its major components: the incoming solar radiation and the latent heat flux. Limited area and time were used for this EOF analysis due to excessive missing values in certain areas of the oceans. It is found that the nonseasonal net heat flux variation is almost identical to that of the latent heat flux. The only significant mode for both the net heat flux and latent heat flux anomalies is the first mode which explains about 5% of the total variance. The time series associated with the first EOF mode of the net heat flux indicates a significant upward trend. This means that less latent heat was lost to the atmosphere in the second period due to the cooler SST observed. The first mode of the incoming solar radiation has a time series that resembles the time series of the El Nino mode. This may be an indication of the proposed relationship between the cloudiness change and the El Nino pattern observed in the first EOF of SST anomalies.

9) Correlation studies were carried out between global SST anomalies and components of the heat flux anomalies. It is found that SST anomalies are positively correlated with net heat flux. This means that a warmer SST is associated with a larger net heat loss and a colder SST with a smaller heat loss. Similar relationships are found between latent heat flux anomalies and SST anomalies (i.e. warmer SST induces

larger latent heat loss). This implies that it is the SST anomalies that determines the amount of heat loss to the atmosphere rather than the net surface heat available determining the SST. The tropical SST anomalies show the best correlation with all components of the heat fluxes except the incoming solar radiation. Here the only region that exhibits a relationship between changes in cloud cover and SST is the north central Pacific.

10) The net heat flux does have an effect on the month to month **change** of SST anomalies. This is evident in the correlation between net flux anomalies and the finite difference form of $\partial(\Delta\text{SST})/\partial t$. Again, this effect is most pronounced in the tropics. The overall results indicate that the SST anomaly determines the anomalous heat loss to the atmosphere mostly through latent heat. This net heat anomaly, in turn, modifies the month to month change of the SST anomaly.

To summarize, we have presented results from two major areas of investigation in this thesis. One is a detailed documentation of the global seasonal and nonseasonal variations of the sea surface temperature and the components of the surface heat fluxes. The other is the calculation of oceanic meridional heat transport for the three oceans individually and combined.

We have not attempted to specify all possible factors that contribute to sea surface temperature fluctuations. The inadequacy of empirical formulas, the lack of current data to account for the

advective effects and a lack of subsurface data are major factors that make the task extremely difficult, if not impossible. We have shown that nonseasonal sea surface temperature anomalies are related to the heat flux anomalies through preliminary correlation studies. Further more detailed studies would add tremendously to our understanding of sea surface temperature fluctuations: variations of SST on a smaller scale both in time and in space; relationships between parameters for specific events and periods are just two the possible areas that need to be investigated.

Our estimates of the oceanic meridional heat transport use the most complete coverage of global heat flux data. However, the transport estimates using the surface balance method do not permit us to estimate the interannual variations of the heat transport. Heat storage in the subsurface layer would be needed on an interannual variations basis. A knowledge of this subsurface variability would help us a great deal in describing factors that control SST changes. We should mention as a last note that although there are many parameters we cannot calculate due to the limitation of our data set, there are still a great many more studies one can perform using this data set. The complete coverage both in space and time, and the surface parameters available makes this data set a tremendous research aid in realizing the long term goal of climate forecasting.

APPENDIX A. LIST OF PARAMETERS AVAILABLE ON THE DATA SET

For reference, Table A.1 lists the parameters available on each of the marine observations in the Consolidated Data Set. In this thesis, nine meteorological parameters are extracted from the list for the necessary calculations. They are: sea-level pressure, sea surface temperature, air temperature, wind direction, wind speed, total cloud cover, lower cloud cover, dew point temperature, and wet bulb temperature.

Figure A.1

FNWC MARINE CONSOLIDATED DATA SUBSET
PARAMETER SUMMARY

PARAM	PARAM NAME	CODE	BITS(WD)	TOTAL BITS	REMARKS
1	SOURCE		59 (1)	1	0=TOF-11; 1=FNWC SPOT
2	LATITUDE	LAT	58-48 (1)	11	+/- 90 TO NEAREST TENTH; SOUTH IS COMP
3	LONGITUDE	LONG	47-36 (1)	12	+/- 180 TO NEAREST TENTH; WEST IS COMP
4	CLASSIFICATION	C	35-34 (1)	2	
5	SHIP DIR	KDS	33-30 (1)	4	REF (1), P. 11
6	SHIP VELOCITY	KVS	29-26 (1)	4	KNOTS/5
7	PRESSURE	KPS	25-15 (1)	11	TOF-11 P*10-9000; SPOT MODULO 100
8	AIR TEMP	KRY	14-4 (1)	11	RANGE: -60 TO 55 DEG C*10
9	SEA TEMP	KSA	59-54 (1)	4	RANGE: -8 TO 50 DEG C*10
10	SEA TEMP	KSA	3-0 (2)	* 6	SAME AS ABOVE
11	DEEP POINT TEMP	KDP	53-47 (2)	7	RANGE: -60 TO 40 DEG C
12	PRESSURE CHANGE	KAP	46-37 (2)	10	REF (1), P. 12
13	INDICATOR	IND	36-35 (2)	2	*10, ADD TO PP ONLY
14	WAVE PERIOD	LPN	34-30 (2)	5	REF (1), P. 10, WHOLE METERS
15	WAVE HEIGHT	LHN	29-24 (2)	6	RANGE: 0 TO 63, HALF METERS
16	SWELL PERIOD	KPN	23-20 (2)	4	REF (1), P. 10, WHOLE METERS
17	SWELL HEIGHT	KHN	19-14 (2)	6	RANGE: 0 TO 63, HALF METERS
18	SWELL DIRECTION	KDN	13-7 (2)	7	RANGE: 0 TO 73, BT COMPASS, DEG/5
19	WIND DIRECTION	KDJ	6-0 (2)	7	RANGE: 0 TO 73, BT COMPASS, DEG/5
20	WIND SPEED	KDF	59-53 (3)	7	METERS/SECOND
21	CLOUD AMT	N	52-49 (3)	4	REF (1), P. 7
22	PAST WEATHER	MW	48-45 (3)	4	REF (1), P. 6
23	TOTAL CLOUD TYPE	NL	44-41 (3)	4	REF (1), P. 7
24	LO CLOUD TYPE	LC	40-37 (3)	4	REF (1), P. 7
25	MID CLOUD TYPE	MC	36-33 (3)	4	REF (1), P. 8
26	HI CLOUD TYPE	KHC	32-29 (3)	4	REF (1), P. 9
27	CLOUD HEIGHT	LH	28-25 (3)	4	REF (1), P. 8
28	PRESENT WEATHER	LWN	24-18 (3)	7	REF (1), P. 2
29	VISIBILITY	KVV	17-14 (3)	4	REF (1), P. 2
30	ERROR INDICATOR		13 (3)	1	REF (1), P. 2
31	OSV		12 (3)	1	FLAGS ERROR IN REPORT
32	ICE TYPE	ICT	11-9 (3)	3	0-5
33	ICE THICKNESS	ICTH	8-0 (3)	9	REF (1), P. 11
34	ICE THICKNESS	ICTH	59 (4)	* 1	SAME AS ABOVE
35	ICE ACCRETION	KRAL	58-56 (4)	3	0-4
36	SIG CLOUD AMT	KSIGC	55-50 (4)	6	REF (1), P. 12
37	SIG CLOUD TYPE	KSIGT	49-42 (4)	8	REF (1), P. 13
38	SIG CLOUD HEIGHT	KSIGH	41-30 (4)	12	REF (1), P. 13
39	AIR-SEA TEMP DIF	LTS	29-24 (4)	6	WHOLE DEG C
40	YEAR	NYEAR	23-14 (4)	10	1800-1980
41	MONTH	NOV	13-10 (4)	4	01-12
42	DAY	KDAY	9-5 (4)	5	01-31
43	HOUR	JHJR	4-0 (4)	5	00-24
44	SHIP ID	SHIP	59-24 (5)	36	REF (1), P. 13
45	NET BULB		23-0 (5)	24	REF (1), P. 8

REF (1): TOF-11 SURFACE MARINE OBSERVATION-- (REVISED SEPT 1969)
*--PARAMETER CROSSES WORD BOUNDARIES.

APPENDIX B. PROBLEM ASSOCIATED WITH 5° BY 5° GRID SPACE AVERAGING

In this appendix we illustrate the problem associated with taking 5° latitude by 5° longitude averaging for certain regions of the ocean and the method used to correct the problem.

Figure B.1 presents time series plots of the monthly mean number of observations(B.1a), the monthly mean latitudinal position of the observations(B.1b), and the monthly mean longitudinal position(B.1c) at 40°N and 60°W (the square from 40°N to 45°N and from 60°W to 65°W). From the plot of the mean latitudinal position shown in Figure B.1b, one can clearly see the drift of the ship's movement within this 5° by 5° square in time. The monthly mean position is fairly constant around 41°N to 42°N from 1949 to 1961. From 1961 on, it started to move northwards and by 1979, the mean position is around 43°N to 44°N. As to the reason for this northward movement of ship tracks, one hypothesis is that with better equipment to handle possible ice conditions in the ocean during the latter period, ships were able to take advantage of the shorter northern route. Ordinarily the mean temperature gradient does not vary much within a 5° by 5° square and variations in ship movement would not have much effect on averaged temperatures. This particular location, however, is right on the track of the path where the Gulf Stream leaves the east coast of North America and bends northwards. Large temperature gradients are observed here. A mean latitude difference of 2 degrees would result in a mean monthly temperature difference up to 6° C. Figure B.2 illustrates the monthly

mean SST anomalies obtained from three different averaging methods. Figure B.2c is the anomaly calculated using long term monthly means from 5° by 5° square monthly values. There is a marked trend in this time series, corresponding closely to the time series in Figure B.1b. What we are interested in knowing is how much of this trend is real and how much of it is an artificial result of the ship's northward movement? Figure B.2a is the average of 25 1° by 1° subsquares (within this 5° by 5° square) time series of SST anomalies with respect to 1° by 1° long term monthly means. This can be considered the 'true' anomaly time series for the 5° by 5° square. Figure B.2b is the anomaly obtained by taking the 5° by 5° SST time series and subtracting the respective 1° by 1° long term monthly means according to the mean monthly latitudinal position for any given month. This was intended as a quick correction to compensate for the latitudinal movement of the ship's position. It could be calculated much faster than calculating 25 1° by 1° averages of SST time series. However, the result from this shortcut does not seem to be a true indication of the average anomalous condition for the square. This is probably due to the large standard deviations of the mean latitudinal positions for each month.

Faced with this problem in our data set, we decided to check the mean latitudinal positions for grid squares located in areas with large temperature gradients for significant drifts similar to the one presented. Several more grid square were spotted with the same problem although none of them was as severe as the example illustrated. Either the drift in position was not as significant or the temperature gradient

was not as large. Most of the time, the correction of taking an average of the 25 1° by 1° subsquares merely reduced the amplitudes of the anomaly time series. All together, a total of 16 grid squares were corrected for the Atlantic Ocean and a total of 17 squares were corrected for the Pacific Ocean.

The only other parameter besides SST that was influenced by this drift is air temperature. This is to be expected since variations in air temperature follow closely with that of the sea surface temperature. If we have no reason to suspect the atmospheric temperature gradient to be excessively large in the western boundary region, then this is a good example to verify the thesis that it is the ocean that controls the air temperature directly above it rather than the other way around.

Figure B.1 Time series plots for grid square at 40°N, 60°W

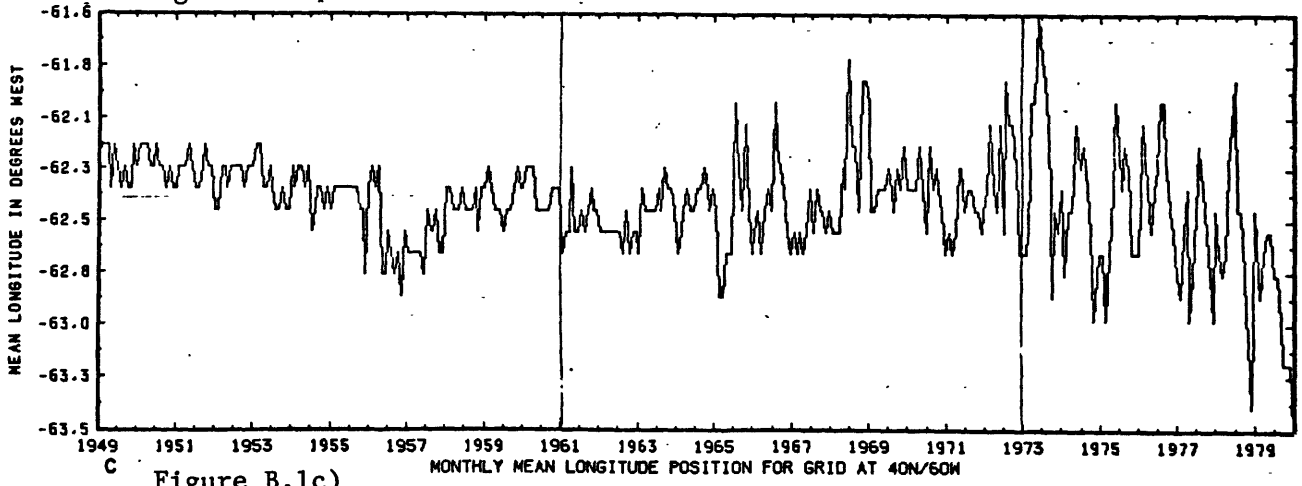
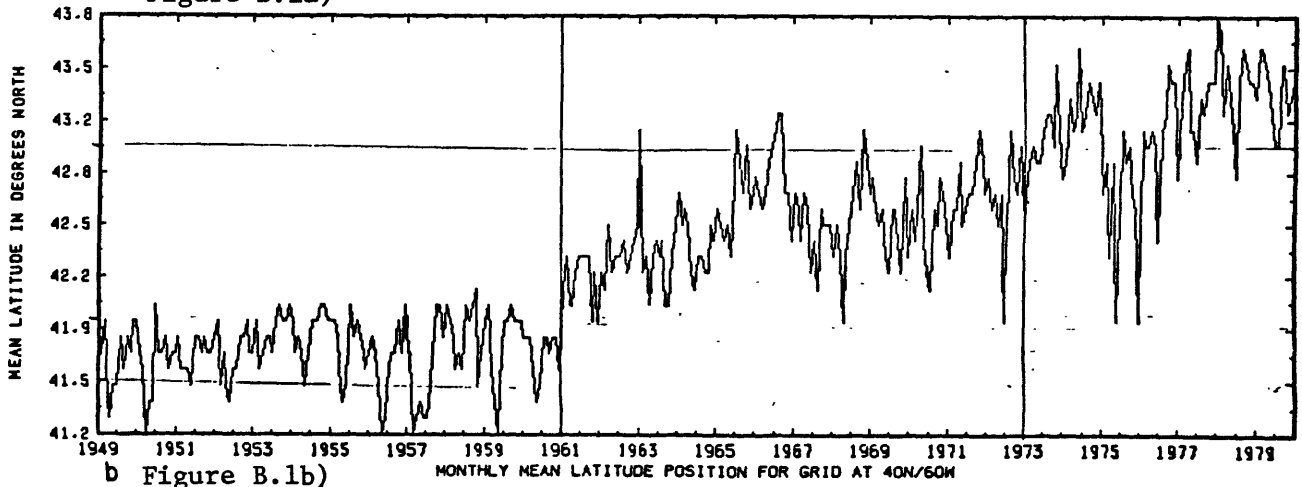
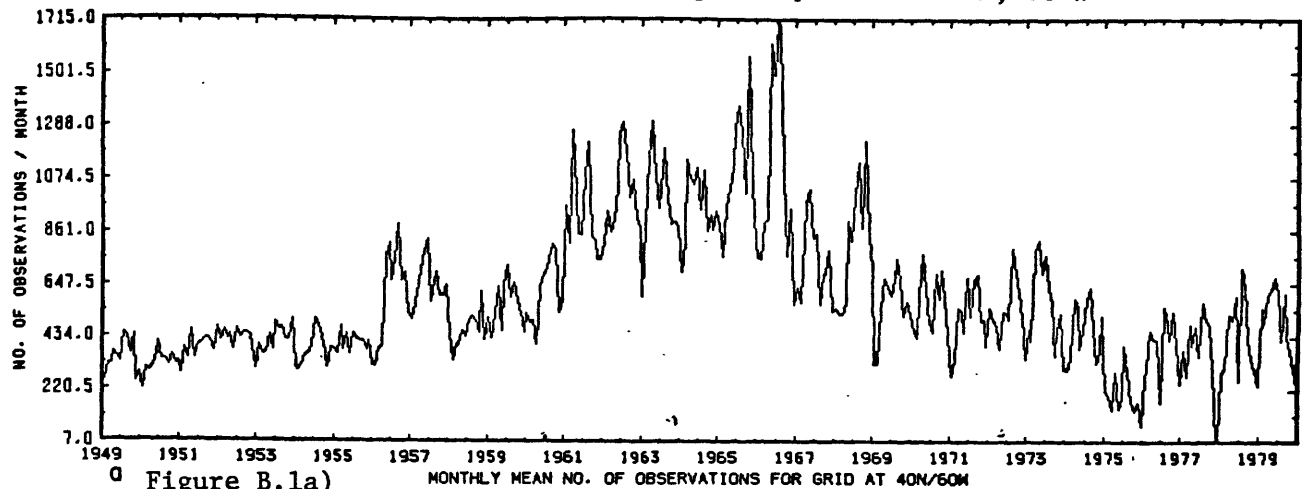
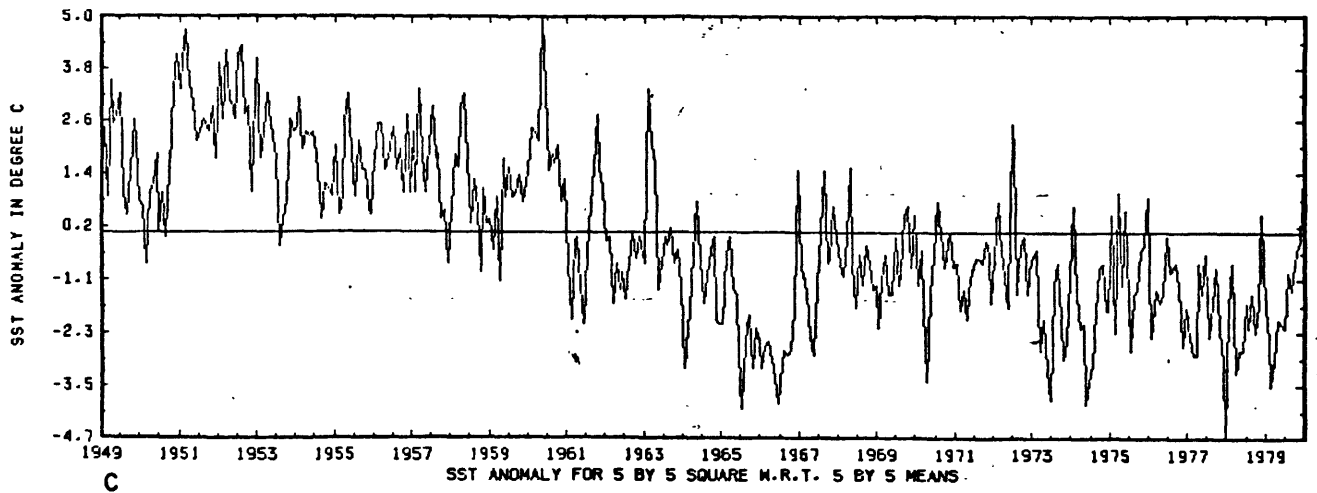
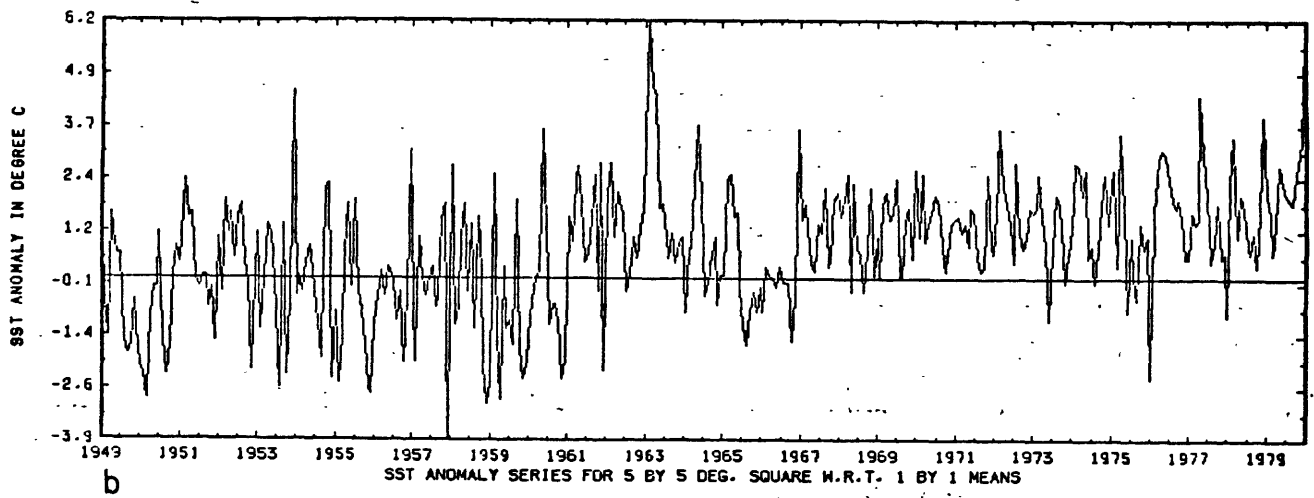
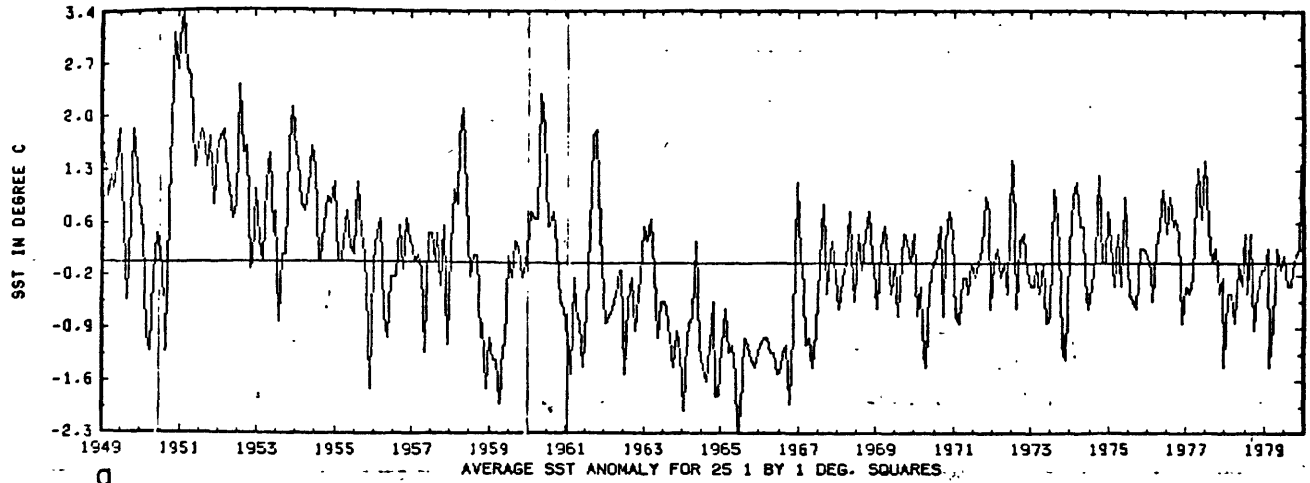


Figure B.2 Time series plots of SST anomalies at 40°N, 60°W



APPENDIX C. LONG TERM MONTHLY MEANS OF RELATED METEOROLOGICAL PARAMETERS

For reference, contour plots of long term monthly means of January, April, July and October are presented in this appendix for the following parameters:

- Wind speed (Figures C1-C4)
- Cloud cover (Figures C5-c8)
- Specific humidity difference (Figures C9-C12)
- Surface wind (Figures C13-C16)
- Air temperature (Figures C17-C20)
- Sea level pressure (Figures C21-C24)

MONTHLY MEAN WIND SPEED MON=1

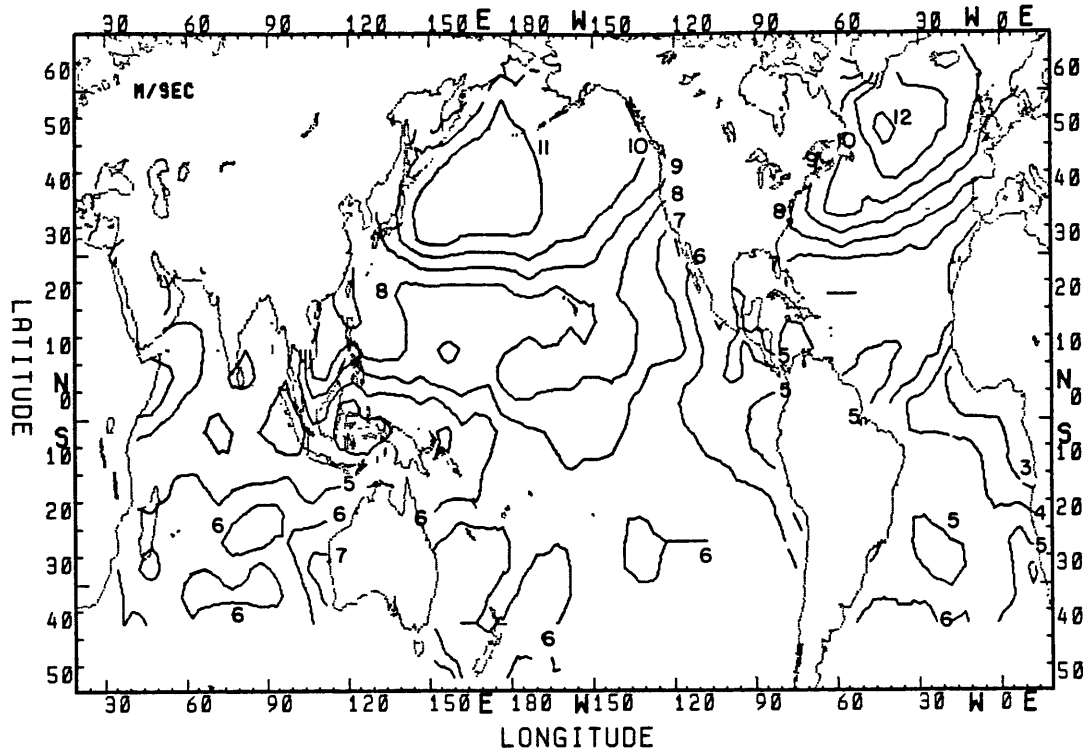


Figure C.1 Long term January means of wind speed

MONTHLY MEAN WIND SPEED MON=4

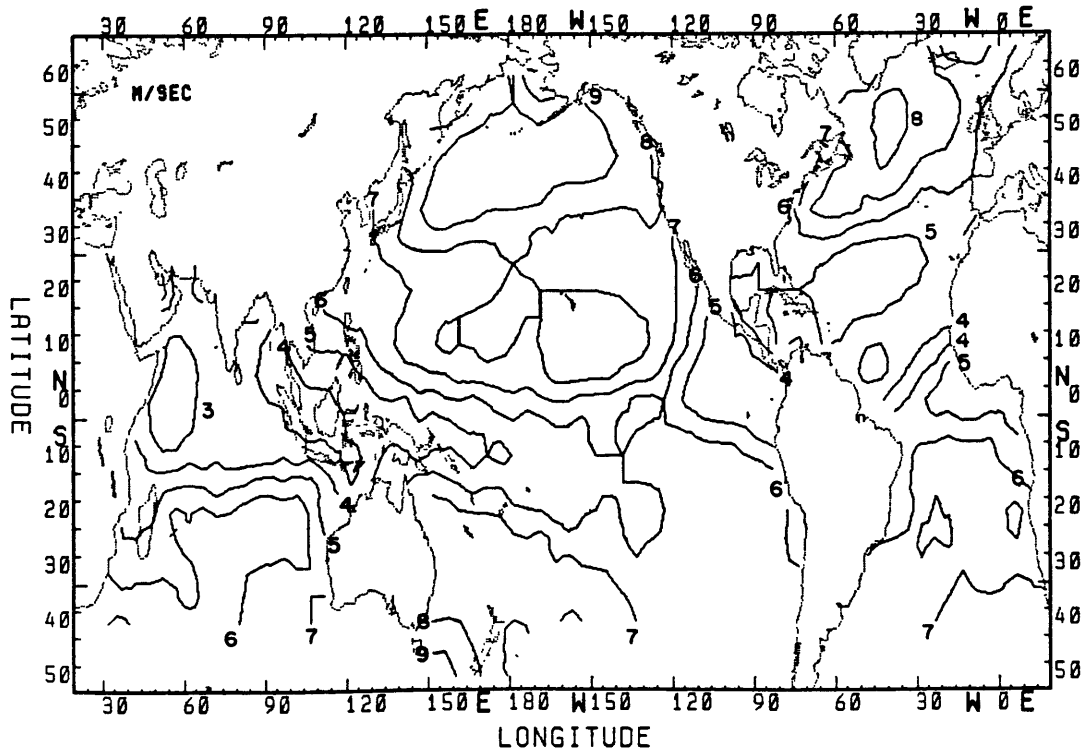


Figure C.2 Long term April means of wind speed

MONTHLY MEAN WIND SPEED MON=7

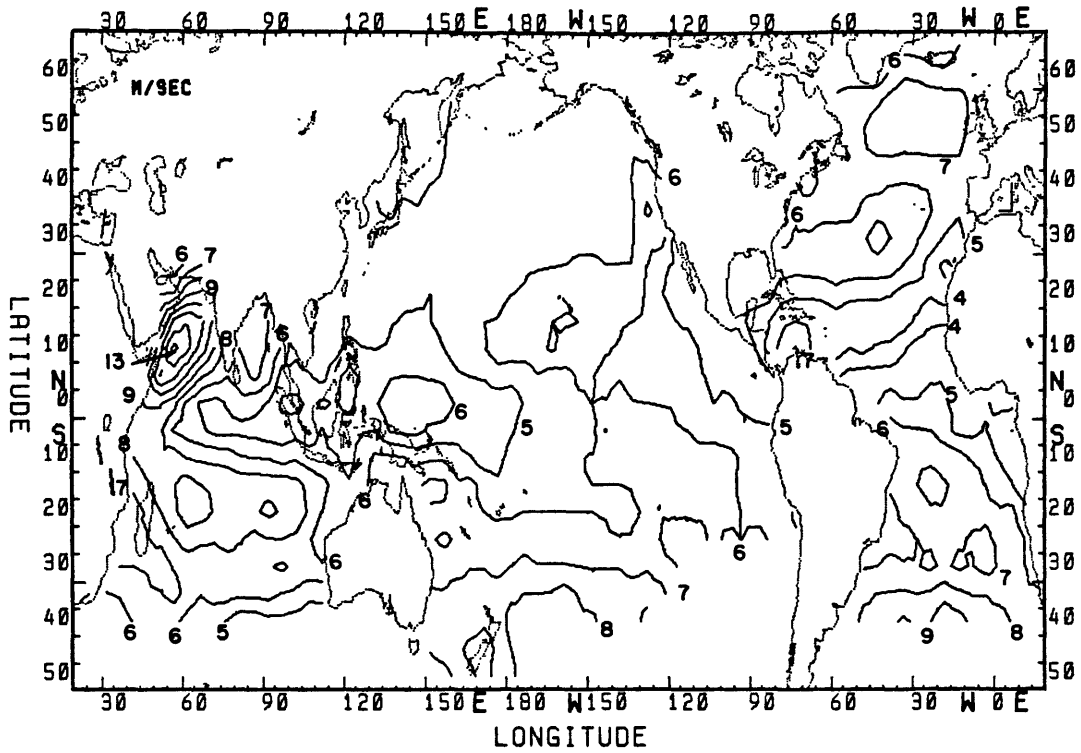


Figure C.3 Long term July means of wind speed
MONTHLY MEAN WIND SPEED MON=10

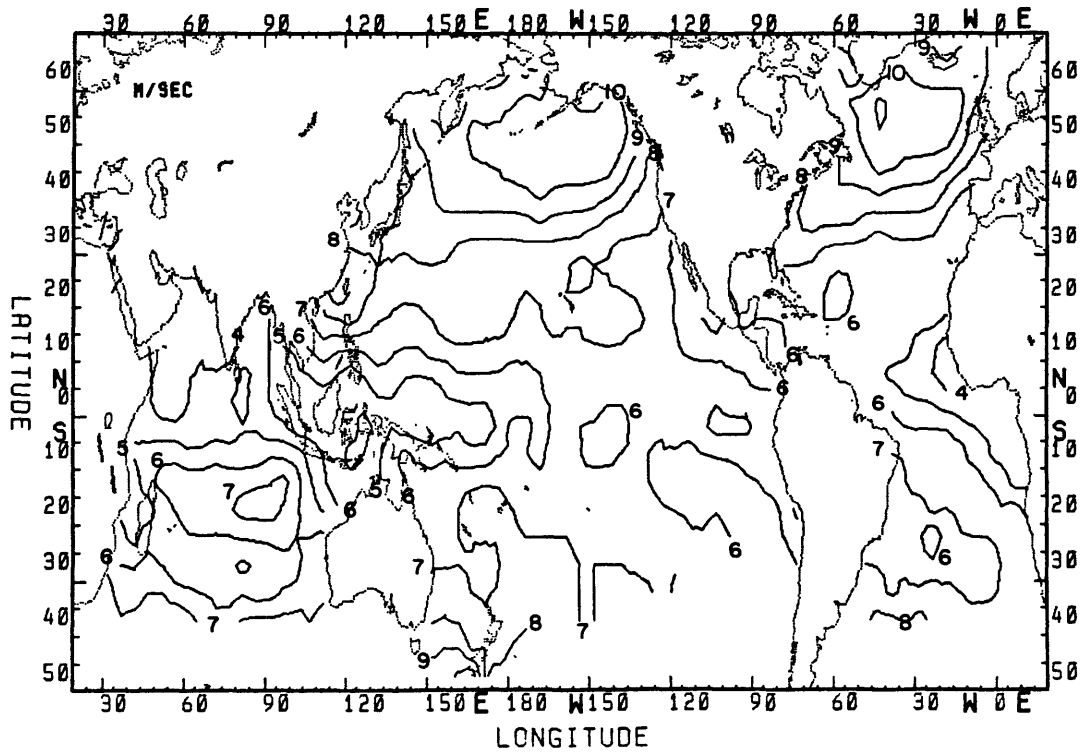


Figure C.4 Long term October means of wind speed

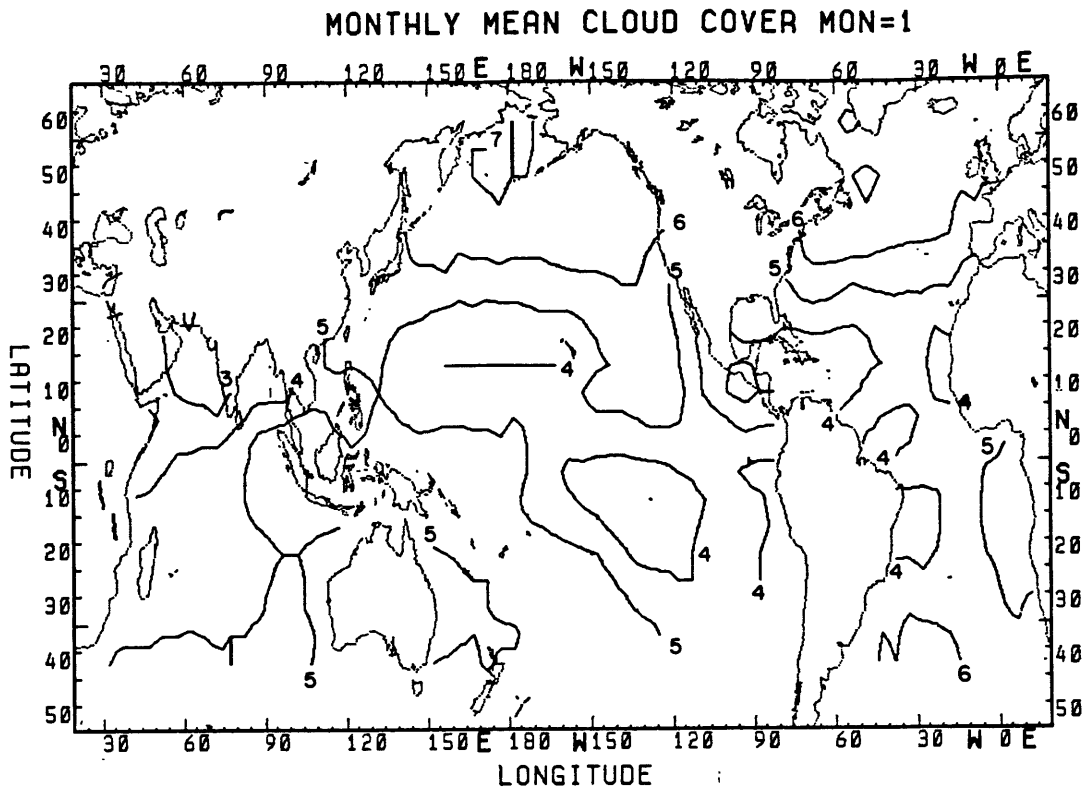


Figure C.5 Long term January means of cloud cover

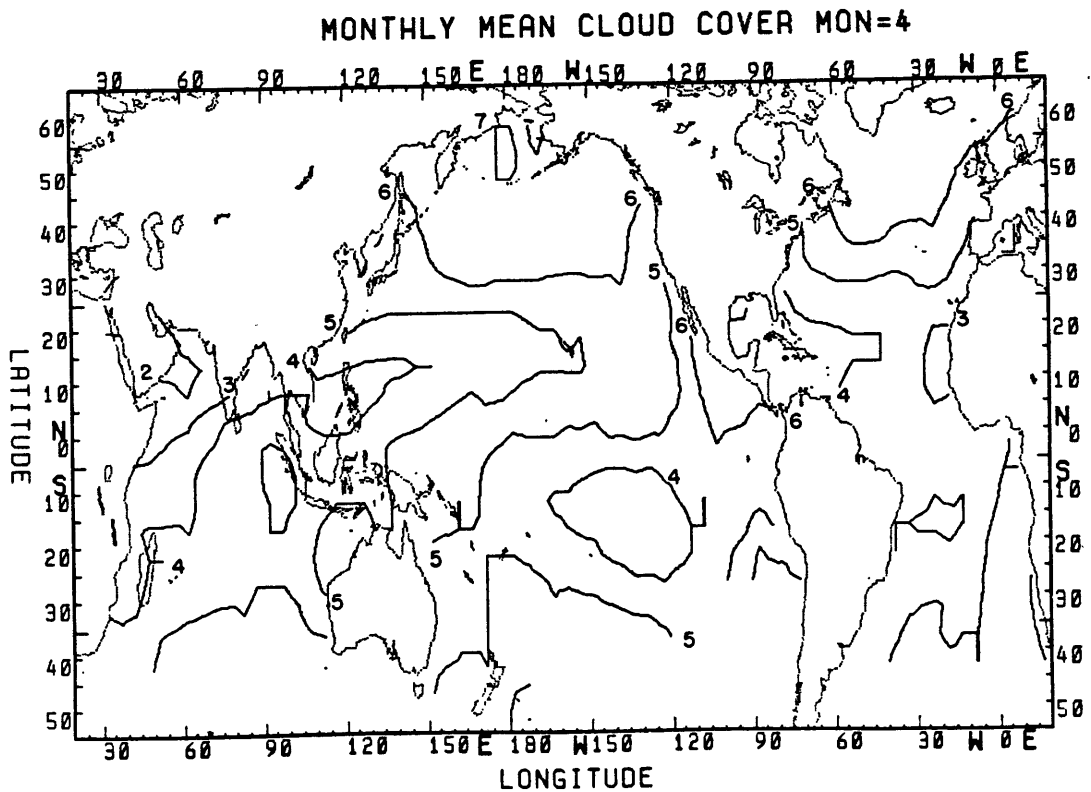


Figure C.6 Long term April means of cloud cover

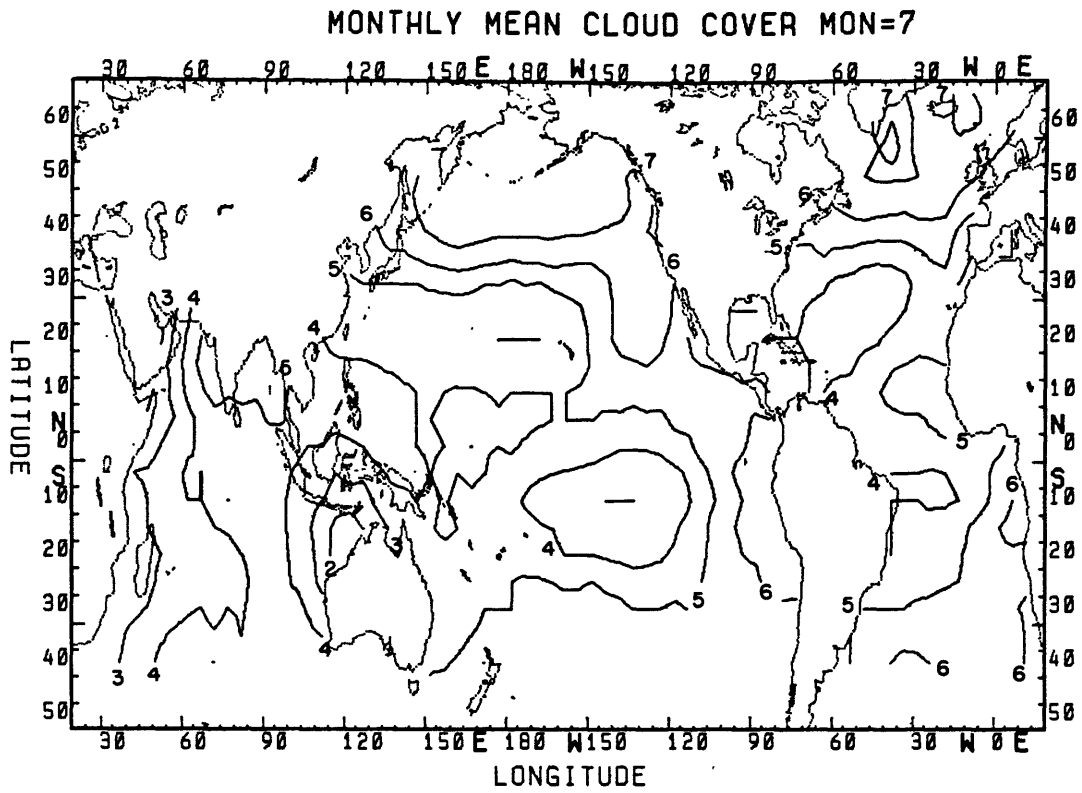


Figure C.7 Long term July means of cloud cover

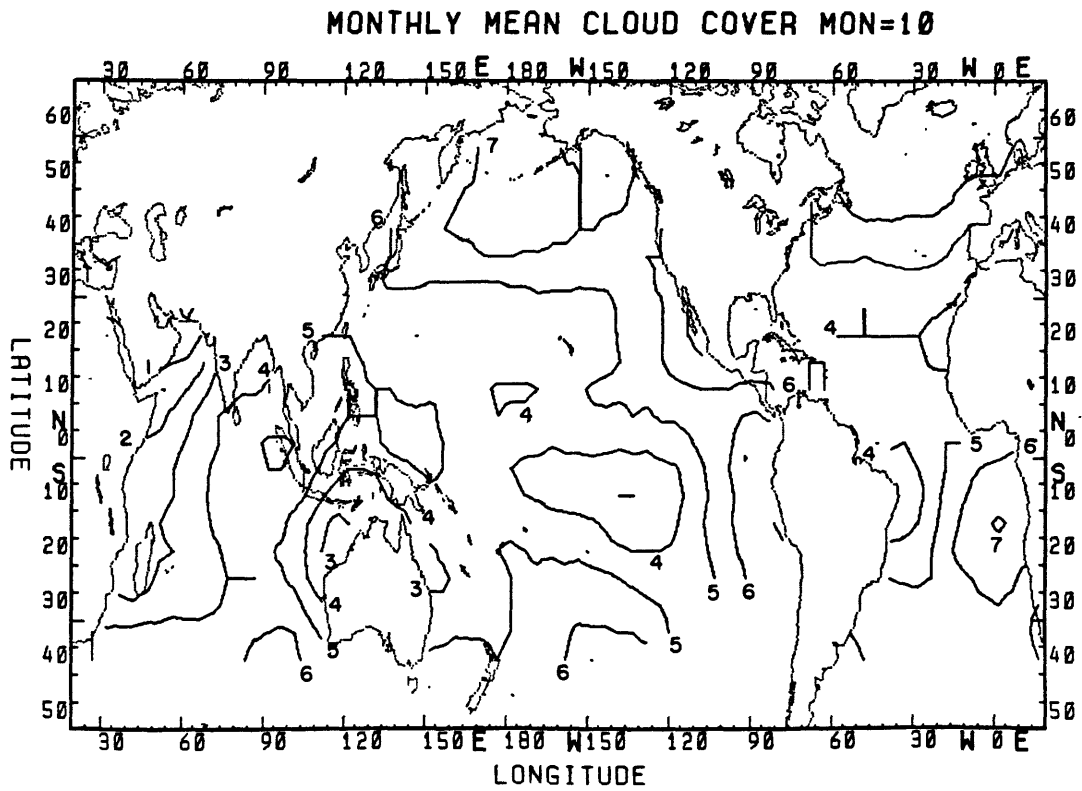


Figure C.8 Long term October means of cloud cover

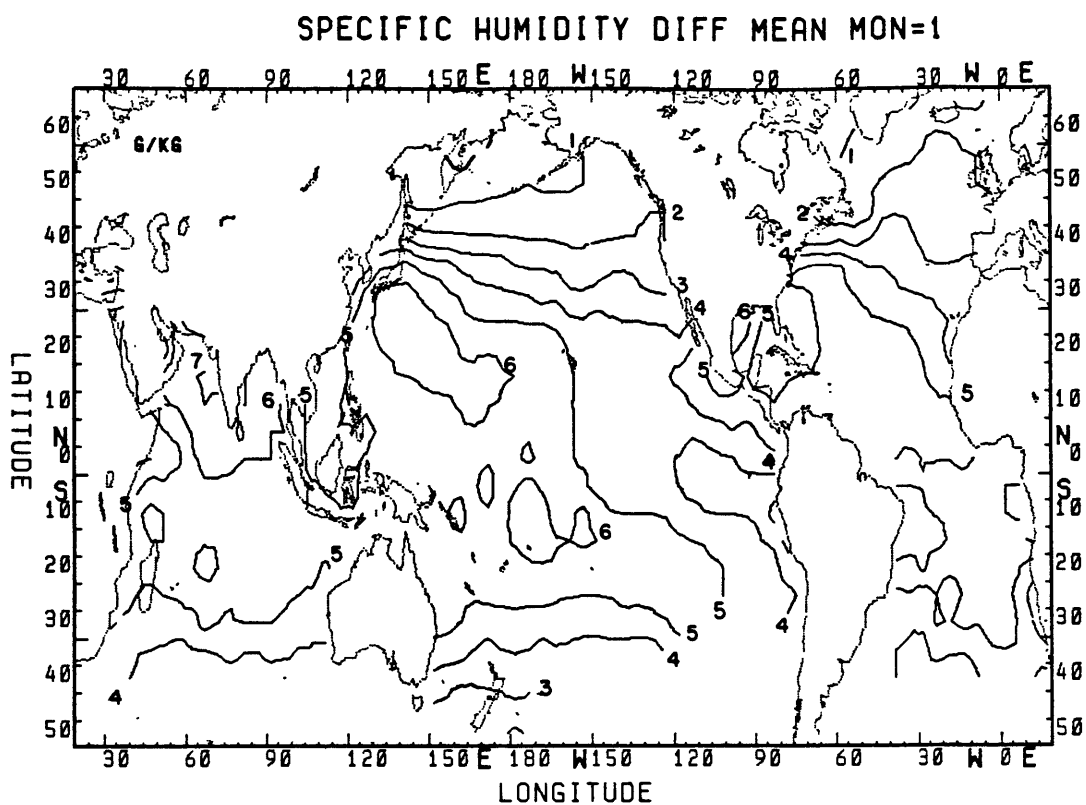


Figure C.9 Long term January means of specific humidity difference

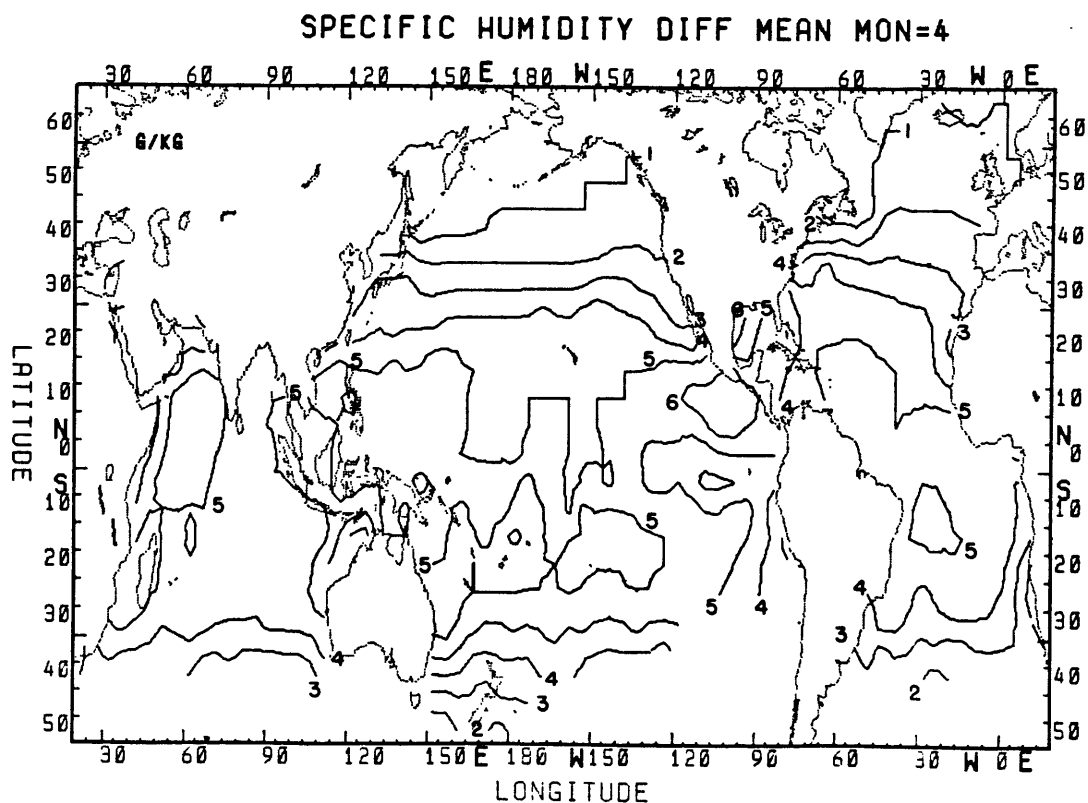


Figure C.10 Long term April means of specific humidity difference

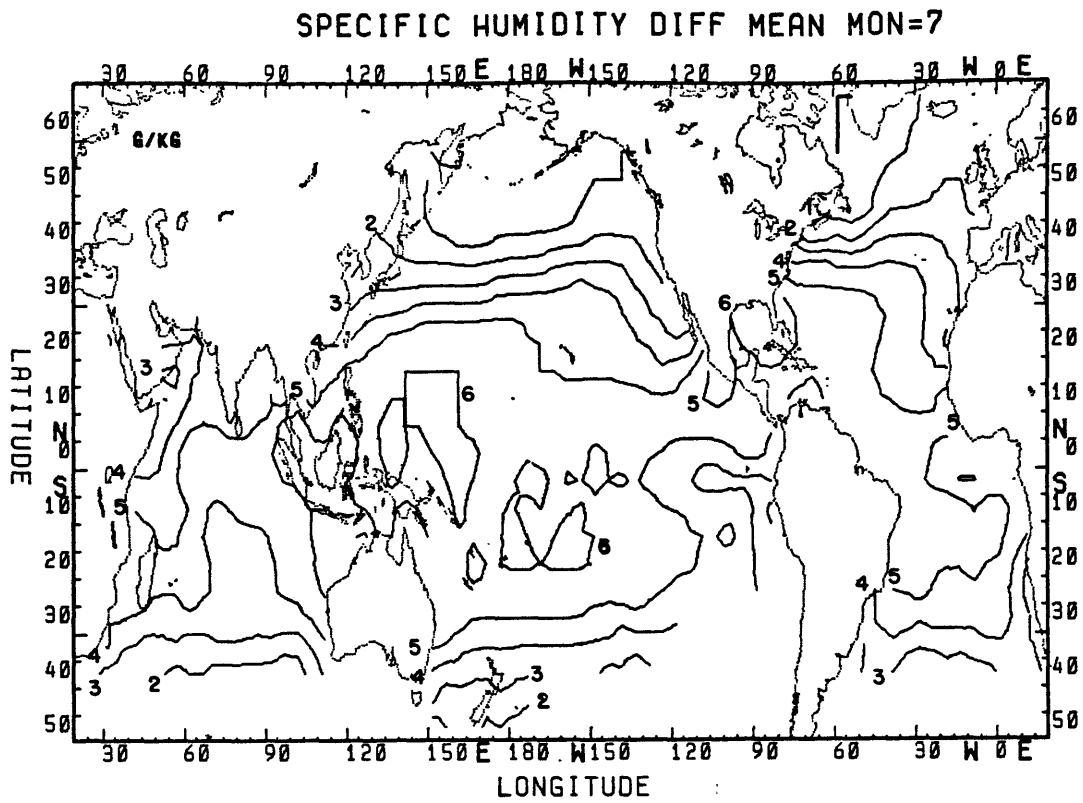


Figure C.11 Long term July means of specific humidity difference

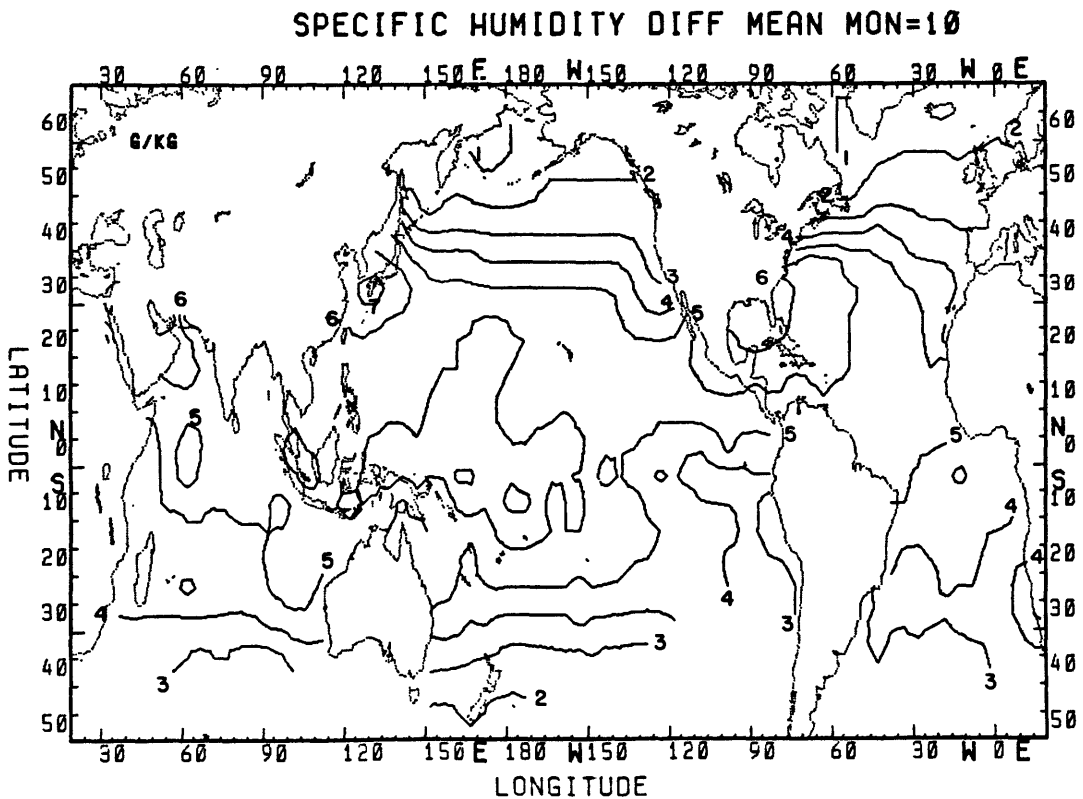


Figure C.12 Long term October means of specific humidity difference

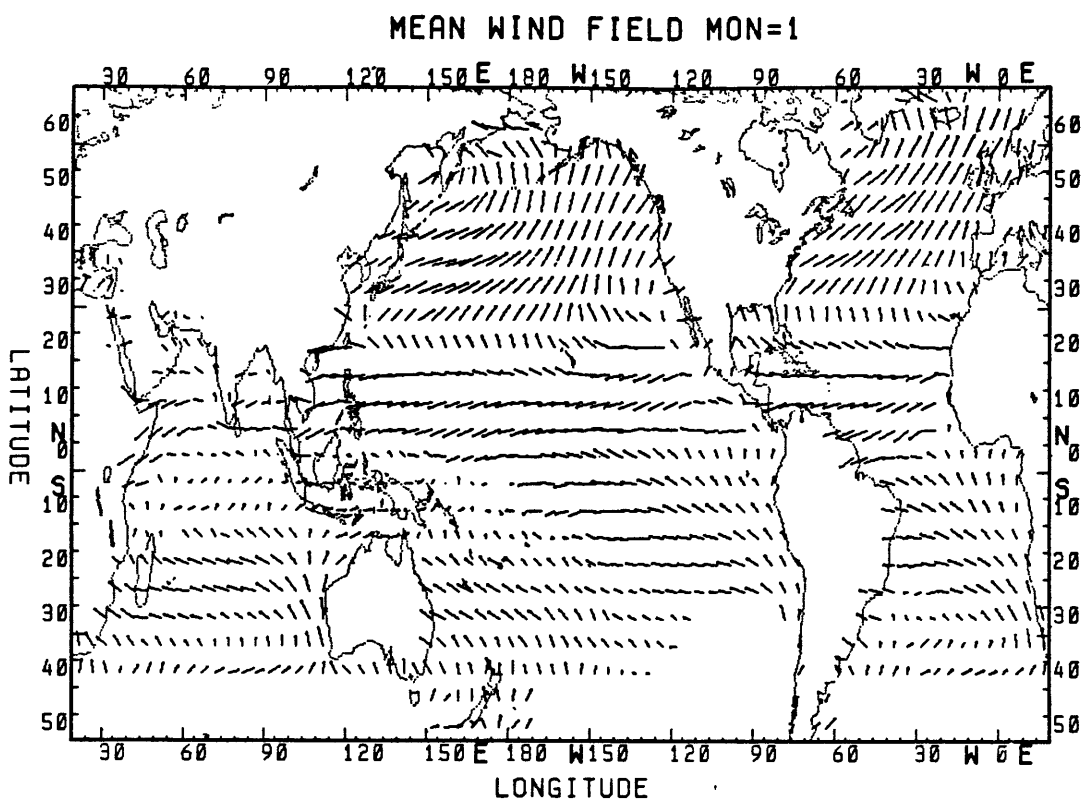


Figure C.13 Long term January means of surface wind

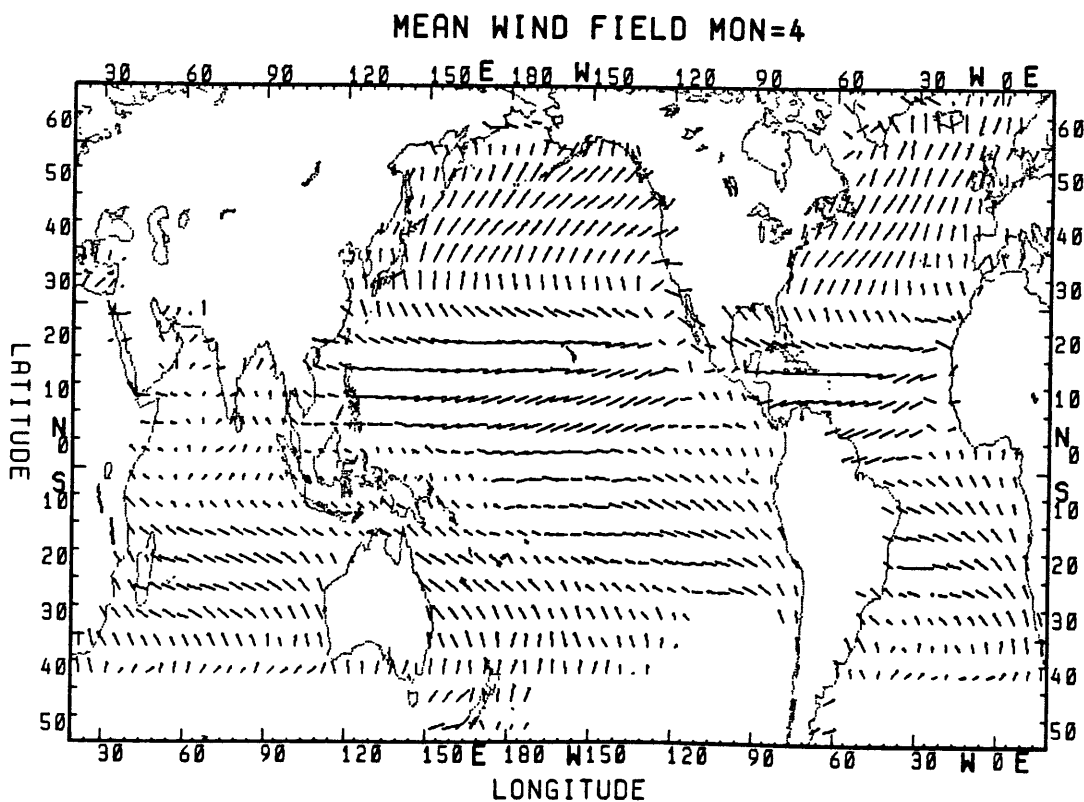


Figure C.14 Long term April means of surface wind

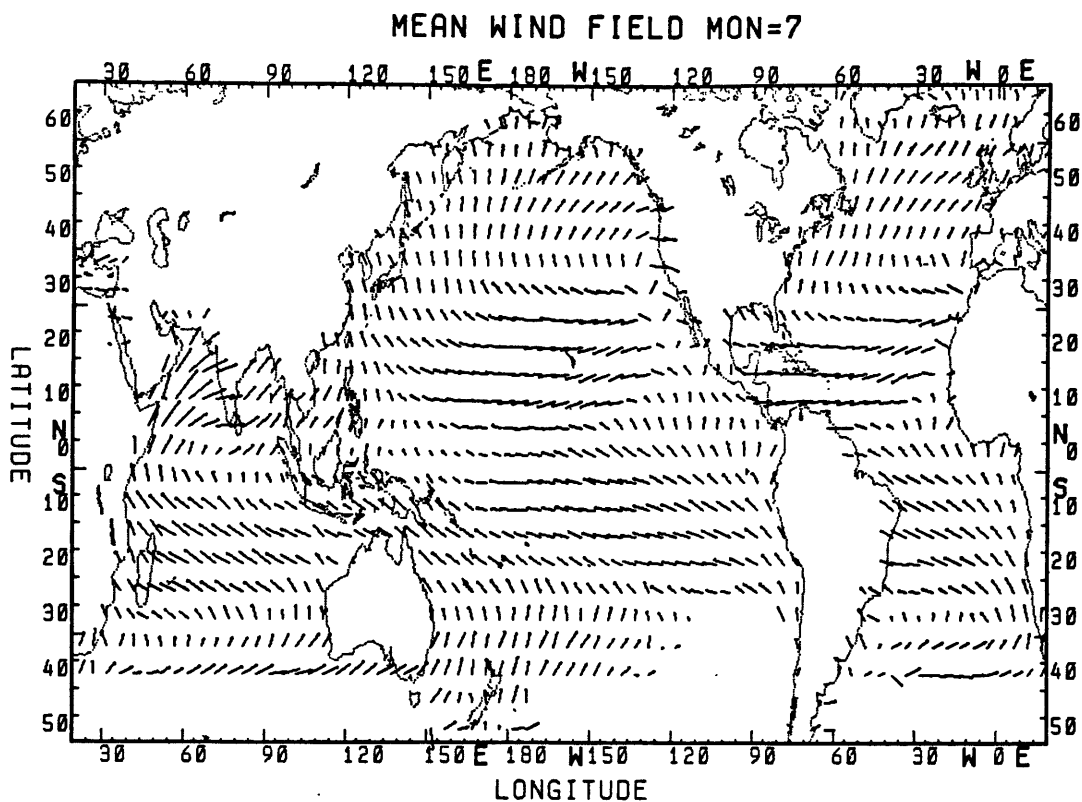


Figure C.15 Long term July means of surface wind

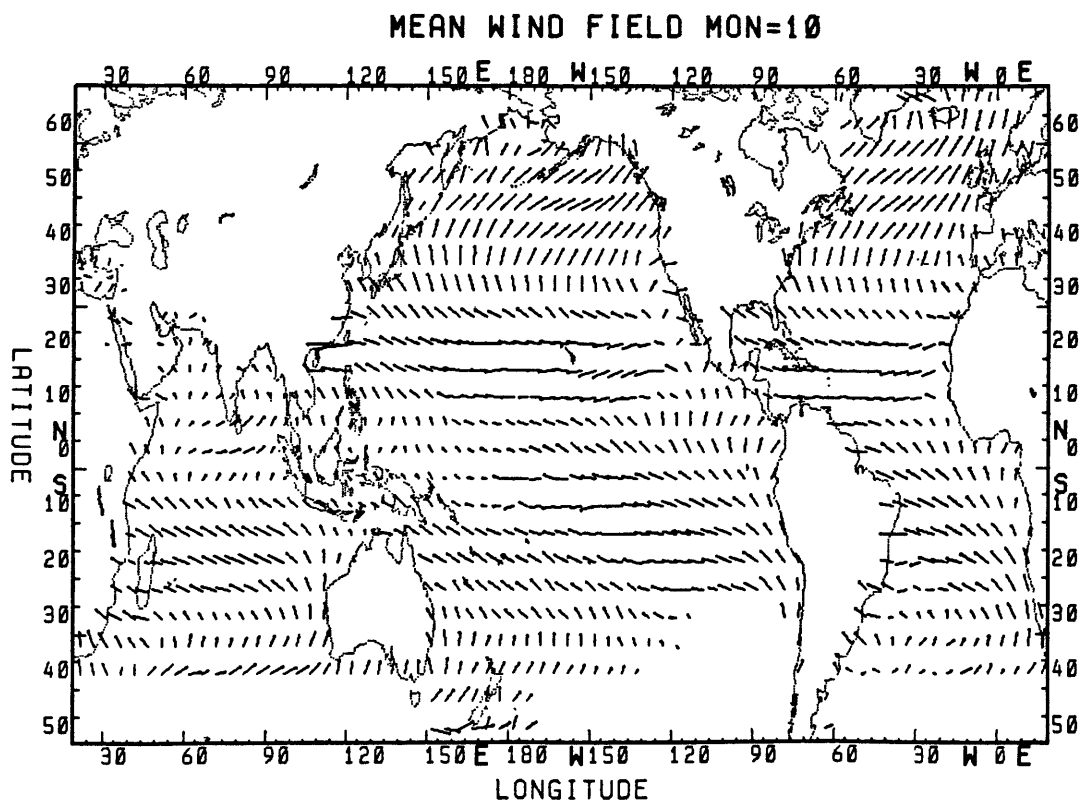


Figure C.16 Long term October means of surface wind

MONTHLY MEAN AIR MON=1

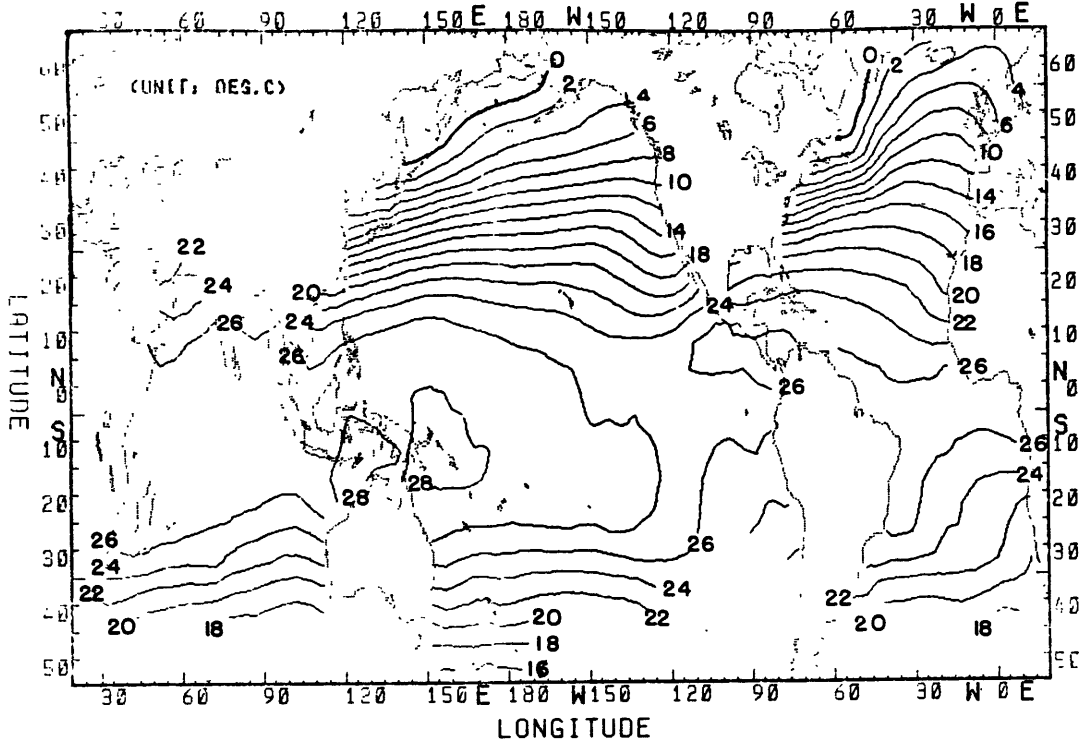


Figure C.17 Long term January means of air temperature

MONTHLY MEAN AIR MON=4

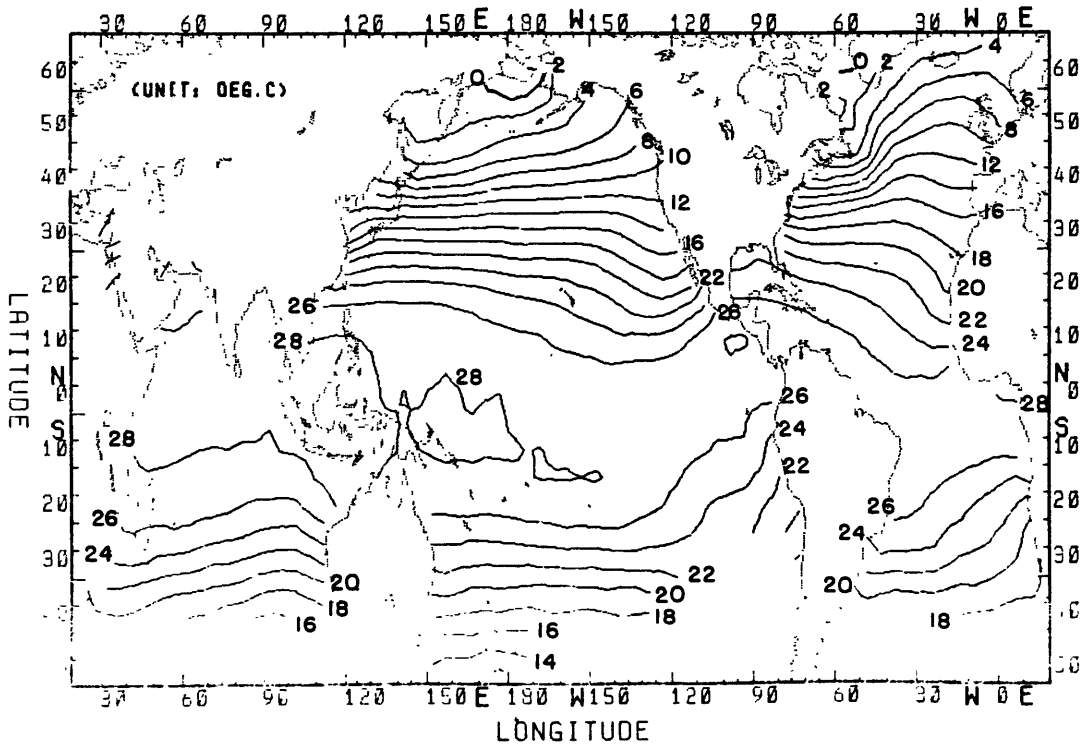


Figure C.18 Long term April means of air temperature

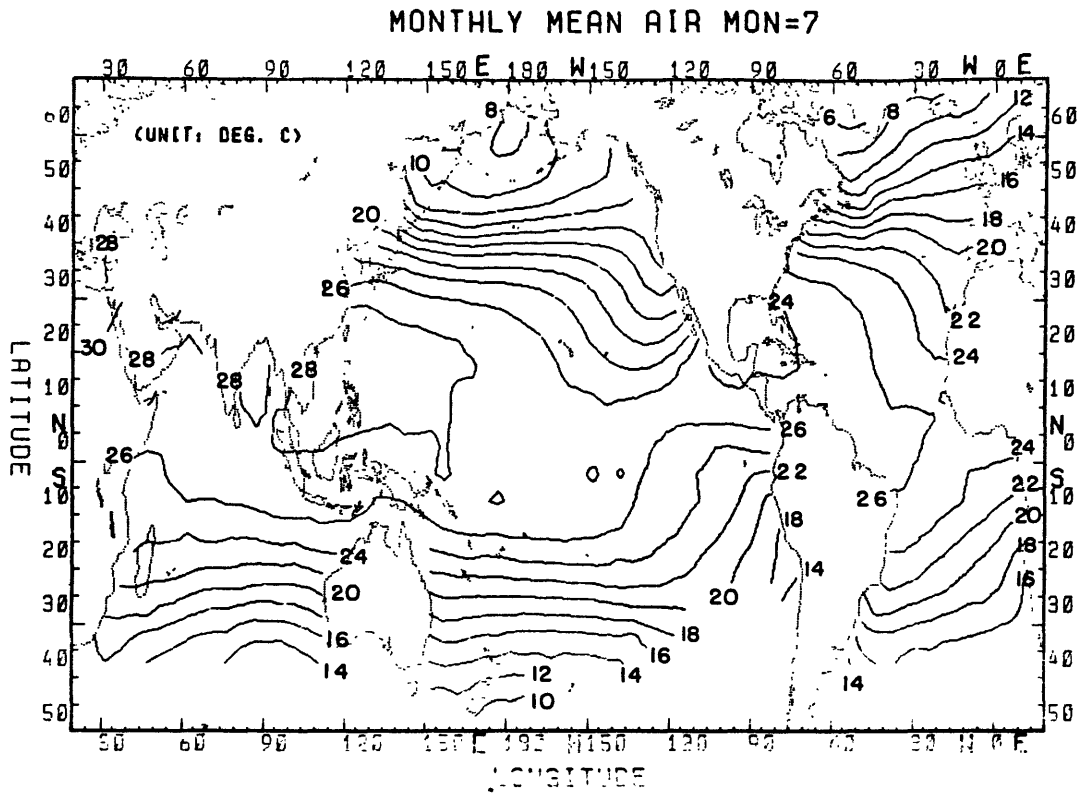


Figure C.19 Long term July means of air temperature

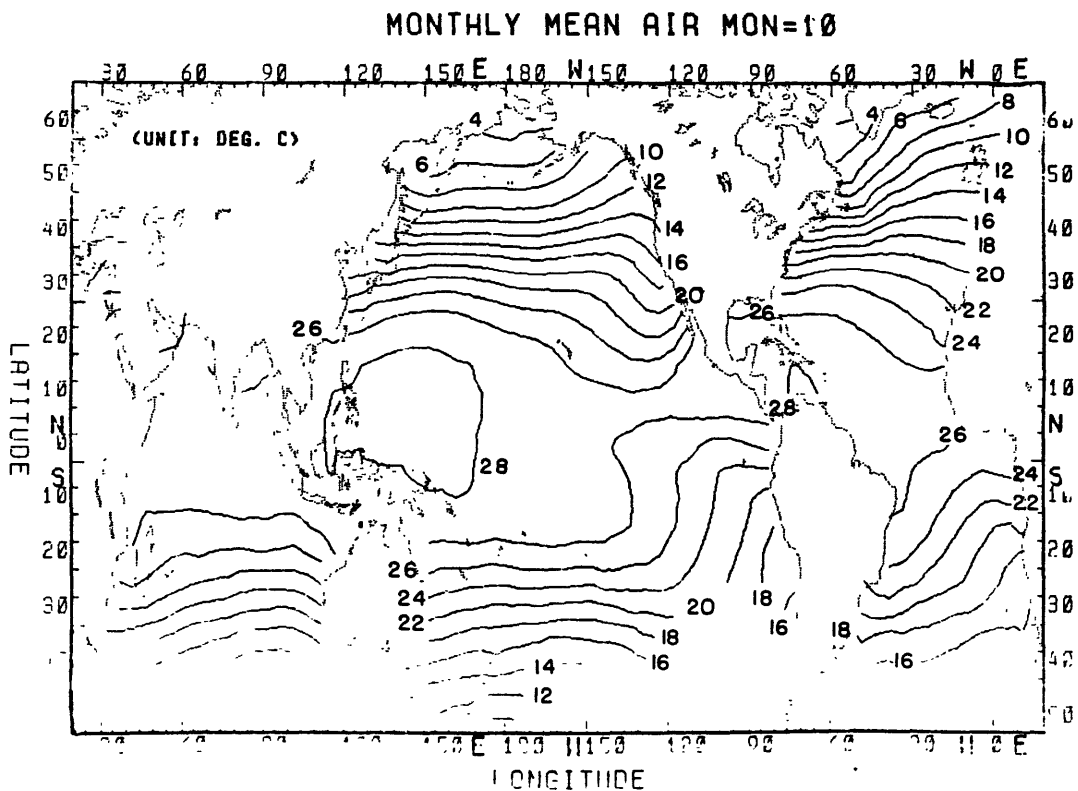


Figure C.20 Long term October means of air temperature

MONTHLY MEAN SLP

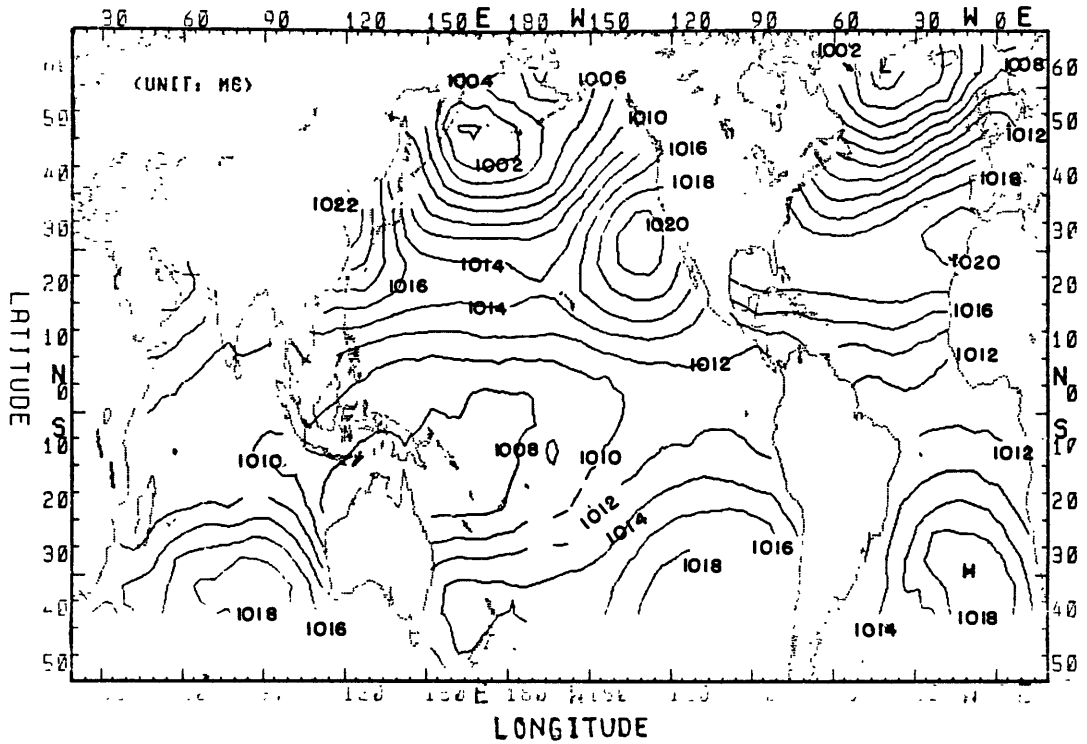


Figure C.21 Long term January means of sea level pressure

MONTHLY MEAN SLP MON=4

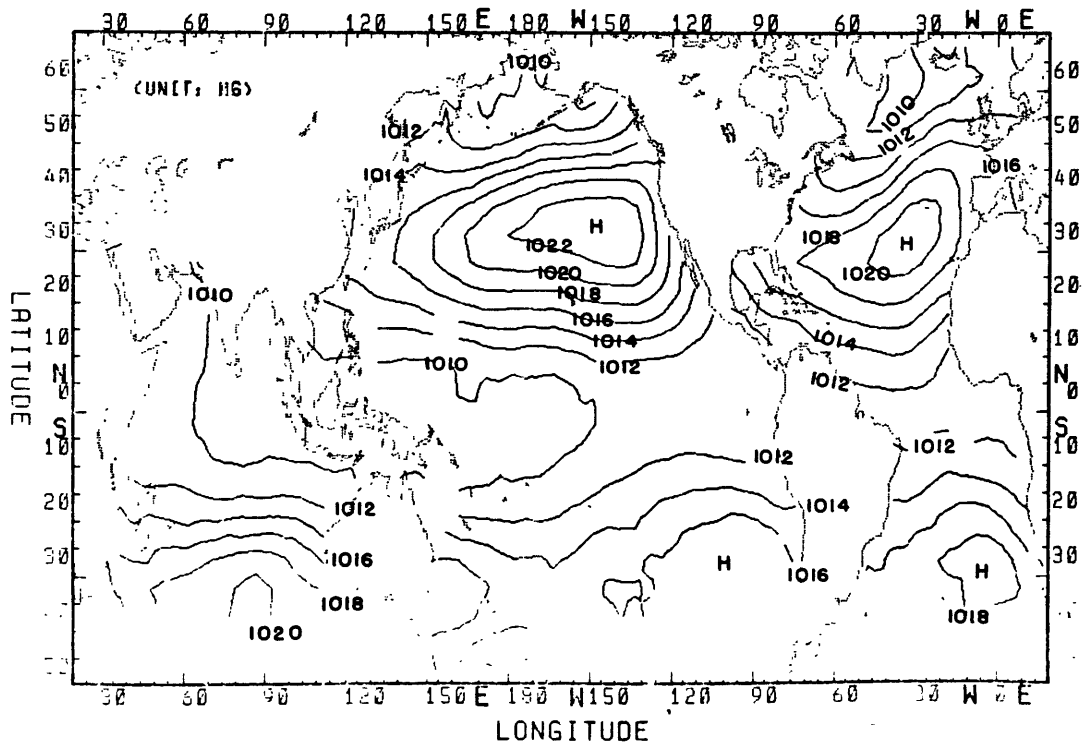


Figure C.22 Long term April means of sea level pressure

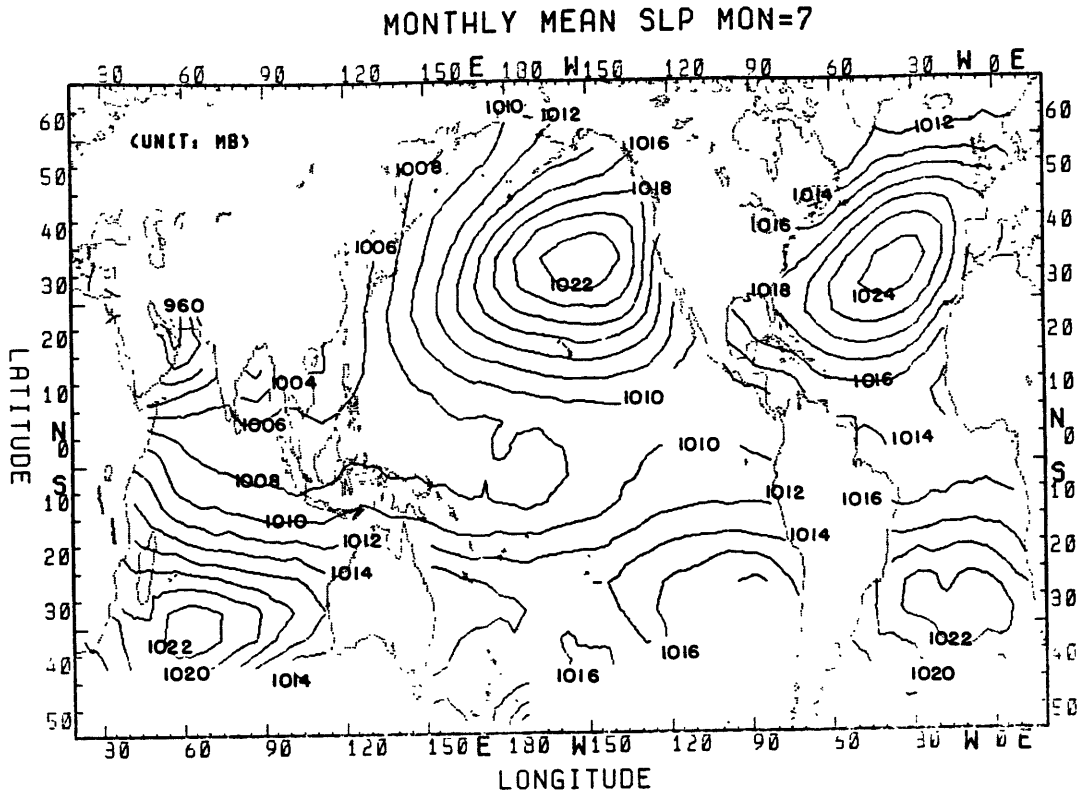


Figure C.23 Long term July means of sea level pressure

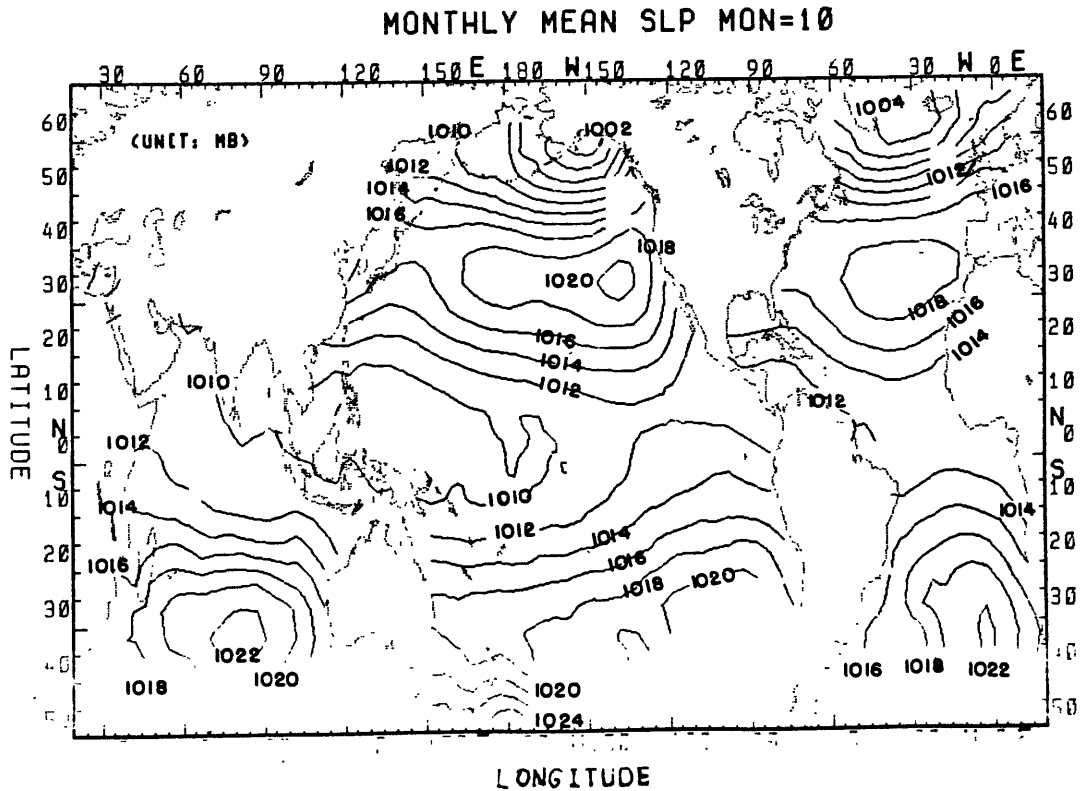


Figure C.24 Long term October means of sea level pressure

APPENDIX D. EMPIRICAL ORTHOGONAL FUNCTIONS AND SINGLE VALUEDECOMPOSITION

Very often in meteorology we have a set of n number of observations for p number of variables. When n and p are large, the amount of information contained in the data set can be overwhelming. Empirical orthogonal function analysis offers a method to 'reduce' the data set to a manageable number of eigenvectors while maintaining the maximum amount of information. The eigenvectors are orthogonal to each other and can be considered as weights for each of the p variables. Associated with each vector is a time series that describes the variation of the particular vector in time. So in addition to the reduction of the data set, EOF analysis conveniently separates the data set into a space component and a time component. To calculate the empirical orthogonal functions of a large data set requires the construction of the variance-covariance matrix. If the number of variables in the data set p is large, this can be a tremendous amount of computation, even for a high speed computer. Single value decomposition is also a technique that decomposes a matrix. It separates any given matrix into products of matrices, one of which is a single-valued diagonal matrix. In this appendix we will show how SVD are related to the EOF analysis and how one could avoid calculating the p by p covariance matrix to obtain the empirical orthogonal functions.

If we denote by x_{ij} the deviation of the i^{th} observed value of the j^{th} variable from its mean \bar{x}_j where

$$x_j = \frac{1}{n} \sum_{k=1}^n x_{kj}$$

Store our deviations into a $n \times p$ matrix X :

$$X = \begin{bmatrix} x_{11} \dots \dots \dots x_{1p} \\ x_{21} \dots \dots \dots x_{2p} \\ \cdot \\ \cdot \\ \cdot \\ x_{n1} \dots \dots \dots x_{np} \end{bmatrix}$$

then each of the columns of X gives the n observed deviation time series from the mean of the j^{th} variable.

In empirical orthogonal function analysis, we assume the existence of two matrices Y and Z such that the matrix X can be factorized into:

$$X = Z \cdot Y \quad (\text{D.1})$$

with the following constraints:

$$Y \cdot Y' = I \quad (\text{D.2})$$

$$Z' \cdot Z = D \quad (\text{D.3})$$

where Y is a $p \times p$ matrix, I is a $p \times p$ identity matrix, Z is a $n \times p$ matrix and D is a $p \times p$ diagonal matrix. Here we are using a capital letter to denote a matrix and a prime to denote the transpose of a matrix. One can think the p columns of Z as the time components with length n and the columns of Y as the space components with size p .

From (D.1) we have

$$X' = Y' \cdot Z' \quad (\text{D.4})$$

Using (D.4) and (D.1) we obtain the following:

$$X'X = Y'Z'ZY = Y'DY \quad (D.5)$$

With the property of orthogonality of the matrix Y , equation (D.5) can be written as

$$Y(X'X)Y' = D \quad (D.6)$$

From (D.6) we see that the matrix Y whose existence we merely assumed is an orthogonal matrix that can be used to diagonalize the product matrix XX' . The matrix Z can be computed using (D.1) as:

$$Z' = XY' \quad (D.7)$$

The problem of finding the matrix Y such that equation (D.6) holds is known in linear algebra as the eigenvalue-eigenvector problem. It turns out that the rows of Y (or equivalently, the columns of Y') are the eigenvectors of the matrix $(X'X)$ and the corresponding diagonal elements of D are the associated eigenvalues.

One can deduce from matrix algebra that in (D.6)

$$\text{Tr}(X'X) = \text{Tr}(D)$$

where $\text{Tr}(A)$ denotes the trace of matrix A (trace being the sum of the diagonal elements). In other words, the sum of the eigenvalues d_i , $i=1, 2, \dots, p$ is equal to the total variance of the p variables (since from the definition of X the product $X'X$ is the variance-covariance matrix.) The fraction

$$r_i = \frac{d_i}{\sum_{j=1}^p d_j}, \quad i=1, 2, \dots, p$$

is the ratio of the variance of the i th eigenvalue to the total variance. We can think of r_i as the percentage of variance 'explained' by the i th vector that is associated with the i th eigenvalue. If we rearrange the order of the eigenvalues in decreasing order of magnitude, then the first k components will account for K percent of the total variance where

$$K = \sum_{i=1}^k r_i$$

Depending on the particular data field, we could have K close to 1. for a k much smaller than p , our original number of variables. Thus the p variables are effectively reduced to k components and in these k components we have an optimal description of the data field using the least number of components.

In single value decomposition, one is interested in decomposing a given matrix into a single-valued matrix (i.e. a diagonal matrix). For example, given the matrix X , we want to find a matrix S such that

$$X = U \cdot S \cdot V' \quad (D.8)$$

Here S is a $p \times p$ diagonal matrix, u is a $n \times p$ matrix and v is a $p \times p$ matrix. In addition, we require

$$U'U = I \quad (D.9)$$

$$V'V = I \quad (D.10)$$

From (D.8) we have

$$X' = V \cdot S' \cdot U' \quad (D.11)$$

and

$$X'X = VS'U' \cdot USV' = VS^2V' \quad (D.12)$$

Rewriting (D.12) using (D.10):

$$V'X'XV = S^2 \quad (D.13)$$

Equation (D.13) is the equivalent of (D.6) except now the matrix V' is the matrix that diagonalizes the product matrix $X'X$ and the diagonal elements of S^2 are the eigenvalues of $X'X$. The equivalent of Z is the product $U \cdot S$.

So far we have shown the equivalence of the matrix V and Y . They are both eigenvectors of the matrix $X'X$ - which is nothing other than the variance-covariance of X if X is a matrix consisted of deviations. The advantage of SVD comes from the fact that one can also form the product XX' such that

$$XX' = USV' \cdot VS'U' = US^2U' \quad (D.14)$$

Again the above equation is

$$U'(XX')U = S^2 \quad (D.15)$$

We can see that the rows of the matrix U' are the eigenvectors of XX' and the diagonal elements of S^2 are the eigenvalues. If in our matrix X n is smaller than p (recall n is the number of observations and p the number of variables), then the size of the product XX' ($n \times n$) would be much smaller than the size of the product $X'X$ ($p \times p$). It is therefore much more efficient to calculate U first and then calculate V from the relationship in (D.8) to obtain the required Y matrix of an EOF analysis.

In summary, to find the eigenvector Y in EOF analysis, one can form XX' first. Calculate its eigenvector U' and from (D.8) find the matrix V (which is equivalent to Y). This approach can be a considerable saving in both computing space and time, especially if p is much larger than n .

APPENDIX E. WIND STRESS CALCULATIONS

E.1 Wind Stress

The bulk aerodynamic formulas used for the zonal and meridional component of wind stress calculations are

$$\begin{aligned}\tau_x &= \rho_a C_d |v| u \\ \tau_y &= \rho_a C_d |v| v\end{aligned}\tag{E.1}$$

Here u and v are the zonal and meridional components of wind, $|v|$ is the wind speed, ρ_a is the air density, and C_d is the drag coefficient. The development of these formulas are from the same equation of vertical flux as the heat fluxes (see Eq.4.7). The specification of C_d is controversial - some use a specified constant and some treat it as the same coefficient as the transfer coefficient for the heat fluxes. For the sake of consistency, we used Bunker's (1976) table of C_d as a function of atmospheric stability and wind speed. This dependence on wind speed is illustrated in Figure 4.1b for various stability conditions. The formulation of wind stress calculations indicate that they are strongly dependent on wind speed because the drag coefficient C_d is a function of wind speed as well as the formulas themselves. At low wind speed (say less than 10 m/s), the dependence of stress on stability becomes as great as the dependence on wind speed.

Contours of the long term monthly means of zonal wind stress for one month of each of the four seasons (months January, April, July and October) are presented in Figures E.1 to E.4. The circulation that is

responsible for the subtropical gyres in the north Pacific and north Atlantic is clearly evident in Figure E.1. There is a lack of such well defined feature in the same season in the southern hemisphere (see Figure E.3.) The northern hemisphere circulation weakens and moves northwards as the season progresses towards summer. In July (Figure E.3), the maximum wind stress in the global ocean is the large scale monsoon wind in the Arabian Sea west of India. The southern hemisphere circulation becomes more noticeable but the strength is weaker than that observed in the northern hemisphere at the same latitudes. Notice that the movement of the zero wind stress line over the year is greater in the Atlantic than it is in the Pacific.

Long term monthly means for the same months of the meridional component of the wind stress are presented in Figures E.5 to E.8. The maximum northward wind is observed in high northern latitudes in winter. In most areas of the ocean, the magnitude of the meridional wind stress is generally much less than that of the zonal wind stress indicating a more east-west orientation of the surface wind. For reference, the vectorial representation of the wind stress fields are presented in Figures E.9 to E.12.

Our results agree well with respect to the zero line contour when compared to Hellerman's (1967, 1968) estimates of wind stress. His maximum values are typically 10% larger than ours. The best agreement is found in the North Atlantic and the North Pacific while the worse agreement is in the Southern Hemisphere where his values are much higher than ours, especially the zonal component of the wind stress. Weare and

Strub (1980) made estimates for the tropical Pacific from 30°N to 30°S. The magnitudes of our zonal wind stress in the Southern Hemisphere agree better with their values.

blank page

ZONAL WIND STRESS MON=1

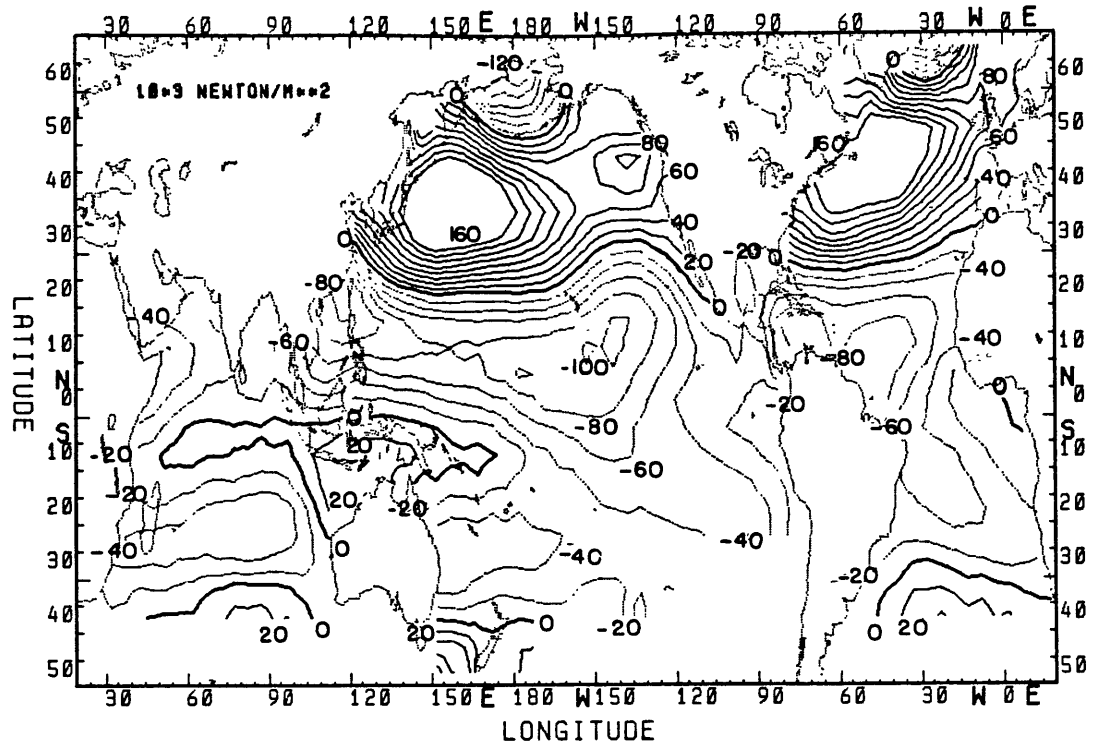


Figure E.1 Long term January means of zonal wind stress

ZONAL WIND STRESS MON=4

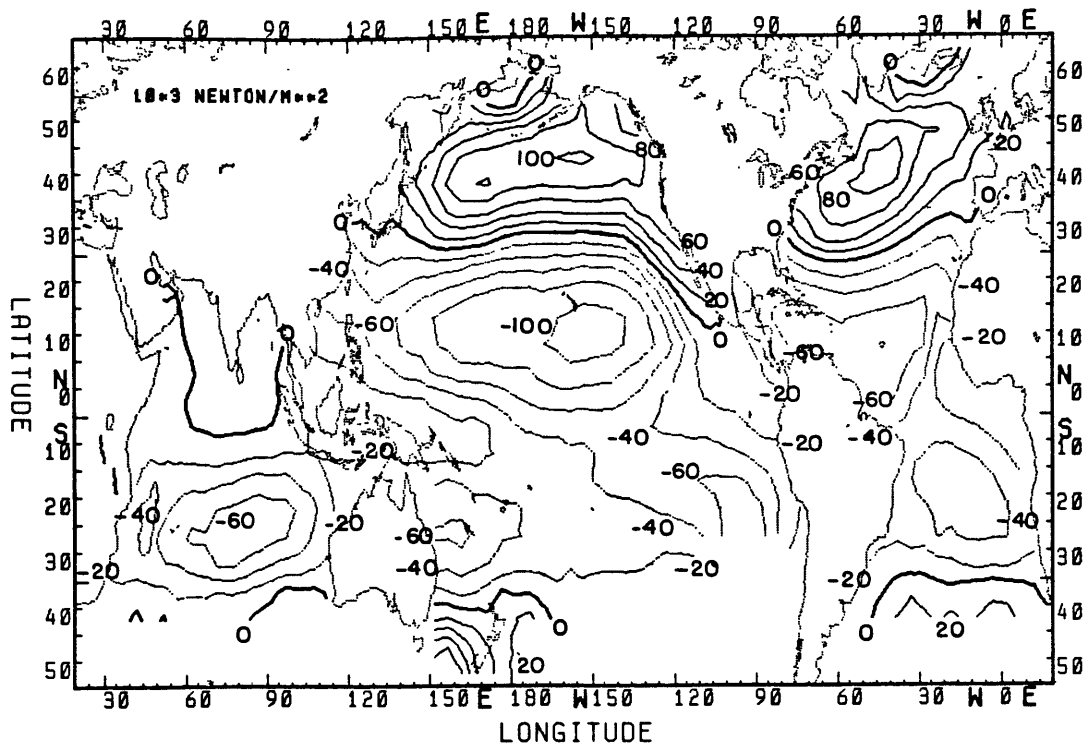


Figure E.2 Long term April means of zonal wind stress

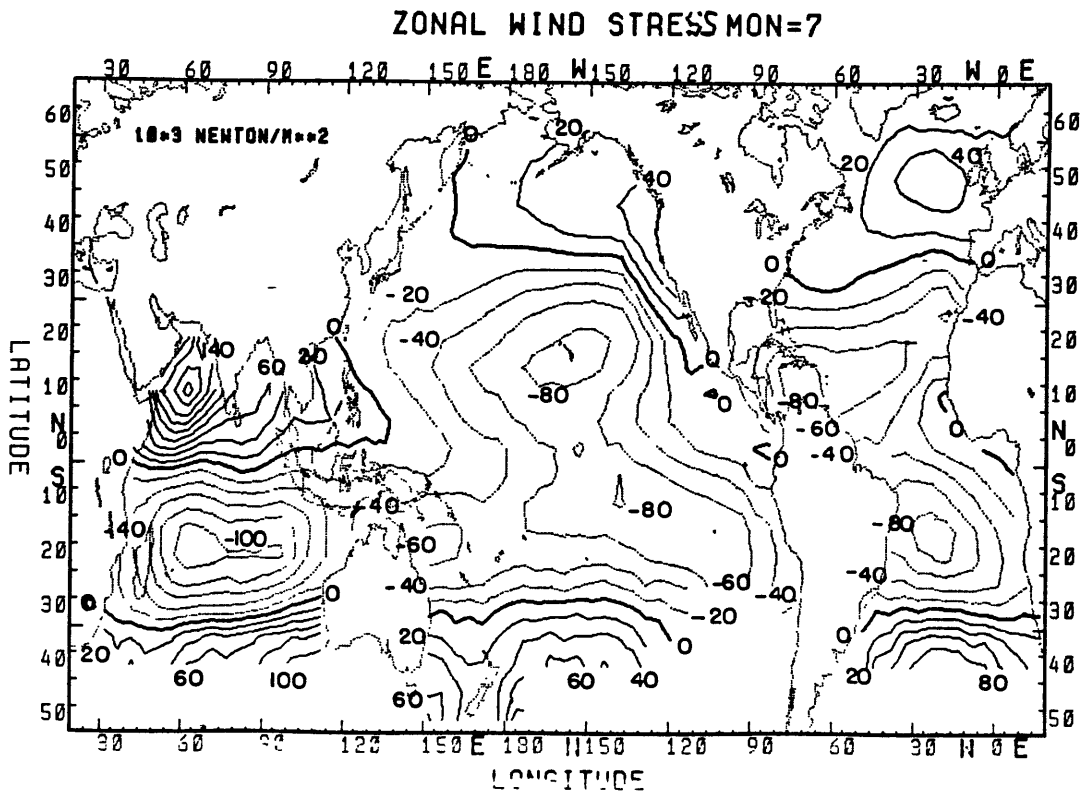


Figure E.3 Long term July means of zonal wind stress

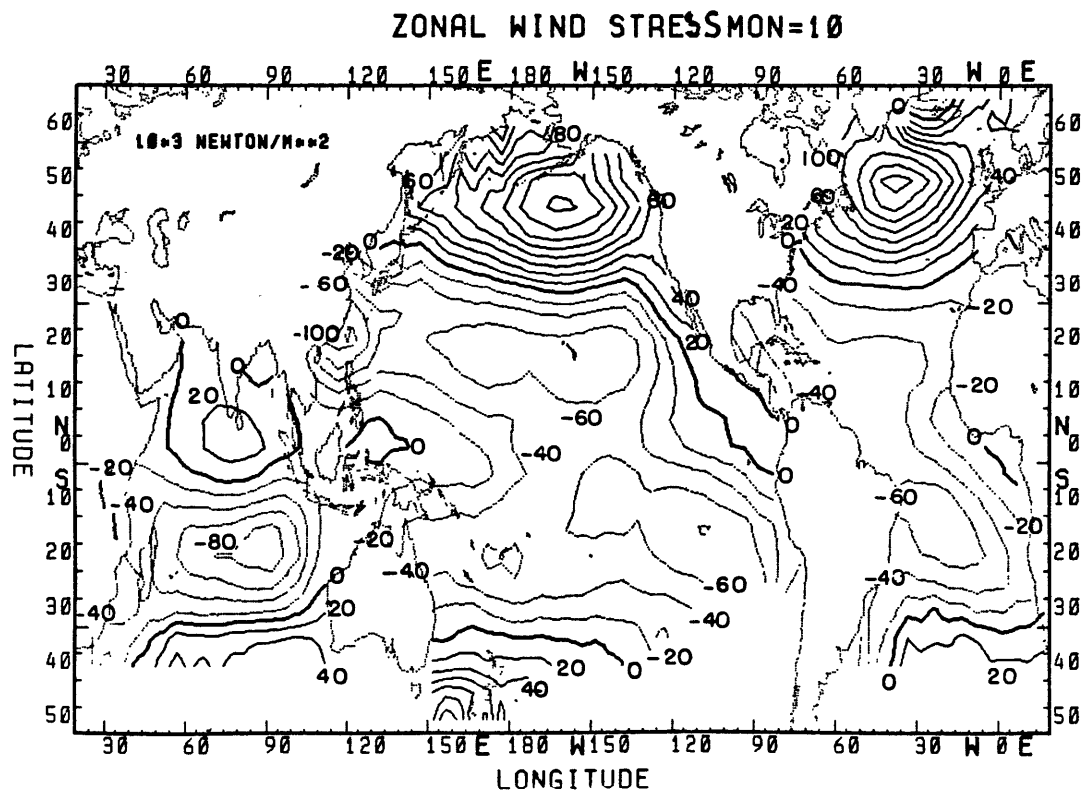


Figure E.4 Long term October means of zonal wind stress

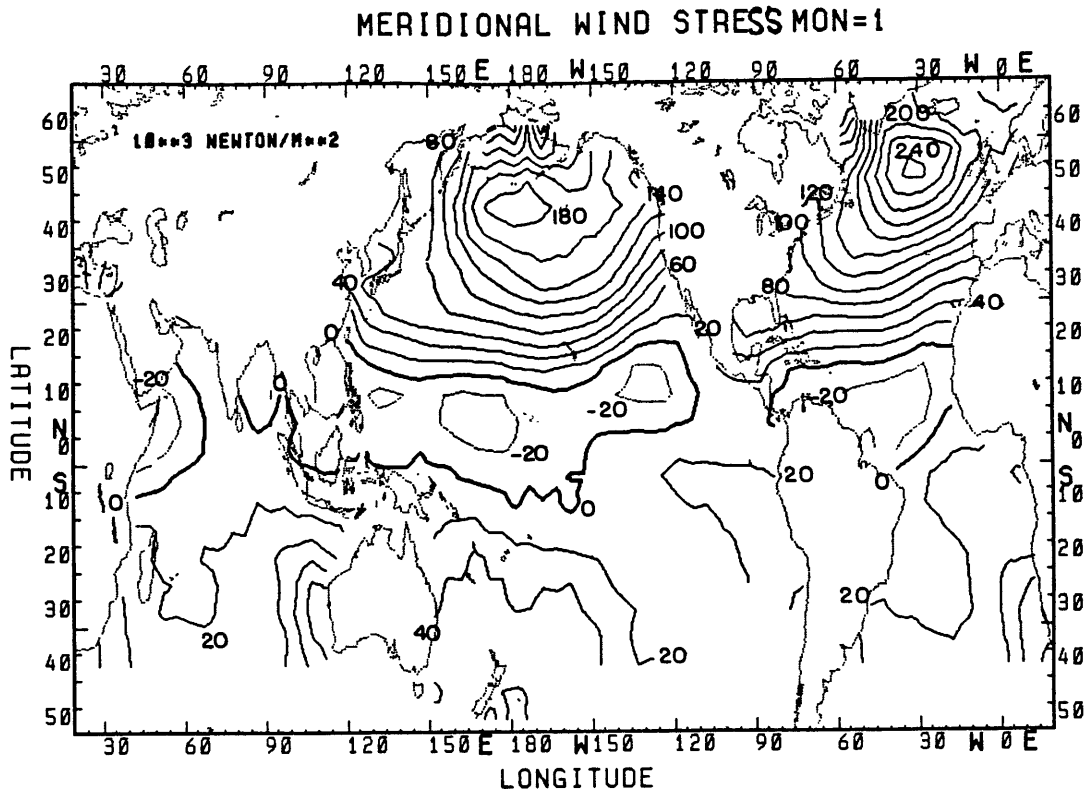


Figure E.5 Long term January means of meridional wind stress

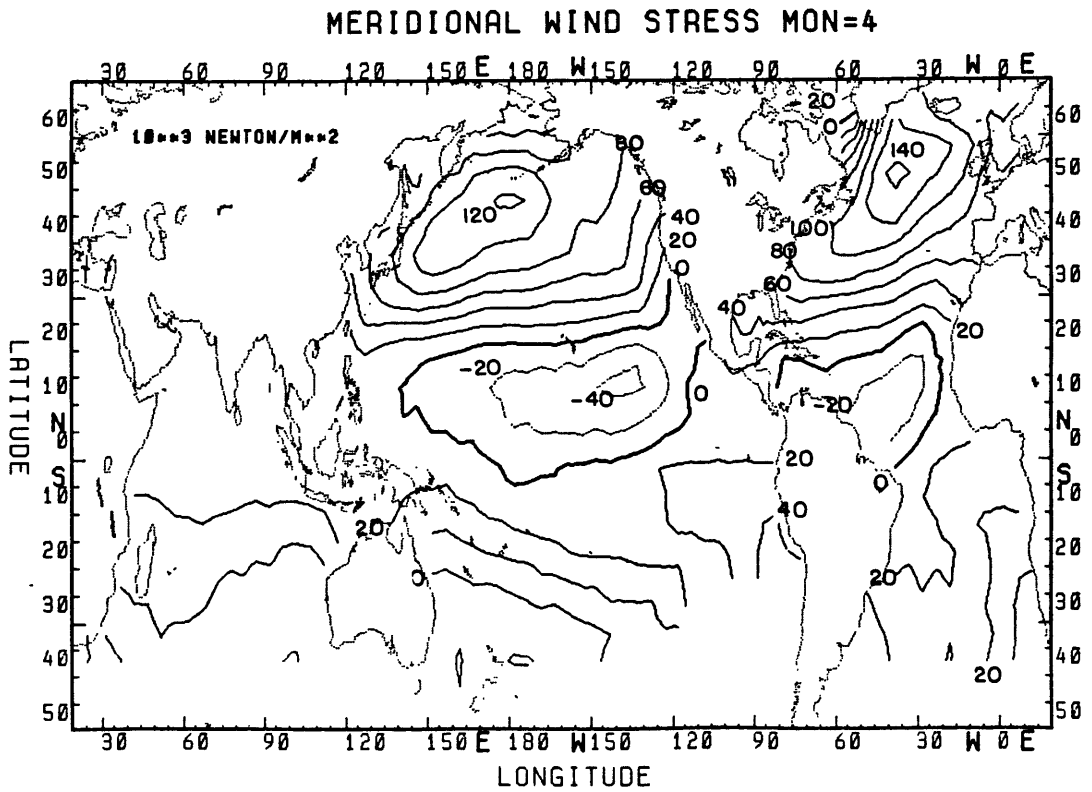


Figure E.6 Long term April means of meridional wind stress

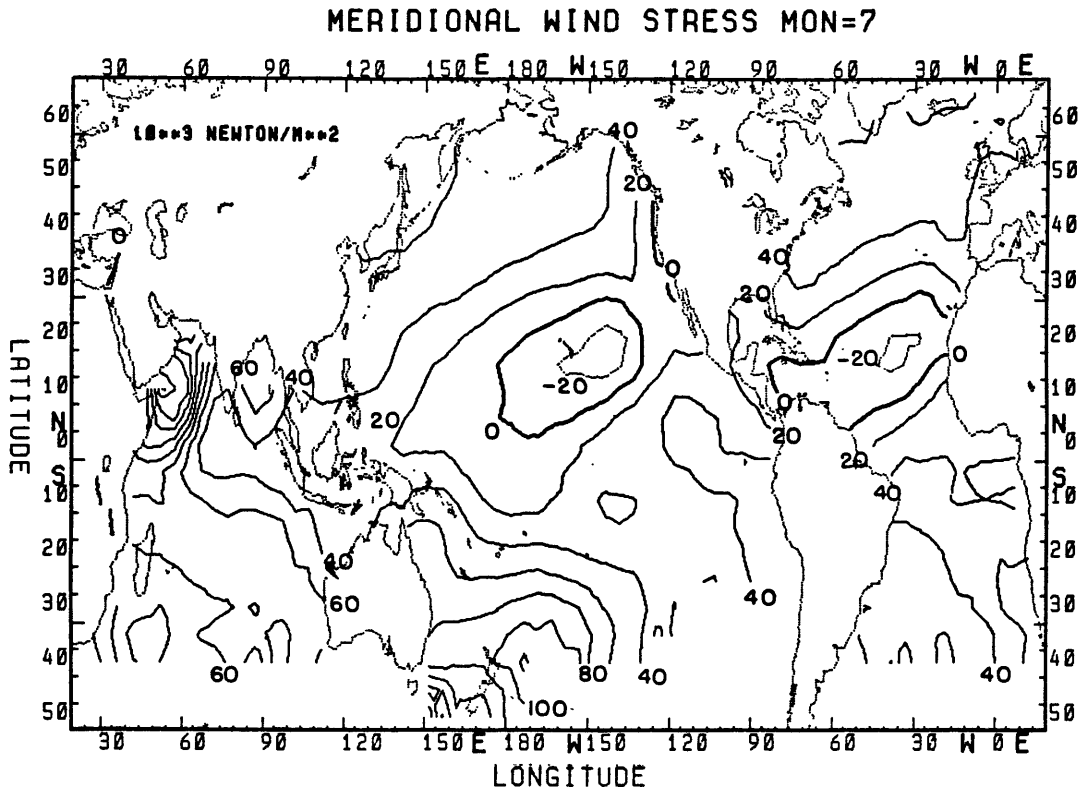


Figure E.7 Long term July means of meridional wind stress

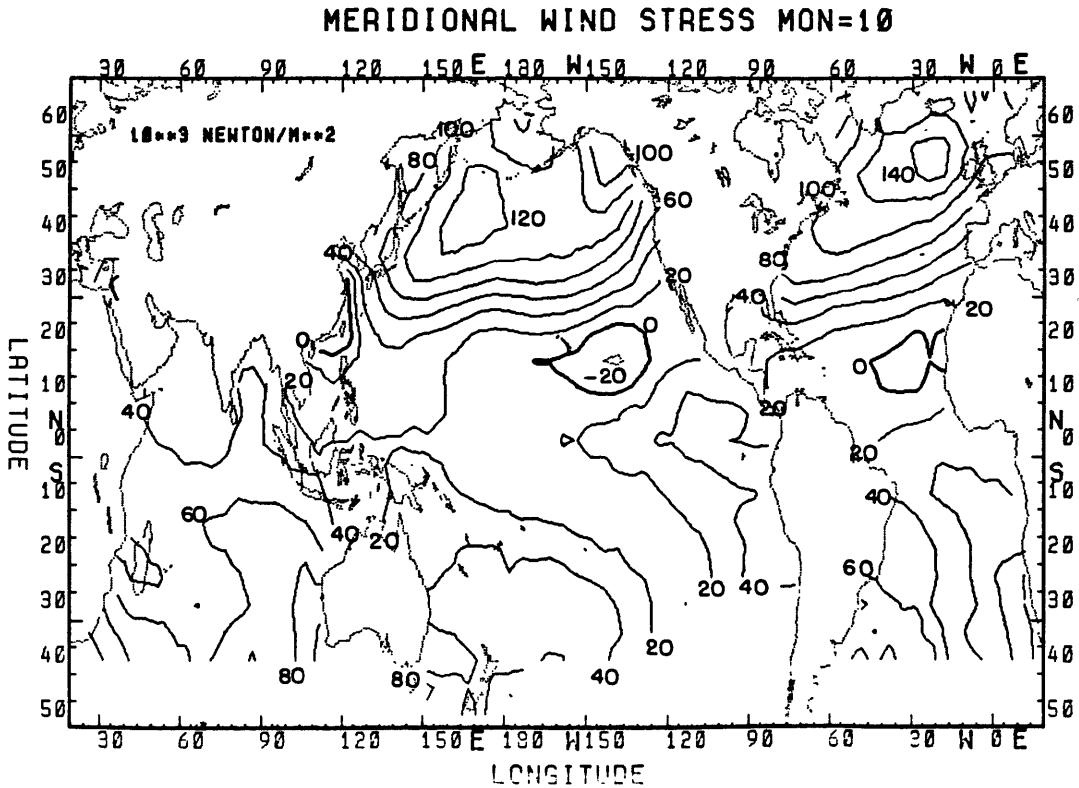


Figure E.8 Long term October means of meridional wind stress

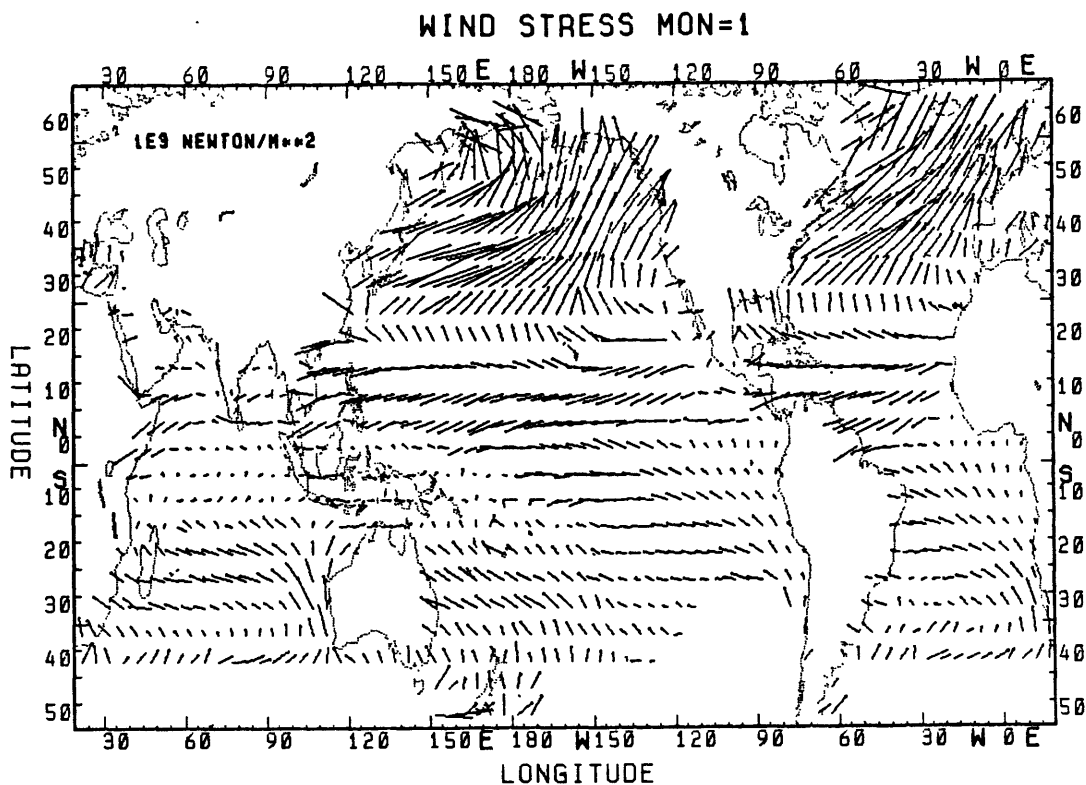


Figure E.9 Long term monthly means of wind stress vector for January

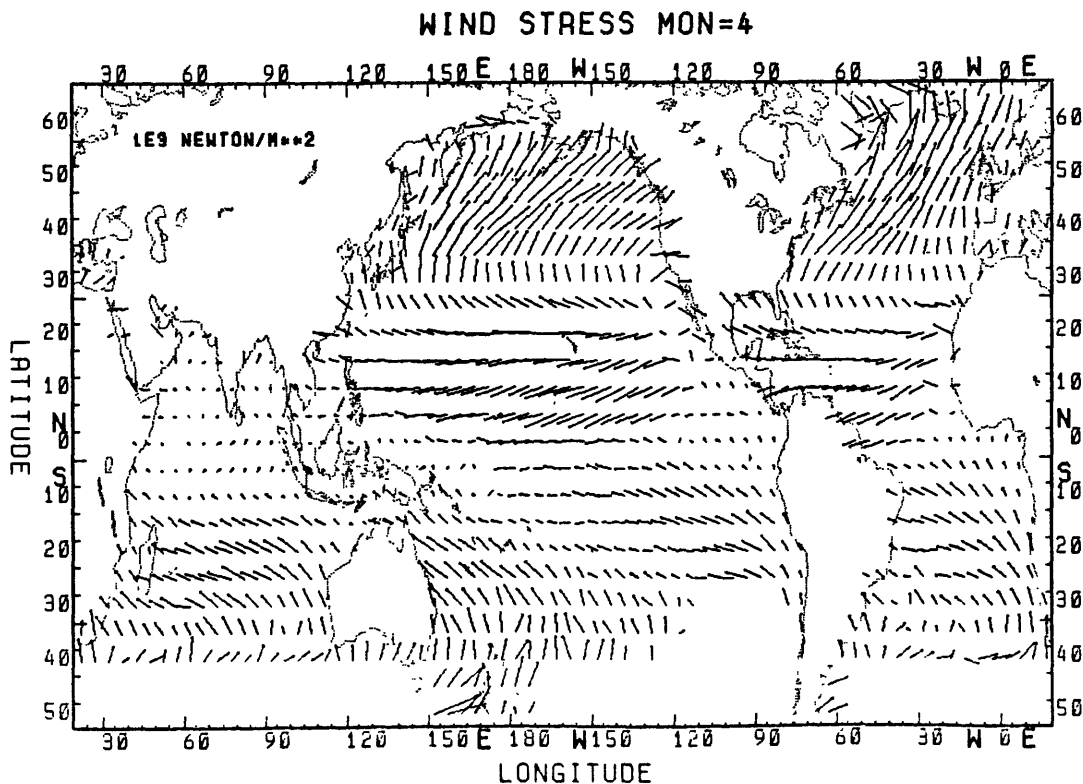


Figure E.10 Long term monthly means of wind stress vector for April

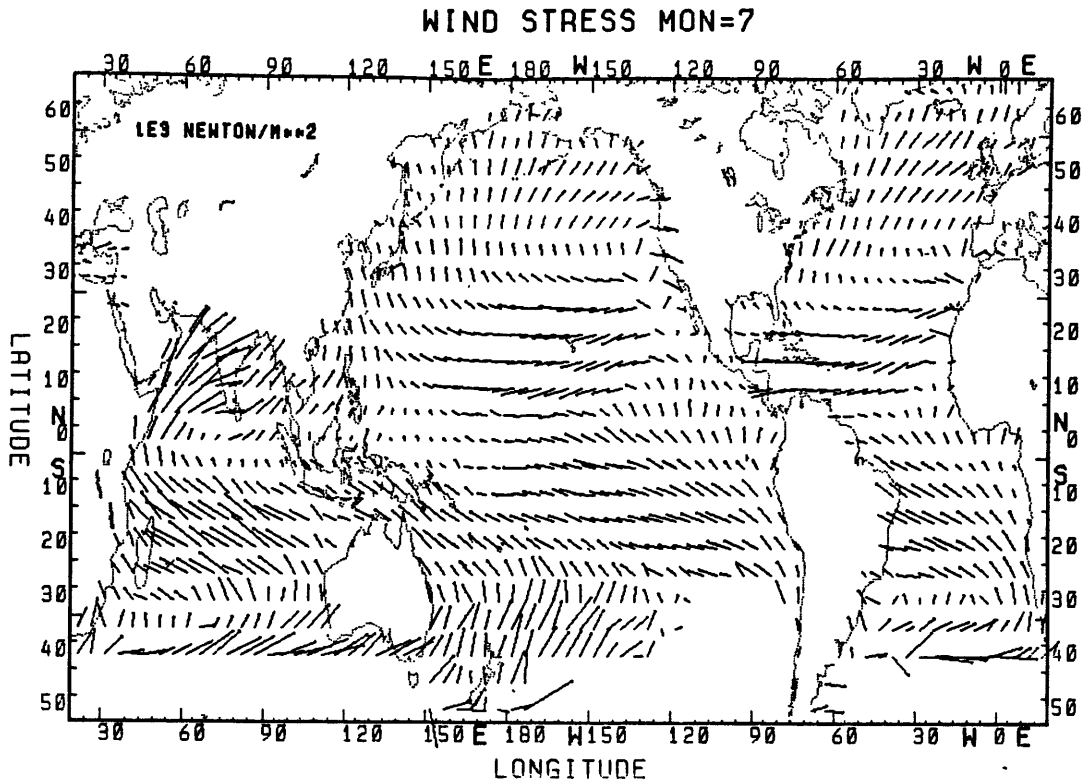


Figure E.11 Long term monthly means of wind stress vector for July

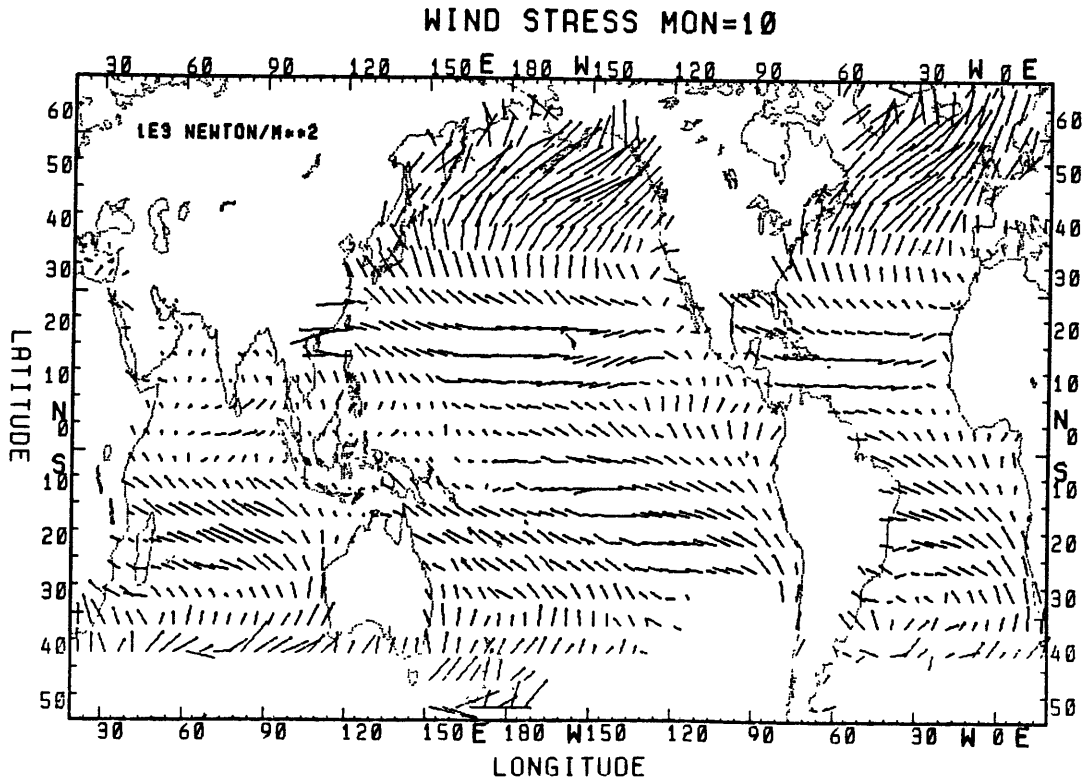


Figure E.12 Long term monthly means of wind stress vector for October

REFERENCES

- Aagaard K. and P. Greisman, 1975: Towards new mass and heat budgets for the Arctic Basin, J. Geophys. Res., 80, 3821-3827
- Angell, J.K., 1981: Comparison of variations in atmospheric quantities with sea surface temperature variation in the equatorial eastern Pacific, Mon. Wea. Rev., 109, 230-243
- Berliand, T.G., 1960: Method of climatological calculation of global radiation, (in Russian), Meteoro i Gidrol., 6, 9-12
- Bennett, A.F., 1978: Poleward heat fluxes in southern hemisphere oceans, J. Phys. Oceanog., 8, 785-798
- Bjerknes, J., 1966: A possible response of atmospheric Hadley circulation to equatorial anomalies of ocean temperature, Tellus, 18, 820-828
- Boer, G., and K. Higuchi, 1980: A study of climatic variability, Mon. Wea. Rev., 108, 1326-1322
- Box, G.E., and G.M. Jenkins, 1976: Time Series Analysis: Forecasting and Control, Holden-Day, Inc., San Francisco, Calif., 575 pp.
- Bryan, K., 1962: Measurement of meridional heat transport by ocean currents, J. Geophys. Res., 67, 3403-3414
- Bryden, H.L., and M.M. Hall, 1980: Heat transport by currents across 25°N latitude in the Atlantic Ocean, Science, 207, 884-886
- Budyko, M.I., 1956: The Heat Balance of the Earth's Surface, Gidrometeorologicheskoe izdatel'stvo, Leningrad, U.S.S.R. 259 pp. (Translation available from U.S. Dept. of Commerce, Washington D.C.)
- Budyko, M.I., 1963: Atlas of the Heat Balance of the Earth, Gidrometeorozdat, 69 pp.
- Bunker, A.F., 1976: Computations of surface energy flux and annual air-sea interaction cycles of the North Atlantic Ocean, Mon. Wea. Rev., 104, 1122-1140
- Bunker, A.F., H. Charnock, and R.A. Goldsmith, 1982: A note on the heat balance of the Mediterranean and Red Seas, J. Marine Res., 40 Suppl., 73-84
- Businger, S., and G.H. Goulb, 1969: Singular value decomposition of a complex matrix, Comm. Acn, 12, 564-565

- Chervin, R.M., and S.H. Schneider, 1976: A study of the response of NCAR general circulation model climatological statistics to random perturbations : Estimating noise levels, J. Atmos. Sci., 33, 391-404
- Chiu, L.S., 1980: An ocean atmosphere energy climate model, Sc.D. thesis, Dept. of Meteorology, Mass. Inst. of Technology, Cambridge, Ma. 159 pp.
- Chiu, L.S., and R.E. Newell, 1983: Variations of zonal mean sea surface temperature and large scale air-sea interations, Quart.J.Roy.Met.Soc., 109, 153-168
- Clark, N.E., 1967: Large-scale heat transfer processes and fluctuations of sea surface temperature in the North Pacific Ocean, Ph.D. thesis, Dept. of Meteorology, Mass. Inst. of Technology, Cambirdge, Ma. 148 pp.
- Covey, D.L., and S. Hastenrath, 1978: The Pacific El Nino phenomenon and the Atlantic circulation, Mon. Wea. Rev., 106, 1280-1287
- Douglas, A., D. Cayan, and J. Namias, 1982: Large scale changes in North Pacific and North American weather patters in recent decades, Mon. Wea. Rev., 110, 1851-1862
- Emig, M., 1967: Heat transport by ocean currents, J. Geophs. Res., 72, 2519-2529
- Essenwanger, D., 1976: Applied Statistics in Atmospheric Sciencés, Part A: Frequencies and curve fitting development in atmospheric sciences, 4A, Elsevier, 252-275
- Frankingoul, C., 1978: Stochastic forcing models of climatic variability, Dynamics of Atmosphere and Oceans, 465-479
- Frankingoul, C., and K. Hasselmann, 1977: Stochastic climatic models: Part II: Application to SST anomalies and thermocline variability, Tellus, 29, 289-305
- Fu, L.-L., 1981: The general circulation and meridional heat transport of the subtropical south Atlantic determined by inverse methods, J. Phys. Oceanog., 11, 1171-1193
- Georgi, D.T., and J.M. Toole, 1982: The Antartic circumpolar current and the oceanic heat and freshwater budgets, Jour. Marine Res., 40 Suppl., 183-197
- Gilman, D.H., 1957: Empirical orthogonal functions applied to 30-day forecasting, Scientific Report No. 1. Contract No. AF19(604)-1238, Dept. of Meteorology, Mass. Inst. of Technology, Cambridge, Ma.

- Goulb, G.H., and C. Reinsch, 1970: Singular value decomposition and least square solutions, Num. Meth., 14, 403-420
- Hastenrath, S. and P. Lamb, 1978: Climatic Atlas of the Tropical Atlantic and Eastern Pacific Oceans, University of Wisconsin Press, 90 pp.
- Hastenrath, S., 1978: On modes of tropical circulation and climate anomalies, J. Atmo. Sci., 35, 2222-2231
- Hastenrath, S. and M.C. Wu, 1982: Oscillations of upper air circulation and anomalies in the surface climate of the tropics, Arch. Met. Geoph. Biokl. Ser. B, 31, 1-37
- Hastenrath, S., 1980: Heat budget of tropical ocean and atmosphere, J. Phys. Oceanog., 10, 159-170
- Hastenrath, S., 1982: On Meridional heat transport in world ocean, J. Phys. Oceanog., 12, 922-927
- Hellerman, S., 1967: An updated estimates of the wind stress on the world ocean, Mon. Wea. Rev., 95, 607-627. With Correction notice in 1968, Mon. Wea. Rev., 96, 63-74
- Horel, J.D., and J.M. Wallace, 1981: Planetary scale atmospheric phenomena associated with the southern oscillation, Mon. Wea. Rev., 109, 813-829
- Katz, R., 1982: Statistical evaluation of climate experiments with general circulation models: A parametric time series modeling approach, J. Atmos. Sci., 39, 1446-1455
- Kendall, M., 1980: Multivariate Analysis, Charles Griffin and Company, Ltd., Bucks., England
- Kukla, G.J., J.k. Angell, J. Korshover, H.Dronia, M. Hoshigi, J.Namias, M. Rodewald, R. Yamamoto, and T. Iwashima, 1977: New data on climatic trends, Nature, 270, 573-577
- Kidson, J.W., 1975: Tropical eigenvector analysis and the southern oscillation, Mon. Wea. Rev., 103, 197-216
- Kutzbach, J.E., R.M. Chervin, and D.D. Houghton, 1977: Response of the NCAR general circulatory model to prescribed changes in ocean surface temperature, Part I: Mid-latitude changes, J. Atmo. Sci., 34, 1200-1213
- Lamb, P.J., 1981: Estimates of annual variation of Atlantic Ocean heat transport, Nature, 290, 766-768

- Ledley, T.S., 1983: A study of climate sensitivity using energy balance cryospheric models, Ph.D. thesis, Dept. of Meteorology, Mass. Inst. of Technology, Cambridge, Ma. 314 pp.
- Levitus, S., 1982: Climatological Atlas of the World Ocean, NOAA Professional Paper 13, U.S. Dept. of Commerce, NOAA, Rockville, Md., 173 pp.
- Liu, W.T., B.K. Kristina, and J.A. Businger, 1979: Bulk parameterization of air-sea exchange of heat and water vapor including the molecular constraints at the interface, J. Atmos. Sci., 36, 1722-1735
- Lorenz, E.N., 1956: Empirical Orthogonal Functions and Statistical Weather Prediction, Scientific Report No. 1, Statistical Forecasting Project, Mass. Inst. of Technology, Cambridge, Ma.
- Lowe, P.R., 1977: An approximating polynomial for the computation of saturation vapor pressure, J. Appl. Met., 16, 100-103
- Munk, W.H. 1960: Smoothing and Persistence, J. Met., 17, 92-94
- Newell, R.E., J.W. Kidson, D.G. Vincent and G.J. Boer, 1974: The General Circulation of the Tropical Atmosphere and Interactions with Extratropical Latitudes, vol. 2, The MIT Press, Cambridge, Ma., 371 pp.
- Newell, R.E., and B.C. Weare, 1976a: Ocean temperature and large scale atmospheric variations, Nature, 262, 40-41
- Newell, R.E., and B.C. Weare, 1976b: Factors controlling tropospheric mean temperature, Science, 194, 1413-1414
- Newell, R.E., and J.Hsiung, 1979: Fluctuations in zonal mean sea surface temperature, Revisita Italiana de Geofisica e Science Affini, 5, 121-125
- Newell, R.E., 1978: Climate and the Ocean, American Scientist, 67, 405-416
- Newell, R.E., L.S. Chiu, W. Ebisuzaki, A.R. Navato, and H.B. Selkirk, 1981: 'The oceans and ocean currents: their influence on climate' in International Conference: Climate and Offshore energy resources, American Meteorological Society, Boston, Ma., 59-112
- Newell, R.E., H.B. Selkirk, and W. Ebisuzaki, 1982: The southern oscillation: Sea surface temperature and wind relationships in a 100-year data set, J. Climatology, 2, 357-373
- North, G.R., T.C. Bell, R.F. Cahaler and F.J. Moeng, 1982: Sampling errors in the estimation of empirical orthogonal functions, Mon. Wea. Rev., 110, 75-82

- Payne, R.E., 1972: Albedo of the sea surface, J. Atmos. Sci., 29, 959-970
- Pedlosky, J., 1975: The development of thermal anomalies in a coupled ocean atmosphere model, J. Atmos. Sci., 32, 1501-1514
- Preisendorfer, R.W. and T.P. Barnett, 1977: Significance tests for empirical orthogonal functions, Preprints, 5th conference on Probability and Statistics in Atmospheric Sciences, Las Vegas, American Meteorological Society, Boston, Ma., 169-172
- Rasmusson, E.M., D.A. Arkin, W.Y. Chen and J.B. Julickee, 1981: Biennial variations in surface temperature over the United States as revealed by singular value decomposition, Mon. Wea. Rev., 109, 587-598
- Reed, R.K., 1977: On estimating insolation over the ocean, Jour. Phys. Oceanog., 7, 482-485
- Reiter, E.R., 1978: The interannual variability of the ocean atmosphere system, J. Atmos. Sci., 35, 349-370
- Roemmich, D., 1980: Estimation of meridional heat flux in the North Atlantic Ocean by inverse methods, J. Phys. Oceanog., 10, 1171-1193
- Rowntree, P.R., 1972: The influence of tropical equatorial Pacific Ocean temperature on atmosphere, Quart. J. Roy. Met. Soc., 98, 290-321
- Rowntree, P.R., 1976: Response of the atmosphere to a tropical Atlantic ocean temperature anomaly, Quart. J. Roy. Met. Soc., 106, 607-625
- Rowntree, P.R., 1979: The effect of changes in SST on atmosphere, Dynamics of atmosphere and oceans, 3, 373-390
- Seckel, G.R., 1970: The trade wind zone oceanography pilot study, Part III: Sea level meteorological properties and heat exchange processes, July, 1963 to June 1965, Report, Fisheries, No. 612.
- Simpson, J.J., and C.A. Paulson, 1979: Mid-ocean observations of atmospheric radiation, Quart. J. Roy. Met. Soc., 105, 487-502
- Sverdrup, H.V., 1957: 'Oceanography' in Handbuch der Physik, 48, 608-670
- Vonder Haar and A.H. Oort, 1973: New Estimate of annual poleward energy transport by northern hemisphere oceans, J. Phys. Oceanog., 2, 169-172
- Walker, G.T., 1923: Correlation in seasonal variations of weather VIII. A preliminary study of world weather. Mem. Indian Met. Dept., 24, 75-131
- Walker, G.T., and E.W. Bliss, 1932: World weather V., Mem. Royal Met. Soc., 4(36), 53-84

- Warren, B.A., 1983: Why is no deep water formed in the North Pacific?, Jour. Marine Res., 41, 327-347
- Weare, B.C., A.R. Navato and R.E. Newell, 1976: Empirical orthogonal function analysis of Pacific Ocean surface temperatures, J. Phys. Oceanog., 6, 671-678
- Weare, B.C., 1977: Empirical orthogonal analysis of Atlantic Ocean surface temperatures. Quart. J. Roy. Met. Soc., 103, 467-478
- Weare, B.C., 1979: A statistical study of the relationship between ocean temperature and the Indian monsoon, J. Atmos. Sci., 36, 2279-2291
- Weare, B.C., and P.T. Strub, 1981: The significance of sampling biases on calculated monthly mean oceanic surface heat fluxes, Tellus, 33, 211-224
- Weare, B.C., P.T. Strub, and M.D. Samuel, 1981: Annual mean surface heat flux in the tropical ocean, J. Phys. Oceanog., 11, 705-717
- Weare, B.C., P.T. Strub, and M.D. Samuel, 1980: Marine Atlas of the Tropical Pacific Ocean, Dept. of Land, Air and Water Resources, Univ. of Calif., Davis, Calif., 147 pp.
- Weare, B.C., 1983: Interannual variation in net heating at the surface of the tropical Pacific Ocean, J. Phys. Oceanog., 5, 873-885
- Webster, P.T., 1981: Mechanisms determining the atmospheric response to SST anomalies, J. Atmos. Sci., 38, 554-571
- Wunsch, C., 1980: Meridional heat flux of the North Atlantic Ocean, Proc. Natl. Acad. Sci., 77, 5043-5047
- Wunsch, C., D. Hu, and B. Grant, 1983: Mass, heat, salt and nutrient fluxes in the South Pacific Ocean, J. Phys. Oceanog., 13, 725-753
- Wyrtki, K., 1965: The average annual heat balance of the North Pacific Ocean and its relation to ocean circulation, J. Geophys. Res., 70, 4547-4549
- Wyrtki, K., 1975: El Nino - the dynamic response of the equatorial Pacific Ocean to atmospheric forcing. J. Phys. Oceanog., 5, 572-584

ACKNOWLEDGEMENT

I would like to express my sincere thanks to my thesis supervisor, Professor Reginal E. Newell. This thesis would not have been possible without his constant guidance and encouragement. His cheerful disposition and his enthusiasm in this work have been a constant source of inspiration throughout the preparation of this thesis.

I thank members of my thesis committee: Professors Ron Prinn, Ed Lorenz and Erik Mollo-Christiansen for their constructive criticisms. Special thanks goes to Professor Mollo-Christiansen for his generosity in given me computer time on his PDP 11/60. The thesis would have taken a lot longer without his assistance.

I like to thank my husband, Michael Wojcik, for putting up with me while this thesis was being done. His encouragement and support were always there when I most needed it. In addition, his painstaking proofreading of my thesis is greatly appreciated.

Members on the 15th floor deserve special mention in their supporting roles during the preparation of my thesis. They have offered their time and encouragement when I needed it.

Initial process of the data set was done at Group 28 at Lincoln Laboratory on their DEC VAX/780. Their support for student research on the computer made this thesis work possible. All the non-computer generated graphs in the thesis were done by the steady hands of Isabelle Kole. This work was done under support from the Department of Energy contract DE-AC02-76EV12195.

BIOGRAPHICAL NOTE

I was born on June 28, 1952 in Taiwan, China. My family came to the United States in 1965 when my father was assigned to the United Nations. I became a naturalized citizen in 1975. I graduated from Barnard College in 1974, majoring in mathematics and geology. I went to work at Meteorology Research, Inc. for a year as a meteorologist and came to Massachusetts Institute of Technology in 1976 for my graduate work in Meteorology. After an M.S. in meteorology, I took a two-year leave of absence and worked as a mathematican programmer at Pacific Gas and Electric Company. I came back to MIT in 1980 to continue my studying towards a Ph.D. degree in meteorology. I married Michael A. Wojcik in July, 1980.